QCD resummation for TeV scale jet substructure

Jack O. Helliwell

A thesis submitted to the University of Manchester for the degree of
Doctor of Philosophy
in the Faculty of Science and Engineering

2022

School of Natural Sciences

Department of Physics and Astronomy

Contents

Contents **2**

List of figures **5**

Abstract **8**

Declaration of originality **9**

Copyright statement **10**

Acknowledgements **11**

1 Introduction **12**

2 Quantum Chromo Dynamics **14**
- 2.1 The QCD Lagrangian 14
- 2.2 Quantisation and Feynman rules 15
- 2.3 Renormalisation and the running coupling 18
- 2.4 The soft and collinear limits of QCD 23
  - 2.4.1 Infra-red divergences 23
  - 2.4.2 The soft limit 25
  - 2.4.3 The collinear limit 26
  - 2.4.4 Large logarithms 27
- 2.5 Resummation 28
  - 2.5.1 Accounting for correlated emissions 31
  - 2.5.2 Resumming multiple emissions 33

3 Jets and jet substructure **36**
- 3.1 Modelling hadron collider events 36
  - 3.1.1 Event generators and parton showers 38
- 3.2 What is a jet? 39
- 3.3 Jet grooming 41
- 3.4 Jet tagging 45
  - 3.4.1 Prong finding 47
  - 3.4.2 Jet shapes 50
  - 3.4.3 Machine learning taggers 55
- 3.5 Jet substructure for the study of QCD 58
- 3.6 Summary 61

4 The NNLL structure of the groomed jet mass at NLO 63
4.1 Introduction 63
4.2 Observable definition and leading-log resummation 65
4.3 Leading order calculation and expansion of NLL result 67
  4.3.1 Leading-order calculation 67
  4.3.2 NLL result at second order 70
4.4 NNLL at second order: the triple-collinear limit 71
  4.4.1 Gluon emission contribution 71
  4.4.2 Gluon decay contributions 81
4.5 Structure of NNLL results 90
4.6 Conclusions 92

5 NNLL resummation of groomed observables 94
5.1 Introduction 94
5.2 Observable definition and approach to resummation 95
5.3 The simplified groomer 97
  5.3.1 Calculating $C^{\mathrm{r.c}}(v)$ 101
5.4 The clustering correction 103
  5.4.1 Independent emission clustering correction 103
  5.4.2 Correlated emission clustering correction 108
5.5 Phenomenology 111
  5.5.1 Finite z_{cut} 112
  5.5.2 Matching 113
  5.5.3 Results 114
5.6 Conclusions 115

6 Understanding boosted top tagging with prong finding and N-subjettiness 118
6.1 Introduction 118
6.2 Monte-Carlo study 120
6.3 $\mathrm{Y_m}$-Splitter splitter with a τ_{32} cut : QCD jets 122
  6.3.1 Leading-order result 122
  6.3.2 Resummed results 124
  6.3.3 Finite τ corrections 126
6.4 Signal jets 137
  6.4.1 Jet mass distribution for top jets 138
  6.4.2 Top jets with $\mathrm{Y_m}$-Splitter 140
  6.4.3 $\mathrm{Y_m}$-Splitter with grooming for signal jets 142
  6.4.4 $\mathrm{Y_m}$-Splitter with τ_{32} and grooming for signal jets 144
6.5 Exploiting jet mass cuts 147
6.6 Conclusions 151

7 Summary 153

References 156

Appendices 179

A Appendices for Chapter 4 180

B Appendices for Chapter 5 185

C Appendices for Chapter 6 187

Word Count: 65023

List of figures

2.1 The Feynman diagrams needed to compute the total cross-section for a virtual photon decaying to hadrons at $\mathcal{O}(\alpha_s)$. 23

2.2 Configurations which together give rise to non-global logarithms for observables computed on the left hemisphere only. 30

2.3 Examples of diagrams that are included by setting the argument of the coupling to the transverse momentum of the primary gluon emission. Although only one and two loop configurations are shown, diagrams with any number of loops inserted into the primary gluon line are resummed by choosing the argument of the coupling to be k_t. . . . 31

2.4 A Lund diagram showing the region of phase space in which real emissions are vetoed when a cut $\frac{m^2}{Q^2} < \rho$ is imposed, where m is the heavy hemisphere mass. 35

3.1 Plot showing the fraction of jets simulated with Pythia with $P_t >$ 2TeV remaining after a cut $\tau_{32} < \tau$ is applied at parton and hadron level with MPI and ISR deactivated and at hadron level with ISR and MPI activated. 42

3.2 47

3.3 ROC curves showing the signal and background tag rates for several combinations of prong-finding and grooming studied in [25], where the plots are taken from. The curves on the left are derived from events generated using Pythia, whist the curves in the right hand plots are calculated analytically. 50

3.4 53

3.5 ROC curves taken from ref. [28] showing the signal vs background tag rates as the cut on τ_{21} is varied. On the left the jets are simply tagged with a cut on τ_{21} whereas on the right they are first groomed using soft drop with $\beta = 2$. 54

3.6 ROC curves comparing the tagging performance of a number of ML based top taggers and a benchmark cut based tagger. Plot taken from [32] 55

3.7 A plot of performance $\left(\frac{\epsilon_s}{\sqrt{\epsilon_b}}\right)$ against resilience to non-perturbative effects for W boson tagging for the LundNet family of taggers, the Lund+LSTM tagger of [125] and two other ML taggers [33], [153]. Plot taken from [34].) 57

3.8 CMS measurement of the mMDT groomed jet mass compared to two different resummed calculations and three different event generator predictions. Plot taken from [123] 59
3.9 61

4.1 An illustration of the parametrisation used for kinematic variables in the gluon emission process, relevant to the triple-collinear limit calculation discussed in the main text. 72
4.2 An illustration of the kinematic parametrisation in the $C_F T_R n_f$ gluon decay channel. 82

5.1 The configuration responsible for the independent emission clustering correction, where two soft emissions with $z_i < z_{\text{cut}}$ are de-clustered from the parent parton as a single branch which as a whole passes the z_{cut} condition. 104
5.2 Lund diagram showing the region of phase space responsible for the independent emission clustering correction in blue. The region shown in red is the vetoed phase space responsible for the Sudakov factor. The two dots represent possible locations in the phase space for the pair of emissions which generate the clustering correction. Discussion of the hashed area, which contributes in principle to the clustering correction but turns out only to beyond NNLL accuracy, is postponed to later in this section. 105
5.3 The configuration responsible for the correlated emission clustering correction. Both gluons have $z_i < z_{\text{cut}}$, but have a combined energy fraction greater than z_{cut}. The two gluons are clustered in separate C/A branches, with branch two being de-clustered from the jet first and groomed away. The other gluon is then de-clustered from the quark and is also groomed way. 108
5.4 Lund diagram showing the region of phase space responsible for the correlated clustering correction in blue, and in red the vetoed phase space responsible for the Sudakov factor. The black dots depict two correlated emissions, which, due to their separation in angle are clustered into different C/A branches, giving rise to the clustering correction, while the black square represents the parent whose branching gives rise to the correlated pair responsible for the clustering correction. 110
5.5 Matched NLL predictions alongside the LL result, both with finite z_{cut} effects showing the central values and uncertainty bands. 114
5.6 Predictions for the cumulative jet mass distribution at various levels of accuracy for three different values of z_{cut} 116

6.1 Plots showing the signal to square-root background of the six variants of the tagging procedure at parton level, hadron level, and with ISR and MPI activated at hadron level. 121

6.2 Lund diagrams showing the region of phase space vetoed for jets which are groomed with Soft Drop and tagged with $\mathrm{Y_m}$-Splitter and a cut on τ_{32}. 133

6.3 Diagram showing the parametrisation of the energy fraction variables used along with our labelling of the partons in the C_F^2 channel. 135

6.4 A comparison of our calculation for background tagging rate against parton show Monte Carlo simulations for no grooming, grooming with Soft Drop $\beta = 2$, and grooming with mMDT. 137

6.5 A comparison between our analytical calculation of the cumulative jet mass distribution $\Sigma(\rho)$ for top quark initiated jets with $\rho = m^2/R^2p_T^2$, with $p_T > 2$ TeV and the same distribution derived from Pythia simulations. 139

6.6 A comparison between different levels of approximation in analytical calculations and a Pythia simulation for top jets tagged with $\mathrm{Y_m}$-Splitter in a mass range $163\,\mathrm{GeV} < m < 225\,\mathrm{GeV}$ with $\zeta = 0.05$ as a function of $m_{\min}$. 143

6.7 A comparison between our analytical calculations and a Pythia simulation for pre-groomed top jets tagged with $\mathrm{Y_m}$-Splitter in a mass range $163\,\mathrm{GeV} < m < 225\,\mathrm{GeV}$ with $\zeta = 0.05$ as a function of $m_{\min}$. . . 144

6.8 Comparison between our analytic calculation (crosses) and Pythia for the tagged signal distribution as a function of the cut on τ_{32} for jets without pre-grooming (left) , with pre-grooming using Soft Drop (centre) and with pre-grooming using the mMDT. 147

6.9 Analytic and Monte Carlo parton level curves showing how the signal tagging rate varies with $m_{\max}$. 148

6.10 Analytic and Monte Carlo (parton level) curves showing how the background tagging rate varies with $m_{\max}$. 149

6.11 Signal significance against efficiency for three variations on the tagging procedure. All jets are groomed with mMDT and tagged with $\mathrm{Y_m}$-Splitter . Either τ or $m_{\max}$ is varied with a fixed cut placed on the other. The samples were produced using Pythia with hadronisation and UE activated. 150

6.12 A measure of resilience to non-perturbative effects as $m_{\max}$ varies for three cuts on τ_{32}. Jets are pre-groomed with mMDT. 150

Abstract

In this thesis we study aspects of jet substructure through first principles calculations in Quantum Chromo Dynamics (QCD). To begin with, a short introduction to QCD, paying particular attention to the soft and collinear limits, is presented, followed by a brief review of jet substructure.

Following this review material, the next-to-next-to-leading logarithmic (NNLL) structure of the groomed jet mass is investigated at $\mathcal{O}(\alpha_s^2)$. This is done by carrying out a next-to-leading-order calculation in the collinear limit of the heavy-hemisphere mass distribution, where each hemisphere has been groomed with the modified mass drop tagger (mMDT), starting from the the triple collinear splitting functions. This calculation sheds light to the relationship between the triple collinear splitting function and NNLL structure of collinear logarithms, which is important for efforts to include triple collinear splitting functions in parton showers [1]–[3]. It also provides the insight needed to carry out the NNLL resummation for distributions of groomed observables, which is the subject of chapter 5. This has potential applications in precision studies of groomed observables at the LHC, or other collider.

In chapter 6, we investigate a method for tagging boosted top quarks, using a combination of grooming, prong finding, and cutting on a jet shape, by carrying out resummed calculations for the tagged fraction of both signal and background jets. This allows us to understand, from first principles, the the interplay between the different steps involved in the tagging procedure.

Declaration of originality

I hereby confirm that no portion of the work referred to in the thesis has been submitted in support of an application for another degree or qualification of this or any other university or other institute of learning.
The work presented in chapter 4 was carried out in collaboration with: Daniele Anderle, Mrinal Dasgupta, Basem Kamal El-Menoufi and Marco Guzzi, and is published in ref. [4], from which much of the text and figures are taken.
The work in chapter 6 was carried out in collaboration with Mrinal Dasgupta, and is published in ref. [5], from which the majority of the text and figures are taken.

Copyright statement

i The author of this thesis (including any appendices and/or schedules to this thesis) owns certain copyright or related rights in it (the “Copyright”) and s/he has given The University of Manchester certain rights to use such Copyright, including for administrative purposes.

ii Copies of this thesis, either in full or in extracts and whether in hard or electronic copy, may be made *only* in accordance with the Copyright, Designs and Patents Act 1988 (as amended) and regulations issued under it or, where appropriate, in accordance with licensing agreements which the University has from time to time. This page must form part of any such copies made.

iii The ownership of certain Copyright, patents, designs, trademarks and other intellectual property (the “Intellectual Property”) and any reproductions of copyright works in the thesis, for example graphs and tables (“Reproductions”), which may be described in this thesis, may not be owned by the author and may be owned by third parties. Such Intellectual Property and Reproductions cannot and must not be made available for use without the prior written permission of the owner(s) of the relevant Intellectual Property and/or Reproductions.

iv Further information on the conditions under which disclosure, publication and commercialisation of this thesis, the Copyright and any Intellectual Property and/or Reproductions described in it may take place is available in the University IP Policy (see `http://documents.manchester.ac.uk/DocuInfo.aspx?DocID=24420`), in any relevant Thesis restriction declarations deposited in the University Library, The University Library’s regulations (see `http://www.library.manchester.ac.uk/about/regulations/`) and in The University’s policy on Presentation of Theses.

Acknowledgements

I would like to thank my supervisor, Mrinal Dasgupta, for his help and guidance whilst carrying out the work presented here.

The work presented in chapter 4 was carried out in collaboration with Daniele Anderle, Mrinal Dasgupta, Basem Kamal El-Menoufi and Marco Guzzi, all of which I am grateful to for their collaboration. I am particularly grateful to Mrinal Dasgupta and Basem Kamal El-Menoufi for also collaborating with me on the work presented in chapter 5. In relation to chapter 5, I would also like to thank Aditya Pathak for helping me to understand aspects of a resummation of the groomed jet mass carried out within the soft collinear effective theory (SCET) framework.

I would also like to thank those that I have shared an office with over the course of this work: Baptiste Cabouat, Kiran Ostrolenk, Jack Holguin, Matthew De Angelis, Farid Hounat, Fernando Torre, Lawrie Smith, and Ross Jenkinson, for helpful discussions. I am particularly grateful to Kiran Ostrolenk for his help with numerous computing issues towards the start of my studentship.

Finally, I am grateful to STFC for the studentship which has enabled me to carry out the work presented in this thesis.

Chapter 1

Introduction

The Standard Model (SM) is a theory describing all known elementary particles and three of the four fundamental forces: the electro-magnetic, weak, and strong forces [6]. The discovery of the Higgs boson by the ATLAS [7] and CMS [8] experiments at the Large Hadron Collider (LHC), in 2012, constituted the observation of the only fundamental particle predicted by the standard model which had not previously been observed. Despite this, and numerous other predictions which have been shown to agree with experiments, the standard model cannot be complete as there are a number of phenomena it fails to explain. Commonly cited examples are: the lack of a dark matter candidate within the SM, which is needed to explain the rotation curves of galaxies, and the SM's inability to explain the observed matter–anti-matter asymmetry of the universe.

The LHC offers new opportunities to precisely test the SM and search for physics beyond the standard model by colliding protons with a center of mass energy of 13 TeV, the highest energy of any collider experiment to date. Collimated jets of hadrons, or simply jets, are ubiquitous in LHC analyses. They are associated with the production of quarks and gluons, collectively known as partons, which interact via the strong force. The evolution of these partons into jets is governed by Quantum Chromo Dynamics (QCD), the part of the standard model which describes the strong force. Because of the high center of mass energy at the LHC, electroweak scale particles, such as W, Z and Higgs bosons can be produced with transverse momentum much larger than their mass, leading to their decay products being highly collimated. In the case that these decay products are quarks, the resulting jets of hadrons can be close enough in angle that they are reconstructed as a single jet. Discriminating such jets from those initiated by a single parton can be accomplished by examining their substructure. Initially driven by the need to tag these jets, the study of jet substructure is now firmly established as a key area of LHC phenomenology, with a large number of jet substructure techniques being proposed and used [9]–[20]. An improved understanding of jet substructure techniques, gained from first principles calculations in QCD, has improved confidence in their robustness, facilitated the improvement of existing techniques, and resulted in the development of new, better, techniques [21]–[31]. Another facet of jet substructure is the use of machine learning techniques for jet tagging. Such techniques can yield impressive performance [32]–[38], though often at the expense of understanding what information is being learnt. Jet substructure is also increasingly being used to study of QCD with precise measurements and theory predictions having been produced and compared for a number of observables [39]–[49]. A brief review of some aspects of jet substructure is presented in chapter 3, where both jet tagging and the study of QCD through jet substructure is discussed. Before this, a short introduction to QCD is presented in chapter 2. The latter half of this chapter focuses on the emission of gluons at energies much lower than the emitting partons (the soft region of phase space), and the branching of partons in collinear limit. It is then demonstrated how the logarithms that arise from these soft and collinear regions of phase space can be resummed to all orders, and why this is necessary.

The work presented in chapters 4 and 5 is concerned with distributions of observables, computed on jets which have been groomed with the modified mass drop tagger (mMDT) [21], at the level of next-to-next-to-leading logarithmic (NNLL) accuracy. In chapter 4, the NNLL structure of the groomed jet mass is studied at second order in the strong coupling. This is done by calculating this distribution directly from the triple collinear splitting functions [50]–[52]. As well as allowing for a better understanding of the link between the triple collinear splitting functions and NNLL structures, this work provided the insight needed to carry out the resummation of any groomed, additive, rIRC safe observable, to NNLL accuracy, for quark initiated jets. This resummation is carried out in chapter 5 in the small z_{cut} limit before being modified to include finite z_{cut} effects at NLL accuracy. This has potential applications in precision phenomenological studies at the LHC or other collider and provides a powerful cross check of previous NNLL resummations carried out within soft collinear effective theory [47].

In chapter 6 a method for tagging top quarks using a combination of the Y_m-Splitter [25] algorithm and N-subjettiness ratio τ_{32} [14] is studied. The effect of pre-grooming the jets with mMDT or soft drop [23] is also considered. These studies are initially carried out using Pythia [53] to asses the performance and impact of non-perturbative effects. Resummed results for the tagged fraction of signal and background jets are then derived, formally at leading logarithmic (LL) accuracy, but including some terms at higher logarithmic accuracy. These resummed results give some insights into the interplay between the various steps involved in the tagging procedure and how this interplay can be used to maximise the effectiveness of the tagger.

Finally the work presented in this thesis is summarised and the outlook for future extensions and applications of it are discussed in chapter 7.

Chapter 2

Quantum Chromo Dynamics

Quantum chromo dynamics, or QCD, is the part of the standard model which describes the strong interaction between quarks (fermions) and gluons (gauge bosons). In this section I describe the construction of the theory and some of its properties. In particular we will focus on perturbative QCD in the soft and collinear limits. We begin by looking at the the Lagrangian and how Feynman rules are calculated from it before moving on to loop diagrams and renormalisation. We then look at QCD in the soft and collinear limits before discussing the logarithms that can arise from these regions of phase space and how they can be resummed.

2.1 The QCD Lagrangian

QCD is a non abelian gauge theory with gauge group SU(3). Particles charged under this gauge group are said to have a colour charge. There are three charges, which are typically called red, green, and blue, and three corresponding anti-charges. The Lagrangian density of QCD can be succinctly written as [54], [55]

$$\mathcal{L} = i\bar{\Psi}_i\gamma^\mu D^{ij}_\mu \Psi_j - m\bar{\Psi}_i\Psi_i - \frac{1}{4}F^a_{\mu\nu}F^{a,\mu\nu} \ . \tag{2.1}$$

Here Ψ_i are the quark fields, with the index i running over the three colours, $F^{a,\mu\nu} = \partial_\mu A^a_\nu - \partial_\nu A^a_\mu - g_s f^{abc} A^b_\mu A^c_\nu$, is the field strength tensor, with A^a_μ the gluon field, and $D^{ij}_\mu = \delta^{ij}\partial_\mu - g_s A^a_\mu t^a_{ij}$ is the covariant derivative, with t^a_{ij} the generators of SU(3) in the fundamental representation. The generators can be represented by the Gell-Mann matrices, which are given in ref. [54], and are typically normalised so that

$$t^a_{ij}t^b_{ji} = T_R\delta^{ab}, \qquad \text{with,} \qquad T_R = \frac{1}{2} \ , \tag{2.2}$$

where the upper index (a, b) runs from 1 to 8. The quark fields transform under the fundamental representation of SU(3), so are a three dimensional vector in colour space, whilst the gluon fields, A^a_μ transform under the adjoint representation of SU(3) [54], [56]. A convenient way of writing the generators in the adjoint representation are the structure constants, f^{abc}, which satisfy $t^a_{ij}t^b_{jk} - t^b_{ij}t^a_{jk} = if^{abc}t^c_{ik}$. The Casimir operator is the square of the generators and commutes with all of the generators [55]. With the normalisation given in eq. (2.2) the Casimir operator in the fundamental representation is

$$t^a_{ij} t^a_{jk} = C_F\, \delta_{ik}, \qquad \text{where,} \qquad C_F = \frac{4}{3}\ , \tag{2.3}$$

and in the adjoint representation

$$f^{abc} f^{abd} = C_A \delta^{cd}, \qquad \text{with,} \qquad C_A = 3\ . \tag{2.4}$$

These operators are extremely common in QCD calculations and are particularly important in the collinear limit as we shall see in section 2.4.3.

2.2 Quantisation and Feynman rules

The aim of this section is to illustrate how the path integral can be used to derive Feynman rules, by deriving the gluon propagator as an example. The need to introduce the ghost fields will be illustrated along the way before finally listing a selection of the other Feynman rules most relevant for this thesis.

We start by examining the path integral for the gauge field kinetic terms in the Lagrangian given in eq. (2.1),

$$\int \mathcal{D}\tilde{A}^a_\mu(k) \exp\left[-i \int \frac{\mathrm{d}^4k}{(2\pi)^4} \frac{1}{2} \tilde{A}^a_\mu(k)(k^2 g^{\mu\nu} - k^\mu k^\nu)\tilde{A}^b_\nu(-k)\right]\ , \tag{2.5}$$

where $\tilde{A}^a_\mu(k)$ is the Fourier transform of $A^a_\mu(x)$. We see that we will run into a problem trying to find the momentum space propagator; the operator we need to invert to find the propagator, $k^2 g^{\mu\nu} - k^\mu k^\nu$, is singular. Another manifestation of this problem is that carrying out the path integral involves integrating over an infinite number of modes where the gauge field is of the form $\tilde{A}_\mu(k) = \tilde{\alpha}(k) k_\mu$, with $\tilde{\alpha}(k)$ being any scalar function of k, which causes the path integral to diverge due to the exponent going to zero. These modes are all physically equivalent as they are related by a gauge transformation, $A'^a_\mu t^a_{ij} = e^{i\alpha^b(x)t^b}[A^a_\mu t^a + \frac{i}{g}\partial_\mu]e^{-i\alpha^c(x)t^c}$, to $A^a_\mu(x) = 0$. The solution is to introduce a gauge fixing term. This is very similar to what is done in QED when quantising the electromagnetic field, but comes with an additional subtlety due to the non abelian nature of QCD.

We proceed, using the method of Faddeev and Popov [55], [57], by inserting,

$$1 = \int \mathcal{D}\alpha^b(x) \delta(G(A^a_\mu)) \det \left| \frac{\delta G(A^a_\mu)}{\delta \alpha^b} \right|\ , \tag{2.6}$$

into eq. (2.5), where A^a_μ transforms with $\alpha^b(x)$, $G(A^a_\mu(x)) = \partial^\mu A^a_\mu(x) - \omega^a(x)$, and $\omega^a(x)$ can be any scalar function. This effectively factors the functional integral over physically equivalent gauge configurations out of the integral over A^a_μ, allowing them to be absorbed into the normalisation, which cancels in physical quantities. Using an expression for the gluon field after an infinitesimal gauge transformation,

$$A'^a_\mu = A^a_\mu + \frac{1}{g_s}\partial_\mu \alpha^a(x) + f^{abc}A^b_\mu \alpha^c(x) = A^a_\mu + D_\mu \alpha^a(x) \ , \tag{2.7}$$

the functional determinant in eq. (2.6) becomes $\det|\frac{1}{g_s}\partial^\mu D_\mu|$. Leaving aside some normalisation constant, which will cancel in all physical quantities, we can insert the functional integral $\int \mathcal{D}\omega^a(x) \exp\left[-i\int \mathrm{d}^4x \frac{\omega^a(x)^2}{2\xi}\right]$ into the path integral. The integral over $\omega^a(x)$ can be carried out using the delta function in eq. (2.6), so that the path integral becomes

$$\int \mathcal{D}A^a_\mu \mathcal{D}\alpha^c \det\left|\frac{1}{g_s}\partial^\mu D_\mu\right| \\ \exp\left[-i\int \frac{\mathrm{d}^4x}{(2\pi)^4}\left(\frac{1}{2}A^a_\mu(g^{\mu\nu}\partial^2 - \partial^\mu\partial^\nu)A^b_\nu + \frac{(\partial^\mu A^a_\mu)^2}{2\xi}\right)\right] \ . \tag{2.8}$$

The term, $\frac{(\partial^\mu A^a_\mu)^2}{2\xi}$, can be included from the beginning by adding a gauge fixing term,

$$\mathcal{L}_{\text{g.f}} = -\frac{(\partial^\mu A^a_\mu)^2}{2\xi} \ , \tag{2.9}$$

to the Lagrangian. The determinant in equation (2.8) is not independent of A^a_μ and so cannot be absorbed into the normalisation. It can be evaluated as a functional integral over scalar, Grassmann valued, fields [55]:

$$\det\left|\frac{1}{g_s}\partial^\mu D_\mu\right| = \int \mathcal{D}\bar{c}^a \mathcal{D}c^b \exp\left[i\int \mathrm{d}^4x \bar{c}^a(-\partial^\mu D^{ab}_\mu)c^b\right] , \tag{2.10}$$

where c^a are the Grassmann fields. The term on the right of eq. (2.10) can be included in the path integral by modifying the Lagrangian to include a term:

$$\mathcal{L}_{\text{Ghost}} = \bar{c}^a\partial^\mu D^{ab}_\mu c^b \ . \tag{2.11}$$

The Grassmann fields describe ghost particles, which couple to gluons and have their own Feynman rules. They are not physical final state particles, but nevertheless need to be included as internal lines, as they cancel un-physical gluon polarisations. One way to see that ghosts are not physical particles is by observing that they are absent for certain choices of gauge, for example, axial gauges [55], [56].
Returning now to finding the gluon propagator, we can write the generating functional:

$$Z[J] = \\ \int \mathcal{D}A^a_\mu \mathcal{D}\bar{c}^b \mathcal{D}c^c \exp\left[i\int \mathrm{d}^4x \left(\mathcal{L}_{\text{kinetic}} + \mathcal{L}_{\text{g.f}} + \mathcal{L}_{\text{Ghost}} + J^\mu_a(x)A^a_\mu(x)\right)\right] , \tag{2.12}$$

where

$$\mathcal{L}_{\text{kinetic}} = -\frac{1}{4}\left(\partial_\mu A^a_\nu - \partial_\nu A^a_\mu\right)\left(\partial^\mu A^\nu_a - \partial^\nu A^\mu_a\right) \ , \tag{2.13}$$

$\mathcal{L}_{\text{g.f}}$ was defined in eq. (2.9), $\mathcal{L}_{\text{Ghost}}$ in eq. (2.11), and where $J(x)A^a_\mu(x)$ is a source term. By re-writing the generating functional in terms of a shifted field, $A^a_\mu = A'^a_\mu + i\int \mathrm{d}^4y D^{ab}_{\mu\nu}(x-y)J^\nu_b(y)$, it can expressed as

$$Z[J] = Z_0 \exp\left[-\frac{1}{2}\int \mathrm{d}^4x\,\mathrm{d}^4y J^a_\mu(x) D^{ab}_{\mu\nu}(x-y) J^\nu_b(y)\right] \;, \tag{2.14}$$

where $D^{ab}_{\mu\nu}(x-y)$ is the Greens function of the operator $(g^{\mu\nu}\partial^2 - (1-\xi)\partial^\mu\partial^\nu)$ and

$$Z_0 = \int \mathcal{D}A^a_\mu \mathcal{D}\bar{c}^b \mathcal{D}c^c \exp\left[i\int \mathrm{d}^4x(\mathcal{L}_{\text{kinetic}} + \mathcal{L}_{\text{g.f}} + \mathcal{L}_{\text{Ghost}})\right] \;. \tag{2.15}$$

The generating functional can be used to find the gluon two point function [55]:

$$\frac{1}{Z_0}\frac{\delta}{\delta J^\mu_a(x_1)}\frac{\delta}{\delta J^\nu_b(x_2)} Z[J]\bigg|_{J^\mu_a(x_1)=J^\nu_b(x_2)=0} = \langle 0|A^a_\mu(x_1)A^b_\nu(x_2)|0\rangle = D^{ab}_{\mu\nu}(x_1-x_2) \;. \tag{2.16}$$

In momentum space, the two point function, or Feynman propagator, reads

$$D^{a,b}_{\mu\nu}(k) = \frac{-i}{k^2+i\epsilon}\left(g_{\mu\nu} - (1-\xi)\frac{k_\mu k_\nu}{k^2}\right)\delta^{ab} \;. \tag{2.17}$$

The factor of $i\epsilon$ in the denominator of the propagator arises because, in relating the path integral to asymptotic states, it proves necessary to perform the integral over x^0 from $-\infty(1-i\epsilon)$ to $\infty(1-i\epsilon)$, which in momentum space leads to $k^0 \to k^0(1+i\epsilon)$. This gives us the Feynman rule for an internal gluon line with momentum k_μ :

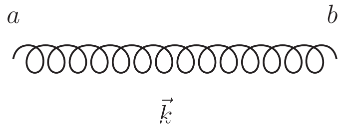

$$= \frac{-i}{k^2+i\epsilon}\left(g_{\mu\nu} - (1-\xi)\frac{k_\mu k_\nu}{k^2}\right)\delta^{ab} \;. \tag{2.18}$$

In practice the Feynman rules can be read off from the Lagrangian. For example, the Feynman rule for the quark gluon vertex diagram can be found by stripping the fields off the term in the Lagrangian involving the gluon and quark fields to give:

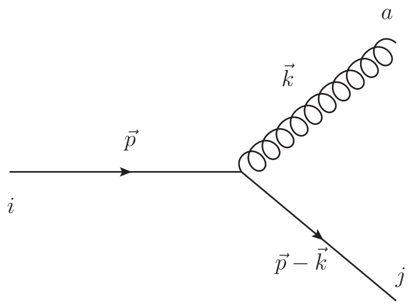

$$= ig_s\gamma_\mu t^a_{ij} \;. \tag{2.19}$$

The Feynman rules for the quark propagator and triple gluon vertex are

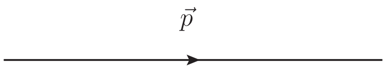

$$=\frac{i(\not p + m)}{p^2 - m^2 + i\epsilon}$$

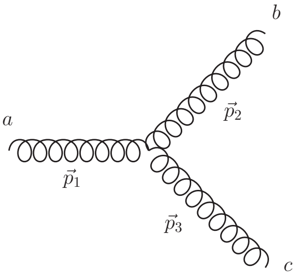

$$=g_s f^{abc}\left[g^{\mu\nu}(p_1^\rho - p_2^\rho) + g^{\nu\rho}(p_1^\mu - p_2^\mu) + g^{\rho\mu}(p_1^\nu - p_2^\nu)\right] \ , \tag{2.20}$$

where $\not p = \gamma_\mu p^\mu$. For the complete set of QCD Feynman rules see for example [54].

2.3 Renormalisation and the running coupling

One typically encounters two types of divergence when studying QCD: infra-red divergences which cancel in physical quantities and will be discussed in section 2.4; and ultra violet (UV) divergences. UV divergences arise due to the unrestricted momentum flow around a loop and need to be removed by renormalisation in order to calculate physical quantities. The process of renormalisation involves re-defining the bare parameters that appear in the Lagrangian in terms of physical, or renormalised, parameters. For example, the bare coupling g_{s0} is related to the renormalised coupling by

$$g_{s0} = g_{sR}\sqrt{Z_g}, \qquad \text{where} \qquad Z_g = 1 + \delta_g, \tag{2.21}$$

with the δ_g term containing the divergences. The renormalised parameters are finite and measurable, the divergences having been absorbed into the definition of the bare parameters.

The consequence of renormalising the parameters of the theory is that they become scale dependent. The rest of this section is devoted to illustrating the renormalisation procedure and deriving the lowest order expression for the running coupling.

We will begin by calculating the divergent piece of the one loop correction to the quark propagator in the Feynman gauge ($\xi = 1$):

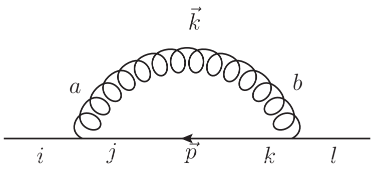

$$= \int \frac{\mathrm{d}^4 k}{(2\pi)^4}(-ig_s)\gamma_\mu t^a_{ij} i\delta^{ab}\frac{-\eta^{\mu\nu}}{k^2}\frac{-i\delta_{jk}}{\not p + \not k}(-ig_s)\gamma_\nu t^b_{kl} \ , \tag{2.22}$$

where the quark mass has been set to zero as it does not play an important role here.

The colour algebra can be factored out of the above diagram and evaluated as

$$t^a_{ij}\delta^{ab}\delta_{jk}\delta_{jk}t^b_{kl} = C_F\,\delta_{il}\ , \tag{2.23}$$

where the remaining delta function enforces that colour is conserved in the above diagram. This delta function can be dropped as it is just a unit matrix in colour space. By multiplying both the numerator and denominator by $\not{p} + \not{k}$ and using the identity $\not{q}\not{q} = q^2$ we find that eq. (2.22) becomes

$$= -C_F g_s^2 \int \frac{\mathrm{d}^4 k}{(2\pi)^4} \frac{\gamma^\nu(\not{p} + \not{k})\gamma_\nu}{(p+k)^2 k^2}\ , \tag{2.24}$$

where the μ indices in the numerator have also been contracted. The term odd in k can be ignored as it goes to zero when integrated over $[-\infty, +\infty]$. Simply by power counting we can see that the remaining $\not{p}$ term is logarithmically divergent as $k \to \infty$. The integral must therefore be regulated in some way to enable it to be evaluated and the divergence subtracted. This can be done in a number of ways, the most obvious being to introduce a cut-off. Although this provides an intuitive link to the Wilsonian picture of renormalisation [58], it turns out to be quite cumbersome to work with, particularly in QCD where one often needs to simultaneously regulate IR divergences which, will not regulated by a UV cut-off. We therefore use dimensional regularisation, where the integral is evaluate in $4 - 2\epsilon$ dimensions. Here ϵ is taken to be a small complex number which can be taken to zero once all of the divergences, which are manifested as poles in negative powers of ϵ, are cancelled. In $4 - 2\epsilon$ dimensions the integral in eq. (2.24) becomes [55]

$$C_F g_s^2 \mu^{2\epsilon} \not{p}(2 - 2\epsilon) \int \frac{\mathrm{d}^{4-2\epsilon} k}{(2\pi)^{4-2\epsilon}} \frac{1}{(p+k)^2 k^2}\ , \tag{2.25}$$

where μ, the dimensional regularisation mass, is introduced so that the coupling constant stays dimensionless. The integration measure $\mathrm{d}^{4-2\epsilon}k = k^{3-2\epsilon}\mathrm{d}k\mathrm{d}\Omega^{3-2\epsilon}$, where $\mathrm{d}\Omega^n$ is the surface element of a unit sphere in $n + 1$ dimensions. Carrying out the integrals in eq (2.25) gives [55]

$$\begin{aligned} &= C_F \frac{i g_s^2}{(4\pi)^{2-2\epsilon}} \left(\frac{\mu}{-p}\right)^{2\epsilon} \not{p}(2 - 2\epsilon) \frac{\Gamma[1-\epsilon]\Gamma[2-\epsilon]}{\Gamma[3-2\epsilon]} \Gamma[\epsilon] \\ &\qquad\qquad \simeq C_F \frac{i g_s^2}{(4\pi)^2} \left(\frac{\mu^2 (4\pi)^2 e^{-\gamma_E}}{-p^2}\right)^{\epsilon} \not{p} \left(\frac{1}{\epsilon} + 1 + \mathcal{O}(\epsilon)\right)\ . \end{aligned} \tag{2.26}$$

The $\frac{1}{\epsilon}$ term needs to be removed by re-normalisation, however we are also free to absorb as much of the finite part of the amplitude into our renormalised quantities as we choose. Different choices of what to absorb corresponding to different renormalisation schemes. The definition of renormalised quantities will obviously differ between schemes, resulting in different values for physical quantities in different schemes, however it is possible to translate from one scheme to another. For example, the minimal subtraction (MS) scheme absorbs only the poles into the renormalisation coefficients, whereas the $\overline{\text{MS}}$ scheme also absorbs the ubiquitous factors of $(4\pi)^{2\epsilon}$ and $\exp[-\epsilon\gamma_E]$. Now that we know the divergence associated with the diagram in eq. (2.22) we introduce a subtraction term to cancel it. In the $\overline{\text{MS}}$ scheme, the subtraction term is

$$-\frac{1}{\epsilon}C_F\frac{ig_s^2}{(4\pi)^2}\left((4\pi)^2e^{-\gamma_E}\right)^{\epsilon}\not{p} = i\not{p}\delta_2 \ , \tag{2.27}$$

which can be expressed as a Feynman rule

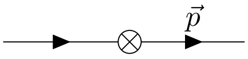

$$= i\not{p}\delta_2 \ , \tag{2.28}$$

where $\delta_2 = -\frac{1}{\epsilon}\frac{g_s^2}{(4\pi)^2}((4\pi)^2e^{-\gamma_E})^{\epsilon}C_F$. This particular counter term is absorbed into the quark field normalization. The relation between the bare and renormalised field is $\psi^{(0)} = \sqrt{Z_2}\psi^{(R)}$ with $Z_2 = 1 + \delta_2$. This modifies the kinetic term in the Lagrangian such that it generates the Feynman rule in equation (2.28). One can go through a similar process for the gluon propagator and vertex corrections, although it turns out that one only needs to find the counter term for one of the vertices in order to fully specify how the QCD Lagrangian is renormalised. The counter terms for the gluon propagator and quark gluon vertex in the Feynman gauge are [56], [59]:

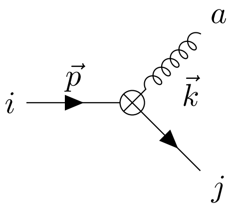

$$= ig_s\gamma_\mu t^a_{ij}\delta_1 \tag{2.29}$$

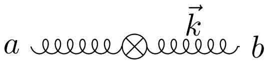

$$= -i(k^2g^{\mu\nu} - k^\mu k^\nu)\delta^{ab}\delta_3 \tag{2.30}$$

where

$$\delta_1 = \frac{1}{\epsilon}\frac{g^2}{(4\pi)^2}\left((4\pi)^2e^{-\gamma_E}\right)^{\epsilon}(-C_F - C_A) \tag{2.31}$$

$$\delta_3 = \frac{1}{\epsilon}\frac{g^2}{(4\pi)^2}\left((4\pi)^2e^{-\gamma_E}\right)^{\epsilon}\left(\frac{5}{3}C_A - \frac{4}{3}T_Rn_f\right) \ , \tag{2.32}$$

where n_f is the number of fermions (quarks).

The counter terms written in this diagrammatic form are convenient for calculating S-matrix elements from Feynman diagrams, however they are not in one to one correspondence with the renormalisation factors multiplying specific parameters in the Lagrangian. In order to find the first order expression for the running coupling we must first find the relationship between the bare and renormalised charge. Equations (2.28) and (2.30) give us the renormalisation factor for the quark and gluon fields respectively, while eq. (2.29) gives the renormalisation factor for the quark gluon vertex term in the Lagrangian, which reads

$$ig_s^R \bar{\Psi}_i^R \gamma_\mu A_\mu^{a(R)} t_{ij}^a \Psi_j^R = ig_s^R \frac{\bar{\Psi}_i^0}{\sqrt{Z_2}} \gamma_\mu \frac{A_\mu^{a(0)}}{\sqrt{Z_3}} t_{ij}^a \frac{\Psi_j^0}{\sqrt{Z_2}} Z_1 \ , \tag{2.33}$$

where the superscript R denotes renormalised quantities, and the superscript 0 the bare quantities. Using the definition $g_s^0 = Z_g g_s^R$ we can read off $Z_g = \frac{Z_1}{Z_2 \sqrt{Z_3}}$.

We can now find an expression for the running coupling. To do this we use a renormalisation group equation which arises because the bare coupling must be independent of μ, the dimensional regularisation scale:

$$0 = \mu \frac{\mathrm{d}g_s^0}{\mathrm{d}\mu} = \lim_{\epsilon \to 0} \mu \frac{\mathrm{d}}{\mathrm{d}\mu} \left(Z_g \left(g_s^R \right) \mu^\epsilon g_s^R \right) \tag{2.34}$$

where the factor of μ^ϵ is, again, needed to keep g_s^R dimensionless. Neglecting, for now, the limit of $\epsilon \to 0$ we can write

$$\mu^{1+\epsilon} \frac{\mathrm{d}g_s^R}{\mathrm{d}\mu} = -\epsilon \mu^\epsilon g_s^R - \frac{\mu^{1+\epsilon}}{Z_g} \frac{\mathrm{d}Z_g}{\mathrm{d}\mu} \ , \tag{2.35}$$

where, because $Z_g = 1 + \mathcal{O}(g_s^2)$ we can, at leading order, ignore the factor of $\frac{1}{Z_g}$, as it will only give higher order corrections. As Z_g only depends on μ through g_s^R we can write $\frac{1}{Z_g} \frac{\mathrm{d}Z_g}{\mathrm{d}\mu} = \frac{\mathrm{d}g_s^R}{\mathrm{d}\mu} \frac{\mathrm{d}\delta_g}{\mathrm{d}g_s^R}$ [56], where δ_g is defined in eq. (2.21). Making the replacement $\frac{(g_s^R)^2}{4\pi} = \alpha_s(\mu)$ and taking the limit of $\epsilon \to 0$, the renormalisation group equation becomes

$$\mu^2 \frac{\mathrm{d}\alpha_s(\mu)}{\mathrm{d}\mu^2} = - \left(\frac{11C_A - 4T_R n_f}{12\pi} \right) \alpha_s^2(\mu) \tag{2.36}$$

where we have also used $\mu^{1+\epsilon} \frac{\mathrm{d}g_s^R}{\mathrm{d}\mu} = -\epsilon \mu^\epsilon g_s^R$. We can make the identification $\frac{11C_A - 4T_R n_f}{12\pi} = \beta_0$, the first coefficient of the QCD β function.

Integrating equation (2.36) between μ_0 and μ gives:

$$\alpha_s(\mu) = \frac{\alpha_s(\mu_0)}{1 + \beta_0 \alpha_s(\mu_0) \ln \left(\frac{\mu^2}{\mu_0^2} \right)}. \tag{2.37}$$

Examining equation (2.37) we see that, provided β_0 is positive, as is the case for QCD, the coupling goes to zero as μ goes to infinity. This property is known as asymptotic freedom [56] and is a property of non-abelian gauge theories [55], [60]. We also see that for some value of μ, less than μ_0 the coupling appears to diverge. This can be made more explicit if we integrate eq. (2.36) from the scale at which α_s diverges, Λ_{QCD}, to some higher scale μ to find

$$\alpha_s(\mu) = \frac{1}{\beta_0 \ln \left(\frac{\mu^2}{\Lambda_{\mathrm{QCD}}^2} \right)}. \tag{2.38}$$

The scale that the coupling diverges at is called the Landau pole, in QCD using the

$\overline{\text{MS}}$ scheme $\Lambda_{\text{QCD}} \simeq 340\,\text{MeV}$ [61]. In fact, the divergence of the coupling is not physical, it signals the breakdown of perturbation theory. As the coupling flows into the infra-red it becomes large and perturbation theory, which we used to derive the running of the coupling, ceases to be valid. Working in the $\overline{\text{MS}}$ scheme the coupling becomes larger than one around 1GeV. The growth of the coupling at low energies is connected to the phenomenon of colour confinement. That is, particles carrying a colour charge are not observed in isolation at energies lower than a few hundred MeV, instead, quarks and gluons are bound inside hadrons [54]. Although qualitatively understood, a rigorous understanding of confinement and how it arises is still an open question. The difficulty in understanding confinement is related to the difficultly with working with strongly interacting quantum field theories where perturbation theory can not be applied. One method for extracting numerical predictions from a non-perturbative quantum field theory (QFT) is lattice QFT [54]. This has many practical difficulties associated with it, and as such cannot typically be used to generate predictions at high energies, such as might be useful for many non-perturbative aspects of collider physics.

The scale μ was introduced as a way to keep the coupling dimensionless and it is not immediately obvious how the dependence of the coupling on it should be interpreted and what effect the choice of μ will have on a calculation. As we should expect, physical quantities are independent of the choice of μ, although this does not mean that the choice of μ is unimportant, as all perturbative calculations will have some residual dependence on μ due to neglected higher order terms. Put another way, any expression for a physical quantity should be independent of the choice of μ up the order in α_s it is calculated to, but the choice of μ will change the calculated value by an amount consistent with neglected higher order terms. It is obviously desirable to reduce the size of these neglected terms, which can often be accomplished by choosing μ approximately equal to some physical scale in the problem, which we shall call Q. This is because, beyond leading order, QCD calculations will typically contain terms proportional to $\ln\left({}^{\mu}\!/_{Q}\right)$, which would become large if μ were taken much different from Q. The coupling can be evaluated at the chosen scale using eq. (2.37) and a measurement of α_s at another scale, μ_0. It is not important that μ_0 be particularly close to μ as the logarithms $\alpha_s^n \ln^{n-1}\left(\frac{\mu^2}{\mu_0^2}\right)$ are resummed to all orders by eq. (2.37).

The expression for the running coupling (eq. (2.37)) is systematically improvable by including higher order subtraction terms in the definition of Z_g so that the RGE reads [56]

$$\mu^2 \frac{\mathrm{d}\alpha_s(\mu)}{\mathrm{d}\mu^2} = -\alpha_s(\mu)(\beta_0\alpha_s(\mu) + \beta_1\alpha_s^2(\mu) + ...) \;, \tag{2.39}$$

which allows for the coupling to be evaluated at different scales with high precision. Higher order coefficients of the beta function can be found, for example, in ref. [56].

2.4 The soft and collinear limits of QCD

In this section we examine some properties of radiative corrections in QCD, focusing on the limit that the gluon is radiated soft and/or collinear with respect to its emitter. The soft and collinear limits are especially important for the study of jet substructure and will play a central role throughout this thesis.

2.4.1 Infra-red divergences

We begin by calculating the total cross-section for a virtual photon decaying to hadrons up to first order in the strong coupling. The relevant Feynman diagrams are shown in figure 2.1

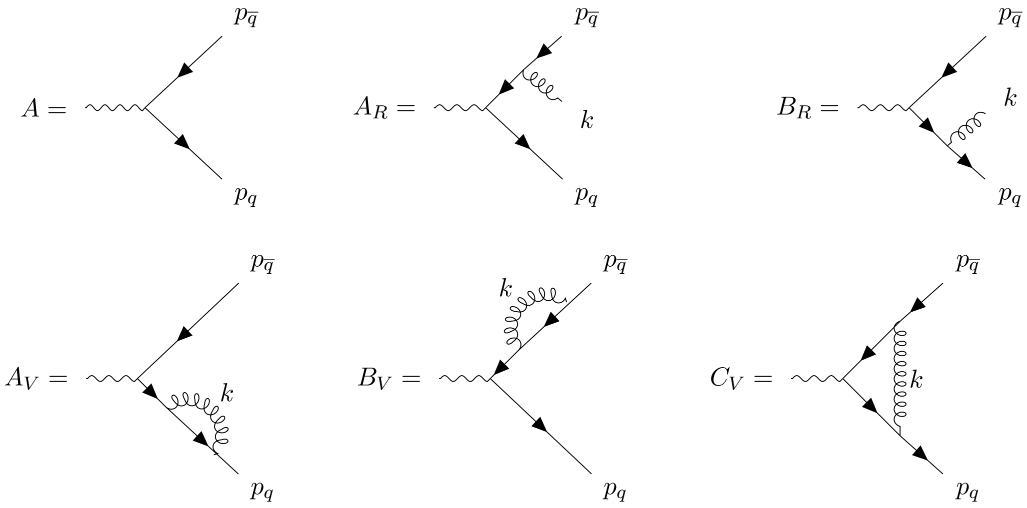

Figure 2.1. The Feynman diagrams needed to compute the total cross-section for a virtual photon decaying to hadrons at $\mathcal{O}(\alpha_s)$.

The Born cross-section is given by [62]

$$\sigma_0 = \frac{1}{2Q}\int |A|^2 \mathrm{d}\Phi^{(2)} = 3Q\alpha_{\mathrm{E.M}} \sum_i e_{qi}^2 \ , \tag{2.40}$$

where A is the amplitude shown in figure 2.1, $\mathrm{d}\Phi^{(2)}$ is the two particle phase space, Q is the virtuality of the photon, and e_{qi} are the electric charge of the quarks in units of the electron charge. At $\mathcal{O}(\alpha_s)$ the squared matrix element for $\gamma^* \to q\bar{q}g$ is given by [63]

$$|M_R|^2 = |A_R|^2 + |B_R|^2 + 2A_R B_R^* = 24C_F e^2 e_q^2 g_s^2 \left(\frac{p_q \cdot k}{p_{\bar{q}} \cdot k} + \frac{p_{\bar{q}} \cdot k}{p_q \cdot k} + \frac{Q^2 \ p_q \cdot p_{\bar{q}}}{p_{\bar{q}} \cdot k \ p_q \cdot k}\right), \tag{2.41}$$

with A_R and B_R denoting the Feynman diagrams in figure 2.1. The real gluon emission contribution to the cross-section is found by integrating $|M_R|^2$ over the three particle phase space. However, this is divergent in four dimensions as the squared matrix element diverges as the gluon momentum goes to zero or becomes collinear with one of the quark momenta. These are known as infra-red and collinear divergences. The result is therefore calculated in $4-2\epsilon$ dimensions, so that the divergences appear as negative powers of ϵ:

$$\sigma_{\text{real}} = \sigma_0 \frac{C_F\,\alpha_s^{\overline{\text{MS}}}}{2\pi}\frac{e^{-\epsilon\gamma_E}}{\Gamma(1-\epsilon)}\left(\frac{\mu^2}{Q^2}\right)^{\epsilon}\left(\frac{2}{\epsilon^2}+\frac{3}{\epsilon}-\pi^2+\frac{19}{2}+\mathcal{O}(\epsilon)\right). \tag{2.42}$$

The matrix element squared for the order α_s virtual corrections can be written as:

$$|M_V|^2 = (A_V + B_V + C_V)A^* \tag{2.43}$$

with A_V, B_V, C_V and A defined in figure 2.1. The renormalised virtual contribution to the cross-section then reads

$$\sigma_{\text{virtual}} = \sigma_0 \frac{C_F\,\alpha_s^{\overline{\text{MS}}}}{2\pi}\frac{e^{-\epsilon\gamma_E}}{\Gamma(1-\epsilon)}\left(\frac{\mu^2}{Q^2}\right)^{\epsilon}\left(\frac{-2}{\epsilon^2}-\frac{3}{\epsilon}+\pi^2-8+\mathcal{O}(\epsilon)\right). \tag{2.44}$$

As the above expression is renormalised, all of the divergences are infra-red in nature. Adding the real and virtual contributions to the Born cross-section, one finds that all of the poles cancel and ϵ can be taken safely to zero so that the total cross-section reads

$$\sigma^{\text{tot}} = \sigma_0\left(1+\frac{3\alpha_s C_F}{4\pi}\right), \tag{2.45}$$

which is free of divergences as a physical quantity should be. The order-by-order cancellation of infra-red divergences in physical quantities is guaranteed by the KLN theorem [64], [65]. This relies on all physical observables being inclusive of final states with different numbers of particles, which may at first seem strange. More specifically, physical observables cannot be sensitive to the addition of very soft or collinear gluons in the final state.

For example, one could imagine trying to measure the cross-section for a virtual photon decaying to three partons. Ignoring the effects of hadronisation for the moment, we can see from eq. (2.42) that this cross-section is divergent even at leading order. What is missing here is that any detector will have some minimum resolution, so what would really be measured is the cross-section for producing three partons each with energy greater than E_{min} and which are separated by some minimum angle δ. This finite resolution cuts out the divergent regions of phase space and regularises the leading order cross-section. Higher order corrections will also be finite as the observable will be inclusive of configurations with extra partons that are softer than E_{min} and emitted at angular scales smaller than δ, the divergences from which will cancel against the loop corrections. Provided one takes into account the finite resolution of the detector, or defines the cross-section with some self imposed minimum resolution, this observable is then perturbatively calculable. Observables which are insensitive to the addition of extra soft and collinear partons in the final state are known as infra-red and collinear safe (IRC safe). More formally we can take the definition of IRC safety for and observable $V(\{k\})$from [66]:

$$\begin{aligned} V(...,k_i,k_j,...) &\to V(...,k_i+k_j,...) \ \text{ if } \ k_i||k_j \\ V(...,k_{i-1},k_i,k_{i+1}) &\to V(...,k_{i-1},k_{i+1},...) \ \text{ if } \ k_i \to 0 \end{aligned} \tag{2.46}$$

where the first line guarantees collinear safety and the second guarantees infra-red safety.

2.4.2 The soft limit

In this section we will look at the soft limit of the real emission matrix element given in the previous section. Keeping only the leading term as $|k| \to 0$ in eq. (2.41) gives

$$|M^{\text{soft}}|^2 = |A|^2 2C_F g_s^2 \left(\frac{p_q \cdot p_{\bar{q}}}{p_{\bar{q}} \cdot k \ p_q \cdot k} \right) \ , \tag{2.47}$$

where A is the matrix element for the Born process. This is known as the eikonal approximation. A notable feature of equation (2.47) is that the emission of a soft gluon is factorised from the Born process. Remarkably, this property does not depend on the details of the process and holds generally such that [63]

$$|M_{n+1}|^2 = -g_s^2 \sum_{i,j} \frac{p_i \cdot p_j}{p_i \cdot k \ p_j \cdot k} \langle M_n | \mathbf{T}_i \cdot \mathbf{T}_j | M_n \rangle \ , \tag{2.48}$$

where $\mathbf{T}_i$ are colour operators acting on the states $|M_n\rangle$, which are vectors in colour space. These colour operators generally make evaluating matrix elements with large numbers of soft gluons extremely difficult, although this is often simplified by taking the large N_c limit, where the colour matrices become diagonal. Additionally, as the IR divergences must cancel between the real and virtual corrections, the virtual corrections must have the same factorised form in the limit that the loop momentum is soft so that the soft singularities will cancel to all orders.

Another important feature of the soft approximation is coherence. That is to say, the soft gluon emission pattern from a dipole is restricted to the opening angle of that dipole. We can demonstrate this using the example of a soft gluon emitted from a $q\bar{q}$ dipole which originated from the decay of a colour singlet, such as was discussed in 2.4.1.

The angular dependence of the matrix element in eq. (2.47) can be written as

$$|M^{\text{soft}}|^2 \propto \left(\frac{1}{1-\cos(\theta_{gq})} + \frac{\cos(\theta_{gq}) - \cos(\theta_{q\bar{q}})}{(1-\cos(\theta_{gq}))(1-\cos(\theta_{g\bar{q}}))} \right) + (q \leftrightarrow \bar{q}), \tag{2.49}$$

where k_0 is the gluon's energy and θ_{ij} is the angle between the particles i and j. Eq.(2.49) can be integrated over the azimuthal component of the phase space with the z axis taken along the direction of p_q for the term given above, and along $p_{\bar{q}}$ for the other term:

$$\int_0^{2\pi} |M^{\text{soft}}|^2 \, \frac{d\phi}{2\pi} \propto \int_0^{2\pi} \bigg(\frac{1}{1-\cos(\theta_{g\bar{q}})} + \frac{\cos(\theta_{g\bar{q}}) - \cos(\theta_{q\bar{q}})}{1 - \sin(\theta_{g\bar{q}})\sin(\theta_{q\bar{q}})\cos(\phi) - \cos(\theta_{g\bar{q}})\cos(\theta_{q\bar{q}})} \bigg) \frac{d\phi}{2\pi} + (q \leftrightarrow \bar{q}). \quad (2.50)$$

When integrated, this gives

$$= \bigg(\frac{\Theta(\cos(\theta_{gq}) - \cos(\theta_{q\bar{q}}))}{(1-\cos(\theta_{gq}))} + (q \leftrightarrow \bar{q}). \bigg) , \quad (2.51)$$

where the step function is zero for $\theta_{gq} > \theta_{q\bar{q}}$, signifying that gluon emission is restricted to the opening angle of the dipole. The reason for this, from a physical perspective, is that at wide angles the large wavelength of soft gluons cannot resolve the individual quarks, but instead is sensitive only to the system as a whole, which in this case is a colour singlet, and thus, emits no radiation. More generally, at angular scales larger than the opening angle of a dipole, soft radiation is emitted coherently, according to the overall colour charge of the dipole. Another simple example would be that a soft gluon emitted collinear to a quark is not sensitive to the presence a much more collinear gluon, also emitted from the quark, as it only *sees* the overall colour charge, which is that of a quark.

2.4.3 The collinear limit

We now turn to the limit where the gluon is emitted collinear to one of the quarks. The cross-section for $\gamma^* \to q\bar{q}g$, differential in the energy of both quarks, can be written as [54]

$$\frac{\mathrm{d}^2\sigma}{\mathrm{d}x_1\mathrm{d}x_2} = \sigma_0 \frac{C_F\,\alpha_s}{2\pi} \frac{x_1^2 + x_2^2}{(1-x_1)(1-x_2)} , \quad (2.52)$$

where $x_i = \frac{2E_i}{Q}$. This can be expressed in terms of $z = \frac{E_q}{E_q+E_g} = \frac{x_1}{2-x_2}$ and k_t, the transverse momentum of the gluon relative to one of the quarks. In the limit that $k_t \ll Q$ we can write [56]

$$\frac{\mathrm{d}^2\sigma}{\mathrm{d}z\mathrm{d}k_t^2} = \sigma_0 \frac{C_F\,\alpha_s}{2\pi} \frac{1}{k_t^2} \frac{1+z^2}{1-z} + \mathcal{O}(\frac{k_t^2}{Q^2}) , \quad (2.53)$$

which captures the leading terms in the collinear limit. The factor of $C_F \frac{1+z^2}{1-z}$ is the collinear splitting function $\langle P_{qq}(z) \rangle$. Like the soft limit, we see that the probability of a collinear splitting is factorised from the Born cross-section. If one considers a sequence of splittings where each subsequent splitting is more collinear than the last, then the cross-section for this process can be factorised into a product of collinear splitting functions. This approximation will be useful in section 2.5, when calculating observables to all orders.

A similar picture emerges for the splitting of a gluon to either a $q\bar{q}$ pair or a pair of gluons, so that the probability of a parton of type a branching to a parton of type b, carrying momentum fraction z, can be factorised from the rest of the cross-section and written as

$$\frac{\mathrm{d}\mathcal{P}}{\mathrm{d}k_t^2\mathrm{d}z} = \frac{\alpha_s}{2\pi}\langle P_{b,a}(z)\rangle\frac{1}{k_t^2} \ . \tag{2.54}$$

Although not necessary for $\langle P_{gq}(z)\rangle$, the splitting functions are averaged over the azimuthal integration as the gluon splitting probability depend on the azimuth. The other splitting functions are [67]:

$$\begin{aligned}
\langle P_{gq}(z)\rangle &= C_F\frac{1+(1-z)^2}{z}\\
\langle P_{qg}(z)\rangle &= T_R(z^2+(1-z)^2)\\
\langle P_{gg}(z)\rangle &= C_A\left(\frac{z}{1-z}+\frac{1-z}{z}+z(1-z)\right)
\end{aligned} \tag{2.55}$$

where $\langle P_{gq}(z)\rangle$ is related to $\langle P_{qq}(z)\rangle$ by $z \to 1-z$. The colour factors associated with collinear splittings are much simpler than for soft emissions. This can be traced back to the fact that the colour factors associated with soft emissions depend on all colour charges in the amplitude, whereas collinear splittings can be thought of as a splitting of a specific parton so that the colour factors are as given by the Casimir of the relevant representation as per eq. (2.55). In equation (2.54), k_t can generally be replaced with any variable which goes to zero as the decay products become collinear, such as θ, the angle between the collinear decay products, or the invariant mass.

The gluon emission probability is particularly simple in the soft and collinear limit. Taking $z = \frac{E_g}{E_p}$ with E_p the energy of the parent parton the emission probability can be written as

$$\frac{\mathrm{d}^2\sigma}{\mathrm{d}z\mathrm{d}k_t^2} = \frac{C_R\alpha_s}{\pi}\frac{1}{z}\frac{1}{k_t^2}, \tag{2.56}$$

which captures just the leading soft and collinear singularity. In the above equation C_R is equal to either C_F or C_A depending on if the parent parton is a quark or gluon respectively.

2.4.4 Large logarithms

Earlier we discussed IRC safety, using the cross-section for a virtual photon decaying to three partons as an example. This was found to be perturbatively calculable as long as the observable was defined such that each parton would have a minimum energy $E_{\min}$ and be separated by some minimum angle δ. We now study the cross-section for the production of two jets defined in this way, the Sterman-Weinberg jet cross-section [66]. The Born cross-section for producing a quark–anti-quark pair will be denoted σ_0. For our purposes it is sufficient to calculate the $\mathcal{O}(\alpha_s)$ correction to this in the soft and collinear limit. Considering the gluon to be emitted collinear the quark and including a factor of two to account for the case that it is collinear to the anti-quark, the real contribution reads

$$\sigma^{\text{real}} = 2\sigma_0 \frac{C_F \alpha_s}{\pi} \int_0^{\frac{Q}{2}} \frac{\mathrm{d}E_g}{E_g} \int_0^{\delta} \frac{\mathrm{d}\theta^2}{\theta^2} + 2\sigma_0 \frac{C_F \alpha_s}{\pi} \int_0^{E_{\text{min}}} \frac{\mathrm{d}E_g}{E_g} \int_{\delta}^{1} \frac{\mathrm{d}\theta^2}{\theta^2} \ , \tag{2.57}$$

where the upper limit on the angular integration is an approximation and has been set to 1 so as to avoid additional terms that are not needed for the purpose of this section and would not be correct anyway, as we would need to use the soft wide angle form of the matrix element. The first term in eq. (2.57) represents a gluon being emitted at an angle less than δ to either the quark or anti-quark. In this case the gluon can have any energy and the event will still satisfy the two jet deffinition. The second term represents the gluon being emitted at angles wider than δ, so for the event to be two-jet-like, the gluon must have energy less than E_{min}. The virtual contribution can then be expressed as

$$\sigma^{\text{virtual}} = -2\sigma_0 \frac{C_F \alpha_s}{\pi} \int_0^{\frac{Q}{2}} \frac{\mathrm{d}E_g}{E_g} \int_0^{1} \frac{\mathrm{d}\theta^2}{\theta^2} \ , \tag{2.58}$$

which is because, as previously mentioned, the virtual corrections must have the same singularity structure as the reals. Combining the real and virtual correction we find that the Sterman-Weinberg jet cross-section, at double logarithmic accuracy, is given, to $\mathcal{O}(\alpha_s)$, by

$$\sigma = \sigma_0 \left(1 - 2\frac{C_F \alpha_s}{\pi} \ln(\delta) \ln\left(\frac{2E_{\text{min}}}{Q}\right)\right) \ . \tag{2.59}$$

This result is somewhat problematic as, for small values of δ and E_{min}, the first order correction can become larger than the Born cross-section and can even cause the cross-section to become negative, which is clearly not physical. The problem is not solved by going to higher orders as each power of α_s is accompanied by two large logarithms, which spoils the convergence of the perturbative series. These logarithms arise because of restrictions placed on the phase space in which real emissions are allowed, a common feature of jet substructure observables. The solution to this problem is to resum these large logarithms to all orders. A method for resumming these large logarithms up to next-to-leading logarithmic accuracy is illustrated in the next section.

2.5 Resummation

In the previous section the need to resum large logarithms which originate from infrared singular regions was illustrated. In this section we will focus on how these infrared and collinear logarithms can be resummed, using the heavy hemisphere mass, M_{H}, as an example. The heavy hemisphere mass is defined by partitioning the phase space into two hemispheres and measuring the invariant mass of the particles in each hemisphere. The larger of the two masses is the heavy hemisphere mass. The partitioning of the event into two hemispheres is traditionally done by a plane perpendicular to the thrust axis[1] [68], although in the soft and collinear limits relevant for resummation we take this plane to be perpendicular to the axis defined by the initial $q\bar{q}$ pair. For convenience we define the quantity $\rho = \frac{M_{\mathrm{H}}^2}{Q^2}$ where Q is the center of mass energy. We will first discus some features of this observable that make it amenable to resummation before discussing, in section 2.5.1, the treatment of correlated emissions in resummation. The cumulative heavy jet mass distribution,

$$\Sigma(\rho) = \frac{1}{\sigma_0} \int_0^{\rho} \frac{\mathrm{d}\sigma}{\mathrm{d}\rho'} \mathrm{d}\rho' \ , \tag{2.60}$$

is then resummed to next-to-leading logarithmic (NLL) accuracy in section 2.5.2. The resummation will be carried out in the context of electron positron collisions as this allows us to focus on final state resummation, the physics of which remains unchanged at hadron colliders due to the factorisation properties of QCD, without many of the additional complications that arise with hadron collider observables. These complicating factors, and how some of them can be mitigated, as well as the need for resummation in jet substructure studies will be discussed in chapter 3. We shall carry out the resummation to next to leading logarithmic (NLL) accuracy, meaning that we capture all terms of the form $\alpha_s^n \ln^{2n-m}(\rho)$ with $m = 0, 1$.

The heavy hemisphere mass has several properties which are helpful in carrying out the resummation:

1. It is IRC safe.
2. It is sufficiently insensitive to collinear branching of an emission that we can, within NLL accuracy, make the replacement $\rho(\vec{k}_1, \vec{k}_2) \to \rho(\vec{k}_1 + \vec{k}_2)$, when $\vec{k}_1$ and $\vec{k}_2$ are the momenta of two emissions resulting from the branching of a gluon emitted from the initial $q\bar{q}$ pair.
3. It is additive in the soft and collinear limit, meaning that $\rho(k_1, k_2) \simeq \rho(k_1) + \rho(k_2)$.
4. It is a global observable, meaning that it is sensitive to emissions anywhere in the phase space.

We shall now discuss why these properties are helpful and make these statements more precise as well as discussing a wider class of observables that can be resummed in a similar fashion.

Point 1 may seem a somewhat obvious requirement as it guarantees that the observable can be computed perturbatively. However, resummations of observables which are not IRC safe but Sudakov safe [2], such as N-subjettiness ratios [14], can be computed using broadly similar techniques [26], [28] albeit without fully achieving NLL accuracy.

---

[1] The thrust axis is defined by the unit vector $\vec{n}$ which maximises $T = \frac{\sum_i |\vec{p_i} \cdot \vec{n}|}{\sum_i |\vec{p_i}|}$.

[2] Sudakov safe observables are discussed further in section 3.4.2.

Point 2 allows us to absorb branchings off a primary emission, i.e. one off the initial $q\bar{q}$ pair, into the strong coupling as is discussed further in section 2.5.1. This allows us to carry out the resummation considering only a sequence of primary emissions, ordered in transverse momentum as is carried out in section 2.5.2. A set of properties which guarantee that an observable can be resummed in this manner were formalised in ref [69] as part of the rIRC safety conditions.
As we shall see in section 2.5.2, point 3 makes it relatively easy to write the observable dependence of the cumulant in a factorised form, which is necessary for carrying out the resummation using the techniques presented here. Perhaps more importantly, because one emission does not influence the way in which another emission contributes to ρ we do not have to consider the details of what happens when two independent emissions have comparable transverse momenta. This allows us to approximate the matrix element for any number of emissions as a product of independent emissions strongly ordered in transverse momentum, or some other variable.

Point 4 guarantees the absence of non-global logarithms (NGLs) [70], [71], which cannot be simply resummed in the manner which is demonstrated here. NGLs are a class of logarithm which is particularly difficult to resum. The resummation of NGLs has up until recently been limited to the leading non-global logs in the leading colour approximation, with NLL at leading colour now being possible [72]. These logarithms arise as a result of configurations where partons are radiated from a region of phase space which the observable is insensitive to into a region that it is sensitive to, as is depicted in figure 2.2 for an observable measured only on the left hemisphere. As an example, consider the left hemisphere mass. The contribution of k_2 (shown in figure 2.2a) to the left hemisphere mass cannot be accounted for by treating primary gluon emissions inclusively of their decay products. Instead $M_{\mathrm{L}}^2 = k_2 \cdot p_1$, with p_1 the momentum of the quark in the left hemisphere. There will be a soft divergence as $k_2 \to 0$ which will cancel against the corresponding virtual correction in the right hemisphere as shown in figure 2.2b. It is this cancellation between real and virtual corrections in different hemispheres that gives rise to non-global logarithms.

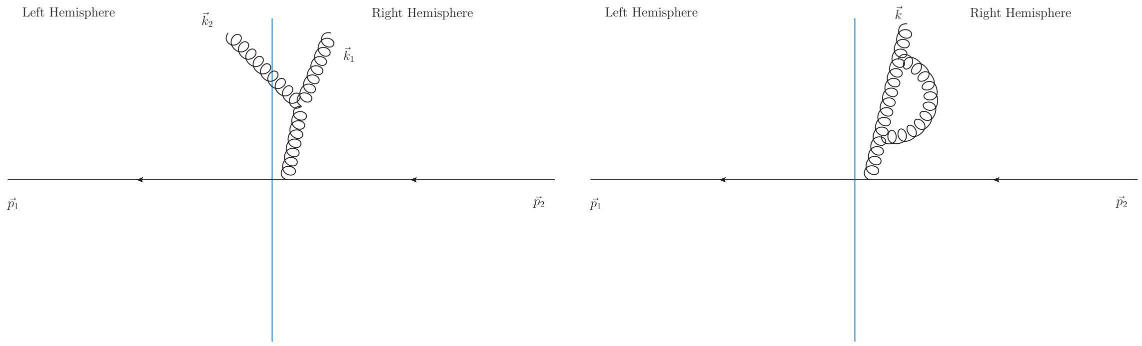

(a) A secondary gluon is radiated from the right hemisphere into the left.

(b) A gluon emitted in the right hemisphere with a loop correction.

Figure 2.2. Configurations which together give rise to non-global logarithms for observables computed on the left hemisphere only.

2.5.1 Accounting for correlated emissions

As discussed above, the branching of primary emissions can be accounted for within NLL accuracy by an appropriate treatment of the coupling, provided the observable is not overly sensitive to collinear branchings of a primary emission. This treatment involves using the CMW [73] scheme for the coupling and setting the argument of the coupling to the transverse momentum of the emission it is associated with, so that, in the collinear limit, the probability of emitting a gluon, inclusive of it branching, after averaging over the azimuthal angle can be written as

$$\frac{\mathrm{d}^2\sigma}{\mathrm{d}k_t^2\mathrm{d}z} = \frac{1}{\pi}\alpha_s^{\mathrm{CMW}}(k_t^2)P_{g,p}(z)\frac{1}{k_t^2}\ , \tag{2.61}$$

where p can either denote a quark or gluon. We note that the CMW scheme should only really multiply the soft part of the splitting function, but that the error introduced by letting it multiply the full splitting function is beyond NLL accuracy for rIRC safe double logarithmic observables.

We first show how using the one loop coupling with the argument set to to k_t includes hard collinear branchings and associated virtual corrections before discussing the two loop coupling and CMW scheme.

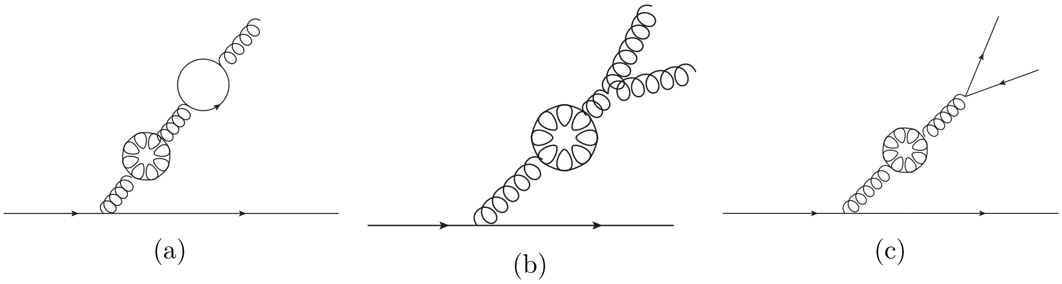

Figure 2.3. Examples of diagrams that are included by setting the argument of the coupling to the transverse momentum of the primary gluon emission. Although only one and two loop configurations are shown, diagrams with any number of loops inserted into the primary gluon line are resummed by choosing the argument of the coupling to be k_t.

To show this one must consider the gluon emission diagrams with any number of loops inserted into the gluon line, an example of which is shown in figure 2.3a, along with the diagrams where a gluon is emitted and then branches, with any number of loops inserted into the primary gluon line, some examples of which are also shown in figures 2.3b and 2.3c. Summing over quark and gluon loops, each loop insertion into these diagrams contributes a factor of $\alpha_s(\mu^2)\beta_0\ln\left(\frac{\mu^2}{m^2}\right)$ to the cross-section, where m^2 is the virtuality of the gluon line off the quark, which is zero when the gluon does not branch. The existence of these terms is demonstrated explicitly in chapter 4 through an $\mathcal{O}(\alpha_s^2)$ calculation. These loops can be resummed using

$$\alpha_s(\mu^2)\sum_{n=0}^{\infty}\left(\alpha_s(\mu^2)\beta_0\ln\left(\frac{\mu^2}{m^2}\right)\right)^n = \frac{\alpha_s(\mu^2)}{1-\beta_0\alpha_s(\mu^2)\ln\left(\frac{\mu^2}{m^2}\right)} = \alpha(m^2). \tag{2.62}$$

The loop corrections re-summed in the expression above are just a product of one loop corrections. Incorporating loop topologies which enter at two loops will give the geometric series for the two loop running of the coupling, which will capture a tower of next to leading logarithms.

The probability of emitting a gluon from a quark, inclusive of that gluon branching and including all possible loops inserted into the gluon line, can then be written as [74]

$$\frac{\mathrm{d}^2\sigma^{\text{inclusive}}}{\mathrm{d}k_t^2\mathrm{d}z} = \frac{1}{\pi}P_{gq}(z)\frac{1}{k_t^2}\left(\alpha_s(0) - \beta_0\int_0^\infty \frac{k_t^2\alpha_s^2(m^2)dm^2}{m^2(k_t^2+m^2)}\right). \tag{2.63}$$

The $\alpha_s(0)$ term is due to the type of diagram shown in figure 2.3a, representing the emission of an on shell gluon. The second term, proportional to β_0, is due to integrating the diagrams where the gluon branches over the virtuality of the intermediate gluon, the soft divergent piece from the gluon splitting having been cancelled against the corresponding virtual corrections [74]. The integral over the virtuality in Eq. (2.63) can be rewritten as

$$\int_0^\infty \frac{k_t^2}{(m^2+k_t^2)}\frac{\mathrm{d}}{\mathrm{d}m^2}\left(\alpha_s(m^2)\right)\mathrm{d}m^2 = -\alpha_s(0) + \int_0^\infty \frac{k_t^2\alpha_s(m^2)}{(m^2+k_t^2)^2}\mathrm{d}m^2, \tag{2.64}$$

where we have used $\frac{\partial}{\partial \ln m^2}\alpha_s(m^2) = -\beta_0\alpha_s^2(m^2)$. The resulting $\alpha_s(0)$ cancels the $\alpha_s(0)$ term in Eq. (2.63). The remaining integral over the virtuality can be evaluated by making the substitution, $\frac{m^2}{k_t^2} = u$, and writing $\alpha_s(u\ k_t^2) = \exp\left[\ln(u)\frac{\mathrm{d}}{\mathrm{d}\ln(k_t^2)}\right]\alpha_s(k_t^2)$, to give [75]

$$\begin{aligned}\frac{\mathrm{d}^2\sigma^{\text{inclusive}}}{\mathrm{d}k_t^2\mathrm{d}z} = \frac{1}{\pi}P_{gq}(z)\frac{1}{k_t^2}\left(\int_0^\infty \frac{\exp\left[\ln(u)\frac{\mathrm{d}}{\mathrm{d}\ln(k_t^2)}\right]\alpha_s(k_t^2)}{(1+u)^2}\mathrm{d}u\right) = \\ \frac{1}{\pi}P_{gq}(z)z\frac{1}{k_t^2}\frac{\pi\frac{\mathrm{d}}{\mathrm{d}\ln(k_t^2)}}{\sin\left(\pi\frac{\mathrm{d}}{\mathrm{d}k_t^2}\right)}\alpha_s(k_t^2).\end{aligned} \tag{2.65}$$

The operator $\frac{\pi\frac{\mathrm{d}}{\mathrm{d}\ln(k_t^2)}}{\sin\left(\pi\frac{\mathrm{d}}{\mathrm{d}k_t^2}\right)}$ can be written as a series and acted on $\alpha_s(k_t^2)$ to give

$$\frac{\mathrm{d}^2\sigma^{\text{inclusive}}}{\mathrm{d}k_t^2\mathrm{d}z} = \frac{1}{\pi}P_{gq}(z)\frac{1}{k_t^2}\alpha_s(k_t^2) + \mathcal{O}\left(\alpha_s^3(k_t^2)\right), \tag{2.66}$$

where in the perturbative domain, where α_s is small, the higher order terms can be dropped so that we are simply left with the single gluon emission probability with the argument of the coupling set to the transverse momentum of the gluon emission. Using the one-loop expression for the running coupling with the argument set to k_t generates a spectrum of logarithms starting at $\alpha_s^n L^{2n-1}$, where L is a large logarithm of some observable. To capture all next to leading logarithms one must run the coupling using the expression generated from the two-loop beta function,

$$\alpha_S(Q^2) = \frac{1}{\beta_0 \ln\left(\frac{Q^2}{\Lambda^2_{\mathrm{QCD}}}\right)} - \frac{\beta_1 \ln\left(\ln\left(\frac{Q^2}{\Lambda^2_{\mathrm{QCD}}}\right)\right)}{\left(\beta_0 \ln\left(\frac{Q^2}{\Lambda^2_{\mathrm{QCD}}}\right)\right)^2}, \tag{2.67}$$

with Λ_{QCD} the position of the Landau pole in QCD, and β_0 and β_1 are the first two coefficients of the beta function [54].

To capture all next to leading logarithms, one must also use the coupling in the CMW scheme, which is related to the $\overline{\mathrm{MS}}$ scheme by

$$\alpha_s^{\mathrm{CMW}} = \alpha_{s,\overline{\mathrm{MS}}} + K\frac{\alpha^2_{s,\overline{\mathrm{MS}}}}{2\pi}\ , \tag{2.68}$$

with $K_{\mathrm{CMW}} = \left(\frac{67}{18} - \frac{\pi^2}{6}\right) C_A - \frac{5}{9} n_f$. This is due to a finite term in the non abelian part of the one to three emission probability, which multiplies the soft part of the single emission probability, giving a tower of logarithms starting at $\alpha_s^2 L^2$ [76], [77]. This can be derived using the two loop splitting functions of [78], as shown in [76]. The origin of the K_{CMW} term is also illustrated through an $\mathcal{O}(\alpha_s^2)$ calculation which is carried out in the collinear limit in chapter 4 for the groomed jet mass distribution.

The inclusion of the possible splitting of a primary gluon through the running coupling relies on the observable, $v(k_1, .., k_n)$, having limited sensitivity to the splitting of a primary gluon. If in the soft and collinear limit, the difference $|v(k_1, k_2) - v(k_1 + k_2)|$, grows as some power of $v(k_1 + k_2)$, where k_1 and k_2 have relative transverse momentum of the same order as their total transverse momentum relative to one of the born partons, then the gluon splitting and virtual corrections can not be simply absorbed into the running of the coupling [69].

2.5.2 Resumming multiple emissions

We now turn to calculating the heavy hemisphere mass distribution, defined in eq. (2.60). As mentioned in section 2.4.3, the cross-section for n collinear emissions can be written as a product of splitting functions in the limit that emissions are strongly ordered in k_t, or some other variable which goes to zero in the collinear limit. As terms proportional to powers of ρ are neglected in this derivation, we can replace the splitting function with $\frac{2}{z} + B_q\delta(1-z)$ where $B_q = \int_0^1 (z-2)\mathrm{d}z = \frac{-3}{2}$ is the integral over $[0, 1]$ of the hard part of the splitting function, i.e. $P_{gq}(z) - \frac{2}{z}$. For any number of soft and collinear emissions we can write $\rho = \sum_i \frac{k^2_{ti}}{Q^2 z_i}$, which is sufficiently accurate for a NLL resummation [69]. The all orders cross-section can then be written, within NLL accuracy, as a product of independent emission probabilities as

$$\begin{aligned}
&\Sigma(\rho) = \\
&\quad \sigma_0 \exp\left[-\left(\frac{C_F}{\pi}\int_0^{z^2Q^2}\alpha_s^{\mathrm{CMW}}(k_t^2)\left(\int_0^1 \frac{2}{z}+B_q\delta(1-z)\right)\mathrm{d}z\frac{\mathrm{d}k_t^2}{k_t^2}\right)\right]\sum_{n=0}^{\infty}\frac{1}{n!}\prod_{i=0}^{n} \\
&\left(\frac{C_F}{\pi}\int_0^{z_i^2Q^2}\alpha_s^{\mathrm{CMW}}(k_{ti}^2)\left(\int_0^1 \frac{2}{z_i}+B_q\delta(1-z_i)\right)\mathrm{d}z_i\frac{\mathrm{d}k_{ti}^2}{k_{ti}^2}\right)\Theta\left(\rho-\sum_i\frac{k_{ti}^2}{Q^2z_i}\right)
\end{aligned} \tag{2.69}$$

where the exponential factor captures the virtual corrections up to NLL accuracy, and the upper limit on the integrals over k_{ti}^2 are a result of dividing the phase space into two hemispheres at the point where the rapidity is equal to zero. The step function in the above equation constrains the squared hemisphere mass, normalised to Q^2, to be less than ρ. The form of the hemisphere mass used in the step function assumes that all emissions are soft and collinear, which is sufficient for NLL accuracy. The single emission probability can be re-written as $\int_0^1 R'(\rho')\frac{\mathrm{d}\rho'}{\rho'}$, where

$$R'(\rho') = \frac{C_F}{\pi}\int_0^{z^2Q^2}\alpha_s^{\mathrm{CMW}}(k_t^2)\left(\int_0^1\frac{2}{z}+B_q\delta(1-z)\right)\mathrm{d}z\frac{\mathrm{d}k_t^2}{k_t^2}\rho\delta\left(\rho'-\frac{k_t^2}{Q^2z}\right)\ . \tag{2.70}$$

Each real emission can be integrated up to ρ while the virtual corrections cover the whole phase space with $0<\rho'<1$ so that the resummed cross-section is

$$\begin{aligned}
&\Sigma(\rho) = \\
&\quad \sigma_0\exp\left[-\int_0^1 R'(\rho')\frac{\mathrm{d}\rho'}{\rho'}\right]\sum_{n=0}^{\infty}\frac{1}{n!}\prod_{i=0}^{n}\left(\int_0^{\rho}R'(\rho_i')\frac{\mathrm{d}\rho_i'}{\rho_i'}\right)\Theta\left(\rho-\sum_i\rho_i\right)\ .
\end{aligned} \tag{2.71}$$

The step function now needs to be written in a factorised form which can be accomplished by writing it as an inverse Melin transform
$\Theta\left(\rho-\sum_i\rho_i\right) = \int\frac{\mathrm{d}\nu}{2\pi i\nu}\exp[-\rho\nu]\prod_i\exp[\nu\rho_i]$. The real emissions can now be exponentiated to give

$$\Sigma(\rho) = \sigma_0\int\frac{\mathrm{d}\nu}{2\pi i\nu}\exp\left[-\int_{\rho}^{1}R'(\rho')\frac{\mathrm{d}\rho'}{\rho'}-R'(\rho)\int_0^{\rho}(1-e^{\rho'\nu})\frac{\mathrm{d}\rho'}{\rho'}\right]e^{-\nu\rho}\ , \tag{2.72}$$

where, in the integral of ρ' over $[0,\rho]$, the factor of $R'(\rho')$ has been approximated as $R'(\rho)$ as the integral is dominated by values of $\rho'\simeq\rho$. This reflects the fact that a single emission dominates the value of the observable as is the case when emissions are strongly ordered.

The integrals over ρ' can be evaluated and the Bromwich integral carried out to give

$$\Sigma(\rho) = \sigma_0\frac{\exp[-R(\rho)-\gamma_E R'(\rho)]}{\Gamma[1+R'(\rho)]}\ , \tag{2.73}$$

where $R(\rho) = \int_0^{\rho}R'(\rho')\frac{\mathrm{d}\rho'}{\rho'}$. The function $\frac{\exp[-\gamma_E R'(\rho)]}{\Gamma[1+R'(\rho)]}$ is a purely NLL piece, i.e. it contains no leading log pieces, and accounts for the fact that multiple real emissions

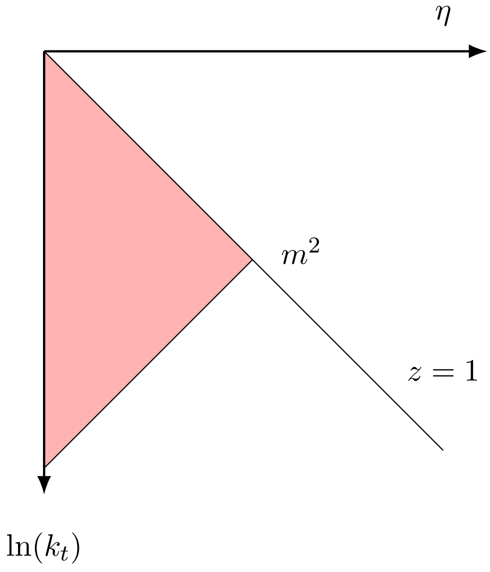

Figure 2.4. A Lund diagram showing the region of phase space in which real emissions are vetoed when a cut $\frac{m^2}{Q^2} < \rho$ is imposed, where m is the heavy hemisphere mass.

can contribute to the hemisphere mass, whilst the factor of $\exp[-R(\rho)]$ contains all of the leading logs and can be found by requiring that no single emission sets a normalised hemisphere mass larger than ρ. At the level of leading log accuracy, the radiating function R can be found simply by integrating the single gluon emission probability over the phase space in which a single real emissions is vetoed by the observable, reflecting the fact that these logarithms can be thought of as coming from uncancelled virtual corrections. A convenient way of representing this is on a Lund diagram, as shown in figure 2.4, where the shaded region shows the vetoed phase space. At double logarithmic accuracy, this representation has the nice property that the emission probability from a colour dipole is uniform over the Lund plane. How the emission probability density is modified beyond the double logarithmic approximation is discussed further in section 3.5.

Chapter 3

Jets and jet substructure

The aim of this chapter is to provide an idea of the huge range of applications that jet substructure has at colliders, focusing mainly on techniques related to the following chapters of this thesis. Particular emphasis is placed on the role that first principles calculations have played, and continue to play, in the development of jet substructure techniques. We begin by looking at how events are modelled at hadron colliders to build up a picture of what an event looks like and assist us in understanding the logic behind the various techniques discussed in the following sections. We then discuss jet grooming and tagging in sections 3.3 and 3.4, before briefly reviewing some precision measurements and calculations of jet substructure observables in section 3.5, an area which has been developing rapidly in recent years.

3.1 Modelling hadron collider events

To understand the motivation behind the techniques applied to jets at the LHC, we should first examine what an event at the LHC, or other hadron collider, looks like, or at least how they are modelled. A particularly important concept in this discussion is factorisation, which allows one to break the physics of a proton proton collision into a convolution of sub-processes rather than one complex process that evolves the initial state protons to the final state particles. This is essential for making quantitative predictions as it would be impossible to consider the collision and subsequent evolution to the final state observed in the detector as a whole with current QFT techniques, owing to the huge range of energy scales and large numbers of particles involved. To this end we will walk through how a typical LHC collision is modelled, discussing the physics at each stage. We then briefly discus the implementation of this physics in event generators, which are key tools for phenomenologists and experimentalists, with particular emphasis on the most crucial aspect for jet substructure; the parton shower.

In a proton proton collision, one can make the approximation that one parton from each proton will scatter off each other at an energy scale much higher than that of the interactions between partons within the proton. This separation of scales gives rise to a picture of interactions between the partons in each proton happening over time scales much longer than those of the hard scattering. Because of this, the hard scattering cross-section can be factorised from the interactions between the partons in each proton and computed, using fixed order perturbation theory, without reference to the other partons in each proton [79]. The momenta of the partons entering the hard scattering process are typically given as a fraction, x, of each proton's momentum. The distribution of the momenta of different species of parton, i, are given by experimentally determined parton distribution functions (PDFs), $f_i(x, \mu^2)$, which are convoluted with hard scattering cross-section [55], [80]. The quantity $f_i(x, \mu^2)\mathrm{d}x$ can be interpreted as giving the probability of finding a given species of parton carrying a momentum fraction between x and $x + \mathrm{d}x$ of the protons momentum when the proton is probed at a scale μ. The evolution of the PDFs with μ is given by the DGLAP equation [54], [67], [81]–[83],

$$\mu^2 \frac{\mathrm{d}}{\mathrm{d}\mu^2} f_i(x, \mu^2) = \frac{\alpha_s(\mu^2)}{2\pi} \sum_j \int_x^1 \frac{\mathrm{d}z}{z} P_{ij}\left(\frac{x}{z}\right) f_j(z, \mu^2) \ , \tag{3.1}$$

named after Dokshitzer, Gribov, Lipatov, Altarelli and Parisi. This allows PDFs that are measured in deep inelastic scattering experiments at one scale, to be used as input in hadron collider experiments at higher energies.

The final state of the hard scattering must then be related to observable objects in the detector. For hard scatterings with stable or long lived particles in the final state this is fairly simple, for example, electrons, muons and photons can all be observed in the detector. Processes involving coloured particles in the final state are more complicated, for example, suppose that the hard scattering produces a $q\bar{q}$ pair. What will then be observed in the detector is two jets of hadrons, one associated with each quark. Along with the decay products of particles emerging from the hard scattering, hadrons associated with other coloured particles in the event are also observed in the detector. These other sources are: QCD radiation from the hard partons in the initial state, known as initial state radiation (ISR); scatterings between other partons within the protons, known as multi parton interactions (MPI); and the remnants of the protons (beam remnants). Beam remnants and MPI are collectively known as underlying event (UE). The work in this thesis is primarily concerned with jets associated to the hard process. The evolution from a small number of high energy partons to jets of hadrons is again factorised from the hard process. Actually, this evolution is typically factorised into two steps, a perturbative parton branching process where the hard parton branches into many coloured partons, and a hadronisation process where the resulting large number of coloured partons are bound into hadrons, which can themselves decay to other hadrons. Properties of the jet due to the parton branching process can be calculated perturbatively using resummation techniques, the subject of much of this thesis, or a parton shower, a type of Monte Carlo simulation that describes this parton branching process and can be used to approximate a resummed calculation. Parton showers will be discussed further in section 3.1.1. The effect of hadronisation on an observable is not generally calculable from QCD, as hadronisation is a non-perturbative effect. [1] Hadronisation models are incorporated into event generators [54], [86]–[90] which can then simulate a complete final state, although such models are not derivable from first principles QCD. The hadronisation process, being at a lower scale than parton branching, is generally taken to be local and not to significantly modify the substructure of a jet [54]. Throughout this thesis we will therefore talk about the substructure of jets mostly in perturbative terms, with the understanding that hadronisation provides a small correction to this. Of course this is only really a suitable picture for IRC safe observables.

3.1.1 Event generators and parton showers

Event generators such as Herwig [86], Pythia [53], and Sherpa [91] model every stage of a proton proton collision as described above, generating (approximately) realistic final states which can be analysed or passed to a simulation of a detector to provide comparisons between theoretical predictions and measurements. Some stages of the evolution are under better theoretical control than others. For example it is now relatively standard for event generators to make use of next to leading order (NLO) matrix elements in the hard scattering process through methods such as POWHEG [92], with next-to-next-to leading order (NNLO) being achievable for certain processes [93]. This represents one of the better theoretically controlled stages of event generators. An example of a process which is less well theoretically controlled is hadronisation, its implementation in event generators relying on models which are tuned to data to provide a realistic description of hadronic final states [88]–[90].

One of the key parts of an event generator for modelling jet substructure is the parton shower. Parton showers approximate high order perturbative QCD calculations involving large numbers of partons, which are not computable exactly with current techniques, by repeatedly mapping an n parton state to an $n+1$ parton state. They aim to correctly reproduce the logarithmically enhanced soft and collinear regions of phase space so that computing observables on the final states produced will approximate a resummed calculation. The final state produced by the parton shower can then be passed to a hadronisation model to produce a realistic final state. The reader is referred to ref [94] for an introduction to the workings of parton showers. Because of the generality of what can be measured on the final states produced by parton showers, ascertaining the level of accuracy achieved by a given parton shower is challenging, even for specific observables [95]–[98]. Parton showers currently available in general purpose event generators typically achieve leading logarithmic accuracy, for double logarithmic observables, at leading colour [96], [99]. By using the CMW scheme for the coupling [73], with an appropriate argument, many showers can also achieve NLL accuracy for certain observables [99]. Recently ref. [95] set out

---

[1] For a few suitably defined observables, non perturbative corrections can be calculated approximately in terms of a universal non-perturbative parameter, which is extracted from experiment [84], [85]. These corrections typically scale as powers of $\frac{\mu_{NP}}{Q}$, where μ_{NP} is the scale of non-perturbative effects and Q the hard scattering scale.

criteria for a parton shower to be NLL accurate and showed that a number of pre existing approaches do not meet these criteria for NLL accuracy.

There is a large amount of activity currently ongoing to understand and improve the accuracy of parton showers including: assessing logarithmic accuracy of showers [95], [96], [100], improving existing showers [100]–[102], developing new algorithms [1]–[3], [95], [101], [103], [104] and capturing subleading colour effects in parton showers [102], [104]–[106]. Following ref. [103] the Pan Scales family of parton showers, which are not yet available as part of a general purpose event generator, meet the criteria set out in [95] to achieve NLL accuracy.

3.2 What is a jet?

In the previous section it was mentioned that jets of hadrons are often used as a proxy for coloured particles produced in some high energy process at a collider. This jet of hadrons forms as a result of the hard parton, which initiates the jet, undergoing collinear branchings and emitting soft gluons, which are boosted along the direction of the initial hard parton. This leads to a perturbative picture of a jet initiated by, for instance, a light quark, as a single hard parton surrounded by soft and collinear radiation. At some stage, before they can be observed in the detector, these partons will bind together into hadrons because of colour confinement. In order to make measurements and perform calculations involving jets, a systematic procedure for grouping particles into jets is needed. There are two main types of jet algorithm: sequential recombination, and cone algorithms.

Broadly speaking, cone algorithms, of which the Sterman Weinberg jet cross-section discussed in section 2.4.4 is an example, consist of a prescription to define a number of cones of a fixed size in an event, with all particles that fall into a cone being deemed to be part of the jet. Some algorithms can generate overlapping cones, in which case some prescription to decide on the jet boundary is needed [107]. Many cone algorithms suffer from either an infra-red or collinear un-safety problem for configurations involving more than two jets. In terms of perturbative calculations, this means that the real emission Feynman diagrams can lead to a different set of jets to the loop corrections, meaning that the infra-red and collinear singularities do not cancel [107]. The issue of IRC un-safety has been solved by the use of seedless cone algorithms, such as the SISCone algorithm [108]. Cone algorithms are also less well suited to jet substructure studies so will not be discussed further in this thesis.

Sequential recombination algorithms are defined by a metric, d_{ij}, between two sub-jets, a recombination scheme, and a parameter, R, the jet radius. They take a set of particles/ sub-jets as input and proceed as follows:

1. Calculate the pairwise distance between each pair of particles/ sub-jets according to the chosen metric, d_{ij}.
2. If the smallest $d_{ij} < R$, cluster this pair into a sub-jet and return to step 1).

3. If all $d_{ij} > R$, the algorithm stops and the remaining sub-jets are the final jets.

The recombination scheme enters in step 2), and defines the way in which the 4-momenta of the sub-jets is combined to give the new sub-jet momentum. The simplest choice, which will be the default in this thesis, is to simply add the 4-momenta together, although other schemes exist [109].

It is typical to choose different coordinate systems at lepton and hadron colliders: spherically symmetric coordinate systems for lepton colliders as the detector is in the center of mass frame of the collision; and coordinates which are cylindrically symmetric about the beam axis for hadron colliders, as the center of mass frame for a collision between one parton from each proton is boosted along the beam axis relative to the detector. At lepton colliders, momenta are usually specified by the magnitude and two angles, whilst at hadron colliders the momentum transverse to the beam (P_t), the rapidity ($y = \frac{1}{2} \ln \left(\frac{E+p_L}{E-p_L} \right)$), and azimuthal angle are typically used. It is common to use pseudo-rapidity ($\eta = \frac{1}{2} \ln \left(\frac{|\mathbf{p}|+p_L}{|\mathbf{p}|-p_L} \right) = -\ln \left(\tan \left(\frac{\theta}{2} \right) \right)$, with $\mathbf{p}$ the three momentum, and p_L the component of the momentum along the beam direction) instead of rapidity, the two quantities being equal for a massless four-vector. Most jet substructure tools, including jet algorithms, can be formulated for either lepton or hadron colliders.

The gen-k_t algorithm [109] is a sequential recombination algorithm which, for hadron colliders, has the distance metric

$$d_{ij} = \min(p_{ti}^{2p}, p_{t,j}^{2p}) \frac{\Delta R_{ij}^2}{R^2}, \tag{3.2}$$

where p is a parameter, p_t is the transverse momentum with respect to the beam axis, $\Delta R_{ij} = \sqrt{y_{ij}^2 + \phi_{ij}^2}$ with y_{ij} and ϕ_{ij} are the separation in rapidity and azimuthal angle respectively. For an e^+e^- collider the deffinition

$$d_{ij} = \min(E_i^{2p}, E_j^{2p}) \frac{1 - \cos(\theta_{ij})}{1 - \cos(R)} \tag{3.3}$$

would be used. For specific values of p, the gen-k_t algorithm reduces to other jet algorithms: $p = -1$ gives the anti-k_t algorithm [110], $p = 0$ gives the Cambridge Aachen (C/A) algorithm [111], [112] and $p = 1$ gives the k_t algorithm [113], [114]. The distance metric of the k_t algorithm is, in the collinear limit, just the squared transverse momentum of the softer particle relative to the harder one. This ensures that as two momenta become collinear they are clustered together, resulting in an IRC safe jet algorithm [2]. This choice of distance metric also gives rise to a clustering sequence ordered in the transverse momentum of emissions, mirroring the structure of a collinear parton branching process, the dominant contribution to which can be captured by considering a sequence of emissions ordered in k_t, as discussed in section 2.4.3. Different choices of distance metric give jets ordered in different variables

---

[2] More generally, any value of p in the gen-k_t algorithm will give an IRC safe jet algorithm.

which are useful in different scenarios. The C/A algorithm, for example, gives jets which are ordered in angle, mirroring the angular ordered description of parton branching which can be used to capture the effects of coherence [54], [98]. This property of producing jets with a branching sequence ordered in some kinematic variable, which can be related to the theoretical description of parton branching in the soft and collinear limits, is one of the major benefits of sequential recombination algorithms. It can be useful in constructing observables which which mirror our understanding of the physics they are are designed to measure, which in turn can facilitate resummations of these observables (eg. [29], [115]). For example, if one uses the the gen-k_t algorithm with $p = \frac{1}{2}$, then, in the approximation that all emissions from the parton which initiated the jet are soft and collinear to that parton, the clustering sequence is ordered in the pairwise mass of the splitting, enabling one to easily study or enforce some cut on the mass of the n highest mass splittings within a jet [25], [29]. Although not used much for jet substructure, the anti k_t algorithm [110], corresponding to $p = -1$ in eq. (3.2), is one of the most widely used jet algorithms at the LHC. its popularity is due to the fact that it produces jets with very regular boundaries compared to other sequential recombination algorithms [116]. Having jets with a more uniform boundary and size is beneficial from an experimental point of view as it assists with the calibration of detector effects and the effect of UE on a jet [107].

3.3 Jet grooming

What one typically wants to capture in a jet are the decay products of a particle produced in a hard process whilst leaving out ISR, MPI, beam remnants, and particles from additional simultaneous *pp* collisions, known as pileup (PU) [117]. [3]. Unfortunately it is not possible to construct a jet algorithm that will do this perfectly. It is worth noting that ISR is perturbatively calculable while MPI and beam remnants are controlled by non perturbative physics. The additional particles generated by the UE and PU are clustered by jet finding algorithms, and degrade the jets properties, spoiling the association of the jet's properties with those of a particular particle [118]–[120]. This can be illustrated by using an event generator such as Pythia to produce two samples of events, one with MPI and ISR deactivated and one with them activated. By computing the same observable on both samples and comparing the distributions, an idea of the size of the effect that UE can have is gained. An example of this is shown in figure 3.1 for the fraction of jets, ϵ, which satisfy $\tau_{32} < \tau$, where τ_{32} is a ratio of N-subjettiness variables [14], which is investigated in the context of top-tagging in chapter 6. The definition of this observable is not important here, rather, the point is that UE, which has nothing to do with the dynamics we are interested in, has a large impact on the distribution. There are three curves corresponding to parton level events with no UE, hadron level events with no UE, and

---

[3] MPI, ISR and beam remnants are absent at electron-positron colliders, although pileup can still be a problem there.

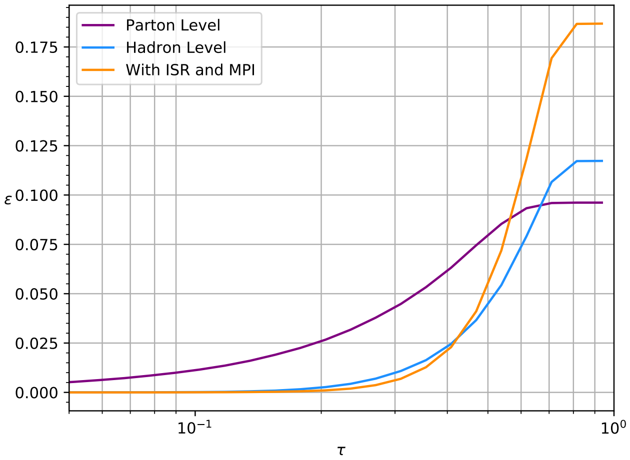

Figure 3.1. Plot showing the fraction of jets simulated with Pythia with $P_t > 2$TeV remaining after a cut $\tau_{32} < \tau$ is applied at parton and hadron level with MPI and ISR deactivated and at hadron level with ISR and MPI activated.

hadron level events with UE.

It is therefore desirable to remove ISR, UE and PU from jets. This is known as grooming. As there is no way to unambiguously distinguish between soft particles emitted from within the jet and those from ISR, UE and PU, grooming will also remove some soft radiation which was emitted within the jet. This is not necessarily a bad thing and can even be part of the intended behaviour of the groomer, as it can aid the identification of any hard substructure within the jet and reduce the impact of non-perturbative effects. In some cases though, this is undesirable as, for example, removal of this radiation can harm the performance of subsequent tagging procedures [29], as will be discussed further in section 3.4.1.
Underlying event can be approximated as soft radiation emerging uniformly from a collision, whereas soft radiation from within a jet, as well as being soft enhanced, is enhanced collinear to the hard parton(s) which initiates the jet. The amount of UE removed can therefore be maximised, whilst minimising the removal of soft radiation originating from within the jet, by removing soft radiation at wide angles to the hard parton(s) in the jet. Many grooming procedures, such as trimming [11] and pruning [12], [13], are designed based on this idea.
Trimming works by re-clustering the jet into multiple smaller sub-jets using the k_t algorithm with radius parameter R_{sub}, which is smaller than the original jet radius, and determines how much collinear radiation will be groomed away. Any sub jets which carry momentum fraction less than z_{cut} are removed, and the remaining sub-jets are deemed to be the trimmed jet.
The pruning algorithm works its way through the clustering sequence of a jet, starting at the final clustering. At each clustering the algorithm discards the softer branch if $\frac{\min(p_{t1},p_{t2})}{p_{t1}+p_{t2}} < z_{\text{cut}}$ and $\Delta R_{1,2} > R_{\text{Prune}}$. The pruning radius is determined by the mass of the jet as $R_{\text{Prune}} = R_{\text{fact}}\frac{2m_{\text{jet}}}{P_t}$, where R_{fact} is a parameter of the algorithm, which, similar to R_{sub} for the trimming procedure, can be used to tune how much

collinear radiation will be removed.

One of the early use of grooming at the LHC, which drove much of the development of grooming and tagging algorithms, was the identification, or tagging, of jets initiated by a boosted electroweak bosons, which is discussed in more detail in section 3.4. This necessitated algorithms which would aid the identification of hard substructure within jets whilst enhancing the characteristic mass peak of jets initiated by boosted electroweak bosons, which is smeared by QCD radiation. Many earlier algorithms had a dual grooming and tagging function, whereas it is now more common to consider these steps separately. Having said this, all of the algorithms discussed in this section can be used in a purely grooming mode or a tagging mode where jets are rejected if all but one branch/sub-jet is removed.

To begin with, much of the testing and development of these grooming and tagging algorithms was carried out using event generators [10], [11]. Whilst this type of study allows the performance to be tested and tuned, it was realised [21] that event generator studies alone can not allow us to understand the gain in performance observed when these techniques are applied, and whether it is a general feature of the algorithm, or a result of the specific choice of parameters. There is also the issue that different event generators (eg. see results presented in section 6.3.3), and even different tunes of the same generator can produce quite different results [116], [121]–[123]. Ref [21] set out to study the effect of three different grooming/ tagging procedures on light QCD jets through analytical leading log resummations. The three algorithms studied were trimming [11], pruning [12], [13], and the mass drop tagger [10].

Trimming and pruning both remove soft branches, where the angular distance from the branch it is clustered to is above some pre-determined threshold, from throughout the whole jet. The mass drop tagger is slightly different in the sense that when it finds a clustering where neither branch is groomed away it stops, leaving splittings at smaller angular scales un-groomed. The mass drop tagger can be stated by the following steps:

1. Take a jet and re-cluster it using the C/A algorithm.
2. Undo the last clustering of the C/A jet to give two sub-jets, with the heavier labelled a, and the lighter b.
3. If $y = \min(p_{ta}^2, p_{tb}^2)\frac{\Delta R_{ab}^2}{m_{\text{jet}}^2} < y_{\text{cut}}$ or $m_a > \mu m_{\text{jet}}$ remove branch b from the jet and return to step 2. y_{cut} and μ are both parameters of the tagger. Otherwise the final jet contains a and b and the grooming process stops and the jet is deemed to be tagged. If only a single branch is left in the jet, then it is rejected.

The y_{cut} condition essentially results in the removal of branches which carry a small fraction of the jet's momentum that are at wider angles than any hard substructure within the jet. The condition on the mass results in the removal of branches which do not contribute significantly to the jets mass, hence the name "mass drop tagger"[4]. The MDT can be used purely as a groomer by not rejecting jets where all branches are groomed away. Ref. [21] found, for light QCD jets, that the removal of the branch with lower invariant mass when one of the conditions in step 3 is met can result in the groomer removing the branch containing the parton which initiates the jet, which was not the intended behaviour. This feature was found to complicate the all orders behaviour of the groomer [21], making it more difficult to calculate resummed results. A modified mass drop tagger (mMDT) was proposed [21], in which the groomer follows the branch with higher transverse mass ($m^2 + P_t^2$) which rectifies this issue. A further modification which somewhat simplifies the statement of the groomer is to replace the condition $y < y_{\rm cut}$ with a cut on the transverse momentum fraction carried by the sub-jet, $\min(z_a, z_b) < z_{\rm cut}$ where $z_i = \frac{p_{ti}}{p_{t,\rm jet}}$.

Several notable features of the jet mass distribution (and other observables) measured on jets groomed with mMDT were identified from their analytical calculations: in the region where $\rho = \frac{m^2_{\rm jet}}{R^2 P_t^2} < z_{\rm cut}$ the leading logarithm is a single collinear logarithm of ρ; non-global logarithms of ρ are completely eliminated, which is due to there being no soft logarithms, only collinear ones; the mass drop condition of step 3 does not play a role at leading logarithmic accuracy. Because of the lack of strong dependence on the mass drop condition, mMDT is most commonly used now without this condition. It is also frequently used purely as a groomer, where jets are not rejected if all of the branches are groomed away.

Ref. [21] also showed that grooming jets with mMDT resulted in a reduction in the size of hadronisation corrections both compared to un-groomed jets and also compared to the other procedures tested. This was initially done using Pythia to investigate the difference in the jet mas distribution computed on parton and hadron level events, before going on to analytically investigate the scaling of hadronisation corrections with the jet mass.

The lack of NGLs and reduced hadronisation effects are particularly important properties of observables groomed with mMDT. The lack of NGLs greatly facilitates the calculation of resummed distributions of jet substructure observables, due to the difficulty in resumming NGLs being removed. This in turn allows such calculations to be pushed to higher accuracy. The reduction of hadronisation effects also makes observables groomed with mMDT excellent candidates for direct comparison between perturbative calculations and measurements from collider experiments, as shall be discussed further in section 3.5.

The mMDT is an excellent example of why it is important to understand jet substructure tools analytically, from first principles. Dissecting the behaviour of the original mass drop tagger allowed the authors of [21] to identify and fix the unintended behaviour of the MDT as discussed above. Carrying out the resummation for the mMDT groomed jet mass distribution allowed them to understand that the mod-

---

[4] This condition reflects the fact that this algorithm was initially proposed as a method for tagging jets initiated by Higgs bosons, where the Higgs decays to two b quarks, resulting in two sub-jets associated to the b quarks, the pairwise invariant mass of which dominates the mass of the jet.

ified groomer had desirable properties, which aside from being helpful for tagging electroweak bosons, made it well suited to precision QCD calculations.

The mMDT has subsequently been generalised to soft drop [23], which is stated, using hadron collider variables, as follows:

1. Take a jet and re-cluster it using the C/A algorithm.
2. Undo the last clustering of the C/A jet to give two branches labelled a and b with transverse momentum fractions $z_a > z_b$, where $z_i = \frac{p_{ti}}{p_{t,a}+p_{t,b}}$.
3. If $z_b < z_{\text{cut}}\theta_{ab}^{\beta}$ remove branch b from the jet and return to step 2. Otherwise the final jet contains a and b and the grooming process stops.

Setting $\beta = 0$ recovers the mMDT grooming procedure. Taking $\beta > 0$ makes the grooming action of soft drop less aggressive as grooming is effectively switched off gradually as the groomer recurses further into the collinear region of the jet. This results in less soft and collinear emissions from within the jet being removed, at the expense of removing less underlying event. Away from $\beta = 0$, soft drop groomed observables will generally contain soft logarithms of the observable, making them double logarithmic. Despite the presence of soft logarithms, soft drop groomed observables are also free of NGLs [5].

3.4 Jet tagging

The identification or tagging of jets initiated by boosted bosons was one of early driving forces behind LHC jet substructure studies. Although substructure techniques for tagging W bosons had been developed in earlier work [9], the usefulness of jet substructure was truly appreciated as a tool for searching for hadronically decaying Higgs (and other) bosons following ref. [10].

At the LHC, electroweak bosons and top quarks can be produced with sufficiently high transverse momentum that their decay products are reconstructed as a single jet. It is then a significant challenge to differentiate between jets initiated by different species of particle. In this section we will discuss the case where these particles decay fully hadronically, as other decay modes can be identified by other means.

As discussed in section 3.1, a jet initiated by a light quark or gluon will typically consist of a single hard parton surrounded by soft and collinear radiation from that parton. This is, of course, a perturbative picture, but the resulting substructure of a single hard core surrounded by soft and collinear particles persists at hadron level. Now consider an electroweak boson which decays to a $q\bar{q}$ pair, both of which are reconstructed inside the same jet. The decay of electroweak bosons does not favour unequal sharing of the momentum between the decay products, and so these jets will typically have two hard cores, each surrounded by soft and collinear radiation. This

---

[5] Soft drop groomed observables actually contain NGLs suppressed by powers of the observable [23], but these are typically ignored in resummed calculations, as are other power suppressed terms.

two-pronged structure is one of the features used to differentiate between QCD jets (light quark and gluon jets) and W, Z and H jets. Top quarks can decay via a W boson to a system of three quarks, all of which will typically carry a significant fraction of the jet's energy, leading to a three pronged structure.
There has been a huge range of techniques developed for tagging jets initiated by boosted heavy particles. As well as the prong finding algorithms, jet shapes, and machine learning methods discussed in sections 3.4.1, 3.4.2 and 3.4.3 respectively, methods based on possible parton shower histories [124] and approximations to the likelihood ratio constructed using the Lund plane [125] have also been investigated. Many studies proposing and evaluating jet tagging techniques were initially carried out using Monte Carlo simulations to assess their performance. Good performance in this instance corresponds to a high signal to background $\left(\frac{\epsilon_s}{\epsilon_b}\right)$ or high signal significance $\left(\frac{\epsilon_s}{\sqrt{\epsilon_b}}\right)$. Whilst using Monte Carlo algorithms in this way allows one to test the performance of an algorithm for a specific use case, it does not give generic information as to how the tagger might perform at different energy scales or with different choices of parameters. Another concern, partly motivated by differences observed between different event generators [21] , was that Monte Carlo generators may not provide a sufficiently accurate description of the substructure of jets to build up an accurate picture of how these methods could be expected to perform when applied to data. Of particular concern were the extent to which jet substructure methods may be sensitive to model dependent non-perturbative effects. There is now a large body of work, which is added to in chapter 6, dedicated to understanding the function and performance of jet substructure methods through analytical calculations. This work has shown that these techniques and the features observed in MC simulations can be understood and reproduced from perturbative calculations, increasing confidence in their robustness [21]–[31], [126], [127]. In some cases, such as the mMDT discussed in the previous section, these studies have been identified problems and been able to design improved tools based on the understanding gained from their calculations [21]–[25]. With the recent revolution in machine learning techniques in particle physics, similar questions are now being asked about the robustness of machine learning algorithms [128], as will be discussed further in section 3.4.3.

As well as discriminating between boosted bosons, top quarks, and QCD jets, it is also desirable to be able to discriminate between light quark and gluon initiated jets.[6] At double logarithmic accuracy the only difference between quark and gluon jets is the difference in the probability of emitting soft and collinear gluons due to the difference in colour factor. Beyond leading logarithmic accuracy the possibility of $g \to q\bar{q}$ splittings, which are not soft enhanced, and hadronisation effects are also important [129]. Discriminating between quark and gluon jets can be achieved using jet

---

[6] The concept of quark and gluon initiated jets in somewhat ambiguous and ill defined [129]. One can adopt a semi-classical picture similar to what happens in an event generator, where a parton from a hard process initiates a shower, the radiation from which is clustered as a jet. The flavour of the parton which initiated the shower can then be thought of as the jet flavour. In reality, the only thing one can do is specify some definition of a quark or gluon jet which can be applied to hadronic final states based on ideas from the aforementioned picture [129].

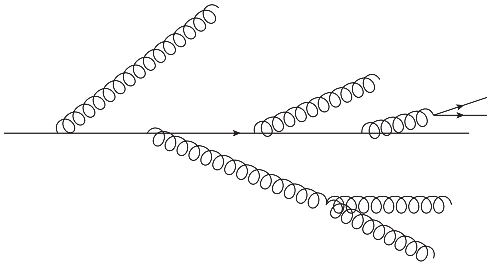

(a) A typical perturbative picture of a quark jet, consisting of a single hard quark which initiates the jet and emits a number of soft and or collinear gluons, which can undergo further branchings.

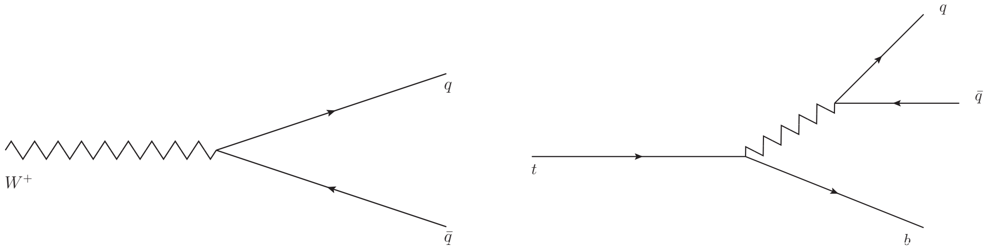

(b) Decay of a W boson to a $q\bar{q}$ pair. The quarks can radiate gluons, which will typically be soft, but this will be confined to the opening angle of the quarks by QCD coherence.

(c) Decay of a top quark to a b quark and a $q\bar{q}$ pair. All of the quarks in this picture can radiate gluons, resulting in a complicated radiation pattern within hadronic top jets.

Figure 3.2

shape observables [130], [131] and machine learning algorithms [34].
The next sub-sections will discuss three of the main classes of jet tagging procedure in more detail: prong finding, jet shapes, and machine learning.

3.4.1 Prong finding

Prong finding algorithms are used to tag heavy boosted particles such as top quarks, Higgs, W, and Z bosons. The idea of a prong finding algorithm is to identify a number of hard sub-jets/prongs within a jet and apply a set of kinematic cuts which discriminate between light QCD jets and signal jets.
As the hard prongs will typically correspond to the leading order decay of the boosted particle, one generally expects them to carry a similar fraction of the jet's energy. This is in contrast to a QCD background jet which will typically consist of a single hard prong along with a number of soft gluons, as shown in figure 3.2a. Therefore, once they have identified a number of candidate sub-jets, prong finding algorithms will typically require the sub-jets to carry a certain fraction of the jet's energy or pass some similar cut so as to select jets containing reasonably symmetric splittings, which are more likely to be signal jets.
Signal jets will typically have an invariant mass associated with the leading order decay of the boosted heavy particle. As an example, consider a W boson decaying to a $q\bar{q}$ pair, as shown in figure 3.2b. The invariant mass of the $q\bar{q}$ pair will be M_W. This

can also be used to discriminate between signal and background, as soft and collinear splittings in light QCD jets will typically have a small invariant mass. Prong finding algorithms can exploit this by introducing a requirement that invariant mass of the candidate prongs is above some threshold. The situation is more complicated for top jets, which decay via a W boson to a b quark and light $q\bar{q}$ pair, as shown in figure 3.2c, as there is no characteristic pairwise invariant mass between the b quark and either of the light quarks. Nevertheless, a minimum pairwise invariant mass cut is still beneficial, as the three prongs must, between them, generate the top mass, leading to relatively large pairwise invariant masses. Additionally the $q\bar{q}$ pair will have an invariant mass of approximately the W boson mass.

One early algorithm with the sole function of prong finding is the Y-splitter algorithm proposed in [9] for tagging boosted W bosons, although it can be equally used for tagging other electroweak bosons. It takes a jet clustered with the k_t algorithm and undoes the last clustering to find two sub-jets, a and b. The distance metric for this clustering algorithm is

$$d_{ij} = \min(p_{ti}^2, p_{tj}^2)\Delta R_{ij}^2 \ . \tag{3.4}$$

Y-splitter then introduces a cut on the ratio of d_{ab} to the square jet mass $\frac{d_{ab}}{m_{\text{Jet}}^2} > y_{\text{cut}}$, where y_{cut} is a parameter of the tagger. In the collinear limit we can write $d_{ab} \simeq P_{t,\text{Jet}}^2 \min(z, 1-z)^2\theta^2$ and $m_{\text{Jet}} \simeq z(1-z)\theta^2$, where z is the energy fraction carried by branch a. For $z < \frac{1}{2}$, the effect of the cut on y is then $\frac{z}{1-z} < y_{\text{cut}}$. This has the effect of rejecting very asymmetric splittings which are likely to be a QCD splitting as opposed to the electroweak decay of a boosted boson.

The action of the Y-splitter algorithm on QCD jets and jets initiated by a boosted Higgs was studied analytically in refs. [29] and [30] along with several other tagging procedures. Along with the prong finding procedure the jets were required to be within a mass window $M_{\text{Higgs}} - \delta M < M_{\text{Jet}} < M_{\text{Higgs}} + \delta M$ about the Higgs mass.

It was shown, that if one neglects ISR and UE, that the signal efficiency is given by

$$\epsilon_s \simeq 1 - 2y_{\text{cut}} \ . \tag{3.5}$$

However, ISR and UE were seen to modify this result quite substantially and degrade the signal efficiency so that Y-splitter by itself has quite poor performance.

It was argued in [30] that this was due to ISR and UE degrading the jet mass and pushing signal jets outside the mass window. Adding a grooming step after the application of Y-splitter but before the mass cut resulted in an increased signal efficiency due to removal of ISR and UE and subsequently improved performance.

The background distribution after application of Y-splitter was calculated to all orders in [29], which if one keeps only the leading logs in ρ is given at fixed coupling by

$$\frac{\rho}{\sigma}\frac{\mathrm{d}\sigma}{\mathrm{d}\rho} = \frac{C_F\alpha_s}{\pi}\ln\frac{1}{y_{\text{cut}}} \times \exp\left[-\frac{C_F\alpha_s}{2\pi}\ln^2\frac{1}{\rho}\right] \ . \tag{3.6}$$

The double logarithmic Sudakov suppression explains the excellent background suppression observed for Y-splitter. After accounting for running coupling effects and hard collinear splittings, good agreement was found with parton level Pythia simulations, indicating that this calculation at modified leading log accuracy can explain the overall performance of the tagger. It was noted that resummation of subleading terms can be simplified whilst leaving the dominant double logarithms of ρ, given above, unchanged by two small modifications: firstly the clustering sequence is changed to gen-k_t with $p = \frac{1}{2}$, giving a jet which in the soft and collinear limit has a clustering sequence ordered in mass; Further simplifications come from replacing the y_{cut} condition with $\frac{\min(p_{ta}, p_{tb})}{p_{ta}+p_{tb}} > z_{\text{cut}}$. This modified algorithm is called Y_m-Splitter , which as well as being theoretically simpler, was seen to have a slightly improved performance.

Adding grooming does not modify the above result at LL accuracy. This explains the observation that grooming after Y-splitter improves performance as the double logarithmic Sudakov suppression of the background is kept, giving good background rejection, whilst the effect of ISR and UE on the jet mass is reduced, resulting in higher signal efficiency. The effect of grooming jets with soft drop before applying Y_m-Splitter was also investigated. In this case the Sudakov factor inherits its structure from the groomed jet mass,

$$\frac{\rho}{\sigma}\frac{\mathrm{d}\sigma}{\mathrm{d}\rho} \overset{\rho<z_{\text{cut}}}{=} \frac{C_F\alpha_s}{\pi}\ln\frac{1}{y_{\text{cut}}}\times$$
$$\exp\left[-\frac{C_F\alpha_s}{\pi}\left(\frac{\beta}{2(2+\beta)}\ln^2\frac{1}{\rho}+\frac{2}{2+\beta}\ln\frac{1}{z_{\text{cut}}}\ln\frac{1}{\rho}-\frac{2}{2+\beta}\ln^2\frac{1}{z_{\text{cut}}}-\frac{3}{4}\ln\frac{1}{\rho}\right)\right] \quad , \qquad (3.7)$$

with correspondingly smaller background suppression and thus generally worse performance. One benefit of pre-grooming the jets is the reduced sensitivity to non-perturbative effects as the tagger is no longer vetoing on the region of phase space most sensitive to them. There is, therefore, a trade-off between robustness against non-perturbative effects and performance depending on whether the jet's are groomed before or after applying Y-splitter.

Prong finding algorithms have also been used to identify high P_t hadronically decaying top quarks which are reconstructed as a single jet by ATLAS [132] and CMS [16], [133]. The CMS top tagger [16], [133] was studied analytically in [25], along with several other prong finding algorithms, where it was found that the CMS top-tagger is not collinear safe and fully IRC safe adaptions of the algorithm were proposed. Another of the algorithms studied was a variant of the Y_m-Splitter adapted for the identification of top jets. The top Y_m-Splitter takes a jet clustered with the gen-$k_t(p = \frac{1}{2})$ algorithm and performs the following steps:

1. Undo the last clustering, to give two sub-jets, both of which are examined for the condition $p_{t,i} > \zeta p_{t,\text{jet}}$. If either sub-jet fails the ζ condition, the jet is rejected.

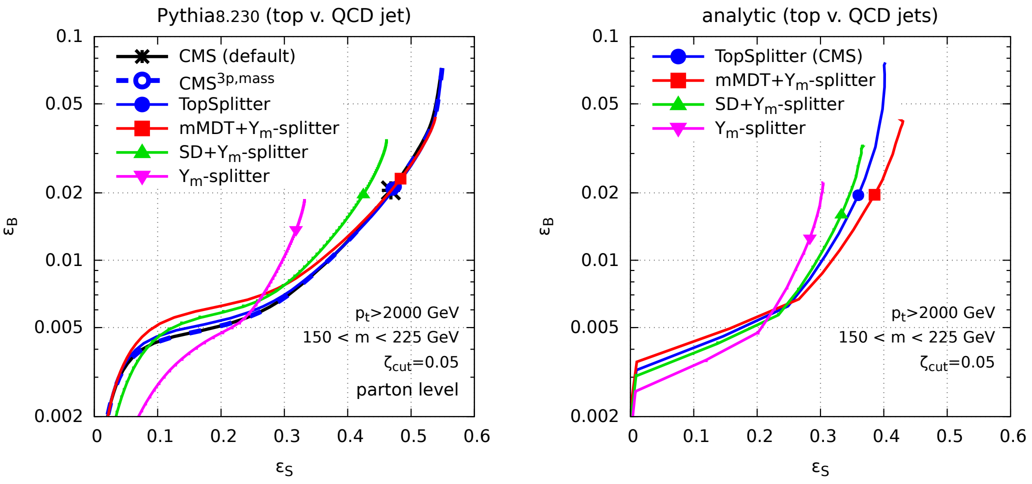

Figure 3.3. ROC curves showing the signal and background tag rates for several combinations of prong-finding and grooming studied in [25], where the plots are taken from. The curves on the left are derived from events generated using Pythia, whist the curves in the right hand plots are calculated analytically.

2. Check which sub-jet produces the larger gen-k_t distance when de-clustered, and undo the last clustering of this sub-jet. Check whether the resulting sub-jets from this de-clustering pass the ζ condition. If either the de-clustering or the ζ condition fail, the jet is rejected.

3. Find the pairwise masses of the three final sub-jets, and require that $\min(m_{12}, m_{13}, m_{23}) > m_{\text{min}}$. If this condition is not met, the jet is rejected.

Unlike when tagging boosted electroweak bosons, the signal (top quarks), carries a colour charge and therefore acquires a Sudakov factor similar to the background. As a result, tagging procedures which generate smaller Sudakov factors were found to give better performance. This can be seen in figure 3.3 from the ordering of the Y_m-Splitter taggers with different levels of grooming: no grooming having the largest Sudakov suppression and correspondingly the worst performance, whilst the most aggressive grooming with mMDT has the smallest Sudakov suppression and the best performance. That the analytic calculations shown in figure 3.3 capture the overall shape of the ROC curves extracted from parton level Pythia simulations and ordering of the taggers can be taken as a sign that the important features of the tagging algorithms have been properly understood, and that a modified leading-logarithmic calculation is sufficient to capture them.

3.4.2 Jet shapes

Jet shapes are a type of observable which are designed to be measured on a jet and are a function of the momenta of all particles within that jet. The invariant mass of a jet is a simple example. Jet shapes can often be used to quantify some qualitative feature of a jet, such as how n-prong like a jet is. Because of this they have been extensively used in boosted object tagging. For run two of the LHC both ATLAS and CMS developed procedures to tag jets initiated by vector bosons involving cutting on the mass of candidate jets and another jet shape variable [116]. ATLAS opted for cutting on the variable $D_2^{\beta=1} = e_3^{(\beta)}/(e_2^{(\beta)})^3$ [24], [134], where $e_n^{(\beta)}$ are n point energy correlation functions [127], whilst CMS opted for cutting on the ratio of N-subjettiness variables $\tau_{21} = \frac{\tau_2}{\tau_1}$ [14]. Ratios of jet shapes such as τ_{21} and $D_2^{(\beta)}$ are generally not fully IRC safe but Sudakov safe.

Sudakov safe observables [135] are ones that are not IRC safe and so cannot be calculated at fixed order in perturbation theory, but are calculable once all orders effects are taken into account. To make this more precise, consider the distribution of an observable u,

$$p(u) = \frac{1}{\sigma}\frac{\mathrm{d}\sigma}{\mathrm{d}u}, \tag{3.8}$$

which is not IRC safe, but which is safe when measured simultaneously with an IRC safe observable, v, so that the probability distribution of u given v, $p(u|v)p(v)$, is finite. We can then integrate out v to get back $p(u)$:

$$p(u) = \int p(u|v)p(v)\mathrm{d}v \ . \tag{3.9}$$

If, having calculated $p(u|v)p(v)$ to all orders, the above integral is finite, u is a Sudakov safe observable, named as such as suppression from the Sudakov factor regulates the divergences of the IRC unsafe observable causing the integral to converge. Although perturbatively calculable, there remain questions about the sensitivity of Sudakov safe observables to non perturbative effects. For IRC safe observables non-perturbative corrections scale as a positive power of $\frac{\Lambda}{Q}$, where Λ is a small non-perturbative scale of order Λ_{QCD}, and Q is the hard scale of the process, which is typically much larger than Λ [136]. For Sudakov safe observables, there is no guarantee that non-perturbative effects scale in this way, and so non-perturbative corrections may be more significant.

It is important to note that a measurement of τ_{21} can be made fully IRC safe either by fixing or putting a lower limit on the jet mass, as this prevents τ_1 from going to zero.

We will now discuss what drives the discriminating power of N-subjettiness ratios, using $\tau_{21}^{\beta=2}$ as applied to tagging two prong jets as an example. We will first discuss this qualitatively before examining the results of a calculation of the signal and background distributions after applying a cut on τ_{21} [28] to see the insight that can be gained from such calculations.

The N-subjettiness variables are defined as

$$\tau_N^{\beta} = \frac{1}{p_{t,\mathrm{jet}} R^{\beta}} \sum_{i\in\mathrm{jet}} p_{t,i} \min\left((\Delta R_{1,i})^{\beta}, (\Delta R_{2,i})^{\beta}, ..., (\Delta R_{N,i})^{\beta}\right), \tag{3.10}$$

with the sum over i running over the jet constituents. The N partition axes, labelled

$1 \cdots N$, can be defined by various methods. One method is to find the axes which minimise τ_N, which is known as finding the the optimal axes. Another method is to re-cluster the jet using the gen-k_t algorithm with $p = \frac{1}{\beta}$ and undo the last $N-1$ clusterings of the jet to find N sub-jets. The partition axes are then taken to lie along these sub-jet axes. This set of axes is referred to as the gen-k_t axes. The idea is to choose axes so that if τ_N^{β} is measured on an N-pronged signal jet, the axes will lie along the direction of the hard prongs corresponding to the LO decay of the boosted particle. For light QCD jets one expects the axes to approximately coincide with the partons which contribute most to τ_N^{β}.
The ratio $\frac{\tau_N^{\beta}}{\tau_{N-1}^{\beta}}$ can be used to discriminate N sub-jet like (or N prong like) jets from QCD background jets, with smaller values of $\frac{\tau_N^{\beta}}{\tau_{N-1}^{\beta}}$ corresponding to more N prong like jets. Intuitively, this is because the contribution from a single soft gluon to τ_N is expected to be small, so that, for light QCD jets, the difference between τ_N^{β} and τ_{N-1}^{β} is expected to be small, and the ratio $\frac{\tau_N^{\beta}}{\tau_{N-1}^{\beta}}$ of order one. On the other hand, jets with N hard prongs should have $\tau_N^{\beta} \ll \tau_{N-1}^{\beta}$ because a hard prong is expected to set a large value of τ_{N-1}^{β} so that $\frac{\tau_N^{\beta}}{\tau_{N-1}^{\beta}} \ll 1$. This configuration is illustrated in figure 3.4b.
The N-subjettiness ratio $\tau_{21}^{\beta=2}$, along with other jet shape variables, was studied through resummed calculations of the tagged fraction of signal (boosted W,H,Z bosons) and background (light QCD jets) events in [28]. They calculated the jet mass distribution with the additional restriction that jets should satisfy $\tau_{21}^{\beta=2} < \tau$ in the limit that $\tau \ll 1$. For background jets they considered a sequence of emissions from a hard parton, which are strongly ordered in mass, $\rho_i \gg \rho_{i+1}$, where, in the soft and collinear limit, $\rho_i = z_i\theta_i^2$ is the pairwise invariant mass of an emission with the parton that initiates the jet. This is sufficient to calculate the resummed distribution to leading logarithmic accuracy. For such configurations the first emission dominates both the jet mass and $\tau_1^{\beta=2}$, which in the soft and collinear limit are equivalent as the first N-subjettiness axis will lie along the parton that initiates the jet, as shown in figure 3.4a. The second N-subjettiness axis will be along this first emission so that radiation around this gluon, as well as that around the parton which initiated the jet, is restricted by the cut on $\tau_{21}^{\beta=2}$. This configuration of emissions along with the relationship of the N-subjettiness axes to them is illustrated in figure 3.4a.

For background jets, normalising θ to R, the jet radius, ref. [28] found that

$$\frac{\mathrm{d}\sigma}{\mathrm{d}\rho} = \int_{\rho}^{1} \frac{\alpha_s(z_1\theta_1 R P_t)}{2\pi}\frac{\mathrm{d}\theta_1^2}{\theta_1^2}\int_{\rho}^{1} P(z_1)\mathrm{d}z_1 \delta(\rho - z_1\theta_1^2)\exp[-R(\rho\tau) - R^{\text{secondary}}(\tau, \theta_1^2, z_1)] \quad (3.11)$$

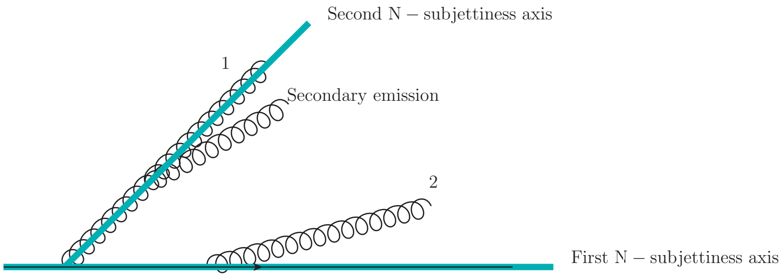

(a) A diagram illustrating a strongly ordered configuration of emissions where $\rho_1 \gg \rho_2$. The direction of two N-subjettiness axes are shown as coinciding with the quark that initiates the jet and emission 1. A secondary emission, which will be constrained by a τ_{21} cut is also shown.

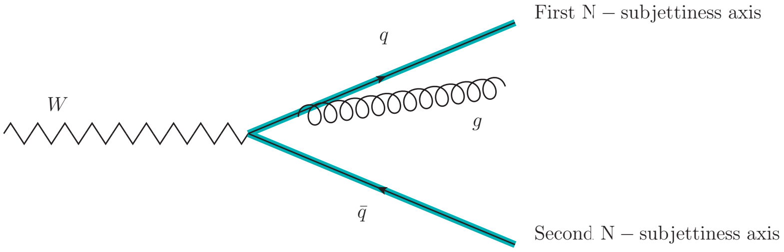

(b) A diagram illustrating the relationship of two N-subjettiness axes to the partons within a jet initiated by a W boson. For τ_1 only one of the axes as would be present, and so one of the hard prongs would contribute to τ_1, as opposed to just the gluon as is the case for τ_2.

Figure 3.4

where

$$R(\rho\tau) = \int_0^1 \frac{\alpha_s(z\theta R P_t)}{2\pi}\frac{\mathrm{d}\theta^2}{\theta^2}\int_0^1 P(z)\mathrm{d}z\Theta(\rho\tau - z\theta^2) \tag{3.12}$$

$$R^{\text{secondary}}(\tau,\theta_1,z_1) = \int_0^{\theta_1^2} \frac{\alpha_s(z_1 z\theta R P_t)}{2\pi}\frac{\mathrm{d}\theta^2}{\theta^2}\int_0^1 P(z)\mathrm{d}z\Theta\left(\tau - z\frac{\theta^2}{\theta_1^2}\right) \quad . \tag{3.13}$$

The term $e^{-R^{\text{secondary}}(\tau,\theta_1,z_1)}$ is responsible for vetoing secondary emissions from the gluon lying along the second N-subjettiness axes of τ_2. Note that due to coherence the secondary Sudakov factor only vetoes emissions up to θ_1, the angle that the gluon which dominates the jet mass is emitted at.

For signal jets, the boson that initiates the jet decays into a $q\bar{q}$ pair which carry fractions of the jet's momentum z_1 and $1 - z_1$ respectively. The N-subjettiness axes will lie along the directions of the $q\bar{q}$ pair, resulting in radiation being constrained around these prongs. For signal jets ref.[28] found that

$$\frac{\mathrm{d}\sigma}{\mathrm{d}\rho} \propto \exp[-R(\tau, z_1, \theta_1^2) - R(\tau, 1 - z_1, \theta_1^2)] \tag{3.14}$$

where

$$R(\tau, z_1, \theta_1^2) = \int_0^{\theta_1^2} \frac{\alpha_s(z_1 z\theta R P_t)}{2\pi}\frac{\mathrm{d}\theta^2}{\theta^2}\int_0^1 P_{gq}(z)\mathrm{d}z\Theta(z_1\theta_1^2\tau - z\theta^2)\ , \tag{3.15}$$

and $\theta_1^2 = \frac{\rho}{z_1(1-z_1)}$, the opening angle of the $q\bar{q}$ pair. The above Sudakov factors are

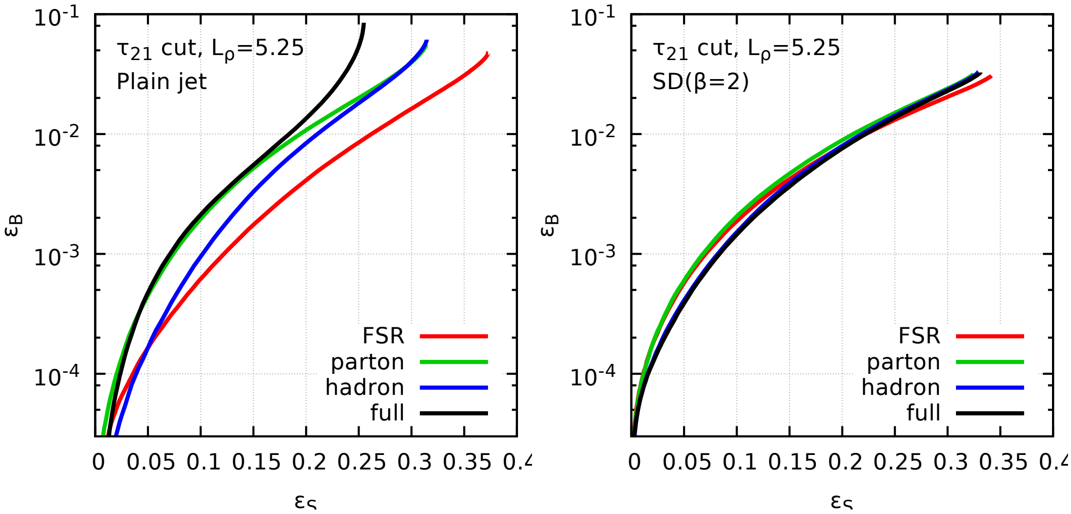

Figure 3.5. ROC curves taken from ref. [28] showing the signal vs background tag rates as the cut on τ_{21} is varied. On the left the jets are simply tagged with a cut on τ_{21} whereas on the right they are first groomed using soft drop with $\beta = 2$.

a result of vetoing emissions from the $q\bar{q}$ pair coming from the decaying boson. The key point to notice here is that emissions from the $q\bar{q}$ pair are only vetoed up to θ_1 due to QCD coherence. The effect of this is that there is much less Sudakov suppression on signal jets than QCD jets which explains the effectiveness of τ_{21} at discriminating between QCD jets and jets initiated by colour singlet bosons. This is a much more precise understanding of the origin of the discriminating power of τ_{21} than the intuitive description presented earlier.

The above calculations are carried out ignoring the effects of ISR, MPI and other non-perturbative effects. The impact of these effects were investigated in ref. [28] using Pythia to generate events, initially with ISR, MPI and hadronisation switched off, before switching these effects on one at a time. The signal and background tagging efficiencies were then extracted as a function of the cut on τ_{21} with $5 < \ln(1/\rho) < 5.5$ and ROC curves constructed, which are shown in figure 3.5. These show that UE and hadronisation negatively impact the performance of the tagger. As well as having a negative effect on the performance of the tagger, both MPI and hadronisation effects are not derivable from first principles QCD and our understanding of them in this context relies on the models implemented in event generators. For both of these reasons it is therefore desirable to reduce the effect of UE and hadronisation on tagged distributions. This can be accomplished by pre-grooming the jets using soft drop. ROC curves computed on jets pre-groomed with soft drop with $\beta = 2$ are also shown in figure 3.5 alongside those for un-groomed jets where the increased resilience to UE can clearly be seen.

For top tagging, the N-subjettiness variable expected to be most useful is τ_{32} [137]. In practice this has often been used by experiments in conjunction with a prong finding algorithm [15], [18], [138]. Investigating this combination of techniques analytically is the subject of chapter 6.

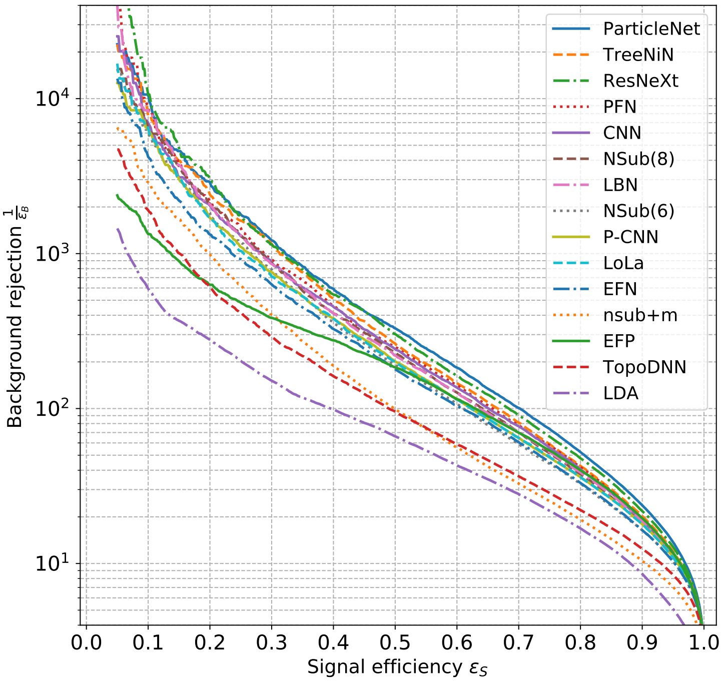

Figure 3.6. ROC curves comparing the tagging performance of a number of ML based top taggers and a benchmark cut based tagger. Plot taken from [32]

3.4.3 Machine learning taggers

In recent years machine learning (ML) has emerged as a powerful tool for discriminating between jets originating from different species of particle. There are a huge number of machine learning tools available for boosted particle classification. These range from boosted decision trees and deep neural networks which take information from a small number of physically motivated observables and combine them to produce a single discriminant [19], [20] , to neural networks which essentially take raw information about the jet, such as the momentum four-vectors of the jet's constituents, from which an approximation to the optimal discriminant is learnt [33], [139]–[141], as well as approaches that fall somewhere in between [35]. Machine learning for boosted particle tagging has been extensively used by ATLAS and CMS as it can often achieve higher signal to background ratios than the more traditional cut based taggers [19], [20], [142]. This high level of performance is illustrated in figure 3.6 by the ROC curves for a number of ML algorithms trained to tag top jets along with a benchmark cut based tagger utilising τ_{32} and the jet mass. Although the performance of this benchmark tagger could probably be improved upon, the point still stands that machine learning typically outperforms cut based taggers in terms of raw performance. The downsides of ML based taggers are the difficulty in estimating uncertainties and lack of control over what information is being learnt.

Due to the difficulty in isolating pure enough samples of actual data, ML algorithms are usually trained on samples simulated with event generators and so can learn features which are artefacts of the simulation and not present in data. Strong dependence on hadronisation models and other non-perturbative effects are the biggest problem as these are not derivable from QCD and exhibit differences between models. However, differences between parton showers can also be significant due to the different approximations used in different showers [95]. The variation in background rejection of a deep neural network on data simulated with different event generators was studied in [143], which found differences of up to 50% between different event generators. Improvements in the accuracy of parton shower algorithms [3], [95], [144]–[148] may help to reduce some of the uncertainty associated with ML algorithms by improving the accuracy of samples they are trained on, although robustness to hadronisation and other NP effects, which are necessarily model dependent, will still be important. Recently there has been a substantial amount of work aiming to understand what information ML algorithms are learning [34], [37], [128], [149], [150] and to to put ML on a more solid theoretical footing [143], [151], [152]. A small selection of this work is briefly discussed below.

Ref. [152] studied the IRC safety of a convolutional neural network trained on hadron level samples, simulated with Pythia, to tag high P_t top quarks. Information is passed to the network as the momenta of all of the final state particles in the event. To check IRC safety, they simulated a sample of hadronically decaying top quarks with an extra gluon in the final state, which they term the un-merged sample. They then defined the merged sample from the same events where the momentum of the gluon was added to the quark closest in angle, to give an effective 3 parton final state. The change in response of the network between the two samples was found to decrease to zero as the transverse momentum of the gluon relative to the closest quark went to zero. Numerically then, the network satisfies IRC safety by the definition given in eq. (2.46) for the final state tested. The authors of this work point out that this is not a full test of IRC safety for this network, both for the reason that only $\mathcal{O}(\alpha_s)$ configurations were studied, and that their analysis cannot distinguish between IRC and Sudakov safety. As such there is no guarantee as to the scaling or size of non-perturbative effects.

The LundNet family of ML algorithms based around Lund diagram representations of jets were introduced [34]. Aside from being extremely high performance methods for tagging boosted tops, electroweak bosons, and for quark gluon discrimination, LundNet also allows one to restrict the amount of non-perturbative information available to the ML algorithm simply by placing a k_t cut in the Lund plane, below which particles are removed. This enabled the authors of [34] to investigate how the resilience to NP effects and performance changed as this cut is varied. The resilience to non-perturbative effects is defined as

$$\zeta_{\mathrm{NP}} = \left(\frac{\Delta\epsilon_s^2}{\langle\epsilon_s\rangle^2} + \frac{\Delta\epsilon_b^2}{\langle\epsilon_b\rangle^2} \right) \,, \tag{3.16}$$

where $\Delta\epsilon_s(\Delta\epsilon_b)$ is the difference between the parton and hadron level signal (back-

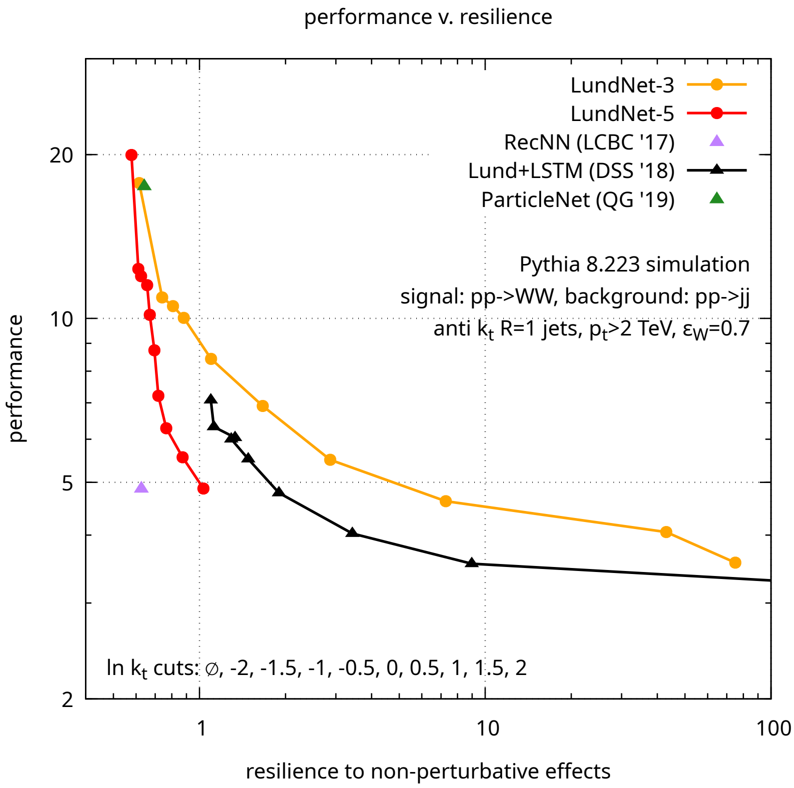

Figure 3.7. A plot of performance $\left(\frac{\epsilon_s}{\sqrt{\epsilon_b}}\right)$ against resilience to non-perturbative effects for W boson tagging for the LundNet family of taggers, the Lund+LSTM tagger of [125] and two other ML taggers [33], [153]. Plot taken from [34].)

ground) tagging efficiency, as computed on samples simulated with Pythia, and the angled brackets denote the average of the parton and hadron level efficiency. A plot of ζ_{Np} against performance is shown in figure 3.7. The ParticleNet [33] and RECNN [153] W tagging algorithms are also shown as benchmarks. Although Lund net achieves similar or better performance for the same resilience as the other algorithms tested, the reduction in performance as resilience increases does show that the algorithm is learning and making use of potentially unreliable non-perturbative information when it is given access to it. The ParticleNet and RecNN algorithms tested both achieved relatively low resilience scores, indicating that they make significant use of non-perturbative information.

Attempting to analytically understand the performance of a particular type of ML based tagger could be considered as the logical extension to the large body of work discussed in the previous sections aiming to understand more traditional cut based tagging algorithms. Work in this direction was published in [128], where the authors analytically studied a simple neural network at leading logarithmic accuracy and were able to determine under what circumstances it achieved optimal performance for quark vs gluon discrimination. It was found that when information was passed to the network as a vector of N-subjettiness variables, optimal performance would not be obtained, whereas passing the information as a vector of the logarithm or logarithm squared of N-subjettiness variables, optimal performance would be obtained. This was hypothesised to be due to the N-subjettiness variables being intrinsically logarithmic, which the simple network struggles to learn when presented with the raw N-subjettiness variables. They showed that performance and training times of the simple network were improved by using logarithmic inputs to the network as opposed to linear ones, with this improvement being understood from their analytic calculations. They compared their results to a more complex network of the type more likely to be used in experimental analyses and found that many of their conclusions were also applicable to the more complicated network.

3.5 Jet substructure for the study of QCD

As well as being a powerful tool for discriminating between jets initiated by one species of particle and another, the substructure of jets is interesting in its own right as a means to study QCD. This section will discuss a number of examples of precise jet substructure measurements, their comparison with perturbative calculations and the application of these comparisons to extracting parameters of the standard model and improving our understanding of QCD and its modelling in event generators.

One of the major barriers of making precise comparisons between perturbative predictions for jet substructure observables and data is the extent to which non-perturbative effects, such as hadronisation and underlying event, modify perturbative predictions. As observables computed on groomed jets are much less sensitive to these effects, they are the obvious candidates for comparing theory predictions directly to data and making measurements of perturbatively defined quantities. Computing observables on jets groomed with mMDT also removes some of the difficulties in producing precise QCD resummations for these observables through the removal of non-global logarithms and lack of sensitivity to ISR. A number of jet substructure observables have now been measured on groomed jets and compared to resummed calculations [43], [123], [154], [155]. The observable which has seen the most attention is the groomed jet mass distribution, with a number of calculations having been produced with different methods and including different effects [44], [45], [47], [48], [156]. A measurement of the groomed jet mass distribution by the CMS collaboration [123] is shown in figure 3.8 alongside predictions generated using Herwig [86], Pythia [53], and POWHEG+Pythia [157] and two resummed calculations [44], [47]. The calculation of Frye et. al. was carried out using soft collinear effective theory at NNLL accuracy [47] in the small z_{cut} limit and is matched to fixed order calculations at LO, whilst the calculation of Marzani et. al. was carried out at NLL accuracy, directly using perturbative QCD, retains finite z_{cut} effects, and is matched to fixed-order calculations at NLO. The ATLAS collaboration has also made measurements of the jet mass after grooming using soft drop with three values of $\beta = 0, 1, 2$, which were also compared to resummed calculations [39].

Other jet-shape observables which have received attention recently are the gener-

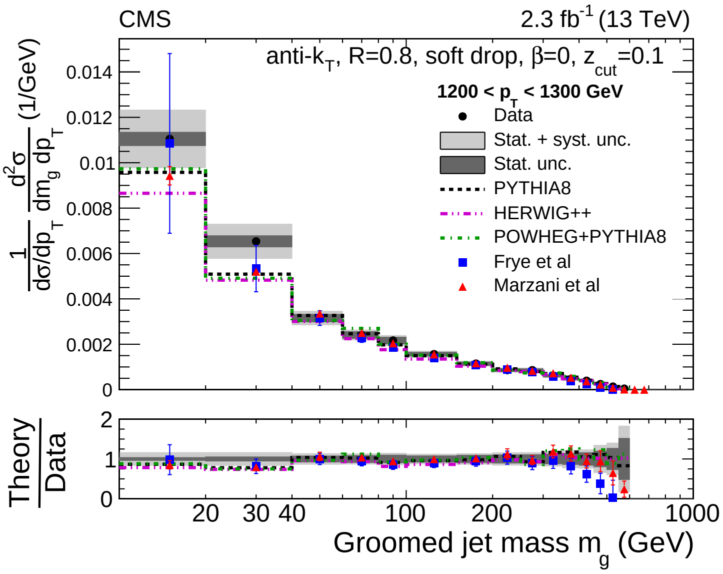

Figure 3.8. CMS measurement of the mMDT groomed jet mass compared to two different resummed calculations and three different event generator predictions. Plot taken from [123]

alised angularities. These are defined as

$$\lambda_\beta^\kappa = \frac{1}{\sum_{i\in\text{jet}} p_{ti}} \sum_{i\in\text{jet}} p_{ti}^\kappa \left(\frac{\Delta R_{ia}}{R_0}\right)^\beta \tag{3.17}$$

where $\Delta R_{ia} = \sqrt{\delta\eta_{ia}^2 + \delta\phi_{ia}^2}$, R_0 is the jet radius, and a labels some axis which the observable is defined relative to. One popular choice is the winner takes all (WTA) axis [27] which is found by de-clustering a jet, following the hardest branch at each de-clustering. The harder of the two branches at the final de-clustering defines the WTA axis. These have been measured, by the CMS collaboration [43], on groomed and un-groomed jets and compared with both Monte Carlo generator predictions and re-summed calculations, produced using the `CAESAR` [69] NLL resummation plug-in for Sherpa [158]. This work motivated the choice of observables in chapter 5 where the NNLL resummed distribution of three angularities computed on e^+e^- events is calculated and matched to NLO.

Precise calculations and measurements of jet substructure observables opens up the possibility of measuring standard model parameters such as the strong coupling using jet substructure, similar to what has been done at electron-positron colliders using event shape variables. The strong coupling has been measured by fitting event shape variables to e^+e^- data [159]–[164]. Event shape distributions are sensitive to non-perturbative effects, which can be approximated using a shape function [161], [163], [165]–[168]. Shape functions can be expanded in moments which are universal to many event shapes, enabling a simultaneous fit of the strong coupling and first moment(s) of the shape function to event shapes. Extractions of α_s from event shapes are in tension with the world average [169], providing motivation for an extraction of the strong coupling from jet substructure, as this is sensitive to much of the same physics as event shape distributions. Their lack of sensitivity to non-perturbative effects makes groomed observables a good candidate for jet substructure extractions of α_s [170]. This has been exploited by CMS to measure the strong coupling by comparing the measured z_g and R_g distributions to Monte Carlo predictions generated using POWHEG+Pythia [53], [157], [171] where z_g is the momentum fraction of the sub-jet that stops the groomer and R_g the jet radius after grooming.

The top quark mass can also be measured using jet substructure. The current world average for direct measurements of the top quark mass give $m_{\text{top}}^{\text{direct}} = 172.9 \pm 0.4\text{GeV}$ [172]. This is measured by comparing kinematic distributions of the decay products of top quarks to Monte Carlo predictions [173]. There has been a significant amount of discussion as to the exact interpretation of this mass, particularly whether or not, at the high level of precision now achieved, it can be identified with the pole mass of the top quark or some other theoretically precise mass scheme [174]–[182]. Suffice to say the PDG [172] lists three separate values for the top mass including the direct measurement mass discussed above and a separate pole mass with slightly larger uncertainty, $m_{\text{top}}^{\text{pole}} = 173.1 \pm 0.9\text{GeV}$, reflecting the fact various theoretical uncertainties in event generators are not under enough control to confidently identify the top mass parameter in event generators with a particular top mass scheme in perturbation theory. These issues are discussed in more depth in ref. [173]. The purpose of this discussion is to put in context a recent proposal to precisely measure the top mass using jet substructure [183]. This is part of a larger body of recent work investigating correlation functions measured on jets as a new type of jet substructure observable [184]. Their proposal shows that there is the potential, using their method, to make a very precise measurement of the top mass in a way where one has theoretical control over the mass scheme.

Another interesting observable recently measured by the ATLAS collaboration [40] is the primary Lund Jet plane density [125]. The primary Lund jet plane density is constructed from a sample of jets clustered with the C/A algorithm as follows. For each jet, undo the last clustering and plot ΔR and transverse momentum (k_t) of the softer branch with respect to the harder branch on the Lund plane. Following the harder branch, this is repeated until there are no more branchings. The Lund planes for each jet are then averaged to find the density of branchings in the primary Lund plane[7],

$$\rho(\Delta R, k_t) = \frac{1}{N_{\text{jet}}} \frac{\mathrm{d}n_{\text{emission}}}{\mathrm{d}\ln k_t \mathrm{d}\ln \Delta R} \; . \tag{3.18}$$

This is closely related to the perturbative picture of gluons being emitted off the hard parton which initiated the jet, so that in the soft and collinear limit one expects

$$\rho(\Delta R, k_t) \simeq \frac{2C_F \alpha_s(k_t)}{\pi} \; , \tag{3.19}$$

where the emission probability is uniform, other than the scaling with $\alpha_s(k_t)$. This nicely shows the onset of non-perturbative effects as the coupling grows at small k_t,

---

[7] The primary Lund plane is the plane constructed by following the harder branch at each declustering. Secondary Lund planes can be constructed for each softer branch as well as tertiary Lund planes and so on.

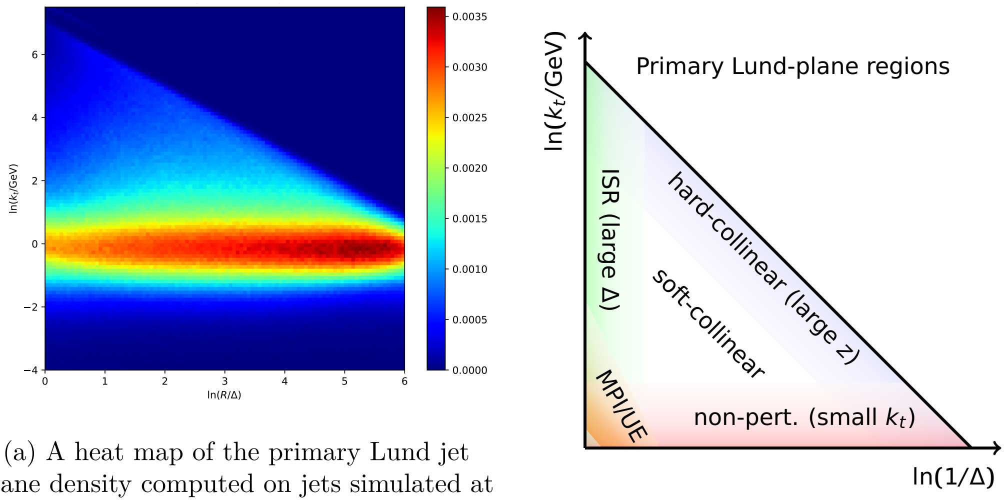

(a) A heat map of the primary Lund jet plane density computed on jets simulated at parton level, with no ISR or UE, with Pythia. The plot was constructed using FastJet [109] and the Lund Plane FastJet contrib [125].

(b) A diagram, taken from ref. [125] showing the effects that different regions of the Lund plane are most sensitive to.

Figure 3.9

as can be seen in figure 3.9a, where a Lund jet plane constructed from parton level Pythia simulations with no ISR or UE is shown. This was produced using FastJet [109] and the Lund plane FastJet contrib [125]. Figure 3.9a shows the density varying with ΔR as well as k_t, reflecting the fact that away from the soft limit one expects [125]

$$\rho(z, k_t) \simeq \frac{\alpha_s(k_t)}{\pi} \bar{z}\left(P_{gq}(\bar{z}) + P_{gq}(1-\bar{z})\right) \tag{3.20}$$

where $\bar{z} = \frac{k_t}{p_{t,\mathrm{jet}}\Delta\eta}$.

It was pointed out in ref. [40] that measurements of the Lund jet plane density could be particularly useful in improving the modelling of QCD in event generators, as different regions of the Lund plane are sensitive to different effects, as shown in figure 3.9b. This allows one to separately tune different effects in event generators to different regions of the Lund plane rather than (or more likely as well as) tuning to observables which may mix these effects together. Since the ATLAS measurement of the Lund plane density, an all orders, single logarithmic calculation of the primary Lund plane density has been presented [155] and compared to the ATLAS measurement [40].

3.6 Summary

Hopefully this section has given an idea of the range of applications that jet substructure has, from jet tagging to precision measurements, and demonstrated that understanding jet substructure techniques from first principles QCD calculations can lead to increased confidence and improvements in existing techniques, as well as the development of new, better, techniques. Intertwined with jet substructure is the ongoing development of event generators, in particular parton showers [2], [3], [95], [100],

[101], [103] and hadronisation models [88], [185]. Improvements in event generators can undoubtedly lead to a reduction in uncertainty in analyses using jet substructure, either through more reliable training of machine learning algorithms or lower uncertainties in observables computed on Monte Carlo samples. Meanwhile, improvements in the understanding of jet substructure observables and resummation can feed back into the development of parton showers, and measurements of jet substructure observables can be used to improve the tuning of event generators [40], [43].

Chapter 4

The NNLL structure of the groomed jet mass at NLO

This chapter and the next present work by myself and my collaborators on the next to leading log structure of additive jet shape observables. The work presented in this chapter was published in [4], from which much of the text is derived.

4.1 Introduction

Jet substructure measurements have proven to be a fruitful way to perform precision tests of QCD at colliders through comparisons between precision calculations and data [39], [41], [42], [44], [45], [47]–[49], [186]–[191]. One of the challenges associated with precision tests of QCD at colliders is finding observables which suffer only modest non-perturbative corrections whilst being perturbatively calculable to a high enough level of precision. At hadron colliders, insensitivity to underlying event and pileup are also important characteristics for observables. As discussed in chapter 3, observables computed on jets groomed with mMDT [21], [22] or its subsequent generalisation, soft drop [23], are less sensitive to UE and hadronisation as well as being more amenable to precise perturbative calculations due to the absence of non-global logarithms (NGL's) which typically appear for observables computed on un-groomed jets. It should be noted that the NGL's are not completely removed, rather the argument of these logarithms is changed from, $\rho = \frac{m_{\mathrm{Jet}}^2}{R^2 P_t^2}$ in the case of the jet mass, to z_{cut}. With $z_{\mathrm{cut}} \simeq 0.1$ being a typical choice, it is not strictly necessary to re-sum these logarithms. As a result of these properties there have been a number of theoretical predictions for distributions of groomed observables, which have been produced using a variety of tools and incorporating different effects. These include: resummations in QCD at NLL accuracy [1] where, terms suppressed by powers of z_{cut} are retained and resummed, matching to full NLO calculations is carried out, and hadronisation corrections derived from Monte Carlo event generators are included [44], [45]; SCET calculations up to N^{3}LL accuracy in the small z_{cut} limit [47], [48], [190]; and calculations treating non-perturbative corrections within the framework of

---

[1] Over the next two chapters a logarithmic counting scheme where the leading logarithms are double logs is used despite double logarithms being absent for observables groomed with mMDT. This differs from the counting scheme adopted in the published version [4] of the work presented in this chapter.

SCET [191]. This has enabled accurate comparisons to be made between calculations for groomed observables and LHC data [39], [41], [42], where generally good agreement between theory and experiment has been found.

As well as being of direct interest for collider phenomenology, observables computed on jets groomed with mMDT, or $\beta = 0$ soft drop, provide a way to study the structure of collinear logarithms without the complications arising from logarithms originating in the soft wide angle region of phase space.

In this chapter the NNLL structure of the jet mass after grooming with mMDT is studied at order α_s^2. Although NNLL, and recently even N^{3}LL, resummed calculations are available through the SCET formalism [47], [48], [190], albeit in the small z_{cut} limit, it is still of interest to understand the structure of the collinear logarithms directly from the QCD matrix element. While an NLL resummed result can be derived in a strongly ordered picture with collinear emissions widely separated in angle, the NNLL structure with terms $\alpha_s^n \ln^{n-1}(\rho)$ stems from lifting the strong ordering on a pair of emissions. At order α_s^2 this leads us to consider two emissions (i.e. three partons) within a jet, which are at small angles, $\theta^2 < \frac{\rho}{z_{\text{cut}}}$ but with no relative strong ordering between them. In this limit the matrix element can be approximated by the triple collinear splitting functions [50]–[52]. In the strongly ordered limit the triple collinear splitting functions reduce to a product of leading order splitting functions, thus recovering the NLL picture.

This motivates us to compute the $\alpha^2 \ln(\rho)$ NNLL term for quark initiated jets in the small z_{cut} limit, starting from the triple collinear splitting functions. Our calculation does not make use of any resummation results or ingredients, rather, terms which one would expect from resummation results, such as the CMW scheme for the coupling, emerge from the calculation. Having identified terms which although NNLL have their origin in NLL dynamics, we identify the NLL hard collinear term, often referred to as B_2 [192]–[195], which originates in the triple collinear limit. We find full agreement with the expansion of the SCET resummations. This constitutes a strong check on the SCET results as, unlike the SCET calculations, we do not rely on any resummation ingredients. Aside from being a strong cross check of existing results, this work is also of interest as it links the structure of collinear logarithms to the triple collinear splitting functions, which is relevant for efforts to include the triple collinear splitting function in parton showers [1]–[3]. This work also informs the NNLL resummation of groomed observables in QCD as is done in chapter 5.

We start, in section 4.2, by defining the groomed heavy hemisphere mass, and writing down the NLL resummed distribution for this observable, including the CMW coupling with the argument set to k_t. In section 4.3.1 we then carry out a leading order calculation and identify the process dependent term, referred to as C_1, which multiplies the Sudakov factor. The NLL resummed result is then expanded to α_s^2 in section 4.3.2, where we identify terms which are NNLL, but which can be accommodated within the NLL resummation, signifying their relation to strongly ordered dynamics. Then, in section 4.4, we compute the groomed heavy hemisphere mass distribution at $\mathcal{O}(\alpha_s^2)$, starting from the triple collinear splitting functions. In section 4.5, we then study the NNLL terms found from this calculation by removing the NNLL terms that we previously identified as being related to strongly ordered dynamics. Finally in section 4.6 we comment on our results in the context of QCD resummation and prospects for future work.

4.2 Observable definition and leading-log resummation

We are interested in the jet mass distribution of a QCD jet after the application of grooming via the modified mass-drop tagger (mMDT) or equivalently SoftDrop ($\beta = 0$). For reasons of convenience, we shall work in the context of e^+e^- collisions, though the NNLL pure collinear terms we will eventually extract are process independent and hence apply also to jets at hadron colliders.

We will compute the standard heavy hemisphere jet mass observable extensively studied in e^+e^- collisions but with the modification that we compute the heavy jet mass after running the mMDT procedure, defined in section 3.3, on the particles in each hemisphere. This was also the observable studied in the first mMDT NNLL resummed calculation performed in ref. [47]. In general one may separate the event into two hemispheres in different ways e.g. by clustering to two jets as in ref. [47] or as is traditional by using the thrust axis. At the level of our calculations and for extracting the terms we seek, we are insensitive to the precise details since, in the soft and/or collinear limit, we can take the hemispheres to be defined by the directions of the initial quark–anti-quark pair. After separating the event into two hemispheres, we groom the hemispheres with mMDT (defined in section 3.3) and measure

$$\rho = \frac{\max(M_R^2, M_L^2)}{Q^2/4}, \tag{4.1}$$

where we select the larger of the left or right hemisphere squared invariant masses (M_L^2 and M_R^2 respectively) and normalise to $(Q/2)^2$ which corresponds to the squared energy of a hemisphere in the Born limit.

We shall work in the formal limit $\rho \ll z_{\text{cut}} \ll 1$, which means that we will examine the structure of $\ln \rho$ enhanced terms, but shall neglect power corrections in z_{cut}. An NLL resummation formula for the mMDT jet mass distribution, based on an independent emission picture with emissions strongly ordered in angles, was first provided in ref. [21] (see Eq. (7.2) of ref. [21] for the result). While that result applies directly to a jet produced in hadron collisions, it can be easily modified to the case of the heavy groomed hemisphere mass in e^+e^- annihilation. We express our next-to-leading-logarithmic resummed result in terms of the integrated distribution,

$\Sigma(\rho) = \int_0^{\rho} \frac{1}{\sigma_0}\frac{d\sigma}{\mathrm{d}\rho'}\mathrm{d}\rho'$ as

$$\Sigma^{\mathrm{NLL}}(\rho) = \left(1 + \frac{C_F \alpha_s}{2\pi} C_1\right) \times \\ \exp\left[-\int_{\rho}^{1} \frac{\mathrm{d}\rho'}{\rho'} \int_0^{1-\max(z_{\mathrm{cut}},\rho')} \mathrm{d}z\, p_{qq}(z) \frac{C_F}{\pi} \alpha_s^{\mathrm{CMW}}\left((1-z)\,\rho' Q^2/4\right)\right], \quad (4.2)$$

where we defined the splitting function $p_{qq}(z) = (1+z^2)/(1-z)$ and σ_0 is the Born cross-section.

The above result modifies the result of ref. [21] by replacing p_T^2 by $Q^2/4$ and is written in terms of the splitting function $p_{qq}(z)$ rather than $p_{gq}(z)$ so that the variable $1-z$ in the above result corresponds to the variable z in Eq. (7.2) of ref. [21]. We have also inserted an additional factor of two in the Sudakov exponent which takes into account the fact that we are considering the result due to two hard partons in the left and right hemispheres respectively, rather than just a single parton initiating a jet. This is accounted for by our definition of the splitting function which has a factor of two relative to that defined in ref. [21]. The above result is labelled NLL since it correctly resums terms $\alpha_s^n L^n$, with $L = \ln\rho$. Additionally a fixed-coupling calculation of the exponent in Eq. (4.2) reveals a term of the form $\alpha_s \ln^2 z_{\mathrm{cut}}$, which although subleading in ρ, correctly resums terms $\left(\alpha_s \ln^2 z_{\mathrm{cut}}\right)^n$[21].

In Eq. (4.2) we have defined the coupling in the CMW or “physical” scheme [73], [196], [197] and have set the argument of the running coupling to be the transverse momentum squared of a soft and collinear emission relative to the direction of its hard parent parton, expressed in terms of the invariant mass ρ' and the energy fraction of the emitted gluon $\frac{Q}{2}(1-z)$, since we have $k_t^2 = (1-z)\rho' Q^2/4$. [2] Both the specification of the CMW scheme and the precise details of the argument of the running coupling (beyond the fact that it scales with ρ) in fact produce terms that are formally NNLL in ρ but with logarithmic enhancements in z_{cut}. These terms are an intrinsic part of the next-to-leading-logarithmic resummation framework and hence naturally belong in our NLL formula. In a similar spirit we have also included in Eq. (4.2), a ρ independent, constant, order α_s coefficient, C_1, which is process dependent and on physical grounds factorises from the leading-logarithmic Sudakov resummation. On expanding the exponent, multiplication by the C_1 term results in an $\alpha_s^2 L$ term. While this term should be reproduced by our order α_s^2 calculations, it is process dependent and unrelated to the collinear NNLL structure we ultimately seek to extract. Hence the explicit identification of C_1 is needed, to account for the role of this piece in our final result.

We then expect that our eventual order α_s^2 result should contain all terms generated by the expansion of (4.2) and additionally all terms of genuine NNLL origin (i.e. unrelated to the strongly-ordered in angle NLL dynamics). These terms should arise

---

[2] Recall that in the soft-collinear limit $\rho' = m^2/(Q^2/4) \approx (1-z)\theta^2$ while $k_t = \frac{Q}{2}(1-z)\theta$.

from collinear physics, and be independent of z_{cut} and the specific hard process.

4.3 Leading order calculation and expansion of NLL result

Throughout this article we shall work in the resummation region where $\rho \ll z_{\mathrm{cut}}$ and hence ignore the presence of a transition point at $\rho \approx z_{\mathrm{cut}}$, beyond which the groomed jet mass result becomes coincident with the plain un-groomed mass. We shall consider for simplicity that $z_{\mathrm{cut}} \ll 1$, so that we can neglect powers of z_{cut}, although this is not a requirement on the validity of our triple-collinear calculations.

Our first step will be to determine the ρ independent coefficient, C_1, that appears in Eq. (4.2). We do this in the following subsection by performing a leading-order calculation in the soft and collinear limit.

4.3.1 Leading-order calculation

Here we derive, in the small ρ and z_{cut} limit as defined before, the order α_s contribution to $\Sigma(\rho)$. At this order we have to consider a single real emission and the one-loop virtual correction to $q\bar{q}$ production. To handle divergences in the real emission calculation, we perform the calculation in conventional dimensional regularisation (CDR) in $d = 4 - 2\epsilon$ dimensions, and combine with the virtual correction before taking $\epsilon \to 0$.

Since we are interested in the region of small jet mass and small z_{cut}, we can work in the soft and/or collinear limit, perform the calculation for a single hemisphere and then double the result. Considering the gluon to be in the same hemisphere as the quark (for example) and applying the mMDT, we have a situation where the z_{cut} condition passes or fails. If it passes then one obtains a non-zero hemisphere mass, while if it fails the hemisphere mass vanishes.

When the z_{cut} condition passes, we are considering a pair of relatively energetic partons which produce a small jet mass, implying that the angle between partons is small, $\theta^2 \sim \frac{\rho}{z_{\mathrm{cut}}} \ll 1$, which allows the use of the collinear approximation. In this region the emission probability is just the $q \to qg$ splitting function in $4 - 2\epsilon$ dimensions, $p_{qq}(z,\epsilon) = p_{qq}(z) - \epsilon(1-z)$, and the result follows by applying the standard d-dimensional collinear phase space [198]:

$$\Sigma_{1,\mathrm{r}_1}(\rho) = 2 \times \frac{C_F \alpha_s}{2\pi} \frac{(4\pi\mu^2)^{\epsilon}}{\Gamma(1-\epsilon)} \left(\frac{Q}{2}\right)^{-2\epsilon} \times \\ \int \frac{\mathrm{d}\theta^2}{\theta^{2(1+\epsilon)}} \int_{z_{\mathrm{cut}}}^{1-z_{\mathrm{cut}}} (z(1-z))^{-2\epsilon} p_{qq}(z,\epsilon) \Theta(z(1-z)\theta^2 < \rho) \mathrm{d}z, \quad (4.3)$$

where the label r_1 indicates the first of three distinct real-emission terms that we encounter, and we have provided an explicit factor of 2 to take account of both hemispheres, which shall apply to all the real-emission terms we compute in this section. The constraint arising from restricting the jet mass is written in terms of a step function involving ρ, while the z_{cut} condition removes any soft singularity in the integral and we obtain just a collinear pole alongside finite corrections. We have not explicitly written, for brevity, the dependence on z_{cut} in the argument of Σ_{1,r_1} which is left implicit here and throughout this chapter.

Next we turn to the region where the z_{cut} condition fails, the softer particle is groomed away, and we obtain a massless hemisphere. This can happen when the quark goes soft ($z < z_{\mathrm{cut}}$), or when the gluon goes soft ($z > 1 - z_{\mathrm{cut}}$), and in either case the jet mass vanishes, so we can replace the step function in Eq. (4.3) by unity. The region corresponding to a soft quark also contributes only a collinear divergence and finite terms which are suppressed by powers of z_{cut} which we neglect. Hence retaining just the collinear divergence, corresponding to a pole in ϵ produced by the θ^2 integral, we can write this contribution as

$$\Sigma_{1,\mathrm{r}_2}(\rho) = -2\frac{C_F\alpha_s}{2\pi}\left(\frac{2\mu}{Q}\right)^{2\epsilon}\frac{1}{\epsilon}\int_0^{z_{\mathrm{cut}}}\left(\frac{1+z^2}{1-z}\right)\mathrm{d}z \quad , \tag{4.4}$$

where we performed the θ^2 integral and discarded all finite terms owing to their suppression with z_{cut}. Accordingly we have dropped the ϵ dependence of the constant prefactor multiplying the integral, since this only leads to finite power suppressed in z_{cut} corrections.

Lastly there is the region $z > 1 - z_{\mathrm{cut}}$ corresponding to a soft gluon emission, which is removed by grooming. As there is no longer a constraint on the angle, one has to replace the soft-enhanced part of the splitting function with the full eikonal function to account for the wide-angle region. For soft-regular pieces, however, one merely needs the collinear pole as any finite contributions are power suppressed in z_{cut}. Hence, using $p_{qq}(z,\epsilon) = 2/(1-z) - (1+z) - \epsilon(1-z)$, to separate the soft enhanced and regular terms of the splitting function, we write

$$\Sigma_{1,r_3} = \Sigma_{1,r_3\,\mathrm{soft}} + \Sigma_{1,r_3\,\mathrm{coll.}} \quad , \tag{4.5}$$

where explicitly

$$\Sigma_{1,r_3\,\mathrm{soft}} = 2\frac{C_F\alpha_s}{2\pi}\frac{(4\pi\mu^2)^\epsilon}{\Gamma(1-\epsilon)}\left(\frac{Q}{2}\right)^{-2\epsilon}\times \int_{1-z_{\mathrm{cut}}}^{1}\frac{2\,\mathrm{d}z}{(1-z)^{1+2\epsilon}}\int_0^1\frac{2\,\mathrm{d}\left(\cos\theta\right)}{\left(1-\cos\theta\right)^{1+\epsilon}\left(1+\cos\theta\right)^{1+\epsilon}} \quad , \tag{4.6}$$

and

$$\Sigma_{1,r_3\,\mathrm{coll.}} = 2\times\frac{C_F\alpha_s}{2\pi}\frac{1}{\epsilon}\int_{1-z_{\mathrm{cut}}}^{1}\mathrm{d}z(1+z)\ . \tag{4.7}$$

In the expression for $\Sigma_{1,r_3\,\mathrm{soft}}$ the upper limit of the $\cos\theta$ integral corresponds to $\theta = \pi/2$ for the boundary of the hemisphere under consideration, while in the expression for $\Sigma_{1,r_3\,\mathrm{coll.}}$ we have retained only the singular contribution as finite corrections vanish with z_{cut}.

Our final ingredient is the well-known virtual correction to $q\bar{q}$ production (see e.g. [198]):

$$\mathcal{V}(\epsilon) = \frac{C_F\alpha_s}{2\pi}\frac{\Gamma(1+\epsilon)\Gamma^2(1-\epsilon)}{\Gamma(1-2\epsilon)}\left(-\frac{2}{\epsilon^2}\left(\frac{4\pi\mu^2}{Q^2}\right)^{\epsilon} + \pi^2 - 8 - \frac{3}{\epsilon}\left(\frac{4\pi\mu^2}{Q^2}\right)^{\epsilon}\right). \tag{4.8}$$

We express our results in terms of the renormalised coupling in the $\overline{\mathrm{MS}}$ scheme, $\alpha_s(\mu_R^2)$, using the relation

$$\mu^{2\epsilon}\alpha_s = S_\epsilon^{-1}\mu_R^{2\epsilon}\alpha_s(\mu_R^2) + \mathcal{O}(\alpha_s^2), \tag{4.9}$$

where we have the standard $\overline{\mathrm{MS}}$ factor

$$S_\epsilon = (4\pi)^\epsilon e^{-\epsilon\gamma_E}, \tag{4.10}$$

and we choose $\mu_R = Q/2$. [3] Carrying out the necessary integrals we obtain the result for the real emission term $\Sigma_{1,r} = \Sigma_{1,r_1} + \Sigma_{1,r_2} + \Sigma_{1,r_3\,\mathrm{soft}} + \Sigma_{1,r_3\,\mathrm{coll.}}$,

$$\Sigma_{1,r} = \frac{C_F\alpha_s\,(Q^2/4)}{2\pi}\Bigg(\frac{2}{\epsilon^2} + \frac{3-4\ln 2}{\epsilon} - \ln\rho\,(4\ln z_{\mathrm{cut}} + 3) + 2\ln^2 z_{\mathrm{cut}} + 8\ln 2\ln z_{\mathrm{cut}} + 4\ln^2 2 - \frac{7\pi^2}{6} + 7\Bigg). \tag{4.11}$$

Combining with the virtual correction we obtain the leading-order result, $\Sigma_1(\rho) = \Sigma_{1,r} + \mathcal{V}(\epsilon)$:

$$\Sigma_1(\rho) = \frac{C_F\alpha_s\,(Q^2/4)}{2\pi}\times \left[-\ln\frac{1}{\rho}\left(4\ln\frac{1}{z_{\mathrm{cut}}} - 3\right) + 2\ln^2 z_{\mathrm{cut}} - 2\ln 2\left(4\ln\frac{1}{z_{\mathrm{cut}}} - 3\right) - 1\right], \tag{4.12}$$

where the argument of the running coupling reflects our choice of μ_R. We have written the above result separating the contributions that arise from expanding the NLL formula (i.e the $\ln 1/\rho$ and $\ln^2 z_{\mathrm{cut}}$ contributions that are associated to the fixed-coupling Sudakov exponent) from the contributions we shall associate to C_1. This allows us to identify

$$C_1 = -2\ln 2\left(4\ln\frac{1}{z_{\mathrm{cut}}} - 3\right) - 1. \tag{4.13}$$

We note that defining the observable as $v = \rho/4$, corresponding to a normalisation to Q^2, would result in the elimination of the term proportional to $\ln 2$ and hence the $\ln z_{\mathrm{cut}}$ dependence from C_1, but the resummation of $\ln z_{\mathrm{cut}}$ terms is beyond the scope

---

[3] Beyond order α_s, the RHS of Eq. (4.9) contains UV poles in ϵ related to the renormalisation of the strong coupling.

of our results.

4.3.2 NLL result at second order

On performing the full order α_s^2 calculation, to our NNLL in ρ accuracy, we should recover all terms produced by the expansion of Eq. (4.2) in addition to terms that are unrelated to the NLL structure, which will then act as one of the checks on our results. To this end we report below the expansion of Eq. (4.2) for the differential distribution $\rho\frac{\mathrm{d}\Sigma}{\mathrm{d}\rho}$ (to correspond to the calculations of the following sections). The leading-order result is given by (for our choice of $\mu_R = Q/2$),

$$\rho\frac{\mathrm{d}\Sigma_1^{\mathrm{NLL}}}{\mathrm{d}\rho} = \frac{C_F\alpha_s\left(Q^2/4\right)}{2\pi}\left(-3-4\ln z_{\mathrm{cut}}\right). \tag{4.14}$$

To obtain the order α_s^2 result one needs to compute the Sudakov exponent with running coupling and switch from the CMW scheme to the $\overline{\mathrm{MS}}$ scheme, which gives

$$\begin{aligned}\rho\frac{\mathrm{d}\Sigma_2^{\mathrm{NLL}}}{\mathrm{d}\rho} &= \left(\frac{\alpha_s}{2\pi}\right)^2\times\\ &\Bigg[C_F^2\Big((3{+}4\ln z_{\mathrm{cut}})^2\ln\rho{-}8\ln^3 z_{\mathrm{cut}}{-}2(3{+}16\ln 2)\ln^2 z_{\mathrm{cut}}{+}(4{-}48\ln 2)\ln z_{\mathrm{cut}}{-}18\ln 2{+}3\Big)\\ &\quad + C_FC_A\left(\frac{11}{6}\left(3+4\ln z_{\mathrm{cut}}\right)\ln\rho+\frac{11}{3}\ln^2 z_{\mathrm{cut}}+\left(\frac{2\pi^2}{3}-\frac{134}{9}\right)\ln z_{\mathrm{cut}}\right)\\ &\quad + C_FT_Rn_f\left(-\frac{2}{3}(3+4\ln z_{\mathrm{cut}})\ln\rho-\frac{4}{3}\ln^2 z_{\mathrm{cut}}+\frac{40}{9}\ln z_{\mathrm{cut}}\right)\Bigg].\end{aligned} \tag{4.15}$$

The above result contains a term which is NLL in ρ originating from the exponentiation of the leading-order result. It also contains NNLL in ρ terms, corresponding to ρ independent terms in $\rho\,\mathrm{d}\Sigma_2/\mathrm{d}\rho$ generated by an interplay of the NLL exponent with C_1 and by fixing the scale and scheme of the running coupling. In particular the $\ln^2 z_{\mathrm{cut}}$ terms in the C_FC_A and $C_FT_Rn_f$ channels derive from the $1-z$ factor in the argument of the running coupling, while the $\ln z_{\mathrm{cut}}$ term in the same channels is generated by changing from the CMW scheme to the $\overline{\mathrm{MS}}$ scheme as can be seen through their coefficient, proportional to $K = \left(\frac{67}{18}-\frac{\pi^2}{6}\right)C_A - \frac{10}{9}T_Rn_f$. In addition to these terms, the $1-z$ factor in the argument of the running coupling and the CMW coefficient, K, applied to the full splitting function rather than just its soft enhanced piece, are also responsible for producing z_{cut} independent NNLL terms, which go beyond the strict jurisdiction of the NLL formula. The full set of such terms will be identified through the calculation we perform here and can be properly accommodated within a consistent NNLL resummation formula.

In the next sections we shall derive the full result at order α_s^2 through to NNLL accuracy, compare it to the expectations from Eq. (4.15) and derive the z_{cut} independent NNLL corrections.

4.4 NNLL at second order: the triple-collinear limit

At NLL accuracy, for the mMDT jet mass, we have a picture of successive collinear parton branchings which are strongly ordered in angle with each branching being described by a leading-order (LO) $1 \to 2$ splitting function. Thus at order α_s^2, the real emission matrix-element simply involves a product of two LO splitting functions. To obtain NNLL accuracy, at order α_s^2, one has to consider three partons that are comparably collinear i.e. the opening angle between any two partons is small $\theta_{ij}^2 \ll 1$ but there is no strong ordering so that $\theta_{12}^2 \sim \theta_{13}^2 \sim \theta_{23}^2$. Such configurations are described by the $1 \to 3$ collinear splitting of an initial parton, and the matrix-element involves triple-collinear splitting functions. In the strongly-ordered limit, the triple-collinear splitting functions reduce to a product of LO splitting functions (in general after azimuthal averaging) thus restoring the NLL picture.

For our current calculations, the relevant functions are the unpolarised triple-collinear splitting functions for a quark (or anti-quark) initiated $1 \to 3$ splitting, denoted $\langle P_{abq} \rangle$ for a splitting $q \to qab$ with a and b representing parton flavours, which were first computed in Refs. [50]–[52], and are listed in the appendix. For the $q \to ggq$ splittings there is both a gluon emission contribution with a C_F^2 colour factor, and a gluon decay contribution with a $C_F C_A$ colour factor. The $q \to q\bar{q}q$ splitting arises from gluon decay and has a $C_F T_R n_f$ colour factor as well as a contribution from an identical particle interference contribution, involving quarks of the same flavour in the final state, which has a colour factor $C_F \left(C_F - C_A/2\right)$, and vanishes in the leading N_c limit. Identical considerations apply for the decay of an initial anti-quark. In the following subsections, we consider the gluon emission and decay contributions in turn.

4.4.1 Gluon emission contribution

Here we study the emission of two gluons from the initial $q\bar{q}$ system, associated with a C_F^2 colour factor. The emitted gluons can either be in the same or in opposite hemispheres, with the latter case being simply related to the leading-order calculations we have already performed. We deal with each contribution in turn below.

Emissions in opposite hemispheres

Consider a gluon emitted in each of the "right" and "left" hemispheres containing the quark and anti-quark respectively. Let us assume that the right hemisphere is heavier after grooming and that its groomed jet mass is ρ. This implies that the branching in the right hemisphere must pass the z_{cut} requirement corresponding to $1 - z_{\text{cut}} > z > z_{\text{cut}}$ and that it must set a mass ρ, while in the left hemisphere the mass must be below ρ for it to be lighter, and hence the grooming can either retain both or remove one of the two particles. The fact that in the right hemisphere the grooming passes, coupled with the limit we are working in, with $\rho \ll z_{\text{cut}}$, allows us to use the collinear approximation, so that the branching in the right hemisphere factorises from the dynamics of the left hemisphere. Here we do not require the triple-collinear splitting functions, as the emissions in opposite hemispheres are well separated.

For the left hemisphere, the constraint on the mass to be below ρ simply gives us $\Sigma_{1,r}/2$, with $\Sigma_{1,r}$, the real emission result, already computed in the previous section (see Eq. (4.11). For the right hemisphere the distribution can be simply calculated in the collinear limit using the LO splitting function and the collinear 1 → 2 phase space. Finally a factor of two accounts for the case when the left hemisphere is heavier after grooming.

For compactness, here and in the sections below, we define the quantity $\mathcal{F}(\rho)$,

$$\mathcal{F}(\rho) = \rho \frac{d\Sigma_2}{d\rho}, \tag{4.16}$$

where Σ_2 is the order α_s^2 contribution to $\Sigma(\rho)$. The result for the emissions in opposite hemispheres can then be written as a product of two leading-order factors[4]:

$$\mathcal{F}^{\text{opp.}}(\rho, \epsilon) = \Sigma_{1,r} \times \frac{C_F \alpha_s}{2\pi} \frac{e^{\epsilon \gamma_E}}{\Gamma(1-\epsilon)} \int_{z_{\text{cut}}}^{1-z_{\text{cut}}} (\rho z(1-z))^{-\epsilon} \, p_{qq}(z, \epsilon) \, \mathrm{d}z. \tag{4.17}$$

Note that although the LO jet mass distribution for the right hemisphere is a finite quantity, we have retained its ϵ dependence in the result above, since $\Sigma_{1,r}$ contains double and single poles in ϵ which interact with ϵ dependence of the right hemisphere mass distribution to generate terms which are finite in the limit $\epsilon \to 0$.

Emissions in the same hemisphere

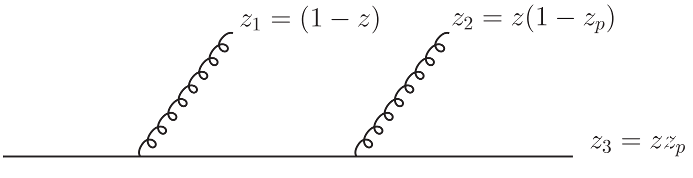

Figure 4.1. An illustration of the parametrisation used for kinematic variables in the gluon emission process, relevant to the triple-collinear limit calculation discussed in the main text.

When two emissions, i.e. three partons, are in the same hemisphere one has to consider the action of the mMDT taking into proper account the Cambridge/Aachen clustering sequence. This involves considering different angular regions where the two emissions can be clustered separately to the quark (or anti-quark according to the hemisphere in question) or are first clustered together and then clustered to the quark. It proves convenient to divide the calculation into two pieces: a first piece

---

[4] Having specified our choice of $\mu_R = Q/2$ we shall not explicitly indicate the argument of α_s in the order α_s^2 pieces.

where in all angular regions we apply the mMDT as if the gluons are clustered separately to the quark, and a second piece which restores the correct action of the mMDT in the angular region where the two gluons are clustered. We are then led to consider the following distinct cases:

- Larger-angle gluon passes z_{cut}: Neglecting the clustering of the two gluons, the mMDT declustering produces two branches, consisting of the larger-angle gluon and a massive branch with the quark and the smaller-angle gluon. When the first declustering passes the z_{cut} condition all three partons are retained. The angle between the branches is small, being set by $\theta^2 \sim \rho/z_{\text{cut}}$ and hence the three partons are constrained to be within a small angular region and the triple-collinear limit generates the full result. The result for the real emission calculation will be divergent due to the smaller-angle emission becoming soft and/or collinear and will contain double and single ϵ poles.
- Larger-angle gluon fails z_{cut} : Another relevant situation is that the larger-angle gluon is soft and hence the first declustering fails the z_{cut} condition.[5] In this case the soft gluon is groomed away while the tagger then declusters the second gluon and we require the second declustering to pass the z_{cut} condition to obtain a massive hemisphere. In this case only the smaller-angle gluon is constrained by the jet mass to be collinear to the quark, while the first emission can be at a large angle. Hence we need to modify the triple-collinear splitting functions to match the correct soft large-angle emission pattern for the first gluon, precisely as we did in section 4.3.1. The result is divergent due to the soft divergence produced by the larger-angle gluon, though it contains only a single pole in ϵ.
- Correction for gluon clustering: In the region where the angle between the two gluons, θ_{12}, is the smallest angle the gluons are clustered first by the C/A algorithm. Hence the first declustering produces a massive branch with the two gluons and a massless branch i.e. the quark. If the quark is soft the z_{cut} condition can fail and the tagger recurses down the massive two-gluon branch. However such configurations with a soft quark are suppressed by powers of z_{cut} and can be ignored consistent with our intended accuracy. The two-gluon branch must also pass the z_{cut} condition, as grooming it away would lead to a massless jet. Hence we can always take the first declustering to pass the z_{cut} condition so that all three partons are retained, implying that the triple-collinear limit is once again the relevant one. In the angular region where the gluons are clustered, we shall *subtract* the contributions already included in the first two scenarios described above, and shall add the correct constraints just discussed. The difference between the correct and subtraction terms is finite and can be calculated in four dimensions.

---

[5] The first declustering can also fail the z_{cut} condition due to the massive quark-gluon branch going soft, but rejection of this branch leads to a massless hemisphere and hence this contribution can be ignored for $\rho \neq 0$.

For calculations in the triple-collinear limit, we work in terms of the energy fractions z_i, defined with respect to the initiating parton's energy, and which satisfy $\sum_i z_i = 1$, and the angles θ_{ij} between any two partons i and j, such that $\theta_{ij} \ll 1$. The triple-collinear phase space in $4 - 2\epsilon$ dimensions may be written as [6] [199]

$$\mathrm{d}\Phi_3 = \frac{1}{\pi}\left(\frac{Q}{2}\right)^{4-4\epsilon} \times \\ \frac{1}{(4\pi)^{4-2\epsilon}\,\Gamma\left(1-2\epsilon\right)} \mathrm{d}z_2 \mathrm{d}z_3 \mathrm{d}\theta_{13}^2 \mathrm{d}\theta_{23}^2 \mathrm{d}\theta_{12}^2 \left(z_1 z_2 z_3\right)^{1-2\epsilon} \Delta^{-1/2-\epsilon}\,\Theta(\Delta), \quad (4.18)$$

where the Gram determinant Δ is defined as

$$\Delta = 4\theta_{13}^2 \theta_{23}^2 - \left(\theta_{12}^2 - \theta_{23}^2 - \theta_{13}^2\right)^2. \quad (4.19)$$

To make contact with the LO splitting functions in the strongly-ordered limit, it is useful to parametrise the variables z_i in terms of variables z and z_p as depicted in Fig. 4.1. Our general method for integrating the triple-collinear functions and extracting its divergences is briefly described in A.2. It involves systematic subtraction of soft and collinear divergences, via a series expansion around divergent limits, to obtain the pole structure and a pure finite contribution which we integrate numerically in four dimensions. Our results shall thus be partly analytical (stemming from performing an ϵ expansion of the coefficients of the pole terms) and partly numerical in nature.

We first provide the details for results neglecting the clustering of gluons starting from the contribution where the larger-angle emission passes the z_{cut}, which we label $\mathcal{F}^{\mathrm{pass}}(\rho, \epsilon)$. We take θ_{13} to be the larger angle and hence for the first declustering to pass the z_{cut} condition we have that $1 - z_{\mathrm{cut}} > z > z_{\mathrm{cut}}$. The smaller angle gluon is not examined for the z_{cut} condition and can be arbitrarily soft and/or collinear, leading to divergences in both limits i.e. from $z_p \to 1$ and $\theta_{23} \to 0$. The relevant splitting function and prefactor is specified by Eqs. (A.1), (A.3) and we obtain

$$\mathcal{F}^{\mathrm{pass}}(\rho, \epsilon) = 2S_\epsilon^{-2}\left(\frac{Q}{2}\right)^{4\epsilon} \times \\ \int \mathrm{d}\Phi_3 \frac{\left(8\pi\alpha_s\right)^2}{s_{123}^2} C_F^2 \left\langle P^{(ab)}_{q\to g_1 g_2 q_3}\right\rangle \delta_\rho(1,2,3)\Theta_{z_{\mathrm{cut}}}(1|23)\Theta(\theta_{23} < \theta_{13}), \quad (4.20)$$

where $s_{123}^2 = \frac{Q^2}{4}\sum_{j>i}^{3}\sum_{i=1}^{2} z_i z_j \theta_{ij}^2$ is the squared invariant mass of the three parton system, the superscript (ab) on the splitting function denotes that it is the abelian contribution, and $\delta_\rho(1,2,3)$ is an abbreviated notation for the condition that the normalised hemisphere jet mass ρ involves all three partons i.e. the condition

$$\delta_\rho(1,2,3) = \rho\,\delta\left(\rho - \frac{4s_{123}^2}{Q^2}\right), \quad (4.21)$$

---

[6] Additionally a 1/2! symmetry factor applies for identical particles in final state.

where the factor of ρ in front of the delta function takes care of the fact that we are studying the logarithmic derivative $\rho \mathrm{d}\Sigma/\mathrm{d}\rho$. We shall also use the notation $\Theta_{z_{\mathrm{cut}}}(a|b)$ to denote the condition that two branches a and b, made up of one or two partons, pass the z_{cut} condition. Partons not included in a and b fail the z_{cut} condition and are removed by grooming. Thus $\Theta_{z_{\mathrm{cut}}}(1|23)$ in Eq. (4.20) indicates that both branches i.e. gluon 1 and the massive branch with gluon 2 and the quark (with index 3) pass the z_{cut} condition. More explicitly we have $\Theta_{z_{\mathrm{cut}}}(1|23) = \Theta\left(z < 1 - z_{\mathrm{cut}}\right)\Theta\left(z > z_{\mathrm{cut}}\right)$, amounting to simply a cut on z.

In Eq. (4.20) we have also introduced the renormalised $\overline{\mathrm{MS}}$ coupling $\alpha_s(\mu_R^2)$ via the use of Eq. (4.10) leading to the appearance of the S_ϵ^{-2} factor and chosen $\mu_R = Q/2$, though for brevity we have not explicitly written the argument of the running coupling above. We have introduced a factor of two to account for the other hemisphere containing the branching of the anti-quark.

Carrying out the integrals with the method discussed in appendix A.2, the result can be expressed in the following form:

$$\mathcal{F}^{\mathrm{pass}}(\rho,\epsilon) = \left(\frac{C_F\alpha_s}{2\pi}\right)^2 \times \int_{z_{\mathrm{cut}}}^{1-z_{\mathrm{cut}}} 2\left(\frac{H^{\text{soft-coll.}}(z,\rho,\epsilon)}{\epsilon^2} + \frac{H^{\text{coll.}}(z,\rho,\epsilon)}{\epsilon} + \frac{H^{\text{soft}}(z,\rho,\epsilon)}{\epsilon} + H^{\text{fin.}}(z)\right)\mathrm{d}z, \tag{4.22}$$

where one notes the presence of a double pole coming from the soft $z_p \to 1$ and collinear $\theta_{23}^2 \to 0$ limit. Single-pole contributions are separated into the contributions from soft ($z_p \to 1$) and collinear ($\theta_{23}^2 \to 0$) divergences alone, given respectively by the H^{soft} and $H^{\text{coll.}}$ functions. We have

$$\begin{aligned} H^{\text{soft-coll.}}(z,\rho,\epsilon) &= p_{qq}(z,\epsilon) z^{-2\epsilon}\rho^{-2\epsilon}\left(1 - \frac{\pi^2}{6}\epsilon^2 + \mathcal{O}(\epsilon^3)\right), \\ H^{\text{coll.}}(z,\rho,\epsilon) &= p_{qq}(z,\epsilon) z^{-2\epsilon}\rho^{-2\epsilon}\left(\frac{3}{2} + \frac{13}{2}\epsilon - \frac{2\pi^2}{3}\epsilon + \mathcal{O}(\epsilon^2)\right), \\ H^{\text{soft}}(z,\rho,\epsilon) &= 0. \end{aligned} \tag{4.23}$$

The function $H^{\text{fin.}}(z)$ represents a finite contribution whose precise analytic form we have not extracted. Instead we study this finite contribution by direct numerical integration over the triple-collinear phase-space in 4 dimensions. The result for the integration of $H^{\text{fin.}}(z)$ gives a constant as $z_{\mathrm{cut}} \to 0$. The result that we obtain using integration with Suave [200], setting $z_{\mathrm{cut}} = 0$ is,

$$2\int_0^1 H^{\text{fin.}}(z)\mathrm{d}z = 1.866 \pm 0.002. \tag{4.24}$$

Next, we study the situation where the larger-angle gluon, i.e. emission 1, fails the z_{cut} condition and is groomed away, corresponding to $1 > z > 1 - z_{\mathrm{cut}}$. This leaves the mass to be set by the smaller-angle emission 2, $\rho = z_2 z_3 \theta_{23}^2 = z^2 z_p(1-z_p)\theta_{23}^2$.

This emission must survive grooming i.e. $1 - z_{\text{cut}} > z_p > z_{\text{cut}}$ and hence $\theta_{23}^2 \ll 1$ for $\rho \ll z_{\text{cut}}$. The softness of emission 1, with energy proportional to $1 - z$, implies that any terms regular in the limit $z \to 1$ produce power suppressed corrections in z_{cut}, which we can neglect. Hence the only contribution comes from the singularity as $z \to 1$, which produces an ϵ pole and associated finite corrections.

We start by considering the triple-collinear splitting function $P^{(ab)}_{q\to g_1 g_2 q_3}$ and its integral over the phase-space, as for the previous case where emission 1 passes the z_{cut} condition. However since now emission 1 fails the z_{cut} condition and is groomed away, it is not constrained to be collinear and has a range of angular integration going from $\theta_{13} \sim \theta_{23} \ll 1$ up to the boundary of the hemisphere at $\theta_{13} = \pi/2$. Near the lower limit of integration the triple-collinear approximation is valid, but to account correctly for soft emission at large angles we have to modify the angular dependence of the integral. This is precisely the same modification we made to account for soft large-angle emission for the calculation of C_1 (c.f. Eq. (4.6)). After neglecting pieces which contribute only an $\mathcal{O}(z_{\text{cut}})$ term on integration, we find the result

$$\begin{aligned}\mathcal{F}^{\text{fail}}(\rho,\epsilon) = &\left(\frac{C_F \alpha_s}{2\pi}\right)^2 \frac{2e^{2\epsilon\gamma_E}}{\Gamma(1-2\epsilon)} \times \\ &\int_{z_{\text{cut}}}^{1-z_{\text{cut}}} \left((1-z_p)z_p\right)^{-2\epsilon} p_{qq}(z_p,\epsilon)\mathrm{d}z_p \int_{1-z_{\text{cut}}}^{1} (1-z)^{-2\epsilon}\,\frac{2\,\mathrm{d}z}{1-z} \\ &\int_0^{1-\frac{\rho}{2z_p(1-z_p)}} \frac{2\,\mathrm{d}\left(\cos\theta_{13}\right)}{\left(1-\cos\theta_{13}\right)^{1+\epsilon}\left(1+\cos\theta_{13}\right)^{1+\epsilon}} \int \frac{\mathrm{d}\theta_{23}^2}{\theta_{23}^{2(1+\epsilon)}}\delta_\rho(2,3)\ ,\end{aligned} \tag{4.25}$$

where $\delta_\rho(2,3)$ is the condition that emission 2 and the quark labelled 3 contribute to the hemisphere invariant mass ρ. In fact, one can directly reach the same equation by realizing that the emission probability of a hard-collinear gluon completely factorizes from that of a soft gluon, i.e. the gluons are emitted independently in this region of phase space. Therefore, the total emission probability is a product of an eikonal function and a LO splitting function. This factorized structure is manifest in Eq. (4.25). The integral over θ_{23}^2 is trivially performed using the delta function constraint which sets $\rho = z^2 z_p(1-z_p)\theta_{23}^2 \approx z_p(1-z_p)\theta_{23}^2$, where we have used the fact that $z \sim 1$ corresponding to the softness of emission 1.[7] We have modified the angular dependence so that at small θ_{13} we obtain the result arising from the triple-collinear splitting functions but for $\theta_{13} \sim 1$ we have the correct angular dependence for a soft emission emitted off the $q\bar{q}$ dipole. This corresponds to the replacement of $\mathrm{d}\theta_{13}^2/\theta_{13}^{2(1+\epsilon)} \to 2\mathrm{d}\cos\theta_{13}/(1-\cos\theta_{13})^{(1+\epsilon)}(1+\cos\theta_{13})^{(1+\epsilon)}$. We have also introduced the renormalised $\overline{\text{MS}}$ coupling and choose $\mu_R = Q/2$ as before. Evaluating the integrals we obtain:

---

[7] Retaining the z dependence in the mass constraint produces terms that vanish with z_{cut} and are beyond our accuracy.

$$\mathcal{F}^{\text{fail}}(\rho,\epsilon) = \left(\frac{C_F\alpha_s}{2\pi}\right)^2 \int_{z_{\text{cut}}}^{1-z_{\text{cut}}} \mathrm{d}z_p\, p_{qq}(z_p,\epsilon)\Bigg[-\frac{2}{\epsilon}\ln\frac{4z_p(1-z_p)}{\rho} \\ -\frac{\pi^2}{3} + 4\ln^2 2 - \ln^2\frac{z_p(1-z_p)}{\rho} + 2\ln\frac{4z_p(1-z_p)}{\rho}\ln(z_{\text{cut}}^2(1-z_p)z_p\rho)\Bigg] \;. \quad (4.26)$$

Finally we account for the correct action of the tagger when emissions 1 and 2, the two gluons, are clustered first by the C/A algorithm and then the gluon pair is clustered to the quark. On applying the tagger one first encounters two branches, consisting of the quark and the massive gluon pair respectively. If the quark fails the z_{cut} condition, one would then follow the branch consisting of the gluon pair. However, such configurations with a soft quark are suppressed by powers of z_{cut} and hence ignored. On the other hand configurations where the massive gluon branch fails the z_{cut} condition would lead to a massless hemisphere. Hence we only need to study the situation where both branches pass the z_{cut} condition and all three partons are retained. The opening angle between the branches is small, being set by ρ/z_{cut}, which implies that all three partons are collinear and we can use purely triple-collinear kinematics. To correct our earlier results, we simply need to calculate the difference between the correct configuration described here and our simplified treatment included as part of $\mathcal{F}^{\text{fail}}(\rho,\epsilon)$ and $\mathcal{F}^{\text{pass}}(\rho,\epsilon)$. The relevant angular region for the calculation is $\theta_{12}^2 < \theta_{23}^2$, which corresponds to the C/A clustering of the two gluons, since we already have the ordering $\theta_{13}^2 > \theta_{23}^2$. Our clustering correction takes the form

$$\mathcal{F}^{\text{clust.}}_{C_F^2} = \lim_{z_{\text{cut}}\to 0} 2\int \frac{(8\pi\alpha_s)^2}{s_{123}^2} C_F^2 \left\langle P^{(ab)}_{q\to g_1g_2q_3}\right\rangle \Theta(\theta_{23}<\theta_{13})\Theta(\theta_{12}<\theta_{23}) \\ \Big(\delta_\rho(1,2,3)\Theta_{z_{\text{cut}}}(3|12) - \delta_\rho(1,2,3)\Theta_{z_{\text{cut}}}(1|23) - \delta_\rho(2,3)\Theta_{z_{\text{cut}}}(2|3)\Big)\mathrm{d}\Phi_3 \;, \quad (4.27)$$

where in the second line the first term in parentheses represents the correct treatment of the tagger, while the second and third terms correspond to the removal of the gluon clustering region from $\mathcal{F}^{\text{pass}}(\rho,\epsilon)$ and $\mathcal{F}^{\text{fail}}(\rho,\epsilon)$ respectively.

In the angular region relevant to their clustering, the smallest angle is that between the two gluons, so there is no collinear divergence in the gluon emission channel. We have potential soft divergences as each of z and z_p tend to 1 (i.e. z_1 or z_2 vanish), but in both those limits the correct calculation cancels with the subtraction terms in the second line of Eq. (4.27), so that the result is purely finite and we can set $\epsilon = 0$ in the integrals that follow.

In the correct treatment, i.e. the first step function on the second line of Eq. (4.27), the condition that the first declustering passes the z_{cut} corresponds to $1 - z_{\text{cut}} > z_3 > z_{\text{cut}}$, where $z_3 = zz_p$. There are then two regions for the integration over energy fractions, according to the range of z:

$$\begin{aligned} z_{\text{cut}} < z < 1 - z_{\text{cut}}, \quad & \frac{z_{\text{cut}}}{z} < z_p < 1, \quad \text{and} \\ 1 - z_{\text{cut}} < z < 1, \quad & \frac{z_{\text{cut}}}{z} < z_p < \frac{1 - z_{\text{cut}}}{z} \quad . \end{aligned} \tag{4.28}$$

For the region $z_{\text{cut}} < z < 1 - z_{\text{cut}}$, this corresponds to the region in z where gluon 1 passes the z_{cut} in our simplified calculations, so we need to correct the calculation of $\mathcal{F}^{\text{pass}}(\rho, \epsilon)$ and the third term in the second line of Eq. (4.27) vanishes. In the region $1 > z > 1 - z_{\text{cut}}$ corresponding to the grooming away of gluon 1 in the simplified calculation, we need to correct the treatment of $\mathcal{F}^{\text{fail}}(\rho, \epsilon)$ and here the second term in Eq. (4.27) vanishes.

In the former case one has a particularly simple situation since both in the simplified calculation and the correct treatment all three partons are retained and contribute to the jet mass via the $\delta_\rho(1, 2, 3)$ condition. This results in an identical angular integration in both cases and the difference between the correct and simplified treatment is purely due to the different limits on z_p. Denoting the result of the angular integrals by $\mathrm{I}(z, z_p)$, we can write the clustering correction as:

$$\begin{aligned} &\int_{z_{\text{cut}}}^{1-z_{\text{cut}}} \left(\int_{\frac{z_{\text{cut}}}{z}}^{1} \mathrm{I}(z, z_p) \mathrm{d}z_p - \int_0^1 \mathrm{I}(z, z_p) \mathrm{d}z_p \right) \mathrm{d}z \\ &\qquad\qquad = - \int_{z_{\text{cut}}}^{1-z_{\text{cut}}} \mathrm{d}z \int_0^{\frac{z_{\text{cut}}}{z}} \mathrm{I}(z, z_p) \mathrm{d}z_p \ , \end{aligned} \tag{4.29}$$

where the subtracted term above represents the removal of the simplified calculation in the gluon clustering region and where

$$\begin{aligned} \mathrm{I}(z, z_p) = 2 \int \frac{(8\pi\alpha_s)^2}{s_{123}^2} C_F^2 \left\langle P^{(ab)}_{q\to g_1 g_2 q_3} \right\rangle \delta_\rho(1, 2, 3) \times \\ \Theta(\theta_{23} < \theta_{13}) \Theta(\theta_{12} < \theta_{23}) \delta(z(1 - z_p) - z_2) \delta(z z_p - z_3) \mathrm{d}\Phi_3. \end{aligned} \tag{4.30}$$

$\mathrm{I}(z, z_p)$ has been written with a factor of two to account for both hemispheres and the angular integration extends only over the region relevant to the clustering of emissions 1 and 2. The simplified and correct calculations differ only in how soft the quark is allowed to be, and, in the limit $z_{\text{cut}} \to 0$, the result after integration over z and z_p vanishes with z_{cut}. This has been verified directly by numerical integration. Hence the correction term, given by Eq. (4.29), can be neglected in our approximation.

The situation in the region $1 - z_{\text{cut}} < z < 1$, where we derive a correction to $\mathcal{F}^{\text{fail}}(\rho, \epsilon)$, is somewhat more subtle. In the simplified version of the calculation, emission 1 is groomed away and the mass is set by emissions 2 and 3 which leads to a different constraint given by $\delta_\rho(2, 3)$ on the angular integration compared to the correct version where all three partons are retained with $\delta_\rho(1, 2, 3)$, so one obtains a different result $\tilde{\mathrm{I}}(z, z_p)$ given by:

$$\tilde{\mathrm{I}}(z,z_p) = 2\int \frac{(8\pi\alpha_s)^2}{s_{123}^2} C_F^2 \left\langle P^{(ab)}_{q\to g_1 g_2 q_3}\right\rangle \delta_\rho(2,3)\times \\ \Theta(\theta_{23}<\theta_{13})\Theta(\theta_{12}<\theta_{23})\delta(z(1-z_p)-z_2)\delta(zz_p-z_3)\mathrm{d}\Phi_3\ . \quad (4.31)$$

Due to the fact that we are restricted to the angular region where the two gluons would be clustered, all angles are constrained to be small and we can use the triple-collinear limit for obtaining $\tilde{\mathrm{I}}(z,z_p)$, ignoring the wide-angle modification required for the full calculation of $\mathcal{F}^{\text{fail}}(\rho,\epsilon)$.

One key point here is that in the limit $z\to 1$, or equivalently $z_1\to 0$, where there is a potential soft divergence, the condition $\delta_\rho(1,2,3)$ reduces to $\delta_\rho(2,3)$ so that the difference between $\tilde{\mathrm{I}}(z,z_p)$ and $\mathrm{I}(z,z_p)$ vanishes, leading to a finite result as already observed above. Moreover in the $z_{\text{cut}}\to 0$ limit we have that $z\to 1$ over the full integration range so that one may simply replace $\tilde{\mathrm{I}}(z,z_p)$ with $\mathrm{I}(z,z_p)$ up to finite corrections suppressed by z_{cut}. Doing so leads to

$$\mathcal{F}^{\text{clust.}}_{C_F^2} = \lim_{z_{\text{cut}}\to 0}\int_{1-z_{\text{cut}}}^{1}\left(\int_{\frac{z_{\text{cut}}}{z}}^{\frac{1-z_{\text{cut}}}{z}}\mathrm{I}(z,z_p)\mathrm{d}z_p - \int_{z_{\text{cut}}}^{1-z_{\text{cut}}}\tilde{\mathrm{I}}(z,z_p)\mathrm{d}z_p\right)\mathrm{d}z \\ = \lim_{z_{\text{cut}}\to 0}\int_{1-z_{\text{cut}}}^{1}\mathrm{d}z\int_{1-z_{\text{cut}}}^{\frac{1-z_{\text{cut}}}{z}}\mathrm{I}(z,z_p)\mathrm{d}z_p, \quad (4.32)$$

where in writing the third line we have replaced $\tilde{\mathrm{I}}(z,z_p)$ with $\mathrm{I}(z,z_p)$ and have exploited the fact that the difference between the lower limits of z_p integration in the correct and subtracted term, corresponding to the region of a soft quark, leads only to terms power suppressed in z_{cut}. We can numerically evaluate the integrals for a given z_{cut} value and on decreasing z_{cut}, to reduce the impact of power suppressed terms, we find the result converges to a constant. For our smallest value $z_{\text{cut}} = 10^{-5}$, using the numerical method suave [200], we obtain

$$\mathcal{F}^{\text{clust.}}_{C_F^2} = \left(\frac{C_F\alpha_s}{2\pi}\right)^2 (4.246\pm 0.002)\,. \quad (4.33)$$

The smallest value of z_{cut} was chosen so that the error on the numerical integration was larger than the difference between the central values for the lowest and second lowest z_{cut} values.

The fact that the result for $\mathcal{F}^{\text{clust.}}_{C_F^2}$ tends to a constant as $z_{\text{cut}}\to 0$ is related to the behaviour of the integrand in the soft limit for both emissions $z_p\to 1$ and $z\to 1$, which allows us to also extract the result analytically. A series expansion of $\mathrm{I}(z,z_p)$ around $z=1$ reveals a leading behaviour $\propto \frac{1}{(1-z)(1-z_p)}$, which derives from the soft limit of the matrix-element, and generates the full result in the limit $z_{\text{cut}}\to 0$. It is straightforward to perform the integrals analytically to obtain:

$$\mathcal{F}^{\text{clust.}}_{C_F^2} = \left(\frac{C_F \alpha_s}{2\pi}\right)^2 \frac{\pi}{12\sqrt{3}} \left(3\psi^{(1)}\left(\frac{1}{3}\right) - \psi^{(1)}\left(\frac{5}{6}\right)\right), \tag{4.34}$$

where we have expressed the result in terms of the Polygamma function $\psi^{(1)}(x)$. Note that one can further write

$$\frac{\pi}{12\sqrt{3}} \left(3\psi^{(1)}\left(\frac{1}{3}\right) - \psi^{(1)}\left(\frac{5}{6}\right)\right) = \frac{4\pi}{3}\text{Cl}_2\left(\frac{\pi}{3}\right) = 4.25138\cdots \tag{4.35}$$

to obtain a compact result in terms of the Clausen function $\text{Cl}_2(x)$ [201]. This analytic result is consistent with the value obtained numerically for $z_{\text{cut}} \to 10^{-5}$, keeping in mind that the latter includes terms suppressed by powers of z_{cut}, varying as $z_{\text{cut}} \ln^2 z_{\text{cut}}$. We also note that ignoring a region of phase space which only contributes a power of z_{cut} to $\mathcal{F}^{\text{clust}}$, the limits on the energy fraction integrals of Eq. (4.32) can be re-written in terms of z_1 and z_2:

$$z_1 < z_{\text{cut}}, \qquad z_2 < z_{\text{cut}}, \qquad z_1 + z_2 > z_{\text{cut}}. \tag{4.36}$$

It is now apparent that clustering the two emissions together only leads to differences from our simplified treatment of the tagger where *both* emissions would separately have failed the z_{cut} condition, but together lead to a cluster which passes the z_{cut} condition.

Our result for the $\mathcal{F}^{\text{clust.}}_{C_F^2}$ turns out to be precisely the same as the result calculated previously, for the corresponding contribution to the non-cusp global soft anomalous dimension for the mMDT jet mass, in SCET [47], [187]. While our starting point using the triple-collinear splitting functions goes beyond just the soft limit, the observation made above that the relevant limit for $\mathcal{F}^{\text{clust.}}_{C_F^2}$ is the limit when emissions 2 and 3 are additionally soft, explains the agreement with the soft limit calculations of Refs. [47], [187]. However it is worth stressing that our approach based on triple-collinear splitting functions remains valid beyond the soft limit, and hence can also be used to compute the finite z_{cut} corrections that we have neglected in this work.

Virtual corrections and combined result

Here we combine the results for double-real emission with the one-real one-virtual corrections to generate a finite result. The one-real–one-virtual terms are provided in appendix A.3. We define the integral of the one-real–one-virtual term over z as $V^{C_F^2}$, given by

$$V^{C_F^2}(\rho, \epsilon) = \int_{z_{\text{cut}}}^{1-z_{\text{cut}}} \mathrm{d}z \, \mathcal{V}^{C_F^2}_{1,1}(\rho, z, \epsilon), \tag{4.37}$$

with $\mathcal{V}_{1,1}^{C_F^2}(\rho, z, \epsilon)$ given in Eq. (A.14). Combining terms, we can write the gluon emission contribution as

$$\left(\rho\frac{d\Sigma_2}{d\rho}\right)^{\text{gluon-emission}} = \mathcal{F}^{\text{opp.}}(\rho,\epsilon) + \mathcal{F}^{\text{pass}}(\rho,\epsilon) + \mathcal{F}^{\text{fail}}(\rho,\epsilon) + \mathcal{F}^{\text{clust.}}_{C_F^2} + V^{C_F^2}(\rho,\epsilon). \quad (4.38)$$

We find that after cancellation of all the singular contributions we are left with

$$\begin{aligned}\left(\rho\frac{d\Sigma_2}{d\rho}\right)^{\text{gluon-emission}} &= \left(\frac{C_F\alpha_s}{2\pi}\right)^2 \times \\ &\Bigg((3+4\ln z_{\text{cut}})^2\ln\rho - 8\ln^3 z_{\text{cut}} - 2(3+16\ln 2)\ln^2 z_{\text{cut}} + (4-48\ln 2)\ln z_{\text{cut}} \\ &\quad - 24\zeta(3) + 2\pi^2 + \frac{7}{2} - 18\ln 2 + \frac{4\pi}{3}\mathrm{Cl}_2\left(\frac{\pi}{3}\right) + 1.866 \pm 0.002\Bigg), \quad (4.39)\end{aligned}$$

where the numerically quoted value 1.866±0.002 represents the contribution to $\mathcal{F}^{\text{pass}}(\rho,\epsilon)$ arising from $H^{\text{fin.}}(z)$ (see Eqs. (4.20), (4.24)). It is then evident that the terms in Eq. (4.39) that depend on $\ln\rho$ and $\ln z_{\text{cut}}$ are in precise agreement with those expected from the C_F^2 term in the expansion of the NLL resummed result, i.e. Eq. (4.15). In addition there is a constant contribution corresponding to an $\alpha_s^2\ln\rho$ NNLL term in $\Sigma_2(\rho)$. We shall analyse the constant contribution in more detail, after including another C_F^2 term coming from the gluon decay terms computed in the next subsection.

4.4.2 Gluon decay contributions

Here we consider the contributions that are associated to the decay of a collinear gluon, emitted off the initiating quark, into a $q\bar{q}$ pair and a gluon pair associated with $C_F T_R n_f$ and $C_F C_A$ factors respectively. For the case of the gluon decay to $q\bar{q}$ with a quark initiated jet i.e. a $q \to q\bar{q}q$ process, there is also an interference contribution from identical fermions in the final state with a colour factor $C_F(C_F - C_A)/2$, which contributes to the overall results for the C_F^2 and $C_F C_A$ channels. We shall first discuss this piece and then turn to the $C_F T_R n_f$ and $C_F C_A$ terms.

$C_F\left(C_F - \frac{C_A}{2}\right)$ contribution

The identical fermion contribution is simple to compute since it is finite, both for the angular and energy integrals. The calculation can therefore be easily carried out numerically in four dimensions. The relevant splitting function is given in Eq. (A.8) and we set $\epsilon \to 0$. Moreover, due to the fact that the splitting function is regular in the energy fractions, the contribution from the region of integration where any parton has energy fraction $z < z_{\text{cut}}$ is suppressed with z_{cut}. For this reason the clustering and grooming sequence does not matter, as the result in the small z_{cut} limit comes from a configuration when all three partons contribute to the jet mass, ρ, and have energy fraction $z > z_{\text{cut}}$ i.e. the un-groomed limit. To obtain the leading term, which is a constant in the small z_{cut} limit, we set $z_{\text{cut}} = 0$ and numerically perform the integral using our general rescaling method discussed in appendix A.2. We then have

$$\mathcal{F}^{\text{id}} = \int \mathrm{d}\Phi_3 \frac{(8\pi\alpha_s)^2}{s_{123}^2} P^{(\text{id})}_{q\to q\bar{q}q} \delta_\rho(1,2,3) = C_F \left(C_F - \frac{C_A}{2}\right)\left(\frac{\alpha_s}{2\pi}\right)^2 (1.4386 \pm 0.0001) \ , \quad (4.40)$$

where we performed the integral numerically with Suave and the result includes a factor of 2 to take account of both hemispheres as well an identical particle 1/2! phase-space symmetry factor. We believe that our result here coincides with an older calculation for the identical fermion contribution that enters initial state splittings, by Grazzini and de Florian, who obtained an analytical result

$$\frac{13}{2} - \pi^2 + 4\zeta(3) = 1.43862\cdots \quad (4.41)$$

which they subtract to construct the relevant non-singlet contribution (see Eq. (71) of ref. [202]). We shall return to this result, its analytical form and its combination with the C_F^2 and $C_F C_A$ results, when summarising our results.

$C_F T_R n_f$ contribution

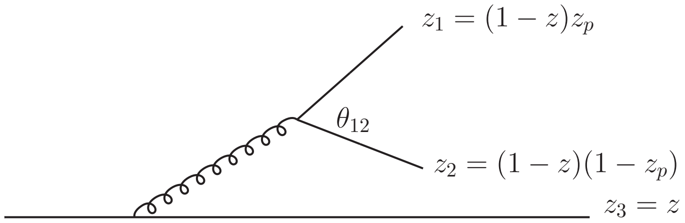

Figure 4.2. An illustration of the kinematic parametrisation in the $C_F T_R n_f$ gluon decay channel.

Next we discuss the $C_F T_R n_f$ term again related to gluon decay to a $q\bar{q}$ pair. The relevant diagram with our parametrisation of the kinematics is shown in Figure 4.2. Since the $g \to q\bar{q}$ splitting is regular in the infra-red, one encounters only a collinear singularity in the squared matrix element as $\theta_{12} \to 0$, which leads to a $1/\epsilon$ pole in the jet mass distribution. We also expect that an analysis of the gluon decay contributions should lead to the emergence of the correct argument of the running coupling i.e. k_t in the soft limit, and the factor associated to the physical CMW scheme.

As we did for the C_F^2 piece, it proves convenient to break the calculation into two pieces: a first piece that simplifies the action of the tagger and contains the divergent pole structure and a correction term which only has support in non-singular regions, leading to a finite result which can be computed numerically in four dimensions. We will also account for virtual corrections which cancel the pole in the real emission piece, leaving a finite result. The divergence occurs as $\theta_{12} \to 0$ which is the region where the q and $\bar{q}$ are clustered first in the C/A algorithm, and then the $q\bar{q}$ pair is clustered to the parton 3. We shall therefore first carry out the calculation always taking the q and $\bar{q}$ to be clustered together which mistreats regions where emissions 1 or 2 could be first clustered with 3. These regions will be subject to our finite clustering corrections.

For the contribution where the q and $\bar{q}$ from the gluon decay are first clustered together, we produce, on declustering, two branches consisting of the quark (or antiquark) labelled 3 and the clustered fermion pair, or equivalently, the massive parent gluon. If the quark labelled 3 is soft and fails the z_{cut} then we obtain only terms power suppressed in z_{cut}. If the massive gluon branch fails the clustering we obtain a massless hemisphere. Thus we have a situation where in order to obtain a finite result in the $z_{\text{cut}} \to 0$ limit, both branches pass the z_{cut} condition so that all three partons are retained and contribute to the jet mass. The condition $\rho \ll z_{\text{cut}}$ once again implies that all three partons are collinear and we can apply the triple-collinear splitting function and phase-space. In order to use our integration strategy based on rescaled angular variables, we consider two regions $\theta_{12}^2 < \theta_{13}^2$ and $\theta_{12}^2 > \theta_{13}^2$, with the first mentioned region contributing the divergence. We denote the respective contributions to $\rho\frac{d\Sigma_2}{d\rho}$ by $\mathcal{F}^{\theta_{12}<\theta_{13}}(\rho)$ and $\mathcal{F}^{\theta_{12}>\theta_{13}}(\rho)$ where explicitly we have for the former,

$$\mathcal{F}^{\theta_{12}<\theta_{13}}(\rho,\epsilon) = \\ 2S_\epsilon^{-2}\left(\frac{Q}{2}\right)^{4\epsilon}\int \mathrm{d}\Phi_3 \frac{(8\pi\alpha_s)^2}{s_{123}^2}\left\langle P_{\bar{q}_1' q_2' q_3}\right\rangle \delta_\rho(1,2,3)\Theta_{z_{\text{cut}}}(12|3)\Theta(\theta_{12}<\theta_{13}), \quad (4.42)$$

where a sum over flavours, leading to a factor n_f, is left implicit on the RHS of the above equation. The notation $\Theta_{z_{\text{cut}}}(12|3)$ denotes that each of the two branches passes the z_{cut} condition equivalent to the constraint on the parent gluon energy $1 - z_{\text{cut}} > z > z_{\text{cut}}$. The result is written in terms of the renormalised $\overline{\text{MS}}$ coupling and a factor of two accounts for both hemispheres.

In terms of the rescaled angular variable $y = \theta_{12}^2/\theta_{13}^2$ and the parent energy fraction z, we obtain a result of the form (where $G(y, z, \epsilon)$ is regular as $y \to 0$)

$$\mathcal{F}^{\theta_{12}<\theta_{13}}(\rho,\epsilon) = \rho^{-2\epsilon}\int_{z_{\text{cut}}}^{1-z_{\text{cut}}} \mathrm{d}z \int_0^1 \frac{\mathrm{d}y}{y^{1+\epsilon}} G(y,z,\epsilon) \\ - \frac{\rho^{-2\epsilon}}{\epsilon}\int_{z_{\text{cut}}}^{1-z_{\text{cut}}} \mathrm{d}z\, G(0,z,\epsilon) + \int_{z_{\text{cut}}}^{1-z_{\text{cut}}} \mathrm{d}z \int_0^1 \frac{dy}{y}\left(G(y,z,0) - G(0,z,0)\right). \quad (4.43)$$

In writing the above we first isolated the singular contribution by taking only the leading term in the expansion of $G(y, z, \epsilon)$ around $y = 0$, and integrated over y to obtain the pole in ϵ in the first term above, while the second term is finite by construction since $(G(y, z, 0) - G(0, z, 0))$ vanishes as $y \to 0$. The finite term can be computed in four dimensions, so we set $\epsilon = 0$. However while the term involving

$(G(y,z,0) - G(0,z,0))$ is finite, it has a leading behaviour in the $z \to 1$ limit proportional to $\frac{1}{1-z}$, which can be extracted through a series expansion about $z = 1$. The limit $z \to 1$ corresponds to a soft parent gluon and gives rise to $\ln z_{\mathrm{cut}}$ terms in the result, which build up the constant K and relate the coupling in the $\overline{\mathrm{MS}}$ scheme to that in the CMW scheme. After separating the $1/(1-z)$ term which can be handled analytically, we integrate the remainder of the finite contribution numerically.

We then have

$$\mathcal{F}^{\theta_{12}<\theta_{13}}(\rho,\epsilon) = \\ C_F T_R n_f \left(\frac{\alpha_s}{2\pi}\right)^2 \int_{z_{\mathrm{cut}}}^{1-z_{\mathrm{cut}}} \left(\frac{H_1^{\mathrm{coll.}}(z,\rho,\epsilon)}{\epsilon} + H_1^{\mathrm{fin.\text{-}soft}}(z) + H_1^{\mathrm{fin.}}(z)\right) \mathrm{d}z \ , \tag{4.44}$$

where

$$\begin{aligned} H_1^{\mathrm{coll.}}(z,\rho,\epsilon) &= \rho^{-2\epsilon}(1-z)^{-2\epsilon} p_{qq}(z,\epsilon)\left(-\frac{4}{3} - \frac{46}{9}\epsilon + \mathcal{O}(\epsilon^2)\right), \\ H_1^{\mathrm{fin.\text{-}soft}}(z) &= \frac{4}{9}\frac{1}{1-z}. \end{aligned} \tag{4.45}$$

$H_1^{\mathrm{fin.\text{-}soft}}(z)$ is the soft parent finite contribution and the finite remainder $H^{\mathrm{fin.}}(z)$ tends to a constant as $z_{\mathrm{cut}} \to 0$. Using Mathematica's NIntegrate [203] with $z_{\mathrm{cut}} = 0$ we obtain

$$\int_0^1 H_1^{\mathrm{fin.}}(z)\mathrm{d}z = -1.479 \pm 0.001 \ . \tag{4.46}$$

Next we need the contribution from the angular region $\theta_{13} < \theta_{12}$ which does not contain any poles. However, as discussed above for $\theta_{12} < \theta_{13}$, there is again a soft enhancement as $z \to 1$ giving rise to a $\ln z_{\mathrm{cut}}$ term related to the CMW constant K. Explicitly we have:

$$\begin{aligned} \mathcal{F}^{\theta_{13}<\theta_{12}}(\rho) &= 2\int \mathrm{d}\Phi_3 \frac{(8\pi\alpha_s)^2}{s_{123}^2} \left\langle P_{\bar{q}_1' q_2' q_3}\right\rangle \delta_\rho(1,2,3)\Theta_{z_{\mathrm{cut}}}(12|3)\Theta(\theta_{13}<\theta_{12}) \\ &= C_F T_R n_f \left(\frac{\alpha_s}{2\pi}\right)^2 \int_{z_{\mathrm{cut}}}^{1-z_{\mathrm{cut}}} \left(H_2^{\mathrm{fin.\text{-}soft}}(z) + H_2^{\mathrm{fin.}}(z)\right) \mathrm{d}z \end{aligned} \tag{4.47}$$

which has no collinear pole i.e. $H_2^{\mathrm{coll.}}(z) = 0$ and where

$$\begin{aligned} H_2^{\mathrm{fin.\text{-}soft}}(z) &= \frac{16}{3}\frac{1}{1-z}, \\ \int_0^1 H_2^{\mathrm{fin.}}(z)\mathrm{d}z &= -6.242 \pm 0.006. \end{aligned} \tag{4.48}$$

where, as before, the final term is evaluated numerically with $z_{\mathrm{cut}} = 0$ to remove power corrections.

A final ingredient for generating the result is the $T_R n_f$ piece of the one-real–one-virtual contribution. This is reported in A.3 (see Eq. (A.17)) and a finite result is obtained on combining the virtual contribution with $\mathcal{F}^{\theta_{13}>\theta_{12}}(\rho)$. Defining

$$V^{C_F T_R n_f}(\rho,\epsilon) = \int_{z_{\mathrm{cut}}}^{1-z_{\mathrm{cut}}} \mathrm{d}z \mathcal{V}_{1,1}^{C_F T_R n_f}(\rho,z,\epsilon) \tag{4.49}$$

and

$$\mathcal{F}^{\mathrm{tot.}}(\rho,\epsilon) = \mathcal{F}^{\theta_{12}<\theta_{13}}(\rho,\epsilon) + \mathcal{F}^{\theta_{13}<\theta_{12}}(\rho), \tag{4.50}$$

we can combine the results to obtain

$$\mathcal{F}^{\mathrm{tot.}}(\rho) + V^{C_F T_R n_f}(\rho,\epsilon) = \\ C_F T_R n_f \left(\frac{\alpha_s}{2\pi}\right)^2 \left(\int_{z_{\mathrm{cut}}}^{1-z_{\mathrm{cut}}} \mathrm{d}z\, G(z,\rho) - 7.721 \pm 0.007\right), \tag{4.51}$$

where

$$G(z,\rho) = \frac{4}{3}p_{qq}(z)\ln(\rho(1-z)) - \frac{20}{9}p_{qq}(z) - \frac{4}{3}p_{qq}(z)\ln z + \frac{26}{9}(1+z). \tag{4.52}$$

It is worth making some remarks on the form of $G(z,\rho)$. Firstly we note a piece corresponding to the n_f term in $-2 \times p_{qq} b_0 \ln(\rho(1-z))$, where $b_0 = \frac{11}{6}C_A - \frac{2}{3}T_R n_f$ is the first perturbative coefficient of the QCD β function. This term produces an NLL contribution from the dependence on $\ln\rho$. In the soft limit, i.e. $z \to 1$ and $p_{qq}(z) \to \frac{2}{1-z}$ it can be absorbed into the leading-order result by correcting the scale of the coupling $\alpha_s\left(\frac{Q^2}{4}\right) \to \alpha_s\left(\frac{Q^2}{4}\rho(1-z)\right) = \alpha_s(k_t^2)$, consistent with the NLL formula (4.2). The term $-\frac{20}{9}p_{qq}(z)$ corresponds to the appearance of the n_f piece of the CMW constant K, as also anticipated in the NLL result. The remaining terms produce a constant in the small z_{cut} limit, on integration over z, which can be combined with the constants we obtained numerically. However before doing so we shall evaluate the correction term due to the proper use of the C/A clustering sequence within the mMDT.

Turning to the clustering correction we first note that, in the angular region where θ_{12} is smallest, our treatment of the tagger, working as if partons 1 and 2 are always clustered, needs no correction. The regions where a correction is needed are when θ_{13} is smallest and when θ_{23} is smallest which is identical due to the symmetry under $1 \leftrightarrow 2$. These regions contain no divergences and hence the calculation of the correction term, i.e. the difference between the correct and simplified calculations, can be performed numerically in four dimensions. We shall also work in the limit $z_{\mathrm{cut}} \to 0$ to eliminate power-suppressed terms in z_{cut}, explicitly take the case that θ_{13} is the smallest angle and double the result to account for θ_{23} being smallest. We can then write

$$\mathcal{F}^{\text{clust.}}_{C_F T_R n_f} = \lim_{z_{\text{cut}}\to 0} 4\int \frac{(8\pi\alpha_s)^2}{s_{123}^2}\left\langle P_{\bar{q}_1' q_2' q_3}\right\rangle \Theta(\theta_{23} > \theta_{13})\Theta(\theta_{12} > \theta_{13})\times$$
$$\Big(\delta_\rho(1,2,3)\Theta_{z_{\text{cut}}}(2|13) + \delta_\rho(1,3)\Theta_{z_{\text{cut}}}(1|3) - \delta_\rho(1,2,3)\Theta_{z_{\text{cut}}}(3|12)\Big)\mathrm{d}\Phi_3. \quad (4.53)$$

The above equation reflects that when θ_{13} is the smallest angle, there are two configurations that yield a massive hemisphere: when parton 2 passes the z_{cut} condition and all three partons are retained (the first term on the second line), and when parton 2 fails the z_{cut} condition but partons 1 and 3 pass (the second term on the second line). The clustering correction may then be expressed as

$$\mathcal{F}^{\text{clust.}}_{C_F T_R n_f} =$$
$$\lim_{z_{\text{cut}}\to 0}\int_0^1 \left(\mathrm{I}_{n_f}(z,z_p)\left(\Theta_{z_{\text{cut}}}(13|2) - \Theta_{z_{\text{cut}}}(12|3)\right) + \tilde{\mathrm{I}}_{n_f}(z,z_p)\Theta_{z_{\text{cut}}}(1|3)\right)\mathrm{d}z\mathrm{d}z_p\ , \quad (4.54)$$

where the subtraction term corresponds to removal of the simplified contribution where 1 and 2 were taken to be clustered first and our usual notation applies where $\Theta_{z_{\text{cut}}}(a|b)$ denotes the two branches a and b that pass the z_{cut} condition in each case.[8] The integrals $\mathrm{I}_{n_f}(z,z_p)$ and $\tilde{\mathrm{I}}_{n_f}(z,z_p)$ arise from the angular integration for the case when all three partons contribute to the jet mass and when only two partons contribute respectively.[9] Explicitly we have

$$\mathrm{I}_{n_f}(z,z_p) = 4\int \frac{(8\pi\alpha_s)^2}{s_{123}^2}\left\langle P_{q\to\bar{q}_1' q_2' q_3}\right\rangle \delta_\rho(1,2,3)\times$$
$$\Theta(\theta_{13} < \theta_{23})\Theta(\theta_{13} < \theta_{12})\delta(z(1-z_p) - z_2)\delta(z z_p - z_3)\mathrm{d}\Phi_3\ , \quad (4.55)$$

and

$$\tilde{\mathrm{I}}_{n_f}(z,z_p) = 4\int \frac{(8\pi\alpha_s)^2}{s_{123}^2}\left\langle P_{q\to\bar{q}_1' q_2' q_3}\right\rangle \delta_\rho(1,3)$$
$$\Theta(\theta_{13} < \theta_{23})\Theta(\theta_{13} < \theta_{12})\delta(z(1-z_p) - z_2)\delta(z z_p - z_3)\mathrm{d}\Phi_3\ , \quad (4.56)$$

where a factor of 4 accounts for both hemispheres and the case when θ_{23} is the smallest angle.

We can evaluate the integrals numerically by choosing a small z_{cut} to suppress power corrections and find that the result tends to a z_{cut} independent constant on decreas-

---

[8] This implies also the condition that partons not included in these branches fail the z_{cut} e.g. for parton 2 in $\Theta_{z_{\text{cut}}}(1|3)$.

[9] In the case when a parton is soft enough to be groomed away it is not constrained by the jet mass and can in principle be at a large angle. For correlated emission such configurations, where one of the gluon decay offspring is at a large angle to the other, are dynamically suppressed and only contribute at the level of power corrections in ρ. This implies that the integrals converge within the triple-collinear region which does not need to be modified, which we have also verified numerically.

ing z_{cut}. On evaluation of the integrals numerically with Suave we obtain, for $z_{\text{cut}} = 10^{-5}$ as for the C_F^2 clustering piece, the result

$$\mathcal{F}^{\text{clust.}}_{C_F T_R n_f} = C_F T_R n_f \left(\frac{\alpha_s}{2\pi}\right)^2 (-1.754 \pm 0.002)\,. \tag{4.57}$$

Further insight into the nature of the clustering correction reported above can be obtained via similar considerations to those for the C_F^2 clustering correction. Firstly one notes that in the limit parton 2 goes soft and fails the z_{cut} condition the angular integral $\tilde{\text{I}}_{n_f}(z, z_p)$ may be replaced by $\text{I}_{n_f}(z, z_p)$ up to terms that vanish with z_{cut}. This lets us combine the constraints on the z integrals and, again, with neglect of power corrections in z_{cut} one obtains the conditions on z_1 and z_2:

$$z_1 + z_2 > z_{\text{cut}}\ , \qquad z_1 < z_{\text{cut}}\ , \qquad z_2 < z_{\text{cut}}. \tag{4.58}$$

These conditions are the same as for the C_F^2 case, however here the clustering correction enters with a negative sign while a positive correction was noted for the C_F^2 term. The reason for this is that our simplified treatment in the C_F^2 channel amounted to discarding two emissions that individually failed the z_{cut}, thereby *excluding* the contribution where they pass the z_{cut} when correctly treated as a cluster since $z_1 + z_2 > z_{\text{cut}}$. Here, on the other hand, our simplified picture *includes* configurations where incorrectly treating emissions as a cluster causes them to pass the z_{cut} condition, while in the correct treatment of clustering, where the gluon decay products are not clustered, the emissions each fail the z_{cut}, leading to a massless hemisphere.

Furthermore, we note once again that our clustering corrections originate in the soft region, albeit still also within the triple-collinear regime and that our calculations can be extended to include finite z_{cut} terms. The numerical value we obtain for the clustering piece, $\mathcal{F}^{\text{clust.}}_{C_F T_R n_f}$, is once again in agreement within errors (and potential $z_{\text{cut}} \ln^2 z_{\text{cut}}$ terms) to that previously obtained, for the n_f part of the clustering term for the non-cusp global soft anomalous dimension for mMDT, in the SCET framework [47], [187].

Finally we quote our overall result for the $C_F T_R n_f$ channel, combining the different contributions i.e. performing the integral over z in Eq. (4.51) and adding in the clustering correction:

$$\begin{aligned}\rho\frac{\mathrm{d}\Sigma_2^{C_F T_R n_f}}{\mathrm{d}\rho} &= C_F T_R n_f \left(\frac{\alpha_s}{2\pi}\right)^2 \bigg(-\frac{2}{3}(3 + 4\ln z_{\text{cut}})\ln\rho \\ &\quad -\frac{4}{3}\ln^2 z_{\text{cut}} + \frac{40}{9}\ln z_{\text{cut}} + \frac{4\pi^2}{9} + \frac{25}{3} - 7.721 \pm 0.007 - 1.754 \pm 0.002\bigg),\end{aligned} \tag{4.59}$$

where the -1.754 is the clustering correction computed above, and the other terms are the full result for our simplified treatment of the tagger. We note that the $\ln\rho$ and $\ln z_{\text{cut}}$ dependent terms in Eq. (4.59) are in exact agreement with expectations from the expansion of the NLL result (4.15). Further light can be shed on the constant term $\frac{4\pi^2}{9} + \frac{25}{3} - 7.721 \pm 0.007$ following an analytic calculation carried out in [4], which gives

$$\rho \frac{\mathrm{d}\Sigma_2^{C_F T_R n_f}}{\mathrm{d}\rho} = C_F T_R n_f \left(\frac{\alpha_s}{2\pi}\right)^2 \times \\ \left(-\frac{2}{3}(3 + 4\ln z_{\text{cut}}) \ln\rho - \frac{4}{3}\ln^2 z_{\text{cut}} + \frac{40}{9}\ln z_{\text{cut}} + 5 - 1.754 \pm 0.002 \right), \quad (4.60)$$

which is fully consistent with eq. (4.59).

$C_F C_A$ contribution from $q \to qgg$

The same kinematic variables apply as in Fig. 4.2 for the gluon decay to $q\bar{q}$. One of the key differences with the n_f piece is now the presence of soft divergences as $z_p \to 0$ and $z_p \to 1$.[10]

We can organise the calculation in precisely the same way as for the n_f piece by first computing a simplified term where for applying the grooming the offspring gluons are always treated as a cluster equivalent to the parent gluon. We then correct for the proper C/A clustering so that, as before, our correction term is finite and calculable in four dimensions. Again as done before for the n_f piece, we can further divide the simplified calculation into two pieces where $\theta_{12} < \theta_{13}$ and vice-versa. The region with $\theta_{12} < \theta_{13}$ contains all the divergences, resulting in $\frac{1}{\epsilon^2}$ and $\frac{1}{\epsilon}$ poles. The region $\theta_{13} > \theta_{12}$ gives only a finite contribution in spite of the presence of soft divergences in the $g \to gg$ splitting, as a consequence of the angular ordering property of soft radiation, ie coherence, as discussed in section 2.4.2. The $C_F C_A$ contribution in the region $\theta_{12} < \theta_{\theta_1 3}$ can then be expressed as

$$\mathcal{F}_{C_F C_A}^{\theta_{12}<\theta_{13}}(\rho, \epsilon) = 2 S_\epsilon^{-2} \left(\frac{Q}{2}\right)^{4\epsilon} \times \\ \int \mathrm{d}\Phi_3 \frac{(8\pi\alpha_s)^2}{s_{123}^2} \left\langle P_{q\to g_1 g_2 q_3}^{(\text{nab})} \right\rangle \delta_\rho(1,2,3) \Theta_{z_{\text{cut}}}(12|3) \Theta(\theta_{12} < \theta_{13}) \ , \quad (4.61)$$

which is written as before in terms of the renormalised $\overline{\text{MS}}$ coupling with $\mu_R = Q/2$, and a factor of 2 to account for both hemispheres. Further analysis using our general integration method, outlined in appendix A.2, gives

$$\mathcal{F}_{C_F C_A}^{\theta_{12}<\theta_{13}}(\rho, \epsilon) = C_F C_A \left(\frac{\alpha_s}{2\pi}\right)^2 \times \\ \int_{z_{\text{cut}}}^{1-z_{\text{cut}}} \left(\frac{H^{\text{soft-coll.}}(z, \rho, \epsilon)}{\epsilon^2} + \frac{H^{\text{coll.}}(z, \rho, \epsilon)}{\epsilon} + H^{\text{finite}}(z) \right) \mathrm{d}z \ , \quad (4.62)$$

---

[10] In order to avoid considering both limits one can simply take the region $z_p < 1 - z_p$, where the divergence only comes from $z_p \to 0$, and double the result exploiting the symmetry between the gluons.

where

$$\begin{aligned} H^{\text{soft-coll.}}(z,\rho,\epsilon) &= \rho^{-2\epsilon}(1-z)^{-2\epsilon}p_{qq}(z,\epsilon)\left(2-\frac{\pi^2}{3}\epsilon^2+\mathcal{O}(\epsilon^3)\right), \\ H^{\text{coll.}}(z,\rho,\epsilon) &= \rho^{-2\epsilon}(1-z)^{-2\epsilon}p_{qq}(z,\epsilon)\left(\frac{11}{3}+\frac{134}{9}\epsilon-\frac{4\pi^2}{3}\epsilon+\mathcal{O}(\epsilon^2)\right). \end{aligned} \tag{4.63}$$

As in section 4.4.2 the finite term $H^{\text{finite}}(z)$ is enhanced in the limit of a soft parent, $z \to 1$, and produces $\ln z_{\text{cut}}$ terms, which we wish to separate since they relate to the CMW scheme. As before we use a series expansion about $z = 1$, to make the decomposition

$$H^{\text{finite}}(z) = \frac{c}{1-z} + f(z), \tag{4.64}$$

where $f(z)$ is finite as $z \to 1$. The constant, c is evaluated numerically (on integrating over the angular variables and z_p), as is the integral over $f(z)$ and, again using NIntegrate with $z_{\text{cut}} = 0$, we obtain:

$$\int_{z_{\text{cut}}}^{1-z_{\text{cut}}} H^{\text{finite}}(z) = (2.4361 \pm 0.0002)\ln z_{\text{cut}} - 0.117 \pm 0.001. \tag{4.65}$$

In the region $\theta_{13} < \theta_{12}$ there are no poles in ϵ and we can perform the calculation setting $\epsilon \to 0$, so we have

$$\mathcal{F}^{\theta_{13}<\theta_{12}}_{C_F C_A}(\rho) = \int \mathrm{d}\Phi_3 \frac{(8\pi\alpha_s)^2}{s_{123}^2}\langle P_{q\to g_1 g_2 q_3}\rangle\, \delta_\rho(1,2,3)\Theta_{z_{\text{cut}}}(12|3)\Theta(\theta_{13}<\theta_{12}). \tag{4.66}$$

Again separating the integrand into pieces which diverge as $z \to 1$ and those which do not, we obtain, after numerical integration with $z_{\text{cut}} = 0$,

$$\mathcal{F}^{\theta_{13}<\theta_{12}}_{C_F C_A}(\rho) = C_F C_A\left(\frac{\alpha_s}{2\pi}\right)^2\left[(5.8730 \pm 0.0006)\ln z_{\text{cut}} + (6.795 \pm 0.006)\right]. \tag{4.67}$$

Finally we account for the clustering corrections. This is done as for the n_f piece in Eq. (4.53) and the result is finite as soft divergences cancel in the combination of the correct and simplified treatments. The result can be computed numerically in four dimensions. Using Suave with $z_{\text{cut}} = 10^{-5}$ we obtain:

$$\mathcal{F}^{\text{clust.}}_{C_F C_A} = C_F C_A\left(\frac{\alpha_s}{2\pi}\right)^2(-1.161 \pm 0.001). \tag{4.68}$$

The same comments apply to the origin of the clustering correction here as for the n_f piece, namely it originates from incorrectly allowing, in the simplified result, the gluon pair to pass the clustering due to the fact that the parent passes the z_{cut}. The correct tagging procedure would be applied to the individual gluons instead, which fail the clustering leading to a massless jet and a nil contribution. The result again agrees with previous calculations of the clustering piece in the mMDT SCET non-cusp soft anomalous dimension [47], [187] to within errors and potential $z_{\text{cut}}\ln^2 z_{\text{cut}}$

corrections.

Finally we combine all pieces and include the one-real–one-virtual correction $V^{C_F C_A}(\rho,\epsilon) = \int_{z_{\text{cut}}}^{1-z_{\text{cut}}} \mathrm{d}z \mathcal{V}_{1,1}^{C_F C_A}(\rho, z, \epsilon)$ defined in appendix A.3 to obtain the result

$$\rho \frac{d\Sigma_2}{d\rho}^{q\to qgg,\text{nab.}} = C_F C_A \left(\frac{\alpha_s}{2\pi}\right)^2 \left[\frac{11}{6}\left(3 + 4\ln z_{\text{cut}}\right)\ln\rho \right. \\ + \frac{11\ln^2 z_{\text{cut}}}{3} + \left(\frac{4}{3}\pi^2 - \frac{268}{9} + (8.3091 \pm 0.0006)\right)\ln z_{\text{cut}} \\ \left. + 16\zeta(3) - \frac{11\pi^2}{9} - \frac{121}{6} + (6.678 \pm 0.006) - (1.161 \pm 0.001)\right] , \quad (4.69)$$

where the labelling $q \to qgg$, nab. indicates the non-abelian contribution to the $q \to qgg$ process and where we have separately written the numerically computed clustering contribution and the numerically computed part of the simplified calculation. The result above is in agreement with our expectations from the expansion of the NLL resummed result Eq. (4.15) for the terms involving $\ln\rho$ and $\ln z_{\text{cut}}$ since the numerical value 8.3091 ± 0.0006 is in good agreement with $\frac{134}{9} - \frac{2\pi^2}{3}$, signalling again that the $\ln z_{\text{cut}}$ term is associated with the CMW scheme, while the $\ln\rho$ and $\ln^2 z_{\text{cut}}$ terms are associated to the argument of the running coupling i.e. k_t in the soft limit. This leaves us to comment on the constant term, other than the clustering correction, which we shall do in the next section, where we shall consider the full $C_F C_A$ result including that from the $C_F(C_F - C_A/2)$ term.

4.5 Structure of NNLL results

In this section we discuss the structure of our results for each of the C_F^2, $C_F C_A$ and $C_F T_R n_f$ channels. As has already been noted for every channel, the result at order α_s^2 reproduces the terms expected from the expansion of the NLL formula (4.15) in addition to producing genuine NNLL corrections.[11] Therefore we may focus only on the additional terms not produced as part of the NLL expansion and hence we write:

$$\rho\frac{d\Sigma_2}{d\rho} = \rho\frac{d\Sigma_2^{\text{NLL}}}{d\rho} + \rho\frac{d\Sigma_2^{\text{NNLL}}}{d\rho}, \quad (4.70)$$

where $\rho\frac{d\Sigma_2^{\text{NLL}}}{d\rho}$ is reported in Eq. (4.15) and $\rho\frac{d\Sigma_2^{\text{NNLL}}}{d\rho}$ describes the NNLL terms unrelated to NLL dynamics.

To obtain our result for the $\rho\frac{d\Sigma_2^{\text{NNLL}}}{d\rho}$ in the C_F^2 channel we combine the result from gluon emission Eq. (4.39) with the C_F^2 term arising from the gluon decay (4.40) iden-

---

[11] Recall that the expansion of the NLL formula also contains formally NNLL terms but which can be embedded within the NLL strongly ordered dynamics.

tical particle piece. After removal of the NLL contribution we can write:

$$\left(\rho\frac{d\Sigma_2^{\mathrm{NNLL}}}{d\rho}\right)^{C_F^2} = \left(\frac{C_F\alpha_s}{2\pi}\right)^2 \times \\ \left(2\pi^2 - 24\zeta(3) + \frac{1}{2} + (1.866 \pm 0.002) + (1.4386 \pm 0.0001)\right) + \mathcal{F}^{\mathrm{clust.}}_{C_F^2}\,, \quad (4.71)$$

where $\mathcal{F}^{\mathrm{clust.}}_{C_F^2}$ is the clustering contribution Eq. (4.34).

The corresponding result for the $C_F T_R n_f$ term can be obtained partly in numerical form from Eq. (4.59) or fully analytically from Eq. (4.60), using a result presented in [4]. after removal of the NLL contribution we get

$$\left(\rho\frac{d\Sigma_2^{\mathrm{NNLL}}}{d\rho}\right)^{C_F T_R n_f} = C_F T_R n_f \left(\frac{\alpha_s}{2\pi}\right)^2 \times 5.0 + \mathcal{F}^{\mathrm{clust.}}_{C_F T_R n_f}, \quad (4.72)$$

where we used above the analytical result of [4] and the clustering contribution is given in Eq. (4.57).

The result for the $C_F C_A$ channel is obtained by combining Eq. (4.69) with the identical particle contribution in Eq. (4.40) and removing the NLL contributions so that we obtain

$$\left(\rho\frac{d\Sigma_2^{\mathrm{NNLL}}}{d\rho}\right)^{C_F C_A} = C_F C_A \left(\frac{\alpha_s}{2\pi}\right)^2 \left(16\zeta(3) - \frac{11\pi^2}{9} \right. \\ \left. - \frac{121}{6} + (6.678 \pm 0.006) - (0.7193 \pm 0.00005)\right) + \mathcal{F}^{\mathrm{clust.}}_{C_F C_A}\,, \quad (4.73)$$

where $\mathcal{F}^{\mathrm{clust.}}_{C_F C_A}$ is reported in (4.68).

Leaving aside the clustering corrections for the moment, whose soft (and collinear) origin we have already discussed, we focus on the structure of the rest of the result. It is well-known that the intensity of collinear radiation from a quark at second order in α_s is related to a coefficient in the quark form factor generally referred to as $B^{(2)}$ [192]–[195]. While there is not a unique definition of $B^{(2)}$ since it depends on the details of how the full resummation formula is organised, i.e. the resummation scheme, it is always related to the endpoint $\delta(1-z)$ contribution to the NLO DGLAP splitting functions via the form (for a quark initiated jet) [204]–[206],

$$B^{(2)} = -2\gamma_q^{(2)} + C_F b_0 X, \quad (4.74)$$

where $b_0 = \frac{1}{6}(11C_A - 4T_R n_f)$ and where $\gamma_q^{(2)}$, the DGLAP endpoint contributions for a quark jet, are [207], [208]

$$\gamma_q^{(2)} = C_F^2\left(\frac{3}{8} - \frac{\pi^2}{2} + 6\zeta(3)\right) + C_F C_A\left(\frac{17}{24} + \frac{11\pi^2}{18} - 3\zeta(3)\right) - C_F T_R n_f\left(\frac{1}{6} + \frac{2\pi^2}{9}\right). \quad (4.75)$$

We note that our analytic result for the coefficient of $C_F T_R n_f \alpha_s^2/(2\pi)^2$ in Eq. (4.72) is precisely consistent with the form in Eq. (4.74) with

$$X = \frac{2\pi^2}{3} - 7. \quad (4.76)$$

Taking this value of X we obtain a result -7.03766 for the $C_F C_A$ term in Eq. (4.74) in good agreement with the numerical value for our result in Eq. (4.73) without the clustering corrections, where we get -7.03791 ± 0.006. Finally Eq. (4.74) gives a value -5.30508 for the coefficient of C_F^2, which again agrees well with the result in Eq. (4.71) without the clustering correction, which has the numerical value -5.30556 ± 0.002. Furthermore, using the de Florian and Grazzini analytical result (Eq. (4.41)), for the identical particle gluon decay contribution, we can identify the remaining numerical contributions with analytic results i.e. the result 1.866 for the C_F^2 piece in Eq. (4.71) corresponds to $8\zeta(3) - \frac{31}{4}$ while the result 6.678 in Eq. (4.73) corresponds to $\frac{13\pi^2}{18} - 8\zeta(3) + \frac{55}{6}$.

We conclude that without the clustering corrections our NNLL results for the mMDT, as defined above, are given by the general collinear form Eq. (4.74) with the value of X specified in (4.76). Thus, excluding the clustering corrections, which are of soft origin, our NNLL result for the mMDT has a simple correspondence to the collinear order α_s^2 contribution to the quark form factor. Moreover the results for the $C_F C_A$ and $C_F T_R n_f$ channels, without the clustering correction, agree exactly with the order α_s^2 NNLL term in the expansion of the un-groomed heavy jet mass [196], [209], [210], a consequence of grooming affecting only soft emissions in the small z_{cut} limit. Finally we note that our overall results in every channel are in agreement with those from previous SCET calculations. An explicit expansion of the SCET results to order α_s^2, for the jet mass distribution, was provided in ref. [190] as this work was being finalised.[12]

4.6 Conclusions

In this work we have computed the groomed jet mass distribution at $\mathcal{O}(\alpha_s^2)$ and find full agreement with the SCET resummation of the same quantity, constituting a powerful cross check of the SCET result. In carrying out this calculation we have established a connection between the NNLL result for the groomed jet mass and standard

---

[12] Note that we have removed $\ln 2$ terms in the $C_F C_A$ and $C_F n_f$ channels present in the results of [190] via the choice of $Q^2/4$ in the scale of α_s for our leading-order result.

QCD resummation ingredients. Specifically, we recover: the scale of the coupling as expected in the soft limit, k_t, and find that this also holds in the collinear limit, as expanded upon in [211]. We also recover terms proportional to K^{CMW}, which are typically included through use of the CMW scheme for the QCD coupling. We also establish a connection between the triple collinear limit and the $B^{(2)}$ coefficient which governs the intensity of collinear radiation from a quark at second order, which emerged from a simplified treatment of the groomer where all partons were assumed to be clustered to their parent parton. We then corrected for treating the groomer in this simplified manner via the $\mathcal{F}^{\text{clust.}}$ terms. These terms originate in the soft and collinear limit without any ordering between the two emissions. Aside from being of theoretical interest, the understanding gained in this work paves the way for the NNLL resummation of groomed jet shape observables as in chapter 5. It can also be considered as a step towards addressing other collinear problems such as that involving the small jet radius limit of QCD jets [212], which has not yet been achieved at NNLL, or the inclusion of triple collinear splitting functions in an NNLL accurate parton shower. Another possible extension to this work would be to address finite z_{cut} corrections beyond NLL accuracy. Although expected to be numerically small, they may well be relevant in the context of the N^3LL resummation carried out in the SCET formalism.

Chapter 5

NNLL resummation of groomed observables

The work presented in this chapter follows on from the preceding chapter and is currently being prepared for publication by myself and collaborators: Mrinal Dasgupta and Basem El-Menoufi. As such, there will be significant overlap of text between this chapter and the forthcoming publication. As the forthcoming publication is not finalised yet, this chapter, although substantially complete, should be regarded as work in progress.

5.1 Introduction

In this chapter we present an NNLL resummed result for rIRC safe additive observables computed on jets groomed with mMDT [21], or equivalently soft drop with $\beta = 0$[23]. This builds on the work presented in the previous chapter where the NNLL structure was investigated at $\mathcal{O}(\alpha_s^2)$. As was discussed in section 3.3, observables computed on groomed jets are less sensitive to hadronisation, UE and PU than un-groomed observables, making them good candidates for direct comparisons between perturbative QCD calculations and experimental measurements. On top of this, grooming with mMDT removes any non-global logarithms (NGLs) which would be present for the same observable computed on un-groomed jets [21]. This lack of NGLs removes one of the major difficulties associated with producing precise predictions for jet shape observables. Because of these favourable properties a number of calculations have been carried out for groomed observables and compared directly to unfolded LHC data [40], [44], [46], [47], [123], [154], [213], [214].
The resummation for the groomed jet mass was first carried out in ref. [21] at NLL accuracy. This resummation was matched to NLO [44] and compared with unfolded LHC data in refs. [41], [123] which also show a comparison with an NNLL calculation carried out in the small z_{cut} limit [47] without NLO matching. This latter calculation was carried out in the SCET formalism and has since been extended to N^{3}LL accuracy by extracting the relevant anomalous dimensions from fixed-order codes [48], [190]. Although the SCET factorisation theorem has been presented for energy correlation functions [47] and angularities [49], NNLL predictions for observables other

than those equivalent to the jet mass have not, to our knowledge, been presented. Many un-groomed observables satisfy the conditions for recursive infra red and collinear safety (rIRC safety) and continuous globalness, allowing one to use the `CAESAR` and `ARES` programs to generate NLL and NNLL resummed predictions respectively. Although observables computed on groomed jets do not satisfy rIRC safety and continuous globalness, the `CAESAR` plug-in for Sherpa [46], [158], [213] does produce the correct result at NLL accuracy because, as we shall see in this work, the rIRC un-safety of groomed observables only starts to matter at NNLL accuracy.

In this work we build on the NLL resummation carried out in ref. [21] using the understanding gained from the work presented in chapter 4, combined with known NNLL results from [196], [210], to derive the resummed distribution for additive rIRC safe observables, computed on jets groomed with mMDT, up to NNLL accuracy. This is done directly in perturbative QCD, in the regime where $v \ll z_{\text{cut}} \ll 1$. Our general approach to the resummation is outlined in section 5.2 in which we show how the resummation can be computed as an inclusive piece, which is evaluated in section 5.3, and a clustering term, calculated in section 5.4. Having derived the NNLL resummed distribution for additive observables in the small z_{cut} limit, we show, in section 5.5.1, how to include the NLL accurate $\mathcal{O}(z_{\text{cut}})$ corrections first calculated in [44]. We then define our NLO matching procedure in section 5.5.2, before presenting our NNLL results including both finite z_{cut} terms at NLL accuracy and NLO matching for the heavy jet mass, width and Les Houches angularity [215], in section 5.5.3. Finally we comment on the context of our results and possible developments of this work in section 5.6.

5.2 Observable definition and approach to resummation

Our goal is to derive the cumulative distribution for additive jet shapes computed on jets groomed with mMDT, $\Sigma(v, z_{\text{cut}}) = \frac{1}{\sigma_0}\int_0^v \frac{\mathrm{d}\sigma}{\mathrm{d}v'}\mathrm{d}v'$, up to NNLL accuracy in $\ln(v)$, in the regime where $v \ll z_{\text{cut}} \ll 1$. Here v represents some jet shape observable. Taking $v < z_{\text{cut}}$ restricts us to the region where grooming is active. In this region the distribution is single logarithmic in v as the argument of soft logarithms becomes z_{cut}, whereas for $v > z_{\text{cut}}$ one finds that the distribution coincides with that of the un-groomed observable, which is double logarithmic. For phenomenological purposes it is typical to take $z_{\text{cut}} \simeq 0.1$, making resummation of $\ln(z_{\text{cut}})$ unnecessary. This hierarchy of scales also allows us to ignore terms suppressed by powers of v, z_{cut} and ${}^{v}/_{z_{\text{cut}}}$. For simplicity we work in the context of e^+e^- collisions and separate the event into two hemispheres. This separation is traditionally done by a plane perpendicular to the thrust axis, although, as we are concerned only with the soft and/or collinear limits this plane can be taken as perpendicular to the initial $q\bar{q}$ pair. We then run mMDT (defined in section 3.3) on each hemisphere and compute our observable on each of the groomed hemispheres. We then require that the larger value of the observable from the two hemispheres is less than v.

We define $V(\{\tilde{p}\},,k_1,...,k_n)$ to be a rIRC safe additive observable [69], which in the soft and collinear limit can be parametrised as

$$V_{\rm s.c}(\{\tilde{p}\},k_1,...,k_n)=\sum_{i=1}^{n}d\left(\frac{k_{ti}}{Q}\right)^{a}e^{-b\eta_i}\ , \tag{5.1}$$

where d is just a normalisation constant, $\{\tilde{p}\}$ represents the momenta of the primary $q\bar{q}$ pair and k_i are the momenta of emissions off the initial $q\bar{q}$ pair. In this work we need the groomed variant of such an observable which we write as

$$\begin{aligned}V^{\rm mMDT}(\{\tilde{p}\},k_1,...,k_n)=&\\ &\sum_{i=1}^{n}\bigg(V(\{\tilde{p}\},k_i)\Theta^{\rm mMDT}(k_i,\{\tilde{p}\},k_1,...,k_{i-1},k_{i+1},...,k_n)\bigg)\ ,\end{aligned} \tag{5.2}$$

where $\Theta^{\rm mMDT}(k_i,\{\tilde{p}\},k_1,...,k_{i-1},k_{i+1},...,k_n)=1$ if the $i^{\rm th}$ emission is retained by the groomer and zero if it is removed. It is the dependence of $\Theta^{\rm mMDT}$ on emissions other than the i^{th} that causes mMDT and, more generally, soft drop groomed observables to fail the rIRC safety condition. This is because part of rIRC safety is that the observable should scale in the same way for multiple emissions as for a single emission [69], whereas groomed observables may or may not scale at all for an emission with $z_i<z_{\rm cut}$, depending on if there is a wider angle emission with $z_j>z_{\rm cut}$.
We can then write the cumulative distribution as

$$\begin{aligned}\Sigma(v;z_{\rm cut})=&\\ &\mathcal{H}(Q)\sum_{n=0}^{\infty}\frac{1}{n!}\prod_{i=1}^{n}\int[{\rm d}^4k_i]\mathcal{M}^2(k_1,...,k_n)\Theta\left(v-V^{\rm mMDT}(\{\tilde{p}\},k_1,...,k_n)\right)\ ,\end{aligned} \tag{5.3}$$

where $\mathcal{H}(Q)$ encodes the (normalized) all orders virtual corrections to the Born process up to NNLL accuracy, $\mathcal{M}^2(k_1,...,k_n)$ is the squared matrix-element for n soft and/or collinear emissions and the factor of $\frac{1}{n!}$ is the symmetry factor for n identical particles.
The QCD resummation of this type of observable to NLL accuracy is already well known [21] and can be expressed as

$$\begin{aligned}\Sigma(v,z_{\rm cut})=&\left(1+\frac{\alpha_sC_F}{2\pi}C_1\right)\times\\ &\exp\left[-\int\frac{C_F\alpha_s^{\rm CMW}(k_t^2)}{\pi}\left(\frac{2}{z}+\gamma^0_{\rm h.c}\delta(1-z)\right){\rm d}z\frac{{\rm d}k_t^2}{k_t^2}\Theta\left(V_{\rm s.c}(z,k_t)-v\right)\right]\ .\end{aligned} \tag{5.4}$$

Where $\gamma^0_{\rm h.c}=-\frac{3}{2}$ is the endpoint of the LO DGLAP splitting function. In the above expression, use of the CMW scheme for the coupling [73], [196], [197] with its argument set to the transverse momentum squared, as opposed to just scaling with v, as well as inclusion of the C_1 term multiplying the exponential, introduces terms which are actually NNLL, but can be accommodated within the strongly ordered picture, as is also well known. The term proportional to C_1 is the difference between the full leading-order result and what is captured by the Sudakov factor.

The groomed jet mass distribution at NNLL accuracy was investigated in chapter 4, where it was demonstrated, via a fixed-order calculation, that the NNLL part of the groomed jet mass distribution not related to the strongly ordered picture is structured as an inclusive hard-collinear piece, often referred to as $B^{(2)}$ [216]–[219], plus a term accounting for the effect of the C/A clustering sequence in the grooming procedure. This motivates us to structure the resummation in a similar way, by resumming a suitably inclusive version of the groomed observable, which is added to a clustering correction to give the resummed distribution we seek. Motivated by this we define an observable, $V^{\mathrm{simp.}}(\{p\}, k_1, ..., k_n)$, computed using a *simplified groomer* which functions exactly as mMDT except that the C/A clustering sequence is replaced by one where all partons are clustered to their parent partons. The distribution (eq. (5.3)) is then written as

$$\Sigma(v; z_{\mathrm{cut}}) = \Sigma_{\mathrm{simp.}}(v; z_{\mathrm{cut}}) + \Sigma_{\mathrm{clust.}}(v; z_{\mathrm{cut}}) \ , \tag{5.5}$$

where the first contribution reads

$$\Sigma_{\mathrm{simp.}}(v; z_{\mathrm{cut}}) = \\ \mathcal{H}(Q) \sum_{n=0}^{\infty} \frac{1}{n!} \int \prod_{i=1}^{n} [\mathrm{d}^4 k_i] \mathcal{M}^2(k_1, ..., k_n) \Theta\left(v - V^{\mathrm{simp.}}(\{\tilde{p}\}, k_1, ..., k_n)\right) \quad , \tag{5.6}$$

and represents the integrated distribution computed using the inclusive groomer. The second contribution embodies the difference between the standard and inclusive groomers as follows

$$\Sigma_{\mathrm{clust.}}(v; z_{\mathrm{cut}}) = \mathcal{H}(Q) \sum_{n=0}^{\infty} \frac{1}{n!} \prod_{i=1}^{n} \int [\mathrm{d}^4 k_i] \mathcal{M}^2(k_1, ..., k_n) \\ \times \left[\Theta\left(v - V^{\mathrm{mMDT}}(\{p\}, k_1, ..., k_n)\right) - \Theta\left(v - V^{\mathrm{simp.}}(\{p\}, k_1, ..., k_n)\right)\right] \ . \tag{5.7}$$

The clustering correction starts contributing only at NNLL, and arises from the regions of phase space where the C/A declustering sequence differs from that of our simplified groomer, leading to a different set of emissions being groomed away. In the next two sections we shall describe in detail the resummation of both pieces in Eqs. (5.6) and (5.7).

5.3 The simplified groomer

In this section we compute the NNLL resummed cumulant for the simplified groomer given in Eq. (5.6). This should contain all of the structures given in eq. (5.4); the ones which stem from strongly ordered configurations of emissions, as well as hard-collinear terms which enter at $\mathcal{O}(\alpha_s^2)$, often collected together and referred to as B_2 [216]–[219]. At $\mathcal{O}(\alpha_s^2)$ the term proportional to B_2 takes the form

$$\left(\frac{\alpha_s}{2\pi}\right)^2 B_2 \int_{v^{\frac{2}{a+b}}Q^2}^{Q^2} \frac{\mathrm{d}k_t^2}{k_t^2}, \tag{5.8}$$

where a and b are defined through eq. (5.1) and it is known that [204]–[206]

$$B^{(2)} = \gamma_{hc}^{(1)} + C_F b_0 X \ , \tag{5.9}$$

where $\gamma_{hc}^{(1)}$ is the coefficient of the $\delta(1-z)$ term in the the NLO DGLAP splitting function [220], [221]:

$$\gamma_{\mathrm{h.c}}^{(1)} = C_F^2\left(\frac{3}{8} - \frac{\pi^2}{2} + 6\zeta(3)\right) + \\ C_F C_A \left(\frac{17}{24} + \frac{11\pi^2}{18} - 3\zeta(3)\right) - C_F T_R n_f \left(\frac{1}{6} + \frac{2\pi^2}{9}\right) \ , \tag{5.10}$$

$b_0 = \frac{1}{6}(11C_A - 4T_R n_f)$ and X is an observable dependent coefficient. This term was identified, for the groomed jet mass, via an NLO calculation in chapter 4, which found $X = \frac{2\pi^2}{3} - 7$, which is the same as for the un-groomed case [209], [210], as one might expect as hard emissions are not affected by grooming. We note that at our prescribed level of accuracy there is some freedom in how these terms are included in the resummation, i.e. whether on not they are exponentiated.

The $\gamma_{hc}^{(1)}$ term is universal to all observables and is just part of the quark form factor [202], [204]. It should therefore sit in the hard-collinear part of the Sudakov radiator as it does for un-groomed observables [196], which reads

$$R^{\mathrm{h.c}}(v) = \int_{v^{\frac{2}{a+b}}Q^2}^{Q^2} \frac{C_F \alpha_s(k_t^2)}{\pi}\left(\gamma_{\mathrm{h.c}}^{(0)} + \frac{\alpha_s(k_t^2)}{2\pi}\gamma_{\mathrm{h.c}}^{(1)}\right)\frac{\mathrm{d}k_t^2}{k_t^2} \ , \tag{5.11}$$

and is unchanged by grooming. Note that the coupling should be evaluated at two-loop accuracy in order to capture all NNLL terms. The soft part of the Sudakov radiator is almost exactly the same as the NLL result for groomed observables [21], with the modification that the coupling is evaluated at two-loop accuracy using the CMW scheme:

$$R^{\mathrm{s}}(v, z_{\mathrm{cut}}) = \int_0^1 \int_0^{z^2Q^2} \frac{\alpha_s(k_t)}{\pi}\left(\frac{2}{z}\left(1 + \frac{\alpha_s(k_t^2)K_{CMW}}{2\pi}\right)\right. \\ \left.\Theta(z - z_{\mathrm{cut}})\Theta\left(k_t^2 - v^{\frac{2}{a+b}} z_{\mathrm{cut}}^{\frac{2b}{a+b}} Q^2\right)\frac{\mathrm{d}k_t^2}{k_t^2}\mathrm{d}z \ , \tag{5.12}$$

where the upper limit on the k_t^2 integral is due to computing the radiator for a single hemisphere ($0 < \eta < \infty$), and a factor of two is included to account for the opposite hemisphere. The complete Sudakov radiator is then:

$$R(v, z_{\text{cut}}) = R^{\text{s}}(v, z_{\text{cut}}) + R^{\text{h.c}}(v) \ . \tag{5.13}$$

We now discuss how the the observable dependent piece of the hard-collinear terms proportional to $b_0 X$ are included in the resummation. As already stressed, the hard-collinear pieces of the resummation are the same as for un-groomed observables and so can be re-summed using the same methods. By examining refs. [196], [210], we can see that the hard-collinear $b_0 X$ term is related to the leading-order result and can be found by computing the C_1 term of eq. (5.4) with the argument of the coupling set to k_t^2 [1]. The C_1 term was calculated for the heavy hemisphere mass in chapter 4 which found $C_1 = -2\ln 2\left(4\ln\frac{1}{z_{\text{cut}}} - 3\right) - 1$. So as to reduce the number of terms in equations we use the definition $\rho = \frac{M_{\text{H}}^2}{Q^2}$ as opposed to $\rho = \frac{4M_{\text{H}}^2}{Q^2}$ as this removes the factors of $\ln(2)$ so that $C_1 = -1$. If we absorb the factor of $\frac{C_F \alpha_s}{2\pi}$ into the definition of C_1 and repeat this calculation with the argument of the coupling set to k_t we find [2]:

$$\begin{aligned} C^{\text{r.c}}(\rho) &= \frac{C_F}{2\pi}\left(\alpha_s(\rho Q^2)\left(7 - \frac{2\pi^2}{3}\right) + \alpha(z_{\text{cut}}^2 Q^2)\left(\frac{-\pi^2}{2}\right) + \alpha_s(Q^2)\left(\frac{7\pi^2}{6} - 8\right)\right) \\ &\simeq -\frac{C_F \alpha_s(Q^2)}{2\pi} + C_F\left(\frac{\alpha_s(Q^2)}{2\pi}\right)^2 b_0 \left(\frac{2\pi^2}{3} - 7\right)\ln(\rho) + \text{N}^3\text{LL} + \mathcal{O}(\alpha_s^3) \ , \end{aligned} \tag{5.14}$$

which exactly reproduces both the C_1 and $b_0 X = b_0(\frac{2\pi^2}{3} - 7)$ terms identified in chapter 4. Use of the running coupling also results in a term where the argument of the coupling in the final result is proportional to z_{cut}. Expanding this term in powers of $\alpha_s(Q^2)$ results in terms which are N^3LL and beyond. We are therefore free to set $\alpha_s(z_{\text{cut}}^2 Q^2) \to \alpha_s(Q^2)$ within NNLL accuracy.

Due to its dependence on the details of an observable's definition in the hard-collinear limit it is not as simple to write down a general result for $C^{\text{r.c}}(v)$ as it is for the radiator. However, all that is required is, in essence, a leading-order calculation. An example of this is given in section 5.3.1 where we compute $C^{\text{r.c}}(v)$ for the angularities with respect to the winner takes all (WTA) axis, although the method can be applied to any observable which is rIRC safe.

We now consider the effect of multiple emissions. The key point here is that it is possible to drop any emission with $z_i < z_{\text{cut}}$ from $V^{\text{simp.}}(\{\tilde{p}\}, k_1, ..., k_n))$ whilst only neglecting power corrections in v and z_{cut}, as is proven in appendix B.1[3]. By partitioning the energy fraction integrals into regions where $z < z_{\text{cut}}$ and $z > z_{\text{cut}}$, the virtual

---

[1] In ARES [196], [210] the functions $C_{\text{h.c}}^1$ and $\delta\mathcal{F}_{\text{rec}}$ reproduce our $b_0 X$ term and parts of C_1.

[2] see section 5.3.1 for an example of how this calculation is carried out.

[3] We stress that this only applies to the simplified groomer and not to the clustering correction.

corrections can be expressed as

$$\mathcal{H}(Q) = (1 + H_1(Q))\times \\ \exp\left[-\int_0^1 R'(v', z_{\text{cut}})\frac{\mathrm{d}v'}{v'} - \int \frac{\alpha_s^{\text{CMW}}(k_t^2)}{\pi}\frac{2}{z}\mathrm{d}z\frac{\mathrm{d}k_t^2}{k_t^2}\Theta(z_{\text{cut}} - z)\right] , \quad (5.15)$$

where $H_1(Q)$ is the finite part of the one loop virtual correction to the Born process which is absorbed into $C^{\text{r.c}}(v)$, and $R'(v, z_{\text{cut}}) = -\frac{\mathrm{d}R(v,z_{\text{cut}})}{\mathrm{d}\ln(v)}$. The energy fraction integrals are partitioned the same way for real emissions. We can then write $\Theta(v - V^{\text{simp.}}(\{\tilde{p}\}, k_1, ..., k_n))$ as its Laplace representation and drop from it any emissions with $z_i < z_{\text{cut}}$ to write

$$\Sigma_{\text{simp}}(v, z_{\text{cut}}) = (1 + C^{\text{r.c}}(v)) \\ \exp[-\int_0^1 R'(v')\frac{\mathrm{d}v'}{v'} - \int \frac{\alpha_s^{\text{CMW}}(k_t^2)}{\pi}\frac{2}{z}\mathrm{d}z\frac{\mathrm{d}k_t^2}{k_t^2}\Theta(z_{\text{cut}} - z)] \int_c \frac{\mathrm{d}\nu}{2\pi i\nu}e^{-\nu v} \\ \sum_{n=0}^{\infty}\frac{1}{n!}\left(\int_0^v R'(v', z_{\text{cut}})e^{\nu v'}\frac{\mathrm{d}v'}{v'} + \int \frac{\alpha_s^{\text{CMW}}(k_t^2)}{\pi}\frac{2}{z}\mathrm{d}z\frac{\mathrm{d}k_t^2}{k_t^2}\frac{\mathrm{d}\phi_i}{2\pi}\Theta(z_{\text{cut}} - z)\right)^n , \quad (5.16)$$

noting the absence of a factor of $e^{-\nu v'}$ from the term accounting for real emissions with $z < z_{\text{cut}}$, as real emissions have been dropped from the observable in this region of phase space. This can then be evaluated using what are now standard techniques [222] to give

$$\Sigma_{\text{simp}}(v, z_{\text{cut}}) = (1 + C^{\text{r.c}}(v))\frac{\exp\left[-R(v, z_{\text{cut}}) - \gamma_E R'(v, z_{\text{cut}})\right]}{\Gamma[1 + R'(v, z_{\text{cut}})]} . \quad (5.17)$$

Here we can see that the emissions which are softer than z_{cut} have cancelled completely against the corresponding virtual corrections. By expanding $\frac{\exp[-\gamma_E R'(v)]}{\Gamma[1+R'(v)]}$, we find that, as $R(v)$ is single logarithmic, this factor is actually N^{3}LL and so can be neglected, giving a remarkably simple NNLL result of

$$\Sigma_{\text{simp}}(v, z_{\text{cut}}) = (1 + C^{\text{r.c}}(v))\exp[-R(v, z_{\text{cut}})] . \quad (5.18)$$

This result bears a strong resemblance to the NLL result of [21]. The NLL result is recovered if one neglects the $C^{\text{r.c}}(v)$ term as well as the $\gamma_{\text{h.c}}^{(1)}$ and K_{CMW} terms in the Sudakov factor.

We now discuss how the above result for $\Sigma_{\text{simp}}(v, z_{\text{cut}})$ is related to NNLL resummations of un-groomed observables as carried out using `ARES` [210]. The Sudakov factor reported in eq. (5.13) has the same structure as that given in [196], the only differences being the boundary of the energy fraction integrals and that here there is no $K^{(2)}$ term in the soft physical coupling as this would be N^{3}LL. Our $C^{\text{r.c}}(v)$ function is related to the terms $H^1(Q)$, $\delta\mathcal{F}^{\text{rec}}$, C_{hc}^1, and $\delta\mathcal{F}^{\text{wa}}$ in [210], although $\delta\mathcal{F}^{\text{wa}}$ would be zero for groomed observables as groomed observables do not differ from their soft and collinear parametrisation in the soft wide angle region of phase space. As `ARES` is not formulated for groomed observables it should not be expected to, and indeed does not, completely reproduce $C^{\mathrm{r.c}}(v)$. The `ARES` terms $\mathcal{F}^{\mathrm{NLL}}$, $\delta\mathcal{F}^{\mathrm{h.c}}$ and $\delta\mathcal{F}^{\mathrm{s.c}}$ are related to multiple emission effects which we have shown start at $\mathrm{N^3LL}$ for the observables considered in this work, although they could come into play at NNLL for non-additive observables such as the broadening [223]. Finally, for un-groomed observables one should, at NNLL accuracy, correct for the inclusive treatment of correlated emissions for a single correlated pair, giving a correction starting at $\alpha_s^2\ln(v)$ which in `ARES` is called $\delta\mathcal{F}_{\mathrm{correl.}}$. This logarithm is of soft origin and for groomed observables is replaced by a logarithm of z_{cut}, making the correction $\mathrm{N^3LL}$.

5.3.1 Calculating $C^{\mathrm{r.c}}(v)$

We now turn our attention to illustrating more precisely what is captured by the function $C^{\mathrm{r.c}}(v)$ and how it can be calculated. $C^{\mathrm{r.c}}(v)$ is the difference between the leading-order result, computed with the argument of the coupling set to k_t^2, and what is found by expanding the Sudakov factor to $\mathcal{O}(\alpha_s)$. Rather than carrying out the full leading-order calculation and expanding the Sudakov factor, we can equivalently calculate the difference between the real contribution to the leading-order result and the part of this that is exponentiated and add to this $H_1(Q) = \frac{C_F\alpha_s}{2\pi}(\frac{7\pi^2}{6} - 8)$, the piece of the leading-order virtual corrections that are not included in the Sudakov factor, to write

$$C^{\mathrm{r.c}}(v) = H_1(Q) + \int [\mathrm{d}^{4-2\epsilon}k]\mathcal{M}^2(k;\epsilon)\Theta\left(v - V^{\mathrm{mMDT}}(\{\tilde{p}\},k)\right) - \\ \int_0^1\int_0^{z^2Q^2} \frac{C_F\alpha_s(k_t^2)}{\pi}\left(\frac{2}{z^{1+2\epsilon}} + \gamma_{\mathrm{h.c}}^{(0)}\delta(1-z)\right)\frac{\mathrm{d}k_t^2}{k_t^{2(1+\epsilon)}}\mathrm{d}z\Theta\left(v - V_{\mathrm{s.c}}^{\mathrm{mMDT}}(\{\tilde{p}\},z,k_t)\right)\ . \tag{5.19}$$

This calculation is carried out in $4-2\epsilon$ dimensions as the two integrals are separately divergent, however the difference is finite in four dimensions. The integral on the first line is the real contribution to the leading order result, with the argument of the coupling set to k_t^2, while the second line is the part of the real $\mathcal{O}(\alpha_s)$ result which is exponentiated, where the argument of the coupling is retained as k_t^2.
Although eq. (5.19) cannot be evaluated in a completely general manner, all that is required is a leading-order calculation, which can be carried out without too much difficulty. We now evaluate $C^{\mathrm{r.c}}(v)$ for the angularities [130], [224] with respect to the WTA axis [27], which are defined for e^+e^- colliders as [196], [224]

$$\lambda_\beta^1 = \frac{\sum_i E_i|\sin(\theta_i)|^{2-\beta}(1-|\cos(\theta_i)|)^{\beta-1}}{\sum_i E_i}\ , \tag{5.20}$$

where the sum runs over all particles in the hemisphere after grooming and θ_i is the angle between a particle and the WTA axis. In the soft and collinear approximation these observables can be parametrised as per eq. (5.1) with $a = 1$ and $b = \beta - 1$.

Evaluating $C^{\text{r.c}}(v)$ is achieved most simply by considering the region of phase space where the gluon is retained by the groomer ($z > z_{\text{cut}}$) separately from the region where it is removed ($z < z_{\text{cut}}$), as when it is retained it can be treated in the collinear limit, whilst when it is removed it can be treated as soft, up to power corrections in z_{cut}, which we neglect. The soft part of eq. (5.19) is then given by

$$
\begin{aligned}
&C^{\text{r.c}}_{\text{soft}}(v) = \\
&\int_0^{z_{\text{cut}}} \frac{\alpha_s(Q)C_F}{\pi}\frac{2\mathrm{d}z}{z^{1+2\epsilon}}\left(\int_0^1 \frac{e^{-\epsilon\gamma_E}}{\Gamma[1-\epsilon]}\frac{2^{1+2\epsilon}\mathrm{d}\cos(\theta)}{(1+\cos(\theta))^{1+\epsilon}(1-\cos(\theta))^{1+\epsilon}} - \int_0^1 \frac{\mathrm{d}u}{u^{1+\epsilon}}\right) \\
&\qquad\qquad = \frac{\alpha_s(Q)C_F}{2\pi}\left(\frac{-\pi^2}{2}\right) , \qquad (5.21)
\end{aligned}
$$

where $u = \frac{k_t^2}{z^2Q^2}$ and we have set the argument of the coupling to Q^2 as setting it to k_t^2 only gives rise to logarithms of z_{cut} which we have argued will be N^{3}LL. This part of the calculation is the same for any observable.

For the collinear part of eq. (5.19) we need an expression for the observable in the presence of a single collinear emission, which for the angularities with respect to the WTA axis reads

$$
\lambda^1_\beta = \frac{\min(z,1-z)}{(z(1-z))^\beta}\left(\frac{k_t}{Q}\right)^\beta . \qquad (5.22)
$$

The collinear part of eq. (5.19) is then[4]

$$
\begin{aligned}
C^{\text{r.c}}_{\text{col.}}(v) = &\int_0^{Q^2}\int_{z_{\text{cut}}}^1 \frac{\alpha_s(k_t^2)}{\pi}P_{gq}(z;\epsilon)\Theta\left(\lambda^1_\beta - \frac{\min(z,1-z)}{(z(1-z))^\beta}\left(\frac{k_t}{Q}\right)^\beta\right)\mathrm{d}z\frac{\mathrm{d}k_t^2}{k_t^{2(1+\epsilon)}} \\
&- \int_0^{Q^2}\int_{z_{\text{cut}}}^1 \frac{\alpha_s(k_t^2)C_F}{\pi}\left(\frac{2}{z} - \gamma_0^{\text{h.c}}\delta(1-z)\right)\mathrm{d}z\Theta\left(\lambda^{\frac{2}{\beta}}z^{2\frac{\beta-1}{\beta}}Q^2 - k_t^2\right)\frac{\mathrm{d}k_t^2}{k_t^{2(1+\epsilon)}} . \qquad (5.23)
\end{aligned}
$$

To evaluate this within NNLL accuracy, we can make the approximation [210] that

$$
\alpha_s\big(k_t^2\big) \simeq \alpha_s\big(\lambda^{\frac{2}{\beta}}Q^2\big) , \qquad (5.24)
$$

or more generally, for any rIRC safe observable,

$$
\alpha_s\big(k_t^2\big) \simeq \alpha_s\big(v^{\frac{2}{a+b}}Q^2\big) , \qquad (5.25)
$$

where a and b are defined through eq. (5.1). This can be justified by making the change of variables $k_t^2 \to \zeta = \frac{1}{v}\frac{d}{z^b}\left(\frac{k_t}{Q}\right)^{a+b}$, so that $\alpha_s(k_t^2)$ becomes $\alpha_s\left(\left(\frac{z^b\zeta v}{d}\right)^{\frac{2}{a+b}}\right)$, and arguing that, for rIRC safe observables, the integral is dominated by values of ζ close to 1 [210]. Expanding $\alpha_s\left(\left(\frac{z^b\zeta v}{d}\right)^{\frac{2}{a+b}}\right)$ about $\zeta = 1$, one finds that terms beyond the zeroth order correspond to corrections to eq. (5.25) which are at least

---

[4] This piece of the calculation is equivalent to evaluating the functions C^1_{hc} and $\delta\mathcal{F}^{\text{rec}}$ in [210].

N^{3}LL. With this in hand we can now evaluate eq. (5.24) to find

$$C^{\mathrm{r.c}}_{\mathrm{col.}}(v) = \frac{C_F\alpha_s\left(\lambda^{\frac{2}{\beta}}Q^2\right)}{2\pi}\left(-\frac{6}{\beta}+\frac{2\pi^2}{3\beta}-\frac{6\ln(2)}{\beta}-\frac{4\pi^2}{3}+13\right)\,. \tag{5.26}$$

Adding together eq. (5.21), eq. (5.26) and H^1, we can then write the expression for $C^{\mathrm{r.c}}(v)$ for the angularities with respect to the WTA axis:

$$\begin{aligned}&C^{\mathrm{r.c}}(v) = \\ &\frac{C_F}{2\pi}\left(\alpha_s(\lambda^{\frac{2}{\beta}}Q^2)\left(-\frac{6}{\beta}+\frac{2\pi^2}{3\beta}-\frac{6\ln(2)}{\beta}-\frac{4\pi^2}{3}+13\right)+\alpha_s(Q^2)\left(\frac{2\pi^2}{3}-8\right)\right)\,.\end{aligned} \tag{5.27}$$

Expanding this to second order in powers of $\alpha_s(Q^2)$ we find

$$\begin{aligned}C^{\mathrm{r.c}}(v) = {}&\frac{C_F\alpha_s(Q^2)}{2\pi}\left(5-\frac{6}{\beta}+\frac{2\pi^2}{3}\left(\frac{1}{\beta}-1\right)-\frac{6\ln(2)}{\beta}\right)\\ &-\frac{C_F\alpha_s^2(Q^2)}{2\pi}\beta_0\ln\left(\lambda^{\frac{2}{\beta}}\right)\left(-\frac{6}{\beta}+\frac{2\pi^2}{3\beta}-\frac{6\ln(2)}{\beta}-\frac{4\pi^2}{3}+13\right)\,,\end{aligned} \tag{5.28}$$

which contains a leading order term, $C_1 = \left(5-\frac{6}{\beta}+\frac{2\pi^2}{3}\left(\frac{1}{\beta}-1\right)-\frac{6\ln(2)}{\beta}\right)$, and an NLO piece, $\beta_0 X$, with $X = -\left(-\frac{6}{\beta}+\frac{2\pi^2}{3\beta}-\frac{6\ln(2)}{\beta}-\frac{4\pi^2}{3}+13\right)$, which forms part of the hard-collinear coefficient B_2.

5.4 The clustering correction

We now turn our attention to the clustering correction which is given by

$$\begin{aligned}\Sigma^{\mathrm{clust.}}(v, z_{\mathrm{cut}}) = \mathcal{H}(Q)\sum_{n=0}^{\infty}\frac{1}{n!}\prod_{i=1}^{n}\int[\mathrm{d}^4k_i]\mathcal{M}^2(k_1,...,k_n)\times\\ [\Theta(v > V^{\mathrm{mMDT}}(\{p\},k_1,...,k_n)) - \Theta(v > V^{\mathrm{simp.}}_{\mathrm{sc}}(\{p\},k_1,...,k_n))],\end{aligned} \tag{5.29}$$

which is added to eq. (5.18) to give $\Sigma(v, z_{\mathrm{cut}})$ as in eq. (5.3). It is in this part of the calculation where the lack of rIRC safety of groomed observables plays a role. This is because, as we shall see, the clustering correction is generated as a result of the observable's scaling with the momentum of one emission depending on the momentum of another.

5.4.1 Independent emission clustering correction

As there are some differences between the clustering corrections for independent and correlated emissions we will first compute $\Sigma^{\mathrm{clust.}}(v, z_{\mathrm{cut}})$ considering only independent emissions. Here independent emissions refers to soft emissions from the born parton i.e. primary emissions, whereas correlated emissions are those which originate from

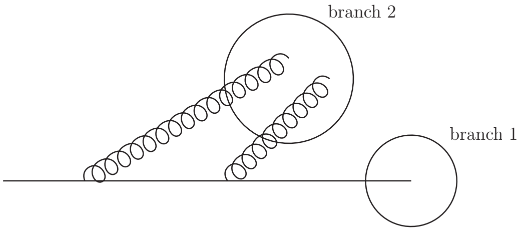

Figure 5.1. The configuration responsible for the independent emission clustering correction, where two soft emissions with $z_i < z_{\text{cut}}$ are de-clustered from the parent parton as a single branch which as a whole passes the z_{cut} condition.

the branching of a primary emission and so carry either a $C_F C_A$ of $C_F T_R n_f$ colour factor. The calculation is carried out considering emissions in a single hemisphere, with a factor of two provided to account for the opposite hemisphere. This piece accounts for the fact that gluons softer than z_{cut}, which in the previous section were always treated as being groomed away, can be retained by the groomer, when, due to the C/A clustering sequence, they are examined for the z_{cut} condition as part of a branch containing another independent soft gluon. This configuration is depicted at $\mathcal{O}(\alpha_s^2)$ in figure 5.1 and was calculated at this order in section 4.4.1.

As per eq. (5.29), the clustering correction $\Sigma^{\text{clust.}}(v, z_{\text{cut}})$ is proportional to

$$\Theta(v - V^{\text{mMDT}}(\{p\}, k_1, ..., k_n)) - \Theta(v - V^{\text{simp.}}_{\text{sc}}(\{p\}, k_1, ..., k_n)) \; . \tag{5.30}$$

Considering only independent emissions, this quantity is only non zero when there is a branch of the C/A clustering sequence containing two or more emissions which:

- would individually be groomed away
- collectively pass the grooming condition
- set a value of the observable larger than the cut on it: $V^{\text{mMDT}}(\{p\}, k_1, ..., k_n) > v$,

resulting in these emissions being allowed by our simplified groomer when in fact they should be vetoed. This corresponds to the region of phase space where $V^{\text{mMDT}}(\{p\}, k_1, ..., k_n) > v$, but $V^{\text{simp.}}_{\text{sc}}(\{p\}, k_1, ..., k_n) < v$, so that the combination of step functions in eq. (5.30) is equal to -1. This region of phase space is illustrated on a Lund diagram in figure 5.2. For such a branch to be examined by the groomer, all branches at wider angles must be softer than z_{cut} and thus groomed away.

At NNLL accuracy it is sufficient to consider that this branch contains two emissions, which we label α and β. We will first compute the clustering correction assuming that this is valid before showing that higher numbers of emissions in a branch

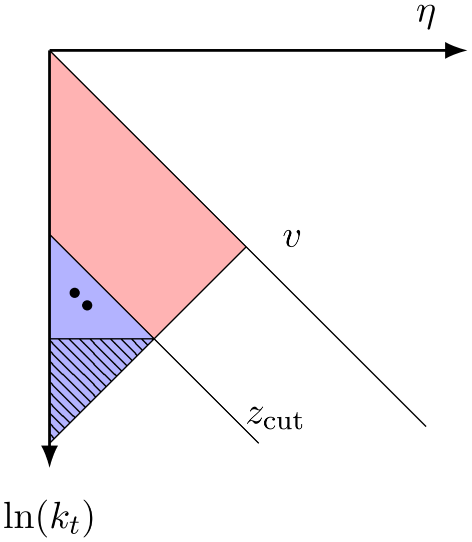

Figure 5.2. Lund diagram showing the region of phase space responsible for the independent emission clustering correction in blue. The region shown in red is the vetoed phase space responsible for the Sudakov factor. The two dots represent possible locations in the phase space for the pair of emissions which generate the clustering correction. Discussion of the hashed area, which contributes in principle to the clustering correction but turns out only to beyond NNLL accuracy, is postponed to later in this section.

correspond to corrections at higher logarithmic accuracy. We define the function

$$\begin{aligned}\Theta^{\mathrm{Ind.}}_{\mathrm{clust.}} = {}& \Theta(\theta_\alpha - \theta_{\alpha,\beta})\Theta(\theta_\beta - \theta_{\alpha,\beta})\times \\ & \Theta(z_{\mathrm{cut}} - z_\alpha)\Theta(z_{\mathrm{cut}} - z_\beta)\Theta(z_\alpha + z_\beta - z_{\mathrm{cut}})\Theta(V^{\mathrm{mMDT}}(\{p\}, k_\alpha, k_\beta) - v)\ , \quad (5.31)\end{aligned}$$

where θ_α is the angle between the quark and α, with θ_β defined similarly and $\theta_{\alpha,\beta}$ is the angle between partons α and β. Provided we also ensure that the groomer examines the branch containing α and β, $\Theta^{\mathrm{Ind.}}_{\mathrm{clust.}}$ isolates the region of phase space which generates the clustering correction. Requiring that $V^{\mathrm{simp.}}_{\mathrm{sc}}(\{p\}, k_1, ..., k_n) < v$ guarantees that the groomer will examine the α, β branch as this forces any emissions with $z_i > z_{\mathrm{cut}}$ to be at smaller angles than the pair responsible for the clustering correction. Emissions other than α and β with $z_i < z_{\mathrm{cut}}$ can be dropped from $V^{\mathrm{simp.}}_{\mathrm{sc}}(\{p\}, \{k_j\})$ as in section 5.3. We can then write

$$\begin{aligned}\Sigma^{\mathrm{clust.}}_{\mathrm{Ind.}}(v, z_{\mathrm{cut}}) = {}& -\mathcal{H}(Q)\frac{1}{2!}\int \mathcal{M}^2_{\mathrm{s.c}}(k_\alpha)\mathcal{M}^2_{\mathrm{s.c}}(k_\beta)[\mathrm{d}^4k_\alpha][\mathrm{d}^4k_\beta]\Theta^{\mathrm{Ind.}}_{\mathrm{clust.}}\sum_{n=0}^{\infty}\frac{1}{n!} \\ & \prod_{j=0}^{n}\int[\mathrm{d}^4k_j]\mathcal{M}^2_{\mathrm{c}}(k_j)\big\{\Theta(z_{\mathrm{cut}} - z_j) + \Theta(z_j - z_{\mathrm{cut}})\Theta\left(v - V^{\mathrm{simp.}}_{\mathrm{sc}}(\{p\}, \{k_j\})\right)\big\}, \quad (5.32)\end{aligned}$$

where $\mathcal{M}_{\mathrm{c}}[\mathrm{d}^4k] = \frac{C_F\alpha_s(k_t^2)}{\pi}\left(\frac{2}{z} + \gamma^0_{\mathrm{h.c}}\delta(1-z)\right)\mathrm{d}z\frac{\mathrm{d}k_t^2}{k_t^2}$, and $\mathcal{M}_{\mathrm{s.c}}[\mathrm{d}^4k] = \frac{C_F\alpha_s(k_t^2)}{\pi}\left(\frac{2\mathrm{d}z}{z}\right)\frac{\mathrm{d}k_t^2}{k_t^2}$, the matrix element for a soft and collinear emission. The real emissions labelled with j, i.e. the ones not responsible for generating the clustering correction, can then be combined with $\mathcal{H}(Q)$ to give.

$$\Sigma^{\text{clust.}}_{\text{Ind.}}(v, z_{\text{cut}}) = \mathcal{F}^{\text{Ind.}}_{\text{clust.}} \exp[-R(v, z_{\text{cut}})], \tag{5.33}$$

where

$$\begin{aligned}\mathcal{F}^{\text{Ind.}}_{\text{clust.}} &= -\int \frac{1}{2!}\mathcal{M}^2_{\text{s.c}}(k_\alpha)\mathcal{M}^2_{\text{s.c}}(k_\beta)[\mathrm{d}^4k_\alpha][\mathrm{d}^4k_\beta]\Theta^{\text{Ind.}}_{\text{clust.}} \\ &= -C_F^2\int \frac{\alpha_s(k_{t\alpha})}{\pi}\frac{\alpha_s(k_{t\beta})}{\pi}\frac{2\mathrm{d}z_\alpha}{z_\alpha}\frac{2\mathrm{d}z_\beta}{z_\beta}\frac{\Delta^{-\frac{1}{2}}}{2\pi}\mathrm{d}\theta^2_{\alpha,\beta}\frac{\mathrm{d}\theta^2_\beta}{\theta^2_\beta}\frac{\mathrm{d}\theta^2_\alpha}{\theta^2_\alpha}\Theta_{\text{clust}}\Theta(\Delta)\Theta(\theta_\alpha-\theta_\beta)\ .\end{aligned} \tag{5.34}$$

In the above equation $\Delta = 4\theta^2_\alpha\theta^2_\beta - (\theta^2_{\alpha,\beta} - \theta^2_\alpha - \theta^2_\beta)^2$ is the Gram determinant [225], [226] and we have used the symmetry between partons α and β to eliminate $\frac{1}{2!}$ in favour of $\Theta(\theta_\alpha - \theta_\beta)$. For the jet mass, this is just the NLL Sudakov factor, multiplied by the NLO clustering correction calculated in chapter 4, where the argument of the coupling has been set to the transverse momentum of the emission it is associated with.

Factorising the clustering correction from the Sudakov factor in this way allows one to write the full resummed distribution as

$$\Sigma(v, z_{\text{cut}}) = (1 + C^{\text{r.c}}(v) + \mathcal{F}_{\text{clust.}})e^{-R(v,z_{\text{cut}})}\ , \tag{5.35}$$

where $R(v, z_{\text{cut}})$ is the NNLL Sudakov factor from section 5.3 and we have anticipated a similar factorisation for the correlated emission clustering correction and grouped the clustering terms together as $\mathcal{F}_{\text{clust.}} = \mathcal{F}^{\text{ind.}}_{\text{clust.}} + \mathcal{F}^{\text{Cor.}}_{\text{clust.}}$. We note that this compact way of writing the result introduces N^{3}LL terms through the interplay of the clustering correction with NNLL terms in the Sudakov factor.

Returning to evaluate the clustering correction, we can make two approximations: firstly, making the replacement $\alpha_s(k_{t\beta}) \to \alpha_s(k_{t\alpha})$ is equivalent to integrating over the phase space of emission β and dropping terms which are beyond NNLL accuracy [5]; secondly we can drop the contribution of emission β to the observable, $V(\{p\}, k_\alpha, k_\beta) \to V(\{p\}, k_\alpha)$. The latter results only in the neglect of terms which do not contain a logarithm of ρ, and so are N^{3}LL or are suppressed by powers of z_{cut}, which are neglected. This can be seen most easily at fixed coupling by exchanging the integral over θ^2_α for an integral over v and neglecting terms which are not singular as z_β or θ^2_β are taken to zero [6]. We can now evaluate the integrals over θ_β and

---

[5] We have checked this by expanding $\alpha_s(k_{t\beta}) \simeq \alpha_s(Q)\left(1+\beta_0\alpha_s(Q)\ln(\frac{k_{t\beta}}{Q})\right)$, evaluating the integrals over $z_\alpha, z_\beta, \theta^2_{\alpha,\beta}$ and θ^2_β and observing that the logarithm of k_β becomes a logarithm of $k_{t\alpha}$. Any additional terms not accounted for in our prescription are just a constant with an additional power of $\alpha_s(Q)$ and so are N^{3}LL.

[6] We have also verified this numerically for the heavy hemisphere mass without any approximations beyond use of the collinear limit.

$\theta_{\alpha,\beta}$ to obtain

$$\mathcal{F}^{\text{Ind.}}_{\text{clust.}} = -\frac{8}{\pi}\text{Cl}_2\left(\frac{\pi}{3}\right)\Bigg(\int_{\max(k_t, \frac{k_t^{\frac{a+b}{b}}}{v^{\frac{1}{b}}})}^{z_{\text{cut}}} \frac{\mathrm{d}z_\alpha}{z_\alpha}\int_{z_{\text{cut}}-z_\alpha}^{z_{\text{cut}}} \frac{\mathrm{d}z_\beta}{z_\beta}\int_{(vz_{\text{cut}}^b)^{\frac{2}{a+b}}Q^2}^{z_{\text{cut}}^2 Q^2} \left(\frac{\alpha_s(k_{t\alpha})}{2\pi}\right)^2 \frac{\mathrm{d}k_{t\alpha}^2}{k_{t\alpha}^2}$$
$$+\,\Theta(b)\int_{k_{t\alpha}}^{\frac{k_{t\alpha}^{\frac{a+b}{b}}}{v^{\frac{1}{b}}}} \frac{\mathrm{d}z_\alpha}{z_\alpha}\int_{z_{\text{cut}}-z_\alpha}^{z_{\text{cut}}} \frac{\mathrm{d}z_\beta}{z_\beta}\int_{v^{\frac{2}{a}}Q^2}^{(vz_{\text{cut}}^b)^{\frac{2}{a+b}}Q^2} \left(\frac{\alpha_s(k_{t\alpha})}{2\pi}\right)^2 \frac{\mathrm{d}k_{ta}^2}{k_{ta}^2}\Bigg)\,, \quad (5.36)$$

where we have made use of the soft and collinear parametrisation of the observable in terms of a and b given in eq. (5.1). The integral in the last line corresponds to the phase space indicated by the hashed region in figure 5.2 and does not contribute at NNLL. It is therefore neglected from here on, and the remaining integrals evaluated, neglecting power corrections, to give

$$\mathcal{F}^{\text{Ind.}}_{\text{clust.}} = -\left(\frac{\alpha_s(Q^2)C_F}{2\pi}\right)^2 \frac{4\pi}{3}\text{Cl}_2\left(\frac{\pi}{3}\right)\times$$
$$\frac{\ln\left(z_{\text{cut}}^{\frac{2}{a+b}}\, v^{\frac{-2}{a+b}}\right)}{(1+\beta_0\alpha_s(Q^2)\ln(v^{\frac{2}{a+b}}z_{\text{cut}}^{\frac{2b}{a+b}}))(1+\beta_0\alpha_s(Q^2)\ln z_{\text{cut}}^2)}\,. \quad (5.37)$$

At leading order $\mathcal{F}^{\text{Ind.}}_{\text{clust.}}$ contains the NNLL term [7] $\left(\frac{\alpha_s(Q^2)C_F}{2\pi}\right)^2 \frac{2\pi}{3}\text{Cl}_2\left(\frac{\pi}{3}\right)\ln(v^{\frac{2}{a+b}})$ as well as an N^{3}LL term proportional to $\alpha_s(Q^2)^2\ln(z_{\text{cut}})$. It also contains NNLL terms to all orders due to the running coupling which generates the term in the denominator proportional to $\alpha_s(Q^2)\beta_0\ln(v^{\frac{2}{a+b}})$. The running coupling also generates the terms in the denominator proportional to $\ln(z_{\text{cut}})$ which start at N^{3}LL. This tells us that it is not really important that the argument of each factor of the coupling is precisely the transverse momentum of the emission it is associated with, only that it scales with the observable as $v^{\frac{2}{a+b}}$. Within NNLL accuracy we could set $z_{\text{cut}} \to 1$ in eq. (5.37) so as to eliminate terms beyond NNLL accuracy [8].

We have shown that a sub-jet consisting of two independent emissions, a and b, generates a correction with a single collinear logarithm of the observable, and that for this to happen

$$z_\alpha, z_\beta < z_{\text{cut}} \ \text{ and } \ z_\alpha + z_\beta > z_{\text{cut}} \quad (5.38)$$

must be satisfied. The generalisation of this to three emissions, α, β, γ, is that

$$\begin{aligned} z_i &< z_{\text{cut}} \\ z_i + z_j &< z_{\text{cut}}\ , \quad i \neq j \\ z_\alpha + z_\beta + z_\gamma &> z_{\text{cut}}\ , \end{aligned} \quad (5.39)$$

where $i, j \in \alpha, \beta, \gamma$. As all three emissions are constrained to be at similar angles, this configuration can have only one logarithm of the observable and so is N^{3}LL. A

---

[7] This term has been checked using `Event2`[227], [228] for the jet mass, width and Les Houches angularity. It also agrees with the collinear $\mathcal{O}(\alpha_s^2)$ calculation carried out in chapter 4.

[8] In practice we have retained these NNLL $\ln z_{\text{cut}}$ terms in our final results

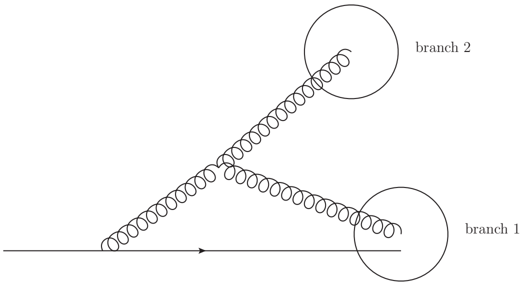

Figure 5.3. The configuration responsible for the correlated emission clustering correction. Both gluons have $z_i < z_{\text{cut}}$, but have a combined energy fraction greater than z_{cut}. The two gluons are clustered in separate C/A branches, with branch two being de-clustered from the jet first and groomed away. The other gluon is then de-clustered from the quark and is also groomed way.

similar argument holds for more emissions so that at N^{n}LL accuracy one only has to consider clustering corrections involving up to n emissions, the exception being NLL accuracy where there is no clustering correction.

Our treatment of the clustering corrections in the C_F^2 colour channel produces results which are equivalent at NNLL accuracy to the relevant pieces of the SCET resummation given in [47], but differs beyond this accuracy. The terms which we account for in our clustering correction are included in the SCET result through the soft, and collinear-soft, two-loop non-cusp anomalous dimensions, which appear in the exponent given in appendix F of ref. [47] [9]. In other words, they are exponentiated, and whilst the two resummations are equivalent at NNLL, we believe that their method leads to errors at N^{3}LL [190]. This is because the groomer stops as soon as it encounters a branch which passes the z_{cut} condition, implying that there should be no terms in the resummed distribution, or its expansion in powers of α_s, involving multiple powers of $\mathcal{F}^{\text{Ind.}}_{\text{clust.}}$. Such terms are present if one expands the resummed distribution presented in ref. [47] up to $\mathcal{O}(\alpha_s^4)$. Note that the square of the two emission clustering correction cannot give part of the four emission clustering correction as, by the arguments outlined in the preceding paragraph, this would have the wrong number of logarithms per power of α_s.

5.4.2 Correlated emission clustering correction

The correlated emission clustering correction shares some similarities with the independent emission correction. The main difference being that it is due to a pair of emissions being groomed away in a region of phase space where the simplified groomer treats them as being retained, as opposed to the other way around for independent emissions. An $\mathcal{O}(\alpha_s^2)$ configuration where this occurs is shown in figure 5.3, which shows a pair of gluons, which are treated as being retained by the simplified groomer, but are actually removed due to the C/A clustering sequence. This configuration of emissions corresponds to the clustering correction computed in the previous chapter for the $C_F C_A$ channel.

We can calculate the correlated emission clustering correction up to NNLL accuracy

---

[9] We would like to thank Aditya Pathak for his help in understanding the SCET resummation.

by considering a pair of correlated emissions which we again label α and β. Configurations involving three emissions would be N^{3}LL as argued for the independent emission clustering correction. The region of phase space responsible for the clustering correction can be summarised as $z_\alpha + z_\beta > z_{\text{cut}}$ with $V_{\text{sc}}^{\text{simp.}}(\{p\}, k_\alpha, k_\beta) > v$ and $V^{\text{mMDT}}(\{p\}, k_\alpha, k_\beta) = 0$, which is illustrated in figure 5.4. The relevant region of phase space for these two emissions is isolated by

$$\begin{aligned}\Theta^{\text{Cor.}}_{\text{clust.}} &= (\Theta(\theta_{\alpha,\beta} - \theta_\alpha)\Theta(\theta_\beta - \theta_\alpha) + (\alpha \leftrightarrow \beta))\times \\ &\quad \Theta(z_{\text{cut}} - z_\alpha)\Theta(z_{\text{cut}} - z_\beta)\Theta(z_\alpha + z_\beta - z_{\text{cut}})\Theta(V_{\text{sc}}^{\text{simp.}}(\{p\}, k_\alpha, k_\beta) - v)\ . \end{aligned} \tag{5.40}$$

In the same spirit as eq. (5.32), we can then write:

$$\begin{aligned}\Sigma^{\text{clust.}}_{\text{Cor.}}(v, z_{\text{cut}}) &= \mathcal{H}(Q) \int \frac{1}{2!}\mathcal{M}^2_{\text{cor}}(k_\alpha, k_\beta)[\mathrm{d}^4 k_\alpha][\mathrm{d}^4 k_\beta]\Theta^{\text{Cor.}}_{\text{Clust.}} \sum_{n=0}^{\infty} \frac{1}{n!} \\ &\prod_{j=0}^{n} \int [\mathrm{d}^4 k_j]\mathcal{M}^2_{\text{c}}(k_j)\big(\Theta(z_{\text{cut}} - z_j) + \Theta(z_j - z_{\text{cut}})\Theta(v - V_{\text{sc}}^{\text{simp.}}(\{p\}, \{k_j\}))\big), \end{aligned} \tag{5.41}$$

where $\mathcal{M}^2_{\text{cor}}(k_\alpha, k_\beta)$ is the correlated emission part of the two gluon matrix element. As before we can write this as

$$\Sigma^{\text{clust.}}_{\text{Cor.}}(v, z_{\text{cut}}) = \mathcal{F}^{\text{Cor.}}_{\text{clust.}} \exp[-R(v, z_{\text{cut}})], \tag{5.42}$$

where,

$$\mathcal{F}^{\text{Cor.}}_{\text{clust.}}(v, z_{\text{cut}}) = \frac{1}{2!} \int \mathcal{M}^2_{\text{cor}}(k_\alpha, k_\beta)[\mathrm{d}^4 k_\alpha][\mathrm{d}^4 k_\beta]\Theta^{\text{Cor.}}_{\text{Clust.}}. \tag{5.43}$$

We have not been able to compute these integrals analytically. However, it is possible to re-write them as an integral over the total transverse momentum of emissions α and β, which collects all the observable dependence and is straightforward to evaluate, multiplied by an integral which is computable numerically and is just a constant. We can write the phase space as

$$[\mathrm{d}^4 k_\alpha][\mathrm{d}^4 k_\beta]\delta(\vec{k}_t - \vec{k}_{t\alpha} - \vec{k}_{t\beta})\mathrm{d}k_t, \tag{5.44}$$

As we are working with rIRC safe observables we can immediately make the replacement $V_s(\{p\}, k_\alpha, k_\beta) \to V_{\text{sc}}^{\text{simp.}}(\{p\}, k_\alpha + k_\beta)$ [69], [210], which, due to the ordering $v < z_{\text{cut}}$ can be further simplified to $v^{\frac{2}{a+b}} z_{\text{cut}}^{\frac{2b}{a+b}} < k_t^2 < z_{\text{cut}}^2$.
The argument of both factors of the coupling can be approximated as k_t^2, the total transverse momentum of the two partons [10] similar to what is done for the correlated emission correction in [196], [210]. Like the independent emission case, it is not important exactly what the argument of both powers of the coupling are, only that they scale with the observable as $v^{\frac{2}{a+b}} Q^2$.

---

[10] Due to the separation in angle required for the clustering correction and fact that the parent gluon and both decay products must have z of order z_{cut}, the relative transverse momenta of a and b must be of order the transverse momentum of the parent.

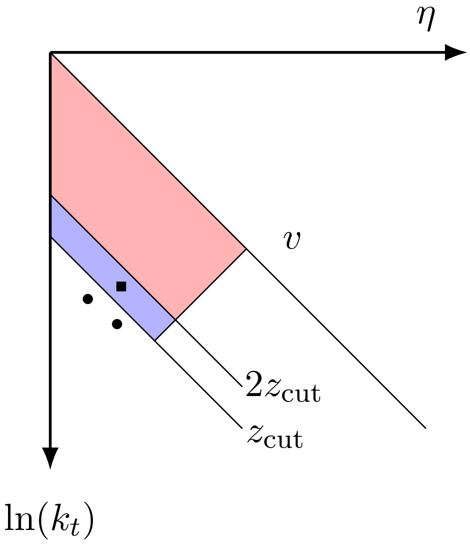

Figure 5.4. Lund diagram showing the region of phase space responsible for the correlated clustering correction in blue, and in red the vetoed phase space responsible for the Sudakov factor. The black dots depict two correlated emissions, which, due to their separation in angle are clustered into different C/A branches, giving rise to the clustering correction, while the black square represents the parent whose branching gives rise to the correlated pair responsible for the clustering correction.

We then choose $\theta_\alpha > \theta_\beta$ and provide a factor of two to account for the opposite ordering to write

$$\begin{aligned}&\mathcal{F}^{\rm Cor.}_{\rm clust.}(v, z_{\rm cut}) = \\ &\quad \int_{Q^2 v^{\frac{2}{a+b}} z_{\rm cut}^{\frac{2b}{a+b}}}^{Q^2 z_{\rm cut}^2} \left(\frac{\alpha_s(k_t^2)}{2\pi}\right)^2 \times \left(\int \frac{1}{2!}\bar{\mathcal{M}}^2_{\rm cor}(k_\alpha, k_\beta) k_t \delta(\vec{k_t} - \vec{k}_{t\alpha} - \vec{k}_{t\beta})\Theta(\theta_\alpha - \theta_\beta)\right. \\ &\quad \left.\Theta(\theta_{\alpha,\beta} - \theta_\beta)\Theta(z_{\rm cut} - z_\alpha)\Theta(z_{\rm cut} - z_\beta)\Theta(z_\alpha + z_\beta - z_{\rm cut})[\mathrm{d}^4 k_\alpha][\mathrm{d}^4 k_\beta]\right)\frac{\mathrm{d}k_t^2}{k_t^2} \qquad (5.45)\end{aligned}$$

where the bar on $\mathcal{M}^2_{\rm cor}(k_\alpha, k_\beta)$ indicates that we have pulled out the two factors of $\frac{\alpha_s}{2\pi}$ from the matrix element. Using the delta function in eq. (5.45) to integrate over θ_β, the remaining integrals within $[\mathrm{d}^4 k_\alpha][\mathrm{d}^4 k_\beta]$ can be re-scaled so that, other than the overall factor of $\frac{\mathrm{d}k_t^2}{k_t^2}$, there is no k_t dependence in the integrals. Leaving aside the integral over k_t^2, we can carry out the rest of the integrals numerically in the limit of $z_{\rm cut} \to 0$, to give:

$$\mathcal{F}^{\rm Cor.}_{\rm clust.} = (C_F T_R n_f 1.754 + C_F C_A 1.161)\int_{Q^2 v^{\frac{2}{a+b}} z_{\rm cut}^{\frac{2b}{a+b}}}^{Q^2 z_{\rm cut}^2} \left(\frac{\alpha_s(k_t^2)}{2\pi}\right)^2 \frac{\mathrm{d}k_t^2}{k_t^2}\ . \qquad (5.46)$$

This is then simply evaluated to give:

$$\mathcal{F}^{\text{Cor.}}_{\text{clust.}} = \left(\frac{\alpha_s(Q^2)}{2\pi}\right)^2 \left(C_F T_R n_f 1.754 + C_F C_A 1.161\right) \frac{\ln\left(z_{\text{cut}}^{\frac{2}{a+b}} v^{\frac{-2}{a+b}}\right)}{(1+\beta_0\alpha_s(Q^2)\ln z_{\text{cut}}^{\frac{2b}{a+b}} v^{\frac{2}{a+b}})(1+\beta_0\alpha_s(Q^2)\ln z_{\text{cut}}^2)} . \tag{5.47}$$

As for the independent emission clustering correction, the terms which contribute at NNLL accuracy are those proportional to $\ln(v^{\frac{2}{a+b}})$, with terms proportional to $\ln(z_{\text{cut}})$ being at least N^{3}LL. We re-iterate that the it is only important that the argument of the coupling scales with the observable so as to produce the factor of $\ln\left(v^{\frac{-2}{a+b}}\right)$ in the denominator of eq. (5.47), and that the precise details of the argument do not matter at NNLL accuracy.

We have checked the leading $\mathcal{O}(\alpha_s^2)$ NNLL term in eq. (5.47) for the $C_F C_A$ channel using `Event2` for the jet mass, width, and Les Houches angularity, and found good agreement. The correlated clustering correction, and our resummed result as a whole, agrees with the collinear $\mathcal{O}(\alpha_s^2)$ calculation carried out for the jet mass in chapter 4 and is consistent with the SCET resummation of the groomed jet mass [47], up to NNLL accuracy.

Within NNLL accuracy it is sufficient to account for a single correlated pair of emissions as described above, as two correlated pairs would give a correction proportional to $\alpha_s^4 \ln^2(\rho)$ an N^{3}LL correction. However as the groomer can remove any number of correlated pairs of emissions without being stopped, it is envisaged that this contribution could be exponentiated to correctly capture a set of corrections beyond NNLL accuracy.

5.5 Phenomenology

Though the main focus of this work has been to compute the resummation of next to leading logarithms in the regime where $v \ll z_{\text{cut}} \ll 1$, this is not the only regime relevant for phenomenology. Firstly, one typically sees $z_{\text{cut}} \sim 0.1$ in experimental analyses. Terms of order $\alpha_s^n z_{\text{cut}}^n \ln^n(v)$ could reasonably be expected to be of a similar size to the NNLL terms which we resum. It is therefore desirable to resum these terms, as was done for the jet mass in ref.[44]. We therefore show in section 5.5.1 how our results can be modified so that such terms are resummed at the NLL level. Although an interesting problem, the resummation of NNLL finite z_{cut} terms (i.e. $\mathcal{O}(\alpha_s^n z_{\text{cut}} \ln^{n-1}(v))$) is beyond the scope of this work. For typical values of $z_{\text{cut}} \sim 0.1$, such terms are, anyway, likely to be small compared to the NNLL terms which survive in the small z_{cut} limit, but could be comparable in size to N^{3}LL correction. Secondly it is desirable to present results that are valid as v approaches z_{cut}, which can be achieved by matching to fixed order calculations. We define a fixed-order matching prescription in section 5.5.2 before studying the impact of including these terms for three commonly studied observables in section 5.5.3.

5.5.1 Finite z_{cut}

We will first deal with the resummation of terms which are leading logarithmic but which vanish with z_{cut}, as this will inform our matching procedure. The leading log resummation including these terms was carried out, for the jet mass distribution, in ref. [44]. Dropping the arguments of the radiators for compactness, their result can be expressed as

$$\begin{aligned}\frac{1}{\sigma_0}\frac{\mathrm{d}\sigma}{\mathrm{d}\ln(1/\rho)} = &\begin{pmatrix} R_q^{\prime\text{NLL}} & R_g^{\prime\text{NLL}} \end{pmatrix} \\ &\exp\begin{pmatrix} -R_q^{\text{NLL}} - R_{q\ z_{\text{cut}}} - R_{q\to g} & R_{g\to q} \\ R_{q\to g} & -R_g^{\text{NLL}} - R_{g\ z_{\text{cut}}} - R_{g\to q} \end{pmatrix}\begin{pmatrix}\sigma_q \\ \sigma_g\end{pmatrix}\,, \end{aligned} \tag{5.48}$$

where σ_q and σ_g are the Born cross sections for quark and gluon initiated jets respectively, and compared to ref. [44] we have expressed the quark and gluon radiators as the small z_{cut} limit of the radiator $R_{q/g}^{\text{NLL}}$, the NLL accurate radiator, plus the functions, $R_{q/g\ z_{\text{cut}}}$ which vanish with z_{cut}. This allows us to easily replace the parts of the radiators which survive in the small z_{cut} limit with the NNLL radiators given in section 5.3. For a general observable v, the other components of the radiators are defined as follows:

$$\begin{aligned}
R_{q\ z_{\text{cut}}}(v, z_{\text{cut}}) = &-\Bigg(\int_{1-z_{\text{cut}}}^{1} P_{gq}(z)\mathrm{d}z\int_0^{Q^2}\frac{\alpha_s(k_t^2)}{\pi}\frac{\mathrm{d}k_t^2}{k_t^2}+ \\
&\int_0^{z_{\text{cut}}}(P_{gq}(z) - \frac{2}{z})\mathrm{d}z\int_0^{Q^2}\frac{\alpha_s(k_t^2)}{\pi}\frac{\mathrm{d}k_t^2}{k_t^2}\Bigg)\Theta(V_{\text{sc}}(z,k_t)-v) \\
R_{g\ z_{\text{cut}}}(v, z_{\text{cut}}) = &\Bigg(\int_{1-z_{\text{cut}}}^{1}\frac{2}{z}\mathrm{d}z\int_0^{Q^2}\frac{\alpha_s(k_t^2)}{\pi}\frac{\mathrm{d}k_t^2}{k_t^2}+ \\
&\int_0^{z_{\text{cut}}}(P_{gg}(z) - \frac{1}{z} - \frac{1}{1-z} + n_f P_{qg}(z))\mathrm{d}z\int_0^{Q^2}\frac{\alpha_s(k_t^2)}{\pi}\frac{\mathrm{d}k_t^2}{k_t^2}\Bigg)\Theta(V_{\text{sc}}(z,k_t)-v) \\
R_{q\to g}(v, z_{\text{cut}}) = &\int_{1-z_{\text{cut}}}^{1} P_{gq}(z)\mathrm{d}z\int_0^{Q^2}\frac{\alpha_s(k_t^2)}{\pi}\frac{\mathrm{d}k_t^2}{k_t^2}\Theta(V_{\text{sc}}(z,k_t)-v) \\
R_{g\to q}(v, z_{\text{cut}}) = &\int_{1-z_{\text{cut}}}^{1} n_f P_{qg}(z)\mathrm{d}z\int_0^{Q^2}\frac{\alpha_s(k_t^2)}{\pi}\frac{\mathrm{d}k_t^2}{k_t^2}\Theta(V_{\text{sc}}(z,k_t)-v)
\end{aligned} \tag{5.49}$$

The definitions of the splitting functions were given in section 2.4.3.

To complete the matching of our NNLL result to the NLL finite z_{cut} result we must also include the NNLL corrections which are not exponentiated. As we do not attempt to capture finite z_{cut} NNLL terms it is sufficient to make sure that however these are included, we reproduce eq. (5.35) on taking the small z_{cut} limit. For our purposes $\sigma_g = 0$, and we can normalize our distributions to the Born cross section for the production of a $q\bar{q}$ pair and finally write the NNLL result including NLL finite

z_{cut} effects as:

$$\frac{1}{\sigma_0}\Sigma(v) = \Big(1 + C_1^q(v) + \mathcal{F}_{\text{clust.}} \quad ,1\Big) \\ \exp\begin{pmatrix} -R_q - R_{q\ z_{\text{cut}}} - R_{q\to g} & R_{g\to q} \\ R_{q\to g} & -R_g - R_{g\ z_{\text{cut}}} - R_{g\to q} \end{pmatrix} \begin{pmatrix} 1 \\ 0 \end{pmatrix}, \quad (5.50)$$

where $\mathcal{F}_{\text{clust.}} = \mathcal{F}^{\text{clust.}}_{\text{Ind.}} + \mathcal{F}^{\text{clust.}}_{\text{Cor.}}$. In the small z_{cut} approximation the off diagonal entries in the exponential vanish and we return to our NNLL result.

5.5.2 Matching

We now turn to matching our resummed calculation to fixed-order, which we do at $\mathcal{O}(\alpha_s^2)$. Although our NNLL calculation captures all logarithms of the observable at $\mathcal{O}(\alpha_s^2)$ which are not suppressed by powers of z_{cut}, there still exist terms at $\mathcal{O}(\alpha_s^2)$ which are $\mathcal{O}(z_{\text{cut}})$ but diverge as $v \to 0$. For this reason we choose to use a multiplicative matching procedure similar to that employed in [46]. This ensures that the $\mathcal{O}(z_{\text{cut}})$ logarithmically divergent terms are suppressed by the Sudakov factor as $v \to 0$, whilst correctly capturing both the NNLL resummed distribution and the full fixed order distribution at NLO.
We introduce the notation $\Sigma^{(1)}_{\text{NNLL}}(v)$ for the $\mathcal{O}(\alpha_s)$ part of the NNLL resummed distribution including the NLL finite z_{cut} effects, with $\Sigma^{(2)}_{\text{NNLL}}(v)$ representing the α_s^2 terms. The n^{th} order contribution to the distribution is written as $\Sigma^{(n)}(v)$. The matched cumulative distribution is then given by

$$\Sigma(v) = \Sigma_{\text{NNLL}}\big[1 + (\Sigma^{(1)}(v) - \Sigma^{(1)}_{\text{NNLL}}(v)) + \\ (\Sigma^{(2)}(v) - \Sigma^{(2)}_{\text{NNLL}}(v)) - \Sigma^{(1)}_{\text{NNLL}}(v)(\Sigma^{(1)}(v) - \Sigma^{(1)}_{\text{NNLL}}(v))\big]. \quad (5.51)$$

The first term above is just the NNLL distribution. The term, $(\Sigma^{(1)}(v) - \Sigma^{(1)}_{\text{NNLL}}(v))$, is the $\mathcal{O}(\alpha_s)$ part of the distribution with the terms already captured by the NNLL distribution subtracted. This term is multiplied by the full NNLL distribution which generates spurious terms at $\mathcal{O}(\alpha_s^2)$, which are removed by the final term in the above equation, $\Sigma^{(1)}_{\text{NNLL}}(v)(\Sigma^{(1)}(v) - \Sigma^{(1)}_{\text{NNLL}}(v))$. The term, $(\Sigma^{(2)}(v) - \Sigma^{(2)}_{\text{NNLL}}(v))$ is the $\mathcal{O}(\alpha_s^2)$ part of the distribution with the terms already captured by the NNLL distribution subtracted. There are no spurious terms within our accuracy generated by the interplay of this term with Σ_{NNLL}.

We perform the matching for the process $e^+e^- \to q\bar{q}$ for three jet shapes: the heavy hemisphere mass, the width (λ^1_1), and the Les Houches angularity$(\lambda^1_{0.5})$. The fixed-order results are calculated, for $z_{\text{cut}} = 0.1$, using `Event2`. Each event was partitioned into two hemispheres by a plane perpendicular to the C/A jet axis. mMDT is then run on each hemisphere and the jet shape calculated on the groomed hemispheres. The larger value of the observable from the two hemispheres is then binned.

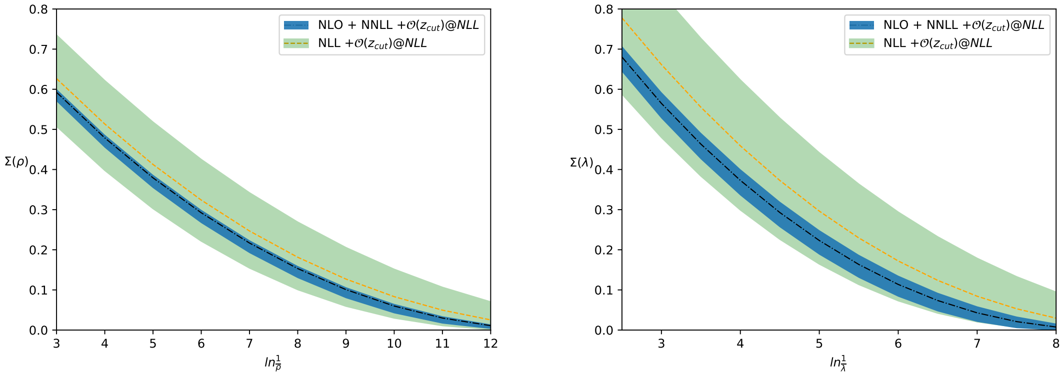

(a) ρ (Jet Mass)

(b) λ_1^1

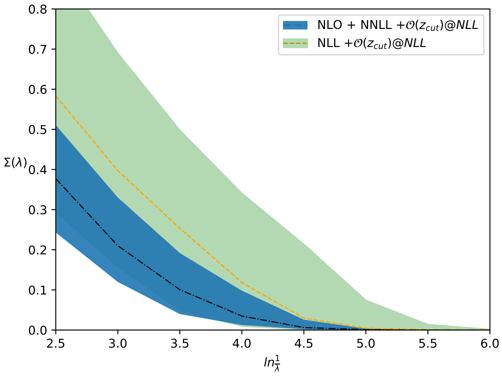

(c) $\lambda_{0.5}^1$

Figure 5.5. Matched NLL predictions alongside the LL result, both with finite z_{cut} effects showing the central values and uncertainty bands.

5.5.3 Results

Having defined the matching procedures for incorporating both the $\mathcal{O}(z_{\text{cut}})$ effects at NLL and the full NLO distribution, we now investigate the impact of including these effects and the size of the uncertainties, which we derive from resummation and renormalisation scale variation. We investigate three observables, the jet mass, the width (λ_1^1) and the Les Houches angularity ($\lambda_{0.5}^1$), the later two with respect to the WTA axis [27]. The functions required for the NNLL resummation of these observables are given in sections 5.3 and 5.4.

Figure 5.5 shows our matched results for the three observables alongside the next to leading log with finite z_{cut} results for a typical value of $z_{\text{cut}} = 0.1$ so as to show the size of the NNLL correction.

For the jet mass and width, the uncertainty bands are found by simultaneously varying the resummation and renormalisation scales by factors of two in such a way as to not introduce any spurious terms within the stated accuracy, similar to ref. [26]. The renormalisation scale enters through the argument of the coupling, and is included by making the replacement

$$\alpha(Q) \to \alpha'(xQ) = \alpha(xQ) + \alpha^2(Q)\beta_0 \ln(x) \tag{5.52}$$

and varying x between 0.5 and 2. This preserves the NNLL result whilst generating our renormalisation scale variation. The resummation scale uncertainty is found for the small $z_{\rm cut}$ NNLL calculation by writing the radiator as $R(v, z_{\rm cut}) = R^{\rm NLL}(v, z_{\rm cut})+$ $R^{\rm remainder}(xv, z_{\rm cut})$, where again, x is varied between 0.5 and 2. Here $R^{\rm NLL}(v, z_{\rm cut})$ contains purely the next to leading logarithms in the small $z_{\rm cut}$ limit, and nothing else, and $R^{\rm remainder}(xv, z_{\rm cut}) = R(v, z_{\rm cut}) - R^{\rm NLL}(v, z_{\rm cut})$. To obtain the resummation scale uncertainty for the NLL accurate results[11] shown in figure 5.5 we simply replace $v \to xv$ which introduces terms due to scale variation at NNLL.
The Les Houches angularity becomes sensitive to very small transverse momentum emissions much faster than the other two observables. It was therefore necessary to introduce a freezing scale for the coupling, which we set at 1GeV, to avoid divergences due to the Landau pole. The uncertainty band shown in figure 5.5 for this observable therefore incorporates variation in the freezing scale by factors of two as well as the uncertainties previously discussed.
Figure 5.6 shows results for the jet mass for $z_{\rm cut} = 0.1, 0.2, 0.3$ at several levels of accuracy along with the ratio of these results to our NNLL result matched to NLO and the $\mathcal{O}(z_{\rm cut})$ NLL calculation.

From figures 5.5 and 5.6 we see that the inclusion of NNLL terms is important both for the noticeable shift in the central value, but also for the large reduction in the uncertainty it provides. We also see from figure 5.6 that, even at moderate values of $\ln(v)$, resummation of NLL finite $z_{\rm cut}$ terms is at least as important as matching to NLO, with the importance of finite $z_{\rm cut}$ terms growing with $\ln(v)$. We also see that as $z_{\rm cut}$ grows the resummation of finite $z_{\rm cut}$ effects even overtakes the size of the NNLL small $z_{\rm cut}$ effects. For values of $z_{\rm cut} \simeq 0.1$ or larger, such as might be used for phenomenology, finite $z_{\rm cut}$ effects at NLL accuracy should therefore be retained, if one is keeping similarly sized NNLL terms, which are not suppressed by powers of $z_{\rm cut}$. One caveat to this is that, if fixed order matching is carried out, the finite $z_{\rm cut}$ effects will automatically be included up to the order which the matching is carried out to, which may decrease the importance of re-summing finite $z_{\rm cut}$ effects. This may explain the small effect of finite $z_{\rm cut}$ resummation observed in previous studies [44].

5.6 Conclusions

In this chapter the distribution of additive rIRC safe observables, computed on jets groomed with mMDT, in the context of e^+e^- collisions, was calculated at NNLL accuracy in the small $z_{\rm cut}$ limit. This result agrees up to NNLL accuracy with a previous resummation of the groomed jet mass carried out in SCET [47], [190], which provides a powerful cross check between the two results [12]. However, there are dif-

---

[11] This includes the finite $z_{\rm cut}$ corrections which we match our NNLL result to.

[12] Our result can be compared to the SCET result by the formulae presented in appendix F of ref. [47]. Our Sudakov factor is captured by the sum of the K_F factors in the SCET resummation. These K_F factors also contain the

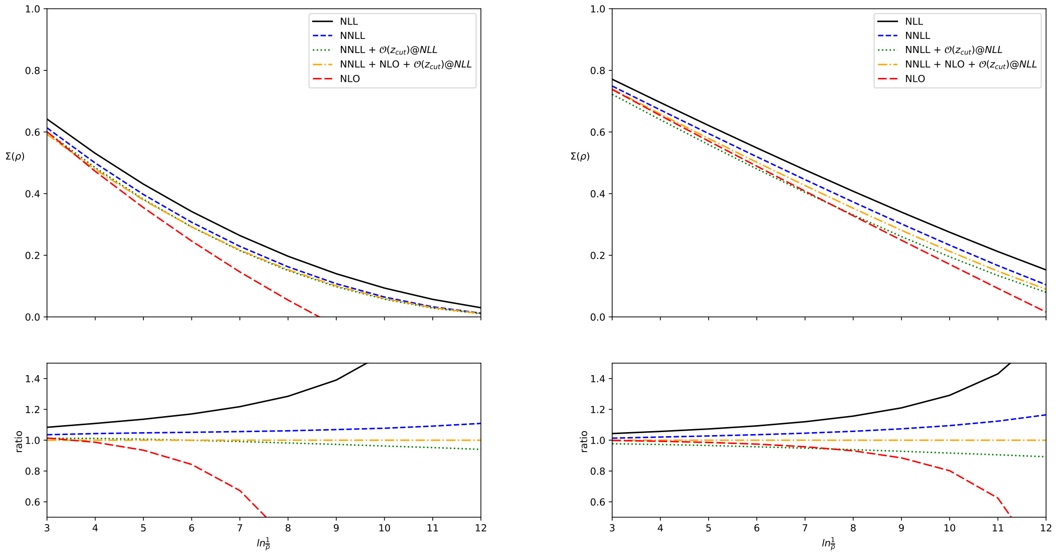

(a) $z_{\text{cut}} = 0.1$ (b) $z_{\text{cut}} = 0.2$

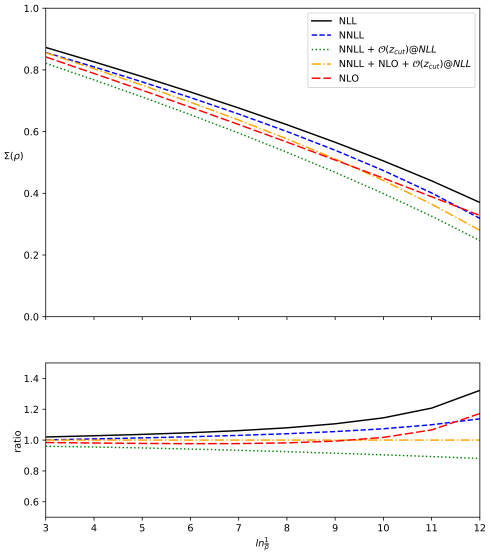

(c) $z_{\text{cut}} = 0.3$

Figure 5.6. Predictions for the cumulative jet mass distribution at various levels of accuracy for three different values of z_{cut}

ferences between the two calculations at N^{3}LL. This is due to the exponentiation of terms in the SCET calculation, which we account for in our independent clustering correction, and argued in section 5.4.1 should not be exponentiated. We believe that this will introduce spurious terms at N^{3}LL accuracy in the SCET resummation [47], [48], [190].

Having presented our NNLL result in the small z_{cut} limit, we then modified our result so as to include NLL terms which vanish with z_{cut} , which were previously re-

---

terms accounted for by our clustering corrections. The combination of the hard, soft, jet, and collinear-soft functions of ref. [47] captures the terms which are referred to as C_1 and β_0 X in this work. Other terms in eq. $F.15$ of [47] are either N^{3}LL for the heavy hemisphere mass, or are a consequence of the SCET result being presented as a differential distribution.

summed in [21], [44]. This was done because NLL terms suppressed by a power of z_{cut} could reasonably be expected to be numerically similar in size to the NNLL terms we resummed in the small z_{cut} limit, for values of $z_{\text{cut}} \sim 0.1$. We then performed fixed order matching to $\mathcal{O}(\alpha_s^2)$ for the heavy jet mass, width, and Les Houches angularity. Our results for these three observables are shown in section 5.5.3 at different levels of accuracy to asses the impact of different effects. From these results we saw that, for values of $z_{\text{cut}} \geq 0.1$, the NLL finite z_{cut} effects are indeed of a similar size to the NNLL terms kept in the small z_{cut} limit, and so, for phenomenology, should be retained if one is keeping the NNLL terms. Although we noted that if matching to NLO fixed order calculations, the effect of resumming finite z_{cut} may well be less noticeable.

One continuation of this work would be to extend the resummation presented here to gluon jets. Together with the work presented here, this could then be used to produce NNLL accurate predictions, matched with NLL finite z_{cut} effects and NLO results, suitable for comparison with hadron collider measurements, for any groomed, additive, rIRC safe observable.

Though this work has only considered additive observables, we believe that it should be possible to extend it, using similar techniques, to non-additive observables such as the broadening [229]. It may also be possible to compute NNLL resummations of groomed observables in an automated way through an extension of the `ARES` formalism. This is prompted by the notion that the simplified groomer can be treated as if it were rIRC safe, a requirement for resummation within `ARES`. In fact, many of the NNLL terms which are resummed by σ_{simp} are already accounted for in `ARES`. How, or even whether the clustering contribution, which is where the rIRC un-safety of groomed observables is manifest, could be included in such a framework is as yet unclear.

Chapter 6

Understanding boosted top tagging with prong finding and N-subjettiness

This chapter covers work investigating top tagging from an analytical QCD perspective which was carried out in collaboration with my supervisor. It is published in [5], from which much of the text and figures are taken.

6.1 Introduction

Jet substructure is now firmly established as a tool for tagging boosted heavy particles. As was discussed in chapter 3, questions were initially raised about the robustness of these techniques, resulting in a large body of work aiming to understand jet substructure techniques, both from first principles calculations and by using event generators to asses the impact of hadronisation and UE. In some cases weaknesses in these techniques were found and improved methods proposed to eliminate or mitigate problems [21], [25]. This program of work has been particularly successful in the case of taggers designed to identify two prong structures such as boosted W,Z and Higgs bosons [21], [22], [26], [28]–[31], [127], [230], however, the understanding of methods designed to tag three prong structures, such as boosted top quarks, is less complete. Even at the level of the background distribution, three pronged taggers are harder to study analytically as they typically require one to consider an extra emission compared to two-pronged tagger, while the signal distribution (top quarks) is more complicated due to the top quark carrying a colour charge, unlike the electroweak bosons relevant for two-pronged jets.
More recently, machine learning algorithms have proven to be extremely powerful tools for tagging boosted objects. Although the performance obtainable from such methods appears to be excellent, there exists the same questions surrounding their robustness as for more traditional jet substructure taggers, as discussed in section 3.4.3. One study that was discussed there [34] highlighted the trade-off between performance and resilience to non-perturbative effects with the Lund net tagger. Fur-

thermore, recent work has identified flaws in the structure of existing dipole shower algorithms [95], [96]. This raises further questions around the reliability of machine learning algorithms owing to the large majority being trained on mock data samples simulated using these parton showers. This further reinforces the need to understand any tagging method as fully as possible from first principles.

With this motivation in mind we build on the work of ref.[25], which analytically studied methods to identify a three prong structure within a jet, to investigate the combination of grooming, prong finding, and cutting on a jet shape ratio as a method for tagging boosted top quarks. These are the three key steps commonly taken in a realistic top tagging procedure, though of course each step can vary from analysis to analysis. In this work we use soft drop [23] as the grooming step, an adaption of the $\mathrm{Y_m}$-Splitter algorithm for top tagging [25], which is described in section 3.4.1 as the prong finding step, and the N-subjettiness ratio [14], [137], $\tau_{32}^{\beta=2}$, as our jet shape. For the N-subjettiness variables we use the gen-k$_t$ ($p = \frac{1}{2}$) axes (henceforth referred to as the gen-k$_t$ axes) described in section 3.4. This combination of techniques was chosen because, as well as being a powerful top tagging method, it is more amenable to resummation than some similar methods. The definitions of these procedures was given in sections 3.3, 3.4.1 and 3.4.2 respectively. Other choices of prong finding algorithm include the CMS top tagger [16], [133], [231], the Johns Hopkins top tagger [232] and the HEP top tagger [233], whilst cuts on Energy Correlation Function ratios [234] are a widely used alternative to N-subjettiness ratios. Other top tagging methods include shower deconstruction [124] and template tagging [235].

In section 6.2 we perform a Monte Carlo study to investigate the performance of various combinations of cutting on τ_{32}, grooming with mMDT and soft drop with $\beta = 2$, and prong finding with $\mathrm{Y_m}$-Splitter , as well as how these procedures are impacted by hadronisation effects, ISR and UE. Having established that using all three steps together maximises both the performance and resilience to non-perturbative effects we go on to calculate the tagged background fraction up to modified LL accuracy in section 6.3. This represents the first time that a realistic top tagging method, such as might be used in an experimental analysis, has been understood analytically. We then carry out similar calculations for the signal jets, starting with a calculation of the tagged fraction of events within a mass window. We then incorporate the effect of applying the $\mathrm{Y_m}$-Splitter algorithm where we go beyond the analysis carried out in [25] to include configurations where a gluon is identified as a prong by $\mathrm{Y_m}$-Splitter and find improved agreement with Pythia as a result. Finally we include the cut on τ_{32} in our calculations where we find interesting interplay between the cut on τ_{32} and the mass cut, which is investigated further in 6.5. Our conclusions are presented in section 6.6.

6.2 Monte-Carlo study

In this section we investigate the performance of various tagging procedures based around the N-subjettiness variable τ_{32} as well as how they are impacted by hadronisation, ISR, and MPI. The tagging procedures considered all have the restriction that the jet mass is between 160 GeV and 225 GeV, corresponding to a window around the top mass, and are studied as a function of the cut on τ_{32}. After examining N-subjettiness cuts with and without pre-grooming we combine these cuts with the $\mathrm{Y_m}$-Splitter method which we again investigate with and without pre-grooming. Two pre-grooming options are considered, SD ($\beta = 2$) and mMDT (equivalent to SD with $\beta = 0$).

We start by generating 1 million $t\bar{t}$ and $q\bar{q}$ events with Pythia [1]. ISR, MPI and hadronisation were initially deactivated, and a generation cut of $p_t > 1600$ GeV was applied. Jets were clustered with the Cambridge/Aachen algorithm with $R = 1$ and $p_{t,\min} = 2\,\mathrm{TeV}$ using Fastjet 3 [109], as was the case for the studies in ref. [25]. Where jets are groomed we use $z_{\mathrm{cut}} = 0.05$, τ_{32} is calculated using the N-subjettiness FastJet contrib [137], and where $\mathrm{Y_m}$-Splitter is used we choose $m_{\min} = 50$ GeV and $\zeta = 0.05$. This information is then used to construct the tagged fraction of events and the signal to square-root–background as a function of a cut on τ_{32}. The same procedure is used both with only hadronisation, and then hadronisation, ISR and MPI activated to assess their impact.
To discuss the features that emerge from our Monte Carlo studies let us first examine the top row of Fig. 6.1, i.e. Figs. 6.1a and 6.1b, which show the signal significance as a function of the τ_{32} cut, τ, without any grooming and without $\mathrm{Y_m}$-Splitter on the left and with $\mathrm{Y_m}$-Splitter on the right. It is clear that in the absence of a grooming step that ISR and MPI significantly damage performance in each case, although the inclusion of $\mathrm{Y_m}$-Splitter results in a higher signal significance after all effects are considered.

Next we come to the plots involving the application of grooming i.e. Figs. 6.1c and 6.1d for SD ($\beta = 2$) pre-grooming and Figs. 6.1e and 6.1f in the bottom row for the mMDT. From these one notes that grooming, especially with mMDT, is an effective method to significantly mitigate ISR and MPI. When combining grooming with $\mathrm{Y_m}$-Splitter we observe that both hadronisation and ISR+MPI are significantly reduced, resulting in high performance with an optimal value of $\tau \sim 0.2$ emerging for mMDT pre-grooming and $\tau \sim 0.3$ for SD ($\beta = 2$). The best performance, i.e. highest signal significance, comes with mMDT pre-grooming and $\mathrm{Y_m}$-Splitter applied in addition to the τ cut, as shown in Fig. 6.1f. This combination is also more resilient to ISR and all non-perturbative effects at the same time. In contrast, although pre-grooming jets and cutting on τ_{32} without $\mathrm{Y_m}$-Splitter (see figure 6.1e) gives good performance at

---

[1] Light quark jets are chosen as the background here as they are the main background to top jets, although we have studied the impact of including gluon jets and found that in the P_t range under consideration they do not significantly modify the distributions presented.

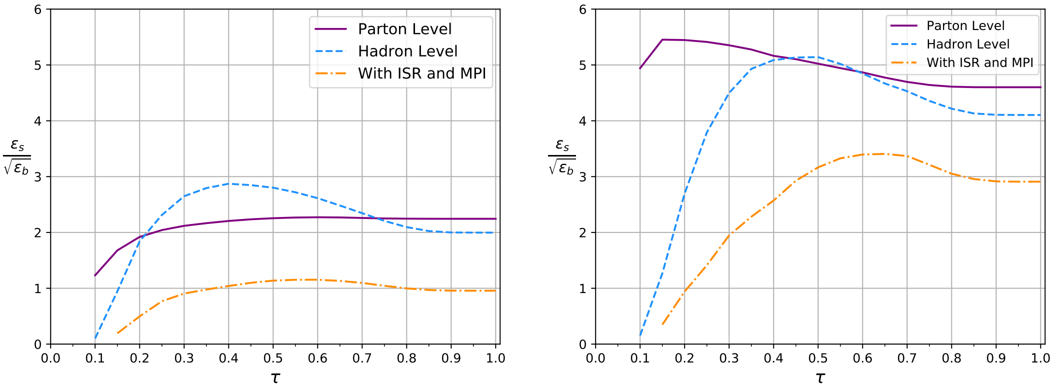

(a) Cut on τ_{32}

(b) Cut on τ_{32} after application of $\mathrm{Y_m}$-Splitter .

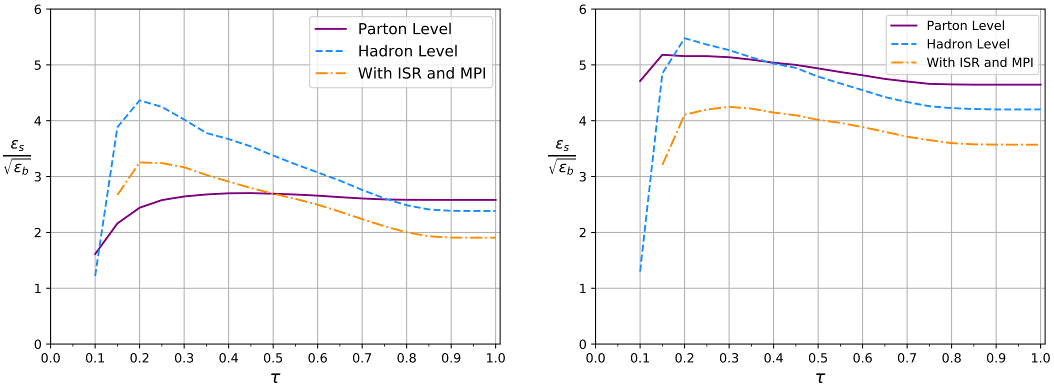

(c) Cut on τ_{32} after application of Soft Drop ($\beta = 2$).

(d) Cut on τ_{32} after application of $\mathrm{Y_m}$-Splitter and Soft Drop ($\beta = 2$).

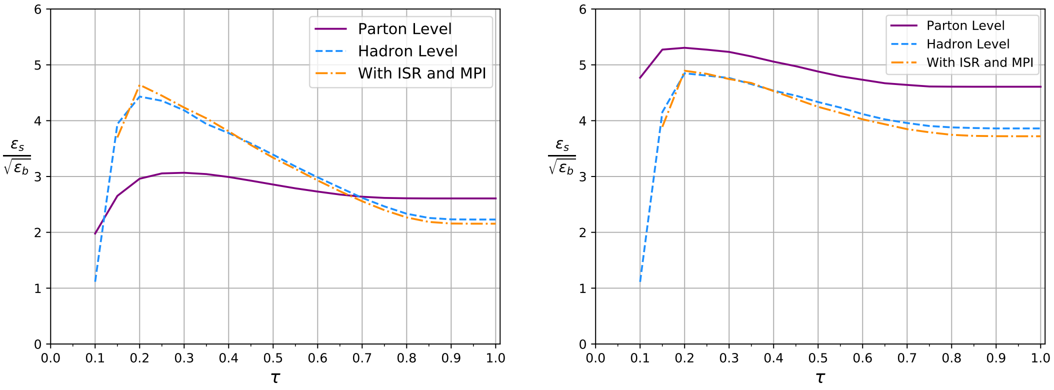

(e) Cut on τ_{32} after application of mMDT.

(f) Cut on τ_{32} after application of $\mathrm{Y_m}$-Splitter and mMDT.

Figure 6.1. Plots showing the signal to square-root background of the six variants of the tagging procedure at parton level, hadron level, and with ISR and MPI activated at hadron level.

hadron level, the discrepancy with the parton level result indicates that the performance of this procedure cannot necessarily be understood from perturbative QCD arguments alone and may be more susceptible to mis-modelling of non-perturbative effects in parton showers [2].

---

[2] A possible reason for this might be that a pure τ_{32} cut is not IRC safe and is instead only Sudakov safe [126], [135] while the application of $\mathrm{Y_m}$-Splitter prior to the subjettiness cut prevents τ_2 from vanishing, resulting in an IRC safe quantity.

In summary, applying $\mathrm{Y_m}$-Splitter to pre-groomed jets with cuts on τ_{32} and the jet mass is a high performing method for tagging hadronically decaying high-p_T top quarks.[3] The performance is also well described by parton level predictions and is therefore reasonably robust against effects which are less well theoretically understood in this context. These observations provide some of the main motivation for detailed theoretical studies using perturbative QCD, which will be the subject of the next two sections.

6.3 $\mathrm{Y_m}$-Splitter splitter with a τ_{32} cut : QCD jets

We start by examining the impact of a τ_{32} cut on QCD jets after applying $\mathrm{Y_m}$-Splitter . Analytical studies for $\mathrm{Y_m}$-Splitter as applied to top-tagging, with and without pre-grooming, have already been carried out in ref. [25]. These studies derived resummed results for the jet mass distribution, and consequently, the efficiency for QCD jets tagged with $\mathrm{Y_m}$-Splitter . Resummation is required in order to address the multi-scale nature of the problem. Crucially the highly boosted limit implies that the invariant jet mass $m^2 \ll p_T^2$, with $m^2 \sim m_t^2$ and p_T values in the TeV range, which leads to large logarithms in $\rho = m^2/R^2p_T^2$. A good description of the jet-mass distribution then requires resummation of the logarithms in ρ. Additionally for $\mathrm{Y_m}$-Splitter we have $\rho_{\min} = m_{\min}^2/p_T^2R^2 \ll 1$ and a further small scale ζp_T, the minimum energy of an emission that passes the ζ condition, with $\zeta \ll 1$. Large logarithms are then expected and do arise in ρ, $\rho_{\min}$, ζ and in $\rho_{\min}/\rho$. In ref. [25] a modified leading logarithmic resummation was performed which included all double-logarithmic terms and a subset of single-logarithmic terms such as those arising from hard-collinear emissions. The logarithms that are most crucial to resum are those in the smallest parameters ρ and $\rho_{\min}$. Typical values of $\zeta \sim 0.05$ and $\rho_{\min}/\rho \sim m_W^2/m_{\text{top}}^2$ are larger and hence we only aim to retain logarithms in these parameters at leading double-logarithmic accuracy.

Here, relative to previous work [25] we shall additionally include the τ_{32} cut, considering the possibility that τ_{32} is not small. In doing so we shall follow closely the treatment of ref. [26] for resummation of jet mass with a τ_{21} cut.

6.3.1 Leading-order result

We start with the leading-order result, computed in the soft and collinear approximation, which yields the leading logarithmic terms. For $\mathrm{Y_m}$-Splitter this starts at order α_s^2 for QCD jets, since one requires at least two emissions within the jet (i.e. at least three partons) in order to be accepted by $\mathrm{Y_m}$-Splitter . Since for three par-

---

[3] We find that, for comparable signal significance, these methods appear, in the high p_T region, to outperform the dense neural net and boosted decision tree used by ATLAS in [20], although it should be noted that the two studies are perhaps not equivalent, as no attempt was made here to examine detector effects, which were included in the ATLAS study.

tons τ_3 vanishes, a cut requiring $\tau_{32} < \tau$ is trivially satisfied. Therefore the leading-order result is unchanged from the pure $\mathrm{Y_m}$-Splitter case of ref. [25]. For the case of a quark initiated jet and in the abelian C_F^2 channel it is given by [4]

$$\frac{1}{\sigma}\left(\frac{d\sigma}{d\rho}\right)^{\text{LO,soft}-\text{collinear}} = \bar{\alpha}^2 \int \frac{dz_1}{z_1}\frac{dz_2}{z_2}\frac{d\theta_1^2}{\theta_1^2}\frac{d\theta_2^2}{\theta_2^2} \times \Theta(\theta_2^2 < \theta_1^2 < 1)\times \\ \delta(\rho - \max(z_1\theta_1^2, z_2\theta_2^2))\Theta(z_1 > \zeta)\,\Theta(z_2 > \zeta)\,\Theta(\min(z_2\theta_2^2, z_1 z_2\theta_1^2) > \rho_{\min}), \quad (6.1)$$

where we defined $\bar{\alpha} = \frac{C_F\alpha_s}{\pi}$, taking for definiteness the case of a quark initiated jet. In deriving the above result we have taken a configuration which is strongly-ordered in angle with $\theta_2 \ll \theta_1$, made a leading logarithmic approximation that the jet mass is dominated by the emission that makes the larger contribution, and imposed the tagger conditions by requiring both emissions to pass the ζ and implemented the $\rho_{\min}$ condition in the strongly-ordered limit where $\theta_{12} \sim \theta_1$.

We then obtain:

$$\frac{\rho}{\sigma}\left(\frac{d\sigma}{d\rho}\right)^{\text{LO,soft}-\text{collinear}} \overset{\frac{\rho_{\min}}{\rho}<\zeta}{=} \bar{\alpha}^2 \ln^2\frac{1}{\zeta}\ln\frac{\rho}{\rho_{\min}}, \quad (6.2)$$

$$\overset{\frac{\rho_{\min}}{\rho}>\zeta}{=} \bar{\alpha}^2 \ln^2\frac{\rho}{\rho_{\min}}\left(\frac{3}{2}\ln\frac{1}{\zeta} - \frac{1}{2}\ln\frac{\rho}{\rho_{\min}}\right).$$

A similar result is obtained for the $C_F C_A$ colour factor while in the $C_F T_R n_f$ channel the result is one logarithm down due to the lack of a soft enhancement in the p_{gq} splitting function. For future convenience we note that the leading-order result can also be expressed in terms of the highest-mass emission ρ_a and the next-highest–mass emission ρ_b. Written in these terms we have

$$\frac{1}{\sigma}\left(\frac{d\sigma}{d\rho}\right)^{\text{LO,soft}-\text{collinear}} = \bar{\alpha}^2 \int \frac{dz_a}{z_a}\frac{dz_b}{z_b}\frac{d\rho_a}{\rho_a}\frac{d\rho_b}{\rho_b}\,\delta(\rho-\rho_a)\Theta\left(\rho_a > \rho_b\right)\times \\ \Theta(z_a > \zeta)\,\Theta(z_b > \zeta)\Theta(\min\left\{\rho_b, z_a z_b \max(\theta_a^2, \theta_b^2)\right\} > \rho_{\min}), \quad (6.3)$$

where in the $\rho_{\min}$ condition we used strong angular ordering to replace θ_{ab}^2 by $\max(\theta_a^2, \theta_b^2)$. Finally, we note that beyond double logarithmic accuracy a more precise result at order α_s^2 can be achieved by considering three collinear partons within a jet without imposing strong ordering between the partons. Such configurations are described by triple-collinear splitting functions and calculations implementing the triple-collinear result were included in the studies of $\mathrm{Y_m}$-Splitter carried out in ref. [25].

---

[4] We shall define all our angles to correspond to the actual angles rescaled by the jet radius R.

6.3.2 Resummed results

Now we turn to the resummed result. We first consider the case where $\tau_{32} < \tau \ll 1$. Then we shall lift the requirement that $\tau \ll 1$ i.e. we shall account for finite τ effects.

The small τ limit

For the case of $\mathrm{Y_m}$-Splitter one considers, as in ref. [25], two real emissions that pass the tagger cuts accompanied by an ensemble of soft and collinear emissions which are constrained to set a smaller gen-k_t distance (i.e. mass) than either of the two leading emissions. This constraint on real emissions produces a Sudakov form factor. In the current case the emissions are additionally constrained by the τ cut. Here we shall derive the Sudakov form factor at leading-logarithmic (LL) accuracy, capturing all double-logarithmic terms including those in τ and running coupling effects, and also include some important single logarithmic effects such as accounting for hard-collinear radiation.

For the two emissions accounted for at leading-order, Eq. (6.2), we shall again label ρ_a as the emission that sets the larger mass and ρ_b the smaller mass. Consider first all subsequent *primary* emissions, i.e. emissions from the hard parton initiating the jet. These emissions must not give rise to larger mass (gen-k_t) values than the first two emissions de-clustered by $\mathrm{Y_m}$-Splitter *and* they must set a value of $\tau_{32} < \tau$. Recall that the contribution of an emission i to τ_N is given by $z_i \min(\theta_{i1}^2, ..., \theta_{iN}^2)$. As was the case for τ_2 [28], the limit of strong angular-ordering ensures that, for emissions coming from a leg lying along one of the N-subjettiness axes, the smallest of the θ_{ia} angles is either the angle between the emission and its emitter, or can be approximated by this angle to LL accuracy. For a primary emission this implies that the contribution to τ_3, $\tau_{3i} = z_i\theta_i^2$ where z_i is the energy fraction and θ_i is the angle of the emission with respect to the hard initial parton. The value of τ_2 on the other hand is dominated, to LL accuracy, by the second highest mass emission ρ_b, due to the strong ordering in masses relevant at LL accuracy. [5] The condition on primary emissions then reads:

$$\Theta\left(\frac{\sum_{i=3}^{\infty} z_i\theta_i^2}{\rho_b} < \tau\right)\prod_{i=3}^{\infty}\Theta\left(z_i\theta_i^2 < \rho_b\right). \tag{6.4}$$

The first step function reflects the condition on τ_{32} while the second condition reflects the constraint on mass which gives the primary emission Sudakov form factor for $\mathrm{Y_m}$-Splitter in ref. [25], i.e. that none of the emissions i have a gen-k_t distance larger than ρ_b by assumption. Since $\tau < 1$ the second condition is automatically satisfied and the condition on primary emissions is just given by the stronger constraint $\Theta\left(\sum_{i=3}^{\infty} z_i\theta_i^2 < \rho_b\tau\right)$. The primary emission Sudakov factor then arises from

---

[5] For going beyond the small τ limit and including finite τ effects we shall, in the next subsection, lift this requirement of strong ordering in masses as was done in ref. [26].

a veto on any emissions violating this condition. More precisely it takes the form $S = e^{-R^{(\text{primary})}}$ with the "radiator" $R^{(\text{primary})}$ given by

$$R^{(\text{primary})}\left(\tau\rho_b\right) = \frac{C_R}{2\pi}\int \alpha_s(z^2\theta^2R^2p_T^2)p(z)\mathrm{d}z\frac{\mathrm{d}\theta^2}{\theta^2}\Theta(z\theta^2 > \rho_b\tau), \tag{6.5}$$

where C_R is a colour factor that depends on the identity of the initiating jet i.e. C_F for a quark and C_A for a gluon jet, and $p(z)$ is the QCD splitting function describing collinear emission from a quark ($p(z) = p_{gq}(z)$) or gluon ($p(z) = p_{gg}(z)$). For the argument of the running coupling we have used the k_t of the emission (in terms of z and θ) as required in the soft and collinear limit.

As well as vetoing primary emissions from the parton initiating the jet, the overall Sudakov factor must also account for a veto on secondary emissions which would set a value of τ_{32} larger than τ from either of the two emissions included in the leading order pre-factor. In the case of soft secondary emissions the angle of emission θ_i is limited by angular-ordering to be less than the angle of the parent θ_a or θ_b. Apart from this constraint, for emissions off parton a we have the same constraint as for primary emissions and hence we obtain, for emissions off parton a:

$$\begin{aligned}R^{(\text{secondary,a})}\left(\tau,\rho_a,\rho_b\right) &= \\ &\frac{C_A}{2\pi}\int \alpha_s(z^2z_a^2\theta^2R^2p_T^2)p_{gg}(z)\mathrm{d}z\frac{\mathrm{d}\theta^2}{\theta^2}\Theta(zz_a\theta^2 > \rho_b\tau)\Theta(\theta^2 < \theta_a^2),\end{aligned} \tag{6.6}$$

where we note that z represents the energy fraction of parton a's energy carried by the soft secondary emission. We also note that for secondary emissions, the gen-k_t distance, entering the veto condition above, differs from the mass even in the soft limit, involving one less factor of z_a. A similar equation gives the result for emissions off parton b, with the obvious replacement of z_a and θ_a by z_b and θ_b.

The overall result can be written as a Sudakov form factor weighting the leading-order, order α_s^2 result which serves as a pre-factor. For simplicity if one retains just the leading-logarithmic expression for the pre-factor reported in Eq. (6.3), we can obtain the resummed result by inserting the factor $S = e^{-R}$ in the integrand in Eq. (6.3) where $R = R^{(\text{primary})} + R^{(\text{secondary,a})} + R^{(\text{secondary,b})}$. While our results include the full running coupling and hard-collinear effects we report below a simplified result for the Sudakov factor S in the limit of a fixed coupling and retaining only the soft-collinear behaviour i.e. replacing $p(z)$ and $p_{gg}(z)$ by the soft limit expression $2/z$:

$$S^{(\text{fixed-coupling, soft})} = \exp\left[-\frac{C_R\alpha_s}{2\pi}\ln^2\frac{1}{\tau\rho_b} - \frac{C_A\alpha_s}{2\pi}\ln^2\frac{\rho_a}{\tau\rho_b} - \frac{C_A\alpha_s}{2\pi}\ln^2\frac{1}{\tau}\right], \tag{6.7}$$

where the term involving $\ln^2 1/\rho\tau_b$ comes from primary emissions, the term involving $\ln^2\frac{\rho_a}{\tau\rho_b}$ comes from vetoing emissions from emission a and finally the suppression involving just $\ln^2 1/\tau$ comes from vetoing emissions from emission b. The difference between primary and secondary emissions arises entirely from angular-ordering and the ensuing limitation on emission angle we mentioned previously. Although the logarithms present in S are written above in terms of ρ_a and ρ_b, these will eventually be related to logarithms of ρ, $\rho_{\min}$ and ratios thereof once the integrals in the pre-factor a carried out. In the limit $\tau \to 1$ of the above result we obtain the pure $\mathrm{Y_m}$-Splitter result of ref. [25].

A couple of further remarks are in order concerning the result in Eq. (6.7). First of all the result captures leading double logarithms in τ in addition to the logarithms involved in the resummation of plain $\mathrm{Y_m}$-Splitter [25]. Including hard-collinear emission via using the full splitting functions, rather than just their soft limit, and using the running coupling helps to improve the result beyond double-logarithmic accuracy. The result indicates that the effect of the N-subjettiness cut is to produce an extra suppression relative to the case of $\mathrm{Y_m}$-Splitter [25] just by changing the scale ρ_b to the smaller scale $\tau\rho_b$ and the extra secondary suppression factor we get from emissions off parton b. This suppression of the background is of course desirable but choosing a small τ value potentially also suppresses the signal, which in this case is a coloured particle namely the top quark. Also as is well-known from several prior applications [14], [137] and additionally emerges in the Monte Carlo studies we reported in section 6.2, optimal values of τ do not necessarily satisfy $\tau \ll 1$, so that finite τ effects generally need to be considered [26] in addition to the resummation of logarithms of τ. The inclusion of finite τ corrections is thus the topic of the next subsection.

6.3.3 Finite τ corrections

To obtain an insight into the role of the τ_{32} cut in a phenomenological context, one has to address values of $\tau \sim 1$. From the viewpoint of resummation this has implications identical to those first pointed out in the τ_{21} case [26]. The small τ limit resummation of the previous subsection is designed to fully capture double logarithmic terms of the form $\alpha_s^n L^{2n}$ where, for power counting purposes, we use the symbol L^{2n} to denote double logarithms in any of $\ln\rho$, $\ln\rho_{\min}$, $\ln\frac{\rho}{\rho_{\min}}$, $\ln\tau$ or any combination of them. From the fixed-coupling Sudakov form factor, Eq. (6.7), written in terms of ρ_a, ρ_b and τ we note that we obtain terms that are single logarithmic in jet masses (and jet mass ratios) but double logarithmic overall due to the role of $\ln\tau$ i.e. terms of the form $\alpha_s \ln\rho_b \ln\tau$ and $\alpha_s \ln\frac{\rho_a}{\rho_b}\ln\tau$. Beyond the small τ limit we need to account for such terms beyond just their $\ln\tau$ dependence i.e. obtain the full function f_τ that multiplies single logarithms in jet mass. However, given that single logarithms in jet mass ratios i.e. $\alpha_s \ln\rho_b/\rho_a$ are smaller, we do not attempt to obtain the finite τ corrections for such terms, which is substantially more involved, and accordingly retain their small τ form only. In the Sudakov form factor with inclusion of running coupling, we therefore wish to control terms of the form $\alpha_s^n L_\rho^n f_n(\tau)$ (where L_ρ generically denotes logarithms in jet masses but not ratios), while the small τ resummation accounts only for terms that approximate $f_n(\tau)$ by its leading small τ behaviour

$\sim \ln^n \tau$.

While in the small τ limit resummation of the previous subsection we assumed that emissions were strongly ordered in terms of their contribution to the jet mass (in addition to strong ordering in angle), in order to achieve resummation of terms $\alpha_s^n L_\rho^n$ with their accompanying τ dependence we no longer assume strong ordering in jet masses. In particular we assumed that τ_2 was set by a single emission b, and hence its value was taken to be ρ_b. Beyond the small τ limit, we must account for the fact that τ_2 receives a contribution from all emissions in the jet except emission a. Since we still desire terms that are at least single logarithmic in jet masses, we continue to assume that emissions are strongly ordered in angle. This approximation of emissions ordered in angle but not in mass is the same as was made in the case of τ_{21} studies for two-pronged decays [26], to obtain the finite τ correction to the small τ results [28]. We can then write

$$\tau_{32} = \frac{\rho - \rho_a - \rho_b}{\rho - \rho_a}, \tag{6.8}$$

where the numerator comes from τ_3 being given by the sum of jet masses contributed by all emissions except a and b, while the denominator is τ_2 which is given by the sum of jet masses contributed by all emissions except emission a. The sum of all emissions' contributions to jet mass, including those of a and b, just gives the total jet mass ρ.

Differential distribution in τ

We begin by presenting a result for the joint distribution in jet mass ρ and τ i.e. the quantity $\frac{\rho\tau}{\sigma}\frac{d^2\sigma}{d\rho d\tau}$, where τ is a set value of τ_{32}. To begin with we shall consider primary emissions only, since it is straightforward to account for secondary emissions in the final result.

We first write the result for the cross-section differential in both τ and ρ, which accounts for the two emissions a and b included in the leading-order formula but now accompanied by an infinite number of additional emissions which are strongly ordered in angle. The strong ordering in angle ensures that these emissions are emitted independently from the hard initial parton which leads to the standard factorised formula for any number of emissions:

$$\begin{aligned}\frac{\rho\tau}{\sigma}\frac{\mathrm{d}^2\sigma}{\mathrm{d}\rho\mathrm{d}\tau} = \bar{\alpha}^2 \int_\zeta^1 \frac{\mathrm{d}z_a}{z_a}\int_0^1 \frac{\mathrm{d}\rho_a}{\rho_a}\int_\zeta^1 \frac{\mathrm{d}z_b}{z_b}\int_0^{\rho_a}\frac{\mathrm{d}\rho_b}{\rho_b}\times \\ \Theta(\min(\rho_b, z_a z_b \max(\frac{\rho_a}{z_a},\frac{\rho_b}{z_b})) > \rho_{\min}) \exp\left[-\int_0^1 R'(\rho')\frac{\mathrm{d}\rho'}{\rho'}\right] \\ \sum_{p=1}^{\infty}\frac{1}{p!}\prod_{i=1}^{p}\int_0^{\rho_b} R'(\rho_i)\frac{\mathrm{d}\rho_i}{\rho_i}\rho\delta(\rho-\rho_a-\rho_b-\sum_{i\neq a,b}\rho_i)\,\tau\delta\left(\tau-1+\frac{\rho_b}{\rho-\rho_a}\right).\end{aligned} \tag{6.9}$$

The above result is written using a fixed-coupling approximation for the emission of partons a and b though we shall account for the running of the coupling, with the k_t of those emissions, in the pre-factor for our final results. It involves considering p factorised real emissions, with a sum over all p, alongside a sum over all virtual corrections included via the exponential form factor. The factor R', appearing in both real and virtual terms above, stems from the integral over the emission probability for a single emission in the soft and collinear limit, at a fixed mass, ρ :

$$R'(\rho) = C_R \int_0^1 \frac{\mathrm{d}\theta^2}{\theta^2} \mathrm{d}z\; p(z) \frac{\alpha_s(z\theta p_T R)}{2\pi} \rho\delta(z\theta^2 - \rho) \overset{\text{f.c.}}{=} \frac{C_R \alpha_s}{\pi} \left(\ln \frac{1}{\rho} + B_i \right), \tag{6.10}$$

where the RHS of the above equation gives the fixed-coupling result and we have replaced the splitting functions $p(z)$ by their soft piece $\propto 1/z$ and incorporated the effect of hard-collinear emissions by introduction of the B_i terms, corresponding to inclusion of the hard-collinear piece of the splitting function to our accuracy. For quark and gluon jets respectively $B_q = -{}^3/_4$ and $B_g = {}^{(-11C_A + 4n_f T_R)}/_{(12C_A)}$.

Integrating over ρ_b in Eq. (6.9) using the delta function constraint involving τ allows us to set $\rho_b = (1-\tau)\,(\rho - \rho_a)$ which then leads to the result, assuming $\tau < 1/2$,

$$\begin{aligned} &\frac{\rho\tau}{\sigma} \frac{\mathrm{d}^2\sigma}{\mathrm{d}\rho \mathrm{d}\tau} = \\ &\quad \bar{\alpha}^2 \frac{\tau}{1-\tau} \int_\zeta^1 \frac{\mathrm{d}z_a}{z_a} \int_\zeta^1 \frac{\mathrm{d}z_b}{z_b} \int_0^\rho \frac{\mathrm{d}\rho_a}{\rho_a} \Theta\left(\rho_a > \frac{1-\tau}{2-\tau}\rho \right) \Theta_{\rho_{\min}}\left(\rho_a, \tau, \rho_{\min}, z_a, z_b\right) \\ &\quad \exp\left[-\int_0^1 R'(\rho') \frac{\mathrm{d}\rho'}{\rho'} \right] \sum_{p=1}^{\infty} \frac{1}{p!} \prod_{i=1}^{p} \int_0^{\rho_b} R'(\rho_i) \frac{\mathrm{d}\rho_i}{\rho_i} \rho\delta\left((\rho - \rho_a)\tau - \sum_{i \neq a,b} \rho_i \right), \end{aligned} \tag{6.11}$$

where we have used the shorthand notation $\Theta_{\rho_{\min}}$ to denote the $\rho_{\min}$ condition and the ρ_b that occurs as an upper limit in the ρ_i integral is understood to be the value set by the delta function i.e $(\rho - \rho_a)(1-\tau)$. The other step function constraint on ρ_a derives from the condition that $\rho_a > \rho_b$ and the value of ρ_b set by the delta function integral we have performed. Finally we observe that we are left to evaluate the multiple emission contribution where the sum over the ρ_i are constrained to be equal to $(\rho-\rho_a)\tau$. Additionally each emission i is constrained so that $\rho_i < \rho_b = (1-\tau)(\rho-\rho_a)$, however for $\tau < 1/2$ this condition is automatically met if the stronger condition on the sum of ρ_i is satisfied. In what follows we restrict our attention to $\tau < 1/2$ as this region is sufficient given the optimal value of τ that emerged from the Monte Carlo studies in section 6.2. Finally we note that one can evaluate the multiple emission contribution on the second line of Eq. 6.9 simply by using known results for the standard jet mass [236], since the constraint on multiple emissions is the same as for the plain jet mass ρ but with ρ replaced by $(\rho - \rho_a)\tau$. Hence without needing to perform any further explicit calculation one can write:

$$\begin{aligned}\frac{\rho\tau}{\sigma}\frac{\mathrm{d}^2\sigma}{\mathrm{d}\rho\mathrm{d}\tau} &\overset{\tau<1/2}{=} \bar{\alpha}^2\frac{1}{1-\tau}\\ &\int_\zeta^1 \frac{\mathrm{d}z_a}{z_a}\int_\zeta^1 \frac{\mathrm{d}z_b}{z_b}\int_0^\rho \frac{\mathrm{d}\rho_a}{\rho_a}\frac{\rho}{\rho-\rho_a}\Theta\left(\rho_a > \frac{1-\tau}{2-\tau}\rho\right)\Theta_{\rho_{\min}}\left(\rho_a,\tau,\rho_{\min},z_a,z_b\right)\\ &R'((\rho-\rho_a)\tau)\frac{\exp[-R((\rho-\rho_a)\tau)-\gamma_E R'((\rho-\rho_a)\tau)]}{\Gamma[1+R'((\rho-\rho_a)\tau)]}.\end{aligned}\tag{6.12}$$

The above result accounts for configurations where the three prongs tagged by $\mathrm{Y_m}$-Splitter are the hard parton which initiates the jet along with two gluons emitted independently from it, however, our final result also contains configurations where a gluon emitted from the hard parton branches, with the resulting three particles corresponding to the three $\mathrm{Y_m}$-Splitter prongs.

For the region $\tau > 1/2$ one could in principle follow the same method as outlined for the τ_{21} calculation in ref. [26], though given our immediate motivation we do not consider this region further in the present study. We could also have initially integrated over ρ_a instead of ρ_b to obtain the result in the equivalent form

$$\begin{aligned}\frac{\rho\tau}{\sigma}\frac{\mathrm{d}^2\sigma}{\mathrm{d}\rho\mathrm{d}\tau} &\overset{\tau<1/2}{=} \bar{\alpha}^2\frac{1}{1-\tau}\int_\zeta^1 \frac{\mathrm{d}z_a}{z_a}\int_\zeta^1 \frac{\mathrm{d}z_b}{z_b}\int_0^{\frac{\rho}{2}} \frac{\mathrm{d}\rho_b}{\rho_b}\frac{\rho}{\rho-\frac{\rho_b}{1-\tau}}\Theta_{\rho_{\min}}\left(\rho_b,\tau,\rho_{\min},z_a,z_b\right)\\ &R'(\rho_b\frac{\tau}{1-\tau})\frac{\exp[-R(\rho_b\frac{\tau}{1-\tau})-\gamma_E R'(\rho_b\frac{\tau}{1-\tau})]}{\Gamma[1+R'(\rho_b\frac{\tau}{1-\tau})]}.\end{aligned}\tag{6.13}$$

A key feature of our results is the presence of an overall $1/(1-\tau)$ factor as was also the case in the τ_{21} result of ref. [26]. Taking the small τ limit of Eq. (6.12) we should return to the small τ result we derived in the previous subsection, which is indeed the case up to subleading terms in the order $\bar{\alpha}^2$ pre-factor. To be more precise, in the previous subsection we had evaluated the pre-factor taking ρ_a to dominate the jet mass, by using the condition $\delta(\rho-\rho_a)\Theta(\rho_a > \rho_b)$, which correctly captures all double logarithmic terms in the pre-factor. If instead one uses the more accurate condition $\delta(\rho-\rho_a-\rho_b)\Theta(\rho_a > \rho_b)$, then after integration over ρ_b we obtain the same result as the small τ limit of Eq. (6.12). Relative to the strong ordering of emissions ρ_a and ρ_b, using the exact jet mass conditions affects only single logarithmic terms $\bar{\alpha}^2L^2$ in the pre-factor where L denotes logarithms in $\rho/\rho_{\min}$ or ζ. Such terms are two logarithms below the leading $\bar{\alpha}^2L^4$ terms in the pre-factor and only involve more modest logarithms than those in the jet mass. We can therefore consider such terms as negligible and hence the small τ limit of Eq. (6.12) is equivalent to the result of the previous subsection. For an explicit calculation demonstrating the argument above, we refer the reader to appendix C.1.

Beyond the small τ limit the most crucial feature of the result is the overall $1/(1-\tau)$ factor in Eq. (6.12). While there is additionally a τ dependence in the step functions in Eq. (6.12), that is again responsible for introducing τ dependent terms of order

$\bar{\alpha}^2 L^2$ in the pre-factor, and hence can be neglected to our accuracy as illustrated in appendix C.1. In what follows we shall use the freedom to set τ to zero in the step function conditions to obtain an analytic form for the cumulative distribution.

Cumulative distribution

It is of direct interest to also obtain the result for the differential distribution in the jet mass with a cut on τ_{32}, $\tau_{32} < \tau$, rather than fixing a value for τ_{32} as required for the double differential distribution above. In order to do this one can integrate the differential distribution, Eq. (6.12), between 0 and τ. Setting τ to zero in the step functions of the pre-factor, which has only a sub-leading impact as discussed before, we can write

$$\rho \frac{d\sigma}{d\rho}\bigg|_{\tau_{32}<\tau} \overset{\tau<1/2}{=} \bar{\alpha}^2 \int_\zeta^1 \frac{\mathrm{d}z_a}{z_a} \int_\zeta^1 \frac{\mathrm{d}z_b}{z_b} \int_0^\rho \frac{\mathrm{d}\rho_a}{\rho_a} \frac{\rho}{\rho-\rho_a} \Theta\left(\rho_a > \frac{\rho}{2}\right) \Theta_{\rho_{\min}}\left(\rho_a, \rho_{\min}, z_a, z_b\right)$$
$$\int_0^\tau \frac{d\tau'}{\tau'(1-\tau')} R'((\rho-\rho_a)\tau') \frac{\exp[-R((\rho-\rho_a)\tau') - \gamma_E R'((\rho-\rho_a)\tau')]}{\Gamma[1+R'((\rho-\rho_a)\tau')]}, \quad (6.14)$$

which corresponds to integrating the distribution up to some maximum value τ for τ_{32}. To single-logarithmic accuracy, we can expand the radiator about some point τ_0 to write:

$$R((\rho-\rho_a)\tau') \simeq R((\rho-\rho_a)\tau_0) - R'((\rho-\rho_a)\tau_0) \ln\left(\frac{\tau'}{\tau_0}\right) + \mathcal{O}\left(R''\right), \quad (6.15)$$

where $R'(x) = -\frac{\partial R}{\partial \ln x}$. With τ_0 chosen such that in the small τ limit τ_0 is of order τ, and given that the integral is dominated by values $\tau' \sim \tau$, terms of order R'' and beyond can be neglected as they are beyond single-logarithmic accuracy and we may replace τ' by τ_0 in the R' terms to obtain:

$$\rho \frac{d\sigma}{d\rho}\bigg|_{\tau_{32}<\tau} \overset{\tau<1/2}{=} \bar{\alpha}^2 \int_\zeta^1 \frac{\mathrm{d}z_a}{z_a} \int_\zeta^1 \frac{\mathrm{d}z_b}{z_b} \int_0^\rho \frac{\mathrm{d}\rho_a}{\rho_a} \frac{\rho}{\rho-\rho_a} \Theta\left(\rho_a > \frac{\rho}{2}\right) \Theta_{\rho_{\min}}\left(\rho_a, \rho_{\min}, z_a, z_b\right)$$
$$R'((\rho-\rho_a)\tau_0) \frac{\exp[-R((\rho-\rho_a)\tau_0) - \gamma_E R'((\rho-\rho_a)\tau_0)]}{\Gamma[1+R'((\rho-\rho_a)\tau_0)]} \times I(R', \tau, \tau_0), \quad (6.16)$$

where

$$I(R', \tau, \tau_0) = \int_0^\tau \frac{d\tau'}{\tau'(1-\tau')} \exp\left[R'\left((\rho-\rho_a)\tau_0\right) \ln \frac{\tau'}{\tau_0}\right]. \quad (6.17)$$

Upon evaluating the integral over τ we obtain

$$I(R', \tau, \tau_0) = \left(\frac{\tau}{\tau_0}\right)^{R'} \frac{{}_2F_1(1, R', 1+R', \tau)}{R'}, \qquad R' \equiv R'((\rho-\rho_a)\tau_0). \quad (6.18)$$

We then have the result for the cumulative distribution given by Eq. (6.16) with finite τ effects encoded in the Hypergeometric function of Eq. (6.18) precisely as for the τ_{21} case [26]. The origin of the Hypergeometric factor is simply the extra overall factor of $1/(1-\tau)$ in the finite τ differential distribution. Without this factor we simply obtain the usual result for the cumulative (integrated distribution) up to terms involving R'' beyond our accuracy, as long as $\tau_0 \sim \tau$. In what follows we shall simply choose $\tau_0 = \tau$ while noting that varying this choice by an $\mathcal{O}(1)$ factor will correspond to an effective resummation scale uncertainty on our results.

To obtain an alternate form of Eq. (6.16) we could have integrated Eq. (6.13) over τ instead. Again, as before, we can drop any τ dependence in the pre-factor other than the overall $\frac{1}{1-\tau}$, which leads to a factor $\rho/(\rho - \rho_b)$, rather than $\rho/\left(\rho - \frac{\rho_b}{1-\tau}\right)$. This again leads one to consider only the overall $1/(1-\tau)$ factor together with the τ dependence in the exponent. Then integrating over τ using the same steps that gave Eq.(6.16) we obtain

$$\rho \frac{d\sigma}{d\rho}\bigg|_{\tau_{32}<\tau} \overset{\tau<1/2}{=} \bar{\alpha}^2 \int_{\zeta}^{1} \frac{\mathrm{d}z_a}{z_a} \int_{\zeta}^{1} \frac{\mathrm{d}z_b}{z_b} \int_{\rho_{min}}^{\frac{\rho}{2}} \frac{\mathrm{d}\rho_b}{\rho_b} \frac{\rho}{\rho - \rho_b} \Theta_{\rho_{\min}}\left(\rho_b, \rho_{\min}, z_a, z_b\right)$$
$$ {}_2F_1(1, R'(\rho_b \frac{\tau}{1-\tau}), 1 + R'(\rho_b \frac{\tau}{1-\tau}), \tau) \frac{\exp[-R(\rho_b \frac{\tau}{1-\tau}) - \gamma_E R'(\rho_b \frac{\tau}{1-\tau})]}{\Gamma[1 + R'(\rho_b \frac{\tau}{1-\tau})]}, \quad (6.19)$$

where we have again used the freedom to neglect factors of τ in the pre-factor which only introduce terms of order $\bar{\alpha}_s^2 L^2$ and set τ_0 to τ.

While so far we have worked with a fixed-coupling approximation in our pre-factor, we now introduce the running of the coupling for “emissions” a and b. In order to do so we replace the $\bar{\alpha}^2$ term with $\bar{\alpha}(z_a \rho_a p_T^2 R^2) \times \bar{\alpha}(z_b(\rho - \rho_a) p_T^2 R^2)$ inside the integral of Eq. (6.16). This corresponds to using the k_t of each emission in the argument of the corresponding coupling factor, with neglect of a factor of $1 - \tau$ in the coupling associated to emission b, i.e. using $\rho_b = (\rho - \rho_a)$ instead of $(\rho - \rho_a)(1 - \tau)$. The $1 - \tau$ factor only results in sub-leading terms involving logarithms of $1 - \tau$ which we neglect, consistent with our general treatment of the pre-factor.

Finally to include secondary emissions we use the full radiator including the secondary emission terms i.e. replace

$$R((\rho - \rho_a)\tau) \to R^{(\text{primary})}((\rho - \rho_a)\tau) + R^{(\text{secondary,a})}((\rho - \rho_a)\tau, z_a, \theta_a^2)$$
$$+ R^{(\text{secondary,b})}((\rho - \rho_a)\tau, z_b, \theta_b^2), \quad (6.20)$$

where $\theta_a^2 = \frac{\rho_a}{z_a}$, $\theta_b^2 = \frac{\rho_b}{z_b}$ and $\rho_b = (\rho - \rho_a)$.

Pre-grooming with Soft Drop

It is known that the Y-Splitter and $\mathrm{Y_m}$-Splitter methods need to be supplemented by some form of grooming in order to yield good performance for the signal significance (signal to square-root of background ratio) [25], [29], [30]. In ref. [29] it was found, in the context of W/Z/H tagging, that pre-grooming jets with Soft Drop was optimal in terms of increasing performance while minimising the sensitivity to non-perturbative effects. Furthermore, in the context of top-tagging there is another advantage to pre-grooming, namely that the pre-grooming procedure leads to a Sudakov form factor inherited from the groomer [29]. In other words for mMDT pre-grooming we obtain the mMDT Sudakov structure, while for Soft Drop with non-zero β we obtain the Soft Drop Sudakov for both signal and background jets. Given that a modest rather than strong Sudakov suppression was found to be beneficial for signal significance in top-tagging [25], pre-grooming with mMDT which has only a single-logarithmic Sudakov form factor, followed by $\mathrm{Y_m}$-Splitter , emerged as the most performant method as well as being resilient to non-perturbative effects.

Here we consider QCD jets pre-groomed with mMDT as well as Soft Drop for $\beta = 2$. In ref. [25] a result was obtained for the jet mass distribution with Soft Drop pre-grooming followed by the application of $\mathrm{Y_m}$-Splitter i.e. without the additional τ cut involved here. As described in detail in ref. [25], three situations can arise : a) the largest gen-k_t emission, i.e. a in the present paper, stops the groomer, b) the next largest gen-k_t emission, i.e. b stops the groomer and c) another emission stops the groomer. For the first situation the result obtained for the primary emission radiator, with mMDT grooming, was shown to be of the form:

$$R^{(1),(\text{primary})}(\theta_a, \rho_b) = R_{\text{mMDT}}(\rho_b) + R^{\text{angle}}_{\text{mMDT}}(\theta_a, \rho_b). \tag{6.21}$$

This corresponds to the usual mMDT Sudakov at the scale ρ_b but modified by the addition of an extra piece, $R^{\text{angle}}_{\text{mMDT}}$ that arises because emissions with angle below θ_a are not examined by the groomer and hence need to be vetoed (if they have mass above ρ_b) even if they have $z < \zeta$. This extra contribution, at fixed-coupling and leading logarithmic accuracy, is given by [25]:

$$R^{\text{angle}}_{\text{mMDT}}(\theta_a, \rho_b) = \frac{C_R \alpha_s}{\pi} \int \frac{dz}{z} \frac{d\theta^2}{\theta^2} \Theta\left(z < \zeta\right) \left(z\theta^2 > \rho_b\right) \Theta\left(\theta_a^2 > \theta^2\right) \ . \tag{6.22}$$

In case b), where emission b stops the tagger, one obtained instead just the standard mMDT result $R_{\text{mMDT}}(\rho_b)$, while for case c) where an emission other than a or b stops the tagger, there is a complete cancellation against virtual corrections and hence no contribution.

For our current work, where we also apply a τ cut, situation a) yields the result reported in Eq. (6.21) but now the mass scale ρ_b is replaced by $\tau(\rho - \rho_a)$ in both terms of Eq. (6.21). In the case b) where emission b stops the tagger we now have to also account for the fact that while emissions with $z < \zeta$ and $\theta < \theta_b$ can never set a mass, or equivalently gen-k_t distance, above ρ_b, they can set a mass larger than $\tau(\rho - \rho_a)$. This is disallowed by the τ cut and hence such emissions have to be vetoed which leads to the appearance of a term $R^{\text{angle}}_{\text{mMDT}}(\theta_b, \tau(\rho - \rho_a))$, in addition to $R_{\text{mMDT}}(\tau(\rho - \rho_a))$, also in case b). For case c) there is no change, i.e. there is complete cancellation with virtual corrections.

Taking into account hard-collinear emissions and the running of the coupling we can write our result in the form

$$\begin{aligned} R^{(\text{primary})}_{\text{groomed-mMDT}}((\rho-\rho_a)\tau,\theta_1) = & \\ & \int \frac{C_R\alpha_s(z\theta p_T)}{\pi}\left(\frac{1}{z}+B_i\right)\mathrm{d}z\frac{\mathrm{d}\theta^2}{\theta^2}\Theta(z\theta^2>(\rho-\rho_a)\tau)\Theta(z>\zeta)+ \\ + & \int \frac{C_R\alpha_s(z\theta p_T)}{\pi}\left(\frac{1}{z}+B_i\right)\mathrm{d}z\frac{\mathrm{d}\theta^2}{\theta^2}\Theta(z\theta^2>(\rho-\rho_a)\tau)\Theta(z<\zeta)\Theta(\theta^2<\theta_1^2), \quad (6.23)\end{aligned}$$

where the first line is just the standard mMDT result [21], the second line is the extra R^{angle} contribution and $\theta_1 = \max(\theta_a,\theta_b)$ is the angle of the emission which stops the groomer. The basic form of the result is then that of the mMDT Sudakov evaluated at the scale $(\rho-\rho_a)\tau$, which corresponds to a single-logarithmic Sudakov suppression. In a fixed-coupling leading log approximation, the R^{angle} term can be written as

$$R^{\text{angle}}(\theta_1,(\rho-\rho_a)\tau) = \frac{C_R\alpha_s}{2\pi}\ln^2\frac{\zeta\theta_1^2}{(\rho-\rho_a)\tau}\Theta(\theta_1^2\zeta>(\rho-\rho_a)\tau)\ , \quad (6.24)$$

where the logarithm involves a ratio of two small quantities similar to be behaviour obtained for secondary emission contributions. Overall therefore we retain the feature that pre-grooming with mMDT results in a reduced Sudakov suppression factor relative to the un-groomed case. The step function in eq. (6.24) switches off the R^{angle} contribution when $\theta_1^2 < \frac{(\rho-\rho_a)\tau}{\zeta}$ leading to the two regimes shown on the Lund diagrams in figure 6.2, where the R^{angle} piece is active only in figure 6.2a and is responsible for vetoing emissions in the region of phase space shown in blue. The standard soft drop Sudakov factor at the scale $(\rho-\rho_a)\tau$ is responsible for vetoing the region of phase space shown in red in figure 6.2.

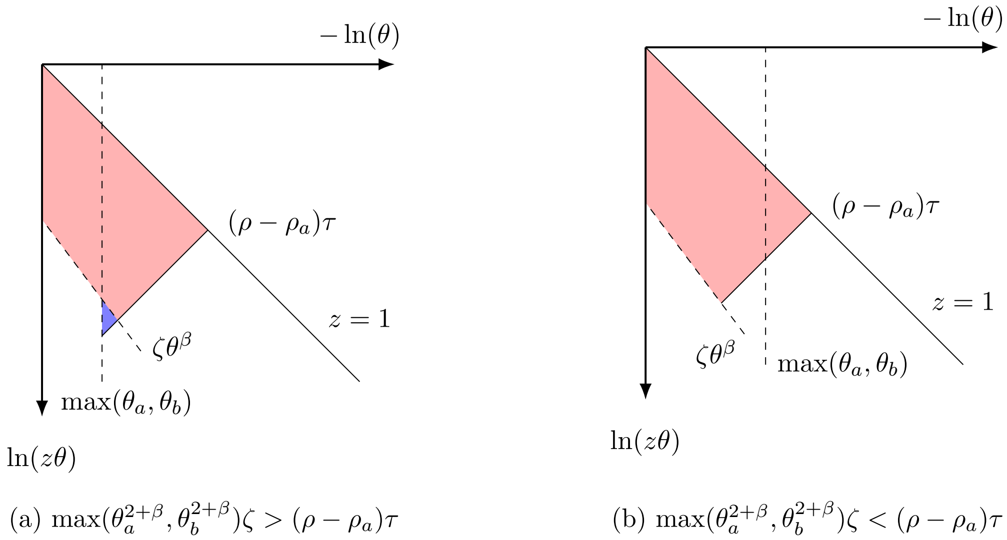

(a) $\max(\theta_a^{2+\beta},\theta_b^{2+\beta})\zeta > (\rho-\rho_a)\tau$ (b) $\max(\theta_a^{2+\beta},\theta_b^{2+\beta})\zeta < (\rho-\rho_a)\tau$

Figure 6.2. Lund diagrams showing the region of phase space vetoed for jets which are groomed with Soft Drop and tagged with Y_m-Splitter and a cut on τ_{32}.

One can also consider pre-grooming with Soft Drop. Identical considerations to the mMDT case apply, with the only difference being in the grooming condition i.e. for an emission to pass the grooming one needs $z > \zeta\theta^{\beta}$. We then obtain a result along similar lines to that for the mMDT above, but with the Soft Drop Sudakov (i.e. radiator) replacing that for the mMDT and a corresponding R^{angle} contribution whose fixed-coupling leading-log form is explicitly reported in ref. [25].

Secondary emissions are unaffected by grooming so the only change to the radiator, relative to the un-groomed case, arises from the primary emission term discussed above. The inclusion of finite τ effects is also unchanged relative to our previous discussions so that we still have the result Eq. (6.12) for the differential distribution and Eq. (6.16) for the cumulant but with the primary emission radiator replaced by that for the groomed case Eq. (6.23) for mMDT and its analogue for Soft Drop.

Numerical implementation and parton shower studies

For the rest of this section we focus on quark initiated jets, as in the jet p_T range under consideration, these are the dominant background to top jets, though most of what follows could equally be applied to gluon initiated jets with minimal modifications. The form of Eq. (6.19) is that of the leading $\mathcal{O}\left(\alpha_s^2\right)$ result multiplied by a factor accounting for further emissions. We now perform a type of matching to improve the accuracy with which we calculate this leading order pre-factor. While we have mentioned in section 6.3.1 that a more precise calculation of the leading order pre-factor based around the triple collinear splitting functions is possible, it was shown in [25] that the numerical difference between such a calculation and one using a product of $1 \to 2$ splitting functions, but the full phase-space, is slightly less than 10% for a jet mass of 175 GeV and $m_{\min} = 50$ GeV. Further to this, when a pair of collinear emissions are strongly ordered in angle, as we have considered them to be throughout this work, the appropriate matrix element is a product of $1 \to 2$ splitting functions. We therefore choose to match our resummed calculation on to a pre-factor calculated by taking the matrix element to be a product of $1 \to 2$ splitting functions but still using the full three-particle phase-space in the collinear limit. This particular matching procedure also potentially serves to bring the effects included in our calculations more in line with what is captured by the parton showers which we will compare our calculations to, as while these may be expected to contain elements of the phase-space, they do not include the full triple collinear splitting functions.

We now re-calculate the LO pre-factor at this higher level of accuracy, before showing how it is matched to the full resummation. As before, we use the C_F^2 channel for illustrative purposes, although our final results contain contributions from the $C_F C_A$ and $C_F n_f$ colour channels where similar modifications can be made to those listed below. In what follows, the parton initiating the jet is labelled as parton 3, with the emission at the widest angle to this parton labelled with 1 and the smaller

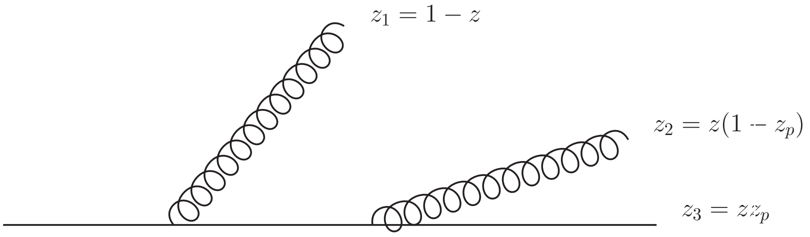

Figure 6.3. Diagram showing the parametrisation of the energy fraction variables used along with our labelling of the partons in the C_F^2 channel.

angle emission labelled 2. So as to ensure that the variables appearing as the arguments of the factorised $1 \to 2$ splitting functions are defined appropriately, we work with the energy fraction variables z and z_p defined so that $z_1 = 1 - z$ and $z_2 = z(1 - z_p)$ as illustrated in figure 6.3. At this level of accuracy, the leading-order calculation in section 6.3.1 becomes

$$\frac{\mathrm{d}\Sigma^{\mathrm{LO}}(\tau,\rho)}{\mathrm{d}\rho} = \left(\frac{C_F\alpha_s}{2\pi}\right)^2 \int p_{gq}(z)p_{gq}(z_p)\mathrm{d}z\mathrm{d}z_p\Delta^{-1/2}\frac{\mathrm{d}\theta_{12}^2}{\pi}\frac{\mathrm{d}\theta_{13}^2}{\theta_{13}^2}\frac{\mathrm{d}\theta_{23}^2}{\theta_{23}^2}\times \\ \delta\left(\rho - \frac{s_{123}}{p_T^2R^2}\right)\Theta_{\mathrm{Y_m\text{-}Splitter}}\,\Theta_{\mathrm{clust.}}\Theta(\theta_{13} > \theta_{23}) \quad (6.25)$$

where the Gram determinant is given by

$$\Delta = 4\theta_{13}^2\theta_{23}^2 - (\theta_{13}^2 - \theta_{12}^2 - \theta_{23}^2)^2, \quad (6.26)$$

and

$$\Theta_{\mathrm{Y_m\text{-}Splitter}} = \Theta(\min(\rho_{12},\rho_{13},\rho_{23}) > \rho_{\min})\Theta(\min(z_1,z_2,z_3) > \zeta), \quad (6.27)$$

where $\rho_{ij} = z_iz_j\theta_{ij}^2$, encapsulating the conditions imposed by Y$_\mathrm{m}$-Splitter without approximating any particles as soft. Similarly, without approximating any particles as soft

$$\Theta_{\mathrm{clust.}} = \sum_{i<j\neq k}\Theta(\theta_{ij} < \min(\theta_{ik},\theta_{jk}))\Theta(\theta_{ij} < R)\Theta(\theta_{ij,k} < R). \quad (6.28)$$

Although the LO part of $\frac{\rho}{\sigma}\frac{\mathrm{d}\sigma}{\mathrm{d}\rho}\Big|_{\tau_{32}<\tau}$ is now calculated without approximating any of the three LO partons as soft, we cannot simply substitute it in place of the $\mathcal{O}(\alpha_s^2)$ part of Eq.(6.19). We must first specify how the quantities appearing in the Sudakov factor of Eq. (6.19), which are defined in the soft and collinear limit, are related to the kinematic variables appearing in our improved LO pre-factor (Eq. 6.25). For the

C_F^2 channel we make the following prescription:

$$\begin{gathered}
\rho_b = \min(\min(z z_p, (1-z))\theta_{13}^2, z\min(z_p, 1-z_p)\theta_{23}^2), \\
k_{t1} = \min(z, 1-z)\theta_{13} R p_T, \qquad k_{t2} = z\min(z_p, 1-z_p)\theta_{23} R p_T, \\
\theta_1 = \theta_{13}, \qquad \rho = \frac{s_{123}}{p_T^2 R^2} + \sum_i \rho_i,
\end{gathered} \tag{6.29}$$

which we note that there is some freedom in choosing, the only constraint being that the correct result must be recovered in the soft and strongly-ordered limit.

Replacing the $\mathcal{O}(\alpha_s^2)$ part of equation (6.19) with Eq. (6.25) and using the matching prescription given in Eq. (6.29) we can write:

$$\begin{aligned}
\rho\frac{\mathrm{d}\Sigma^{\tau<\frac{1}{2}}(\tau)}{\mathrm{d}\rho} = \left(\frac{C_F}{2\pi}\right)^2 \int & \alpha_s(k_{t1})\alpha_s(k_{t2}) p_{gq}(z) p_{gq}(z_p) \Delta^{-1/2}\Theta(\theta_{13} > \theta_{23}) \\
& \delta(\rho - \frac{s_{123}}{p_T^2 R^2})\Theta_{\mathrm{Y_m\text{-}Splitter}}\ \Theta(\theta_{13} > \theta_{23})\ {}_2F_1(1, R'(\rho_b\frac{\tau}{1-\tau}), 1 + R'(\rho_b\frac{\tau}{1-\tau}), \tau) \\
& \frac{e^{-R(\rho_b\frac{\tau}{1-\tau}) - \gamma_E R'(\rho_b\frac{\tau}{1-\tau})}}{\Gamma[1 + R'(\rho_b\frac{\tau}{1-\tau})]} \mathrm{d}z\mathrm{d}z_p \frac{\mathrm{d}\theta_{12}^2}{\pi}\frac{\mathrm{d}\theta_{13}^2}{\theta_{13}^2}\frac{\mathrm{d}\theta_{23}^2}{\theta_{23}^2}\ ,
\end{aligned} \tag{6.30}$$

where the quantities ρ_b, k_{t1}, and k_{t2} are as defined in Eq. (6.29) [6]. Eq. (6.19) can be recovered from Eq. (6.30) by replacing $s_{123} \to \rho_a + \rho_b$, neglecting the hard collinear part of the splitting functions, carrying out the θ_{12} integral (equivalent to an azimuthal integral) and changing phase-space variables back to ρ_a, ρ_b, z_a and z_b. For the sake of brevity, the above result is given only for the C_F^2 colour channel, however, our final results include the $C_F C_A$ and $C_F n_f$ colour channels, where a single gluon is emitted and then decays as opposed to the two independent emissions shown above. We also include secondary Sudakov factors in our final result exactly as before. Our results for pre-groomed jets are obtained by replacing the primary radiator with the groomed variant as discussed in section 6.3.3.

Eq. (6.30) is evaluated numerically using the Suave numerical integrator [237] interfaced to Mathematica [203]. As the cut on τ_{32} restricts emissions down to very low transverse momenta, we freeze the running coupling at $k_t = 1.5$ GeV to prevent divergences due to the Landau pole. The tagged background fraction is constructed from Eq. (6.30) by integrating ρ over the mass window. This is shown in figure 6.4 along with the same quantity derived from parton shower simulations using both Pythia and Herwig [86] for three variations on our calculation: no grooming, Soft Drop with $\beta = 2$ pre grooming, and pre-grooming with mMDT.

---

[6] In deriving equation (6.30) all emissions are considered to contribute to the jet mass as shown in eq. (6.29). As well as allowing us to capture the function of τ multiplying single logarithms in mass scales, this also generates τ dependant terms which are beyond our accuracy. These terms are removed, as discussed in section 6.3.3, by neglecting the τ dependence in the pre-factor beyond the leading $1/1-\tau$ term which leads to the hypergeometric function in eq. (6.30). Specifically, we have set τ to zero inside the delta function, which would otherwise be written as $\delta\left(\rho - \frac{s_{123}}{p_T^2} + \mathcal{O}(\tau)\right)$.

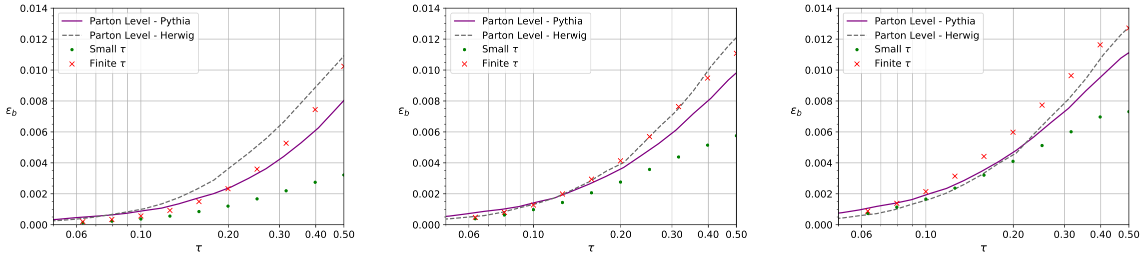

(a) No Grooming.

(b) With $\beta = 2$ Soft Drop

(c) With mMDT

Figure 6.4. A comparison of our calculation for background tagging rate against parton show Monte Carlo simulations for no grooming, grooming with Soft Drop $\beta = 2$, and grooming with mMDT.

In all cases one notes that our results are in reasonable agreement with parton shower predictions, given the uncertainties of the calculations and the shower predictions due to subleading terms present in each case, and also reflected in the difference between Herwig and Pythia showers. In the case of no pre-grooming or grooming with $\beta = 2$ Soft Drop, our finite τ calculation is clearly an improvement of the small τ calculation over a wide range of τ values. Where jets are pre-groomed with mMDT, the finite τ effects we include still have a sizeable impact and improve agreement with the parton showers as $\tau \to \frac{1}{2}$, however, at smaller values of τ it is not clear that agreement with the parton showers is improved by their inclusion. This is potentially due to the fact that the leading logs in this case are single logs and we do not include any sources of next-to–leading logarithms (or their interplay with the τ dependence), other than the finite τ corrections we introduced here.

Figure 6.4 also shows increasing differences between results from parton showers as the level of grooming decreases. Hence the mMDT result, involving more aggressive grooming, is in better agreement between the two shower descriptions over a wider range in τ, while the un-groomed case shows the largest differences. This is likely due to the differences in the modelling of soft gluon effects between the two showers, which is ameliorated by grooming.

6.4 Signal jets

Here we consider the action of the $\mathrm{Y_m}$-Splitter method with a τ_{32} cut on the top quark initiated signal jet. In ref. [25] studies were carried out for top jets with a range of tagging methods including $\mathrm{Y_m}$-Splitter both with mMDT and Soft Drop pre-grooming. Here one has to account, in principle, for gluon radiation in both the top production and top decay processes. In the highly boosted limit the top quark is similar to a light quark and the role of soft gluon radiation and its resummation therefore becomes as important as for the background QCD case. In particular, in the boosted limit one can ignore the dead-cone effect [238], which does not affect our logarithmic accuracy. We shall also consider soft gluon energies well above the top width where we can neglect additional details of the soft gluon emission pattern studied for instance in [239]. In the region relevant to our studies we can therefore consider soft emissions as arising from a single fast moving colour charge aligned with the initial top quark direction. [7]

In spite of these simplifying dynamical assumptions, for top jets, the resummation of large logarithms for the tagging and grooming combinations we consider is more complicated than for the case of background jets. In particular the three-pronged structure of the jet can arise in multiple ways including from the electroweak decay of the top system as well as from soft gluon emission effects. Therefore as in ref. [25] our targeted accuracy will be lower for the signal case and shall omit double logarithms in ζ, $\rho/\rho_{\min}$ and other similar ratios. We shall mainly aim at capturing leading logarithms in $m^2/R^2p_T^2$ where m is a mass-scale which is at most of the order of the top mass.

6.4.1 Jet mass distribution for top jets

We start by computing the fraction of top jets tagged by simply requiring the invariant mass to be within some mass window. Radiation produced by the virtual top quark emerging from the hard process can be recombined with the final top decay products to form the final jet. Placing an upper limit on the jet mass therefore directly constrains this radiation and results in a Sudakov form factor precisely as for a light quark jet. We restrict ourselves to the case where the lower edge of the mass window is below the top mass, so that jets containing all of the top decay products will have mass larger than this. Of course, there will be some fraction of events where not all of the top decay products are reconstructed as a single jet, however such configurations as suppressed by a power of $\frac{m_t}{p_T}$ [30] and hence can be neglected to our accuracy. We can then write the tagged fraction of events as

$$\Sigma(\rho) = \frac{1}{\sigma_0} \int |M_{t\to bq\bar{q}}|^2 \mathrm{d}\Phi_3 \delta\left(\frac{s_{123}}{R^2 p_t^2} - \rho_t\right) \Theta_{\text{Clust}}\ S_{\text{QCD}}, \tag{6.31}$$

where $|M_{t\to bq\bar{q}}|^2$ is the squared matrix-element for the top decay, $\mathrm{d}\Phi_3$ is the three-body phase-space in the collinear approximation, and Θ_{Clust} is the jet clustering condition as for the background case (see Eqs. (6.25) and (6.28)). The normalisation factor σ_0 is just the result without considering QCD corrections i.e. the squared matrix-element for top decay integrated over the final state phase-space with the jet clustering requirement. The factor S_{QCD} takes into account the constraint on QCD radiation through limiting the jet mass. Given that the jet mass can be expressed in terms of multiple soft gluon emissions such that $\rho = \rho_t + \sum_i \rho_i$, with $\rho_t = m_t^2/(R^2p_T^2)$, the constraint on ρ_i just produces a Sudakov form factor which factorises from the

---

[7] To account for large logarithms with a τ_{32} cut we will also need to consider additional collinear radiation from the colour charges arising from W decay within the top jet.

integral over the top-decay phase-space to give:

$$\Sigma(\rho) = \; S_{\mathrm{QCD}} = e^{-R(\rho-\rho_t)}, \tag{6.32}$$

where $R\left(\rho-\rho_t\right)$ is the standard jet mass Sudakov evaluated to NLL accuracy [222] at the shifted scale $\rho-\rho_t$.[8]

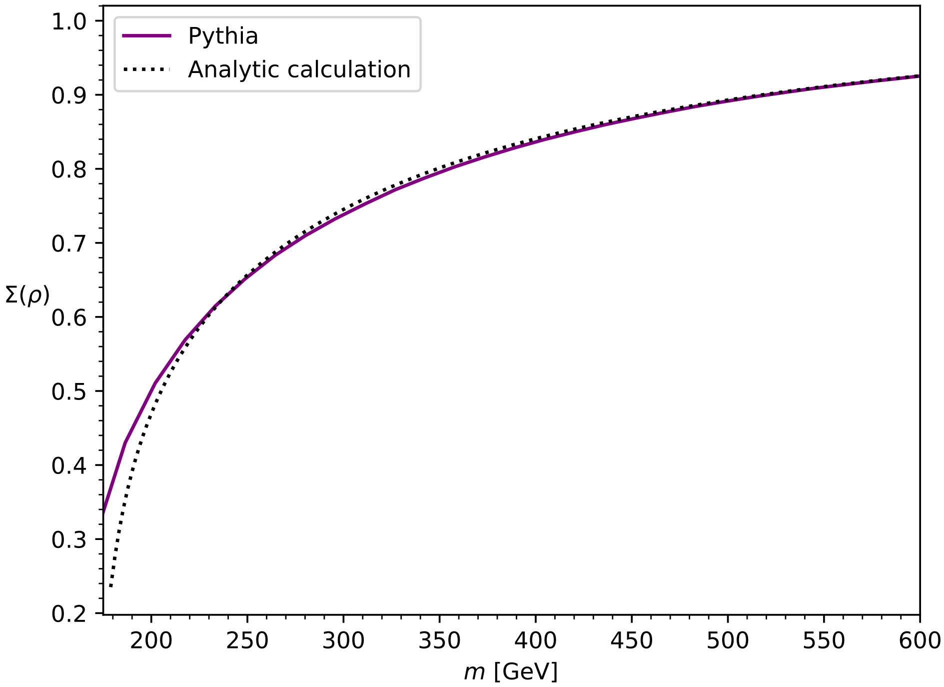

Figure 6.5. A comparison between our analytical calculation of the cumulative jet mass distribution $\Sigma(\rho)$ for top quark initiated jets with $\rho = m^2/R^2 p_T^2$, with $p_T > 2$ TeV and the same distribution derived from Pythia simulations.

In order to test this result and the approximations inherent in deriving it, we compare our result to expectations from Pythia 8. For our Pythia study we choose the lower edge of the mass window to be 10 GeV below the top mass which serves to further reject events where the top decay constituents are not recombined into the final jet. Effects contributing at the lower edge of the mass range should thus only differ from our result by numerically small effects. Pythia was used to create a sample of 1 million $t\bar{t}$ events, with UE, MPI and hadronisation deactivated, and Fastjet [109] was then used to find CA jets with $R = 1$. Figure 6.5 shows the integrated jet mass distribution as the upper limit on the mass range is varied. Our analytical estimate is in good agreement with the distribution obtained with Pythia and Fastjet. As m approaches the top mass the agreement between our calculation and Pythia slightly worsens, which is to be expected, as effects which we neglect, including non-perturbative effects, become relevant for values of m very close to the top mass.

---

[8] Although we use the full heavy jet mass radiator evaluated to NLL accuracy the result is only accurate to modified LL accuracy for our case. In particular we neglect non-global [70] and clustering logarithms [240] that are relevant here at NLL level.

6.4.2 Top jets with $\mathrm{Y_m}$-Splitter

Next we consider the application of $\mathrm{Y_m}$-Splitter to the tagging of top jets. This was already studied in ref. [25] where it was noted that the signal case had a number of additional complications relative to the description of QCD background jets, which made the attainment of leading logarithmic accuracy in each of the parameters ρ, $\rho_{\min}/\rho$ and ζ substantially harder. For this reason only basic leading logarithmic accuracy in ρ (or equivalently in $\rho_{\min}$) was targeted which allowed for a simplified treatment of the Sudakov form factor. Consistently with the accuracy goal of that article, complications including the possibility of soft gluon emissions giving one of the three prongs found by the tagger, and the interplay with the mass window constraint were neglected. The results, broadly speaking, gave a reasonable description of the main behaviour seen with parton showers, but the agreement was not as good as seen for QCD background jets.

Here, prior to discussing N-subjettiness, we shall attempt to at least partially address some of the complications that are mentioned above for pure $\mathrm{Y_m}$-Splitter . In particular we now consider in the soft-collinear limit, the situation where a single soft emission can be de-clustered as one of the prongs found by the tagger in addition to the case where the de-clustered prongs arise from the electroweak top decay process. Let us start by considering the result at leading-order i.e. neglecting all QCD radiative corrections. Then we can write

$$\Sigma(\rho, \rho_{\min}, \zeta) = \frac{1}{\sigma_0} \int |M_{t \to bq\bar{q}}|^2 \mathrm{d}\Phi_3 \delta \left(\frac{s_{123}}{R^2 p_t^2} - \rho_t \right) \Theta_{\mathrm{Clust}} \Theta_{\mathrm{Y_m\text{-}Splitter}} \,, \tag{6.33}$$

where

$$\Theta_{\mathrm{Y_m\text{-}Splitter}} = \Theta(\mathrm{Min}(\rho_{12}, \rho_{13}, \rho_{23}) > \rho_{\min}) \Theta(\mathrm{Min}(z_1, z_2, z_3) > \zeta), \tag{6.34}$$

and $1, 2, 3$ refer to the three prongs identified by $\mathrm{Y_m}$-Splitter . As there is no soft enhancement to the top decay matrix element, we use only a collinear approximation for the pairwise invariant masses, $\rho_{ij} = x_i x_j \theta_{ij}^2$ in our calculations of the leading-order top decay.

Next we consider QCD radiative corrections in the soft and collinear limit. We first take into account the situation that no soft gluon emissions are de-clustered as a prong by $\mathrm{Y_m}$-Splitter . This imposes a constraint on real emissions in addition to the constraint on jet mass, which comes from the requirement that the soft emission must set a smaller gen-k_t distance than those set by the three-pronged top system. Labelling the soft emission by i we then have that $\min(d_{i1}, d_{i2}, d_{i3}) < \min(d_{12}, d_{13}, d_{23})$. This complicated constraint simplifies in the soft and strongly-ordered limit responsible for the leading double logarithms we seek. To be more precise, the three-pronged top decay results in relatively energetic particles owing to the lack of soft enhancement in the electroweak decay. For a soft gluon emission to set a comparable gen-k_t

distance it must be emitted at a relatively large angle compared to the opening angle between the top decay products, $1 \gg \theta_i^2 \gg \theta_{ij}^2$, where θ_i is the angle with respect to the jet axis, or equivalently, the emitting top quark. In this region we can approximate the angle made by the soft emission with any given prong from the top decay simply by the angle with respect to the jet axis which allows us to write the gen-k_t distance for the gluon as $z_i\theta_i^2$.

In addition to the gen-k_t distance, the soft emissions are also subject to the jet mass constraint as before. Therefore the argument of the Sudakov corresponds to whichever is the tighter constraint which gives

$$\begin{aligned}&\Sigma^{(0)}(\rho, \rho_{\min}, \zeta) = \\ &\quad \frac{1}{\sigma_0}\int |M_{t\to bq\bar{q}}|^2 \mathrm{d}\Phi_3 \delta\left(\frac{s_{123}}{R^2 p_t^2} - \rho_t\right)\Theta_{\text{Clust}}\Theta_{\text{Y}_\text{m}\text{-Splitter}}\ e^{-R(\min(d_{12},d_{13},d_{23},\rho-\rho_t))}, \end{aligned} \tag{6.35}$$

where by $\Sigma^{(0)}$ we mean the contribution where we enforce that no soft gluons can give one of the 3 prongs found by the tagger.

Next we correct this picture by allowing a soft emission to form one of the prongs found by Y_m-Splitter , a situation that can first arise at order α_s. Consider a single gluon emerging from the declustering process before one of the top decay products, and thus being identified as a prong. This gluon is constrained so that it has energy fraction $z > \zeta$ and sets a minimum pairwise mass with the other prongs (labelled 1 and 2) of $m_{\min}$, i.e. $\min(\rho_{1g}, \rho_{2g}) > \rho_{\min}$, where g labels the gluon. The gluon must also not set a jet mass which pushes the jet outside of the mass window. The emission of a single soft gluon factorises from the top decay process and gives an order α_s contribution to the pre-factor. Subsequent gluon emissions are constrained by the requirement of not being de-clustered as a prong as well as being subject to the jet mass constraint and again give rise to a Sudakov suppression. Hence we obtain the result:

$$\begin{aligned}&\Sigma^{(1)}(\rho, \rho_{\min}, \zeta) = \\ &\quad \frac{1}{\sigma_0}\int |M_{t\to bq\bar{q}}|^2 \mathrm{d}\Phi_3 \delta\left(\frac{s_{123}}{R^2 p_t^2} - \rho_t\right)\int \mathrm{d}z\frac{d\theta^2}{\theta^2}\frac{\alpha_s(z\theta p_t)C_F}{\pi}p_{gq}(z)\Theta(z\theta^2 < \rho - \rho_{\text{top}}) \\ &\qquad \Theta_{\text{Clust}}\sum_{i<j\neq k}\Bigg(\Theta(d_{ij} < \text{Min}(d_{ik}, d_{kj}))\Theta(z\theta^2 > d_{ij})\Theta(\text{Min}(\rho_{k(ij)},\ z\theta^2) > \rho_{\min}) \\ &\qquad\qquad \Theta(\text{Min}(z, z_k, (z_i + z_j) > \zeta)e^{-R(\text{Min}(d_{k(ij)}, z\theta^2, \rho-\rho_t-z\theta^2))}\Bigg). \end{aligned} \tag{6.36}$$

In the above result the first line gives the pre-factor which, aside from the usual squared matrix-element and phase-space integration for top decay, now also has the QCD pre-factor coming from real emission of the soft gluon. The three prongs are given by the soft gluon, a clustered pair of particles (ij) from the top decay and the remaining particle k arising from the top decay. The condition $\Theta(z\theta^2 > d_{ij})$ alongside the requirement that $z > \zeta$ ensures that the soft gluon is de-clustered as a prong. [9] The condition $\Theta(\mathrm{Min}(\rho_{k(ij)}, z\theta^2) > \rho_{\min}$ is the $\rho_{\min}$ condition where again we used the fact that at our accuracy we can replace the gluon angle with respect to a given prong by that with respect to the jet axis. Finally we discuss the Sudakov which has an argument $\mathrm{Min}(d_{k(ij)},\, z\theta^2,\, \rho - \rho_t - z\theta^2)$, reflecting the competing constraints on subsequent soft emissions. Firstly we have that emissions must not set a gen-k_t distance larger than the smallest gen-k_t distance amongst the 3 prongs found by $\mathrm{Y_m}$-Splitter , given by $\mathrm{Min}(d_{k(ij)},\, z\theta^2)$. Secondly we have that the soft emissions must not push the jet out of the mass window, i.e. the jet mass should be below ρ. Taking into account the additional soft emission we now have as a prong, this condition implies that for multiple subsequent emissions i we must have $\sum_i \rho_i < \rho - \rho_t - z\theta^2$. Taken together these conditions, on gen-k_t and mass, produce the Sudakov in Eq. (6.36).

It is additionally possible for two soft emissions to be resolved i.e. form two of the prongs found by $\mathrm{Y_m}$-Splitter . This occurs at order α_s^2 with only modest logarithmic enhancements [10] and hence such contributions are suppressed relative to the terms we include. We therefore omit them here. We also note that we have ignored soft emissions from the $q\bar{q}$ system produced by the splitting of the W boson. Soft emissions from this dipole are restricted in angle, by virtue of angular ordering, to have an angle less than that of the $q\bar{q}$ pair. Since they are part of the top system they also do not contribute to a shift in mass. Hence to our leading logarithmic accuracy they can also be ignored.

Our results are compared to Pythia 8 in Fig. 6.6, where we plot the signal efficiency as a function of $m_{\min}$ (c.f. similar plots in ref. [25]). We show our results for both cases with (red crosses) and without (blue dots) a resolved gluon prong. Our analytics agrees in both cases with the general behaviour seen with Pythia and we note an improved agreement with Pythia when the $\Sigma^{(1)}$ contribution, amounting to an $\mathcal{O}(15\%)$ correction, is included. As before we choose the lower limit of the mass window to be 10 GeV below the top mass.

6.4.3 $\mathrm{Y_m}$-Splitter with grooming for signal jets

Next we examine the impact of pre-grooming with Soft Drop on our results for $\mathrm{Y_m}$-Splitter applied to top jets. Relative to results from previous studies [25] here we also account for the possibility of a resolved gluon prong as in the previous subsection. The result of pre-grooming with mMDT or Soft Drop is again to essentially replace the Sudakov for the un-groomed case by the Sudakov for the groomer i.e. we make the following replacements in the $\Sigma^{(0)}$ and $\Sigma^{(1)}$ terms of the un-groomed results

---

[9] Note that here we used the same leading-logarithmic simplification for the gen-k_t distance for soft gluon emissions that led to the result in Eq. (6.33).

[10] We remind the reader that resolved emissions are constrained in several ways. They need to have energy larger than ζ as well as a mass large enough to satisfy the $\rho_{\min}$ condition but not large enough to push the jet out of the mass window. These constraints lead to the appearance of only modest logarithmic contributions.

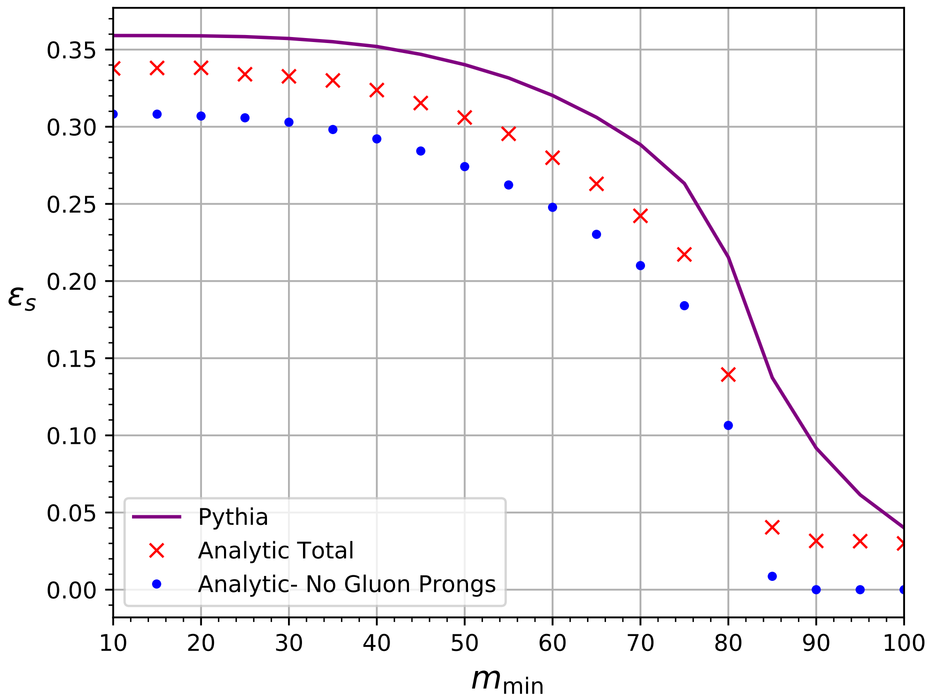

Figure 6.6. A comparison between different levels of approximation in analytical calculations and a Pythia simulation for top jets tagged with $\mathrm{Y_m}$-Splitter in a mass range $163\,\mathrm{GeV} < m < 225\,\mathrm{GeV}$ with $\zeta = 0.05$ as a function of $m_{\min}$.

(see Eqs. (6.35) and (6.36)):

$$\begin{aligned} e^{-R(\min(d_{12},d_{13},d_{23},\rho-\rho_t))} &\to e^{-R_{\mathrm{mMDT/SD}}(\min(d_{12},d_{13},d_{23},\rho-\rho_t)}, \\ e^{-R(\mathrm{Min}(d_{k(ij)},z\theta^2,\rho-\rho_t-z\theta^2))} &\to e^{-R_{\mathrm{mMDT/SD}}(\mathrm{Min}(d_{k(ij)},z\theta^2,\rho-\rho_t-z\theta^2)}, \end{aligned} \tag{6.37}$$

where the suffix mMDT or SD is used to indicate the grooming variant. We note that unlike the case of the QCD background jets, we have not included R_{angle} terms in the signal case. Although such terms would in principle be present, the angular scales involved are of the order of the opening angles between top decay products. At such angular scales the radiation pattern becomes more complicated as one also needs to account for radiation from the $q\bar{q}$ dipole produced by the colour singlet W decay. Given that the terms produced are logarithms in the ratio of two small scales, i.e. of the same level of significance as $\ln \rho/\rho_{\min}$ terms, they are beyond the accuracy we aim for in the case of signal jets.

The tagged signal fraction, with our usual choice of parameter values, is compared to a Pythia simulation in Figure 6.7, again showing the results with and without a resolved gluon prong and for grooming with SD (left) and mMDT(right). We see that except for the extreme region, where the tagged signal fraction is very small, our analytic results, especially after inclusion of the resolved gluon case, are in good overall agreement with the behaviour seen with Pythia.

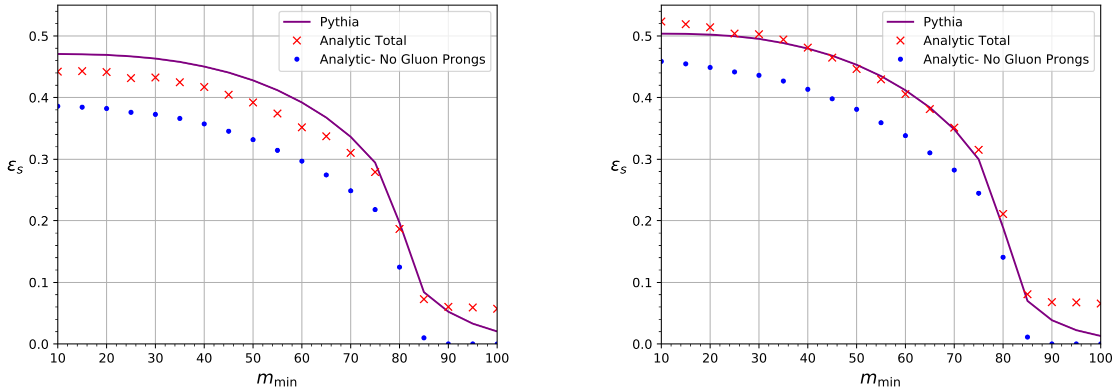

(a) Pre-grooming with Soft Drop ($\beta = 2$)

(b) Pre-grooming with mMDT

Figure 6.7. A comparison between our analytical calculations and a Pythia simulation for pre-groomed top jets tagged with $\mathrm{Y_m}$-Splitter in a mass range 163 GeV $< m <$ 225 GeV with $\zeta = 0.05$ as a function of $m_{\rm min}$.

6.4.4 $\mathrm{Y_m}$-Splitter with τ_{32} and grooming for signal jets

We now wish to understand the effect of adding a cut on τ_{32} to the tagged signal distribution after application of $\mathrm{Y_m}$-Splitter . We shall first consider the un-groomed case and then include the effects of grooming. We begin with the configuration where all three of the LO top decay products are identified as prongs by $\mathrm{Y_m}$-Splitter . With no additional emissions τ_3 vanishes and hence a cut on τ_{32} has no impact. Adding a set of soft and collinear emissions, one has to consider how these emissions are constrained by the τ cut, the mass-window cut and the requirement that they should not give a resolved prong on applying $\mathrm{Y_m}$-Splitter .

We first introduce an approximation into our definition of τ_2 which is valid to within the overall accuracy we can obtain with our current calculations for the signal case, i.e. LL accuracy in ρ with neglect of logs in ratios of mass scales and ζ. Consider the region of phase space where say $d_{12} < \min(d_{13}, d_{23})$, so that the first declustering will lead to two gen-k_t axes lying along p_3 and $p_1 + p_2$. In this region of phase space, to leading order where there are no additional emissions, $\tau_2 = z_1\theta^2_{1,12} + z_2\theta^2_{2,12}$. As the $p_1 + p_2$ direction will be aligned more with the harder of partons 1 and 2 we make the approximation that the gen-k_t axis is aligned with this parton, so that to LO we can approximate $\tau_2 = \min(d_{12}, d_{13}, d_{23})$. As there is no logarithmic enhancement associated with the leading order decay of the top, this approximation will introduce an $\mathcal{O}(1)$ rescaling of the argument of the Sudakov factor, which is consistent with an NLL correction and hence beyond our LL accuracy.

When considering the role of additional soft emissions let us first consider, as in section 6.4.3 before, primary emissions at a large angle to the opening angles of the top decay system. Regardless of which of the gen-k_t axes these emissions are closer to, their contribution to τ_3 and τ_2 may always be approximated by $\sum_i \rho_i$, where $\rho_i = z_i\theta_i^2$ and θ_i is the emission angle with respect to the emitting top quark direction.

The constraint on emissions due to the τ_{32} cut is then $\tau_{32} \approx \frac{\sum_i \rho_i}{\min(d_{12},d_{13},d_{23})+\sum_i \rho_i} < \tau$ which gives the constraint $\sum_i \rho_i < \min(d_{12}, d_{13}, d_{23})\frac{\tau}{1-\tau}$. For $\tau < 1/2$ this subjettiness constraint overcomes the constraint from $\mathrm{Y_m}$-Splitter , $\rho_i < \min(d_{12}, d_{13}, d_{23})$ and hence the argument of the primary emission Sudakov depends only on the competing subjettiness and jet mass constraints.

Until now we have neglected the role of secondary radiation from the $q\bar{q}$ system (arising from W decay) since these emissions bring only enhancements in ratios of similar mass scales. If we wish to obtain a good description of the signal with a τ cut including also the region where $\tau \ll 1$, we need to consider all sources of double-logarithmic corrections in τ. Secondary emissions are a source of such double-logarithmic terms and hence we include them here. The secondary emission terms are given by taking into account soft and collinear emissions from the q and $\bar{q}$ with the constraint that the emission angle is smaller than $\theta_{q\bar{q}}$ the opening angle of the $q\bar{q}$ dipole. This leads to results which have the same form as the corresponding results for the background case (see Eq. (6.6)) with z_a replaced by z_q and θ_a by $\theta_{q\bar{q}}$ for emission from q and similarly for emission from the $\bar{q}$. We note that secondary emissions are part of the decaying top system and hence do not contribute to a shift in mass so that the jet mass constraint is irrelevant here.

Thus we can write

$$\Sigma^{\tau<\frac{1}{2}}(\rho_{\min}, \zeta, \tau) = \\ \frac{1}{\sigma_0}\int |M_{t\to bq\bar{q}}|^2 \mathrm{d}\Phi_3 \delta\left(\frac{s_{123}}{R^2 p_t^2} - \rho_t\right)\Theta_{\mathrm{Clust}}\Theta_{\mathrm{Y_m\text{-}Splitter}}\frac{e^{-R-\gamma_E R'}}{\Gamma[1+R']}, \quad (6.38)$$

with

$$R \equiv R\left(\min(\frac{\tau}{1-\tau}\min(d_{12}, d_{13}, d_{23}), \rho_{\max} - \rho_t)\right) + \\ R^{\mathrm{secondary}}\left(\frac{\tau}{1-\tau}\min(d_{12}, d_{13}, d_{23}), z_q, \theta^2_{q\bar{q}}\right) \\ + R^{\mathrm{secondary}}\left(\frac{\tau}{1-\tau}\min(d_{12}, d_{13}, d_{23}), z_{\bar{q}}, \theta^2_{q\bar{q}}\right), \quad (6.39)$$

where $\rho_{\max}$ is the upper limit on the jet mass. Finally we account for the effect of grooming. To take this into account one makes the usual replacement of the primary emission radiator by its groomed counterpart. An additional subtlety that is present here is the existence of R_{angle} terms (see Eq. (6.22)) which originate from emissions which are not visible to the groomer as they are shielded by larger angle emissions that stop the grooming. Such terms have been ignored for the signal since they are complicated to account for and produce only logarithms of mass ratios which we neglect. However in the presence of a τ cut such terms also induce double logarithms in τ as described by Eq. (6.23). A consistent description of the double logs in τ should also include the double logarithm originating here while we can neglect all other details associated to this term. Grooming is therefore included through the replacement of the radiator as

$$\begin{aligned} &R(\min(\frac{\tau}{1-\tau}\min(d_{12},d_{13},d_{23}),\rho_{\max}-\rho_t)) \to \\ &\qquad R_{\mathrm{mMDT}}(\min(\frac{\tau}{1-\tau}\min(d_{12},d_{13},d_{23}),\rho_{\max}-\rho_t)) + R_{\mathrm{angle}}(\tau), \end{aligned} \tag{6.40}$$

where, at fixed coupling, $R_{\mathrm{angle}}(\tau) = \frac{C_F\alpha_s}{2\pi}\ln^2\tau$.

We have thus far not considered the case where a soft gluon is resolved as a $\mathrm{Y_m}$-Splitter prong, which we took into account in the previous subsections. For such a configuration, the effect of the τ cut is actually to constrain the phase space of partons arising from the LO top decay. As the electroweak top decay is not logarithmically enhanced, the restriction from the τ cut leads to a suppression proportional to τ. Given that the configuration with a resolved gluon prong is already suppressed by a power of α_s, a further suppression with τ implies that we may ignore this term while still retaining a reasonable description of the overall behaviour.[11]

Equation (6.38) is evaluated and compared to the same distribution derived from simulations using Pythia in figure 6.8. Although given the accuracy of the shower and the analytic calculations (each of which is leading-logarithmic albeit with inclusion of some key NLL effects), one would expect to see the moderate level of difference that can be observed in the figure, it is noticeable that the behaviour in τ is well captured by the analytics, especially for the un-groomed case and for pre-grooming with Soft Drop. For grooming with mMDT there is good agreement at smaller τ and a deviation at larger values of τ. Here, given that the leading logarithms are single logarithms, the analytics and the shower would each only contain (at best) a correct leading-logarithmic description, but with potentially larger differences from spurious NLL effects in the shower and their interplay with τ. Moreover our neglect of configurations where a gluon is one of the resolved prongs from $\mathrm{Y_m}$-Splitter would also lead to differences at larger values of τ where the power suppression with τ, which was a factor in our neglecting this configuration, will be less pronounced. Neglect of such configurations may have more of an impact on the distributions where jets are pre-groomed, as they can allow the jet to be tagged even if one of the electroweak top decay products is groomed away.

We note that Eq. (6.38) for the signal case reflects a few features that are different to the corresponding results for the QCD background. In particular for signal jets there is a lack of soft and collinear enhancements in the pre-factor resulting in the absence of the Hypergeometric function. Also, to our accuracy, the jet mass constraint does not affect the distribution for small enough τ cuts, or large enough $\rho_{\max}$, as a result of the fixed invariant mass of the leading-order system. This is clear from the argument of the Sudakov factor in equation (6.38) which contains a competition between

---

[11] We remind the reader that the value of τ that gives the highest signal significance is $\tau \sim 0.2$. We have checked numerically, by studying specific configurations, that the power suppression with τ holds at leading order.

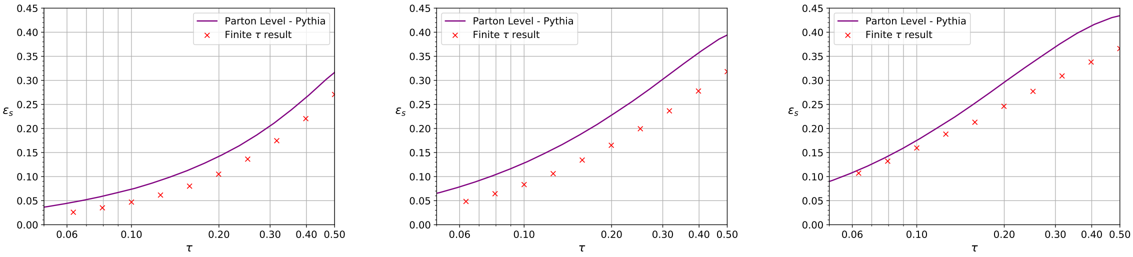

(a) No Grooming.

(b) With $\beta = 2$ Soft Drop

(c) With mMDT

Figure 6.8. Comparison between our analytic calculation (crosses) and Pythia for the tagged signal distribution as a function of the cut on τ_{32} for jets without pre-grooming (left) , with pre-grooming using Soft Drop (centre) and with pre-grooming using the mMDT.

the τ cut and the mass-window. For a given τ_{32} cut we can estimate the threshold below which $m_{\max}$ should be taken if varying it is to have an effect on the tagged signal fraction:

$$m_{\max}^2 < m_t^2 + p_T^2 \frac{\tau}{1-\tau} \min(d_{12}, d_{13}, d_{23}). \tag{6.41}$$

For top jets, where $\min(d_{12}, d_{13}, d_{23}) p_T^2$ may be roughly approximated by the W boson mass squared, we estimate that, for $\tau = 0.3$ and $m_t = 173$ GeV, the jet mass constraint will not significantly affect the signal efficiency unless $m_{\max} \lesssim 181$ GeV. In reality there will not be a hard threshold but some range of parameters over which the Sudakov suppression transitions from being due to the cut on τ_{32} to being due to the jet mass constraint. The application of this will be discussed further in the next section.

6.5 Exploiting jet mass cuts

In this section we discuss a notable feature of our calculations in terms of the differences between signal and background jets. As suggested by Eq. (6.41), one can reduce the cut on jet mass $m_{\max}$, without impacting the signal until we reach a critical value depending on τ. Until we reach this point, reducing $m_{\max}$ results in a decrease in the background tagging rate and hence an increase in performance. While our analytic studies are somewhat simplified and in particular neglect subleading terms, it is interesting to study the extent to which our observations may apply to parton shower studies when subleading effects are present. Figure 6.9 shows, using both analytic calculations (left) and parton level MC simulations (right), how the signal tagging rate varies with $m_{\max}$ for several fixed τ cuts both without grooming and with grooming via Soft Drop and the mMDT.

For the signal distribution the overall shape and dependence on τ is well described by our calculation, although, as before, there is some difference in the overall normalisation. The difference between our calculation and the distribution derived from MC worsens for smaller values of $m_{\max}$, which should be expected, as non-perturbative effects, which can not be completely removed from parton shower simulations, will

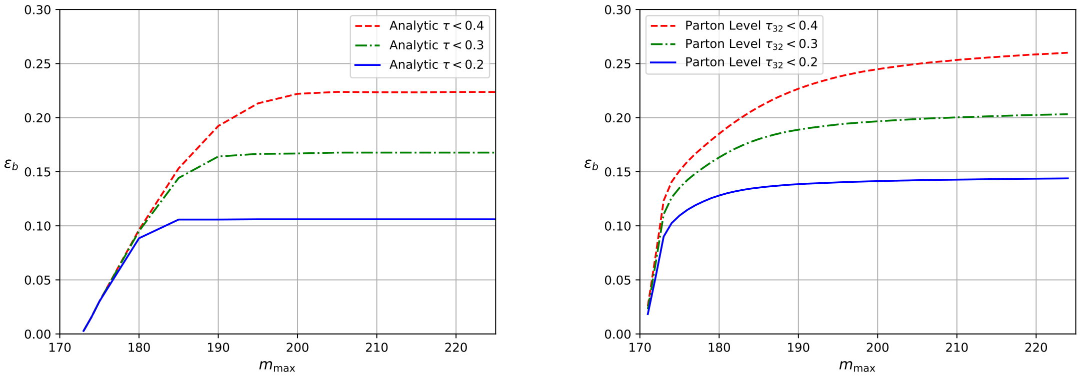

(a) Analytic, un-groomed.

(b) Parton level Monte Carlo, un-groomed.

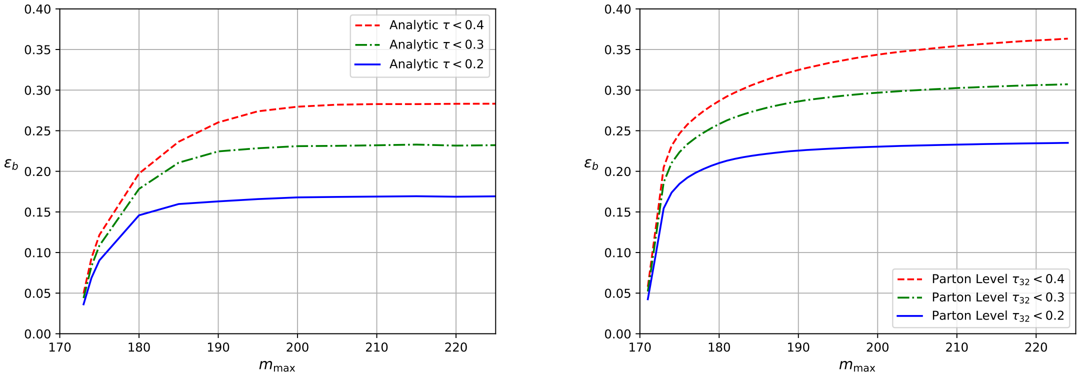

(c) Analytic, groomed with Soft Drop ($\beta = 2$).

(d) Parton level Monte Carlo, groomed with Soft Drop ($\beta = 2$).

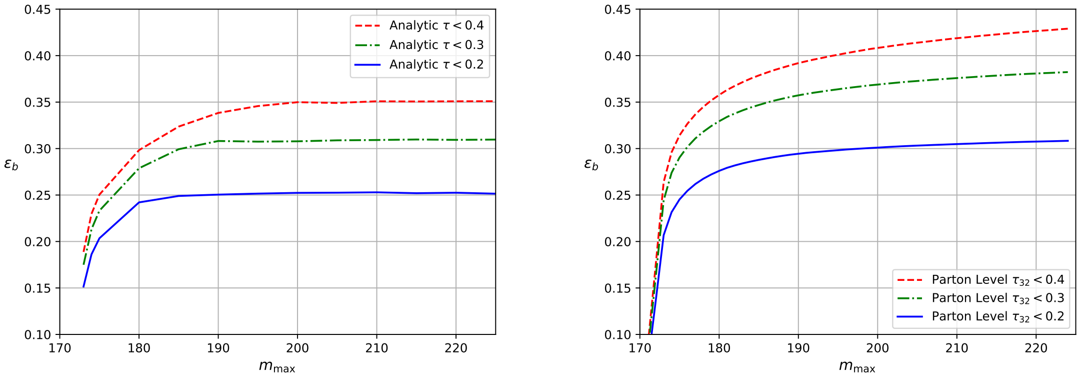

(e) Analytic, groomed with mMDT.

(f) Parton level Monte Carlo, groomed with mMDT.

Figure 6.9. Analytic and Monte Carlo parton level curves showing how the signal tagging rate varies with $m_{\rm max}$.

start to play more of a role in this region. While the signal tagging rate derived from MC simulations does not flatten off to the same extent as the analytic calculations do as $m_{\rm max}$ is increased, it is clear that beyond a certain value of $m_{\rm max}$ the signal efficiency depends only very weakly on $m_{\rm max}$.

Figure 6.10 shows similar plots for the case of quark jets. Our analytic predictions are again seen to be in overall good agreement with the Pythia shower capturing the $m_{\rm max}$ and τ dependences. It is notable that the jet mass constraint affects the background tagging rate in the same way for any cut on τ_{32}, as there are not two competing scales in the Sudakov factor. This opens up the possibility to improve the performance of the tagging procedure by reducing $m_{\max}$ so that the signal tag rate remains approximately constant whilst removing a significant portion of the background.

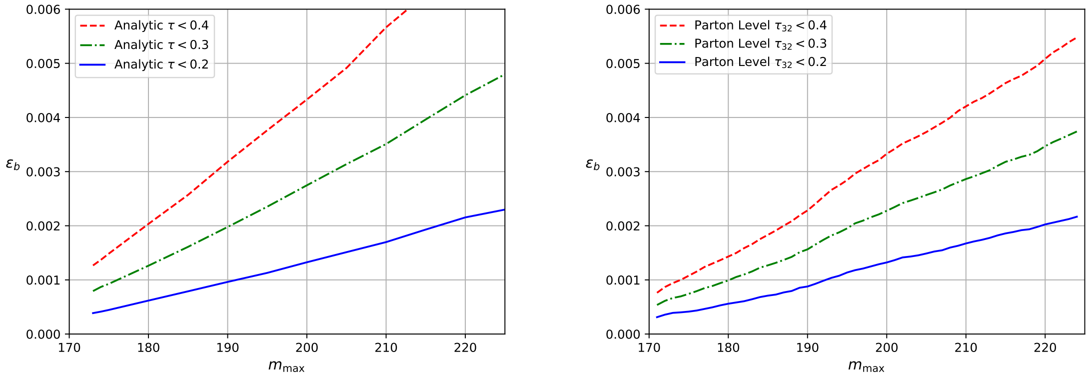

(a) Analytic, un-groomed.

(b) Parton level Monte Carlo, un-groomed.

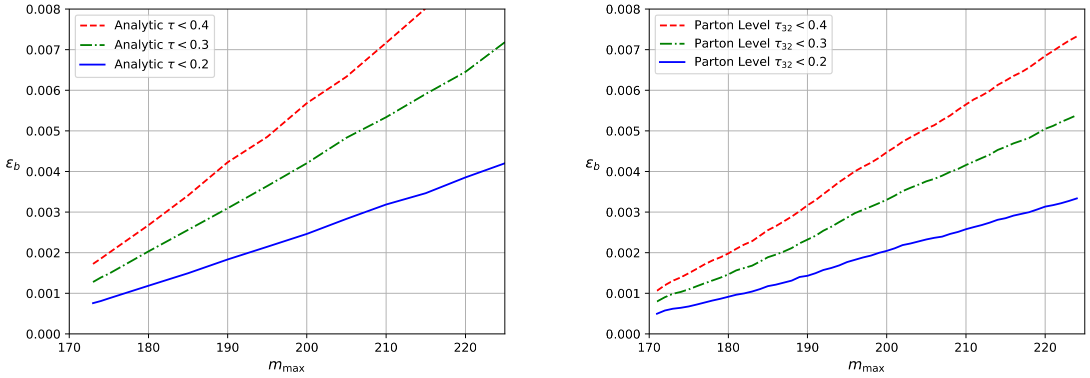

(c) Analytic, groomed with Soft Drop ($\beta = 2$).

(d) Parton level Monte Carlo, groomed with Soft Drop ($\beta = 2$).

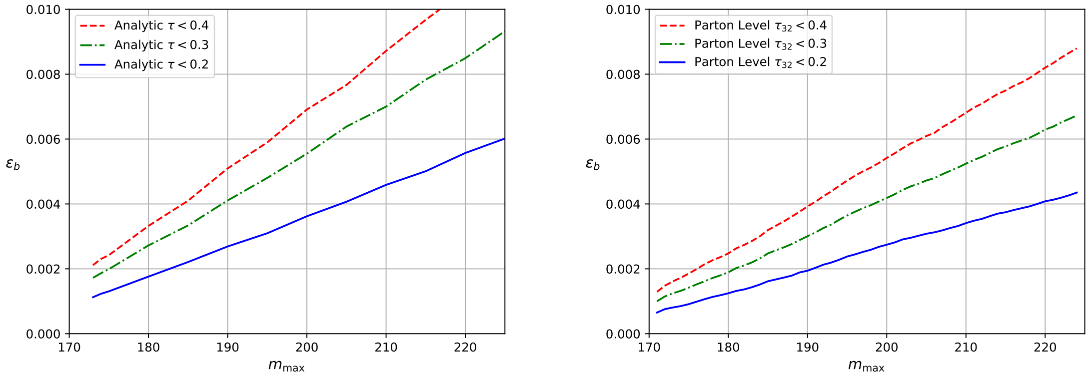

(e) Analytic, groomed with mMDT.

(f) Parton level Monte Carlo, groomed with mMDT.

Figure 6.10. Analytic and Monte Carlo (parton level) curves showing how the background tagging rate varies with $m_{\max}$.

One may wonder, given the effectiveness of a tight cut on the jet mass, what improvement is gained by cutting on τ_{32} in these circumstance. Figure 6.11 also shows a curve generated by varying $m_{\max}$ over the range 173 GeV to 225 GeV, but with no cut on τ_{32}. In this case the signal significance is higher than cutting on τ_{32} with $m_{\max} = 225$ GeV, but cutting on τ_{32} with $m_{\max} = 180$ GeV is still the highest performing tagging procedure.

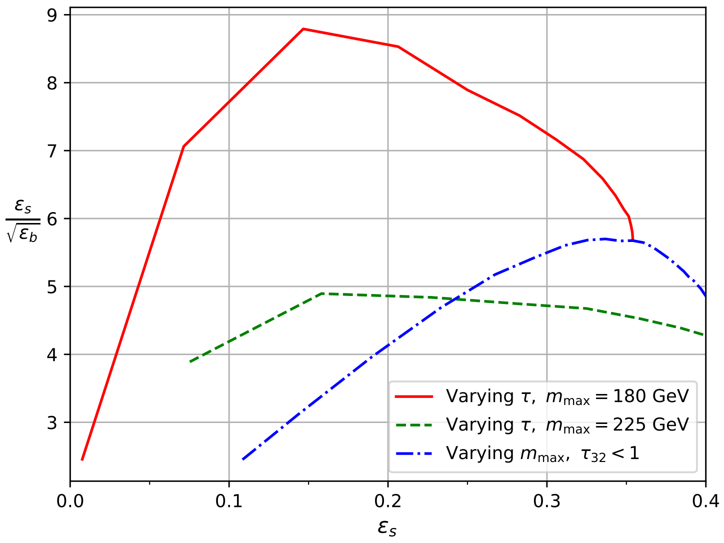

Figure 6.11. Signal significance against efficiency for three variations on the tagging procedure. All jets are groomed with mMDT and tagged with $\mathrm{Y_m}$-Splitter . Either τ or $m_{\max}$ is varied with a fixed cut placed on the other. The samples were produced using Pythia with hadronisation and UE activated.

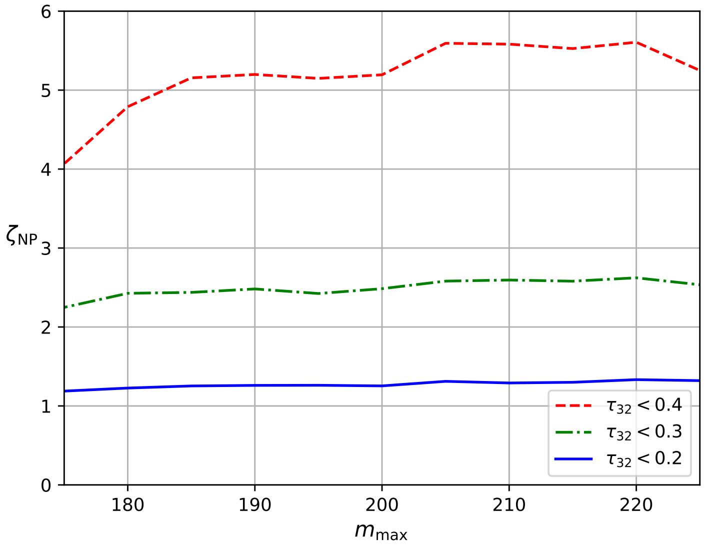

Figure 6.12. A measure of resilience to non-perturbative effects as $m_{\max}$ varies for three cuts on τ_{32}. Jets are pre-groomed with mMDT.

We now investigate the impact of non-perturbative corrections on this tagging procedure as $m_{\max}$ is varied. Figure 6.12 shows the resilience [170] to non-perturbative effects, defined as $\zeta_{\mathrm{NP}} = \left(\frac{\Delta\epsilon_s^2}{\langle\epsilon_s\rangle^2} + \frac{\Delta\epsilon_b^2}{\langle\epsilon_b\rangle^2}\right)^{-1/2}$ where $\Delta\epsilon$ is the difference between the parton and hadron level tagging efficiency and $\langle\epsilon\rangle$ is the mean of the two, for jets pre-groomed with mMDT, as $m_{\max}$ is varied, for three different values of τ. To construct the resilience 10 million $q\bar{q}$ events and 1 million $t\bar{t}$ events were generated at both parton and hadron level using Pythia. From figure 6.12 we see that the resilience to non-perturbative effects does not strongly depend on $m_{\max}$ in the range considered, even with $m_{\max}$ as low as 180 GeV. By contrast, reducing the cut on τ_{32} from 0.4 to 0.2 results in a marked drop in resilience. It would therefore be beneficial, in terms of reducing the impact of non-perturbative effects, to take τ not too small, say $\tau = 0.4$, while imposing a rather tight cut on the jet mass to provide the discriminating power. These cuts provide a signal significance of around 6 with a signal efficiency around 0.35. This is both a higher signal efficiency and significance than was reported in section 6.2 with $m_{\max} = 225$ GeV and $\tau = 0.2$, the highest significance achieved with the higher value of $m_{\max}$.

6.6 Conclusions

In section 6.2 we studied the tagging performance of various combinations of grooming with mMDT or soft drop with $\beta = 2$, $\mathrm{Y_m}$-Splitter and cutting on τ_{32}, using three different levels of Monte Carlo simulation. From this we established that the performance and resilience to hadronisation and UE were simultaneously maximised by the combination of grooming with mMDT, prong finding with $\mathrm{Y_m}$-Splitter and a cut on τ_{32} along with requiring the jet to be within a mass window. We then, in section 6.3, calculated the tagged background fraction for this procedure with and without grooming at modified LL accuracy and matched this to the triple collinear limit at order α_s^2. Having understood the background distribution we moved onto signal jets, starting with a calculation of the tagging efficiency with just a mass window. We then incorporated the effect of tagging with $\mathrm{Y_m}$-Splitter into our calculations and found that configurations where a single gluon is identified as a prong by $\mathrm{Y_m}$-Splitter account for ten to fifteen percent of the tagged fraction. This configuration was neglected in previous work. Finally, we included the cut on τ_{32} in our calculation of the tagged signal fraction. Here we found that the cut on τ_{32} competes with the upper limit on the jet mass for which sets the argument of the Sudakov factor, the scale above which emissions are vetoed. This gave rise to an approximate threshold, dependent on τ, above with the mass cut has little effect on the signal distribution to be determined. This was then exploited in section 6.5 to improve the performance of the tagging procedure as it was understood that the upper limit on the jet mass could be reduced, thus suppressing the background, without significantly reducing the signal efficiency. We then studied the impact of hadronisation and UE with the reduced mass window and concluded that a tight mass window and looser cut on τ_{32} than was initially suggested in 6.2 is optimal if one wants to maintain signal efficiency and resilience to non-perturbative effects whilst increasing the signal significance.

We have demonstrated that it is possible to analytically understand top tagging procedures of the kind widely used in experiment and that this understanding can bring optimisations in the way that the tagger is applied as well as giving confidence as to the robustness of the tagger. Moving forward, future work could investigate τ_{32}^{β} with different values of β. $\tau_{32}^{\beta=1}$ would be particularly of interest as it is a common choice in experiments. Studying similar steps but with a different prong finding algorithm, or exchanging τ_{32} for an energy correlation function would also be of interest.

Chapter 7

Summary

The work presented in this thesis has focused on two topics, groomed observables at NNLL accuracy, and understanding a boosted top tagging method involving a combination of grooming, prong-finding, and a radiation constraining jet shape.

The work on groomed observables was presented in chapters 4 and 5, beginning in chapter 4 with a calculation of the groomed jet mass distribution at $\mathcal{O}(\alpha_s^2)$, starting from the triple collinear splitting functions. It was shown there that the calculation could be structured as an inclusive piece, where the C/A clustering sequence of the groomer was replaced by one where all partons are clustered to their parent parton, and a piece accounting for the effect of the C/A clustering sequence. This clustering correction could be computed in the soft and collinear, but not strongly ordered, limit. Once terms related to strongly ordered dynamics had been removed, it was found that the inclusive piece was simply the $\mathcal{O}(\alpha_s^2)$ collinear contribution to the quark form factor, which is proportional to a coefficient often referred to as $B^{(2)}$ [192]–[195]. This collinear NNLL term is the same as for the un-groomed jet mass, which reflects the fact that grooming only affects soft emissions. This work has not only provided the insight needed to derive resummed results for the distributions of groomed observables, as is done in chapter 5, but has also established a link between the NNLL hard collinear coefficient $B^{(2)}$ and the triple collinear splitting functions. This link between the triple collinear splitting functions and NNLL hard collinear terms has since been investigated further in ref. [211], and is relevant for efforts to include triple collinear splitting functions in parton showers and push their accuracy towards NNLL.

Making use of the insights from chapter 4, an expression for the distribution of additive, rIRC safe, observables, computed on groomed jets, was derived at NNLL accuracy, in the small z_{cut} limit, in chapter 5. It was then shown how finite z_{cut} effects could be included up to NLL accuracy, as per ref. [21], [44]. The heavy hemisphere mass, width, and Les Houches angularity, distributions were then matched to NLO, and the impact of NNLL terms, finite z_{cut} effects, and matching were studied. It was found that finite z_{cut} effects at NLL could be as important as NNLL terms, for values of $z_{\text{cut}} \geq 0.1$, although it was noted that fixed order matching could be used to account for some of this difference, by including finite z_{cut} effects at fixed order. Whilst complete agreement was found with the SCET resummation of the jet mass distribution at NNLL accuracy [47], differences in the treatment of terms which arise due to the C/A clustering sequence were found at N^{3}LL accuracy [48], [190]. It seems that these differences lead to an error at N^{3}LL in the SCET result [47], [48], [190]. As this resummation is currently only formulated for quark jets, it can be applied to the phenomenology of e^+e^- collisions, but not compared to hadron collider data, where one has a mixture of quark and gluon initiated jets. A useful continuation of this work would therefore be to extend the resummation to gluon initiated jets, enabling comparison with measurements of jet shape observables at the LHC. Such comparisons could, for instance, be used to extract a value for the strong coupling, similar to what has been done using event shapes at e^+e^- colliders [159], [161]–[163], [241]. Another possible extension to this work is to extend the resummation to non-additive jet shape observables, such as the broadening [223].

In chapter 6 a top tagging method, utilising the $\mathrm{Y_m}$-Splitter prong finding method, a cut on the N-subjettiness variable τ_{32}, and a mass window constraint, was studied from an analytical QCD perspective. It was established, using a Monte Carlo study, that, out of the variations on the tagging procedure studied, pre-grooming the jets with mMDT before applying $\mathrm{Y_m}$-Splitter , the mass window constraint and the N-subjettiness cut, maximised the performance whilst minimising the effects of hadronisation and UE. Resummed predictions for the background tagging rate were then presented for both groomed and un-groomed jets, initially in the limit that $\tau \ll 1$, before accounting for finite τ effects. Resummed results for the signal were then presented, beginning with the signal efficiency where the only tagging step was a cut on the jet mass. The signal efficiency after application of $\mathrm{Y_m}$-Splitter was then calculated, taking into account configurations where a gluon is identified as a prong by $\mathrm{Y_m}$-Splitter . This builds on previous work [25] where the only configurations considered were ones where a leading order top decay product ($q\bar{q}b$) were identified as a prong. Compared to this work we found improved agreement with the tagging efficiency derived from Pythia simulations. Finally we implemented the cut on τ_{32} in our calculations. Here we found that the cut on τ_{32} competes with the cut on the jet mass for which sets the mass scale above which additional emissions are vetoed. This enabled us to find an approximate expression, in terms of τ, above which, increasing the upper bound on the jet mass will not significantly increase the signal tagging efficiency, but will increase the background tag rate, resulting in a loss of signal significance. An optimal mass cut could then be chosen, based on this understanding, for any given cut on τ, so as to maximise the performance of the tagging procedure. We found that to increase performance, whilst maintaining signal efficiency and minimising the effects of hadronisation, that a very tight cut on the mass with a higher cut on τ_{32} was beneficial. Interesting extensions to this work could include studying τ_{32}^{β} with values of β, $\beta = 1$ being a popular choice in experiment. Other choices of jet shape or prong finding method would also be of interest. Taking a somewhat broader view, machine learning based methods, as discussed in section 3.4, are another important class of jet tagging procedure which are widely used in experimental analyses. Attempting to gain a deeper of these techniques, such as is done in ref.

[128], could be considered as a continuation of the type of work presented in chapter 6. Particularly, it is important to understand what information is being learnt by these algorithms, and how robust they are against non-perturbative effects.

References

[1] S. Höche and S. Prestel, "Triple collinear emissions in parton showers," *Phys. Rev. D*, vol. 96, no. 7, p. 074 017, 2017. DOI: `10.1103/PhysRevD.96.074017`. arXiv: `1705.00742 [hep-ph]`.

[2] S. Höche, F. Krauss, and S. Prestel, "Implementing NLO DGLAP evolution in Parton Showers," *JHEP*, vol. 10, p. 093, 2017. DOI: `10.1007/JHEP10(2017)093`. arXiv: `1705.00982 [hep-ph]`.

[3] H. T. Li and P. Skands, "A framework for second-order parton showers," *Phys. Lett. B*, vol. 771, pp. 59–66, 2017. DOI: `10.1016/j.physletb.2017.05.011`. arXiv: `1611.00013 [hep-ph]`.

[4] D. Anderle, M. Dasgupta, B. K. El-Menoufi, J. Helliwell, and M. Guzzi, "Groomed jet mass as a direct probe of collinear parton dynamics," *Eur. Phys. J. C*, vol. 80, no. 9, p. 827, 2020. DOI: `10.1140/epjc/s10052-020-8411-y`. arXiv: `2007.10355 [hep-ph]`.

[5] M. Dasgupta and J. Helliwell, "Investigating top tagging with Y_m-Splitter and N-subjettiness," *JHEP*, vol. 10, p. 092, 2021. DOI: `10.1007/JHEP10(2021)092`. arXiv: `2108.09317 [hep-ph]`.

[6] S. F. Novaes, "Standard model: An Introduction," in *10th Jorge Andre Swieca Summer School: Particle and Fields*, Jan. 1999, pp. 5–102. arXiv: `hep-ph/0001283`.

[7] G. Aad *et al.*, "Observation of a new particle in the search for the Standard Model Higgs boson with the ATLAS detector at the LHC," *Phys. Lett. B*, vol. 716, pp. 1–29, 2012. DOI: `10.1016/j.physletb.2012.08.020`. arXiv: `1207.7214 [hep-ex]`.

[8] S. Chatrchyan *et al.*, "Observation of a New Boson at a Mass of 125 GeV with the CMS Experiment at the LHC," *Phys. Lett. B*, vol. 716, pp. 30–61, 2012. DOI: `10.1016/j.physletb.2012.08.021`. arXiv: `1207.7235 [hep-ex]`.

[9] J. M. Butterworth, B. E. Cox, and J. R. Forshaw, "WW scattering at the CERN LHC," *Phys. Rev. D*, vol. 65, p. 096 014, 2002. DOI: `10.1103/PhysRevD.65.096014`. arXiv: `hep-ph/0201098`.

[10] J. M. Butterworth, A. R. Davison, M. Rubin, and G. P. Salam, "Jet substructure as a new Higgs search channel at the LHC," *Phys. Rev. Lett.*, vol. 100, p. 242 001, 2008. DOI: `10.1103/PhysRevLett.100.242001`. arXiv: `0802.2470 [hep-ph]`.

[11] D. Krohn, J. Thaler, and L.-T. Wang, "Jet Trimming," *JHEP*, vol. 02, p. 084, 2010. DOI: `10.1007/JHEP02(2010)084`. arXiv: `0912.1342 [hep-ph]`.

[12] S. D. Ellis, C. K. Vermilion, and J. R. Walsh, "Recombination Algorithms and Jet Substructure: Pruning as a Tool for Heavy Particle Searches," *Phys. Rev. D*, vol. 81, p. 094 023, 2010. DOI: `10.1103/PhysRevD.81.094023`. arXiv: `0912.0033 [hep-ph]`.

[13] S. D. Ellis, C. K. Vermilion, and J. R. Walsh, "Techniques for improved heavy particle searches with jet substructure," *Phys. Rev. D*, vol. 80, p. 051 501, 2009. DOI: `10.1103/PhysRevD.80.051501`. arXiv: `0903.5081 [hep-ph]`.

[14] J. Thaler and K. Van Tilburg, "Identifying Boosted Objects with N-subjettiness," *JHEP*, vol. 03, p. 015, 2011. DOI: `10.1007/JHEP03(2011)015`. arXiv: `1011.2268 [hep-ph]`.

[15] "Top Tagging with New Approaches," 2016.

[16] "Boosted Top Jet Tagging at CMS," 2014.

[17] "Boosted hadronic top identification at ATLAS for early 13 TeV data," 2015.

[18] G. Aad *et al.*, "Search for charged Higgs bosons in the $H^\pm \to tb$ decay channel in pp collisions at $\sqrt{s} = 8$ TeV using the ATLAS detector," *JHEP*, vol. 03, p. 127, 2016. DOI: `10.1007/JHEP03(2016)127`. arXiv: `1512.03704 [hep-ex]`.

[19] "Identification of Hadronically-Decaying W Bosons and Top Quarks Using High-Level Features as Input to Boosted Decision Trees and Deep Neural Networks in ATLAS at $\sqrt{s} = 13$ TeV," CERN, Geneva, Tech. Rep., Apr. 2017, All figures including auxiliary figures are available at https://atlas.web.cern.ch/Atlas/GROUPS/PHYSICS/PUBNOTES/ATL-PHYS-PUB-2017-004. [Online]. Available: `https://cds.cern.ch/record/2259646`.

[20] M. Aaboud *et al.*, "Performance of top-quark and W-boson tagging with ATLAS in Run 2 of the LHC," *Eur. Phys. J. C*, vol. 79, no. 5, p. 375, 2019. DOI: `10.1140/epjc/s10052-019-6847-8`. arXiv: `1808.07858 [hep-ex]`.

[21] M. Dasgupta, A. Fregoso, S. Marzani, and G. P. Salam, "Towards an understanding of jet substructure," *JHEP*, vol. 09, p. 029, 2013. DOI: `10.1007/JHEP09(2013)029`. arXiv: `1307.0007 [hep-ph]`.

[22] M. Dasgupta, A. Fregoso, S. Marzani, and A. Powling, “Jet substructure with analytical methods,” *Eur. Phys. J. C*, vol. 73, no. 11, p. 2623, 2013. DOI: `10.1140/epjc/s10052-013-2623-3`. arXiv: `1307.0013 [hep-ph]`.

[23] A. J. Larkoski, S. Marzani, G. Soyez, and J. Thaler, “Soft Drop,” *JHEP*, vol. 05, p. 146, 2014. DOI: `10.1007/JHEP05(2014)146`. arXiv: `1402.2657 [hep-ph]`.

[24] A. J. Larkoski, I. Moult, and D. Neill, “Power Counting to Better Jet Observables,” *JHEP*, vol. 12, p. 009, 2014. DOI: `10.1007/JHEP12(2014)009`. arXiv: `1409.6298 [hep-ph]`.

[25] M. Dasgupta, M. Guzzi, J. Rawling, and G. Soyez, “Top tagging : an analytical perspective,” *JHEP*, vol. 09, p. 170, 2018. DOI: `10.1007/JHEP09(2018)170`. arXiv: `1807.04767 [hep-ph]`.

[26] D. Napoletano and G. Soyez, “Computing N-subjettiness for boosted jets,” *JHEP*, vol. 12, p. 031, 2018. DOI: `10.1007/JHEP12(2018)031`. arXiv: `1809.04602 [hep-ph]`.

[27] A. J. Larkoski, D. Neill, and J. Thaler, “Jet Shapes with the Broadening Axis,” *JHEP*, vol. 04, p. 017, 2014. DOI: `10.1007/JHEP04(2014)017`. arXiv: `1401.2158 [hep-ph]`.

[28] M. Dasgupta, L. Schunk, and G. Soyez, “Jet shapes for boosted jet two-prong decays from first-principles,” *JHEP*, vol. 04, p. 166, 2016. DOI: `10.1007/JHEP04(2016)166`. arXiv: `1512.00516 [hep-ph]`.

[29] M. Dasgupta, A. Powling, L. Schunk, and G. Soyez, “Improved jet substructure methods: Y-splitter and variants with grooming,” *JHEP*, vol. 12, p. 079, 2016. DOI: `10.1007/JHEP12(2016)079`. arXiv: `1609.07149 [hep-ph]`.

[30] M. Dasgupta, A. Powling, and A. Siodmok, “On jet substructure methods for signal jets,” *JHEP*, vol. 08, p. 079, 2015. DOI: `10.1007/JHEP08(2015)079`. arXiv: `1503.01088 [hep-ph]`.

[31] A. J. Larkoski, I. Moult, and D. Neill, “Analytic Boosted Boson Discrimination,” *JHEP*, vol. 05, p. 117, 2016. DOI: `10.1007/JHEP05(2016)117`. arXiv: `1507.03018 [hep-ph]`.

[32] A. Butter *et al.*, “The Machine Learning Landscape of Top Taggers,” *SciPost Phys.*, vol. 7, G. Kasieczka and T. Plehn, Eds., p. 014, 2019. DOI: `10.21468/SciPostPhys.7.1.014`. arXiv: `1902.09914 [hep-ph]`.

[33] H. Qu and L. Gouskos, “ParticleNet: Jet Tagging via Particle Clouds,” *Phys. Rev. D*, vol. 101, no. 5, p. 056 019, 2020. DOI: `10.1103/PhysRevD.101.056019`. arXiv: `1902.08570 [hep-ph]`.

[34] F. A. Dreyer and H. Qu, "Jet tagging in the Lund plane with graph networks," Dec. 2020. arXiv: `2012.08526 [hep-ph]`.

[35] P. T. Komiske, E. M. Metodiev, and J. Thaler, "Energy Flow Networks: Deep Sets for Particle Jets," *JHEP*, vol. 01, p. 121, 2019. DOI: `10.1007/JHEP01(2019)121`. arXiv: `1810.05165 [hep-ph]`.

[36] L. de Oliveira, M. Kagan, L. Mackey, B. Nachman, and A. Schwartzman, "Jet-images — deep learning edition," *JHEP*, vol. 07, p. 069, 2016. DOI: `10.1007/JHEP07(2016)069`. arXiv: `1511.05190 [hep-ph]`.

[37] A. Chakraborty, S. H. Lim, and M. M. Nojiri, "Interpretable deep learning for two-prong jet classification with jet spectra," *JHEP*, vol. 07, p. 135, 2019. DOI: `10.1007/JHEP07(2019)135`. arXiv: `1904.02092 [hep-ph]`.

[38] Y.-C. J. Chen, C.-W. Chiang, G. Cottin, and D. Shih, "Boosted W and Z tagging with jet charge and deep learning," *Phys. Rev. D*, vol. 101, no. 5, p. 053 001, 2020. DOI: `10.1103/PhysRevD.101.053001`. arXiv: `1908.08256 [hep-ph]`.

[39] G. Aad *et al.*, "Measurement of soft-drop jet observables in pp collisions with the ATLAS detector at $\sqrt{s} = 13$ TeV," *Phys. Rev. D*, vol. 101, no. 5, p. 052 007, 2020. DOI: `10.1103/PhysRevD.101.052007`. arXiv: `1912.09837 [hep-ex]`.

[40] G. Aad *et al.*, "Measurement of the Lund Jet Plane Using Charged Particles in 13 TeV Proton-Proton Collisions with the ATLAS Detector," *Phys. Rev. Lett.*, vol. 124, no. 22, p. 222 002, 2020. DOI: `10.1103/PhysRevLett.124.222002`. arXiv: `2004.03540 [hep-ex]`.

[41] M. Aaboud, G. Aad, B. Abbott, O. Abdinov, B. Abeloos, S. H. Abidi, O. S. AbouZeid, N. L. Abraham, H. Abramowicz, H. Abreu, and et al., "Measurement of the Soft-Drop Jet Mass in pp Collisions at 13 TeV with the ATLAS Detector," *Physical Review Letters*, vol. 121, no. 9, Aug. 2018, ISSN: 1079-7114. DOI: `10.1103/physrevlett.121.092001`. [Online]. Available: `http://dx.doi.org/10.1103/PhysRevLett.121.092001`.

[42] A. M. Sirunyan *et al.*, "Measurements of the differential jet cross section as a function of the jet mass in dijet events from proton-proton collisions at $\sqrt{s} =$ 13 TeV," *Journal of High Energy Physics*, vol. 2018, no. 11, Nov. 2018, ISSN: 1029-8479. DOI: `10.1007/jhep11(2018)113`. [Online]. Available: `http://dx.doi.org/10.1007/JHEP11(2018)113`.

[43] A. Tumasyan *et al.*, "Study of quark and gluon jet substructure in Z+jet and dijet events from pp collisions," *JHEP*, vol. 01, p. 188, 2022. DOI: `10.1007/JHEP01(2022)188`. arXiv: `2109.03340 [hep-ex]`.

[44] S. Marzani, L. Schunk, and G. Soyez, "A study of jet mass distributions with grooming," *JHEP*, vol. 07, p. 132, 2017. DOI: `10.1007/JHEP07(2017)132`. arXiv: `1704.02210 [hep-ph]`.

[45] S. Marzani, L. Schunk, and G. Soyez, "The jet mass distribution after Soft Drop," *Eur. Phys. J. C*, vol. 78, no. 2, p. 96, 2018. DOI: `10.1140/epjc/s10052-018-5579-5`. arXiv: `1712.05105 [hep-ph]`.

[46] S. Caletti, O. Fedkevych, S. Marzani, D. Reichelt, S. Schumann, G. Soyez, and V. Theeuwes, "Jet angularities in Z+jet production at the LHC," *JHEP*, vol. 07, p. 076, 2021. DOI: `10.1007/JHEP07(2021)076`. arXiv: `2104.06920 [hep-ph]`.

[47] C. Frye, A. J. Larkoski, M. D. Schwartz, and K. Yan, "Factorization for groomed jet substructure beyond the next-to-leading logarithm," *JHEP*, vol. 07, p. 064, 2016. DOI: `10.1007/JHEP07(2016)064`. arXiv: `1603.09338 [hep-ph]`.

[48] A. Kardos, A. J. Larkoski, and Z. Trocsanyi, "Groomed jet mass at high precision," 2020. arXiv: `2002.00942 [hep-ph]`.

[49] Z.-B. Kang, K. Lee, X. Liu, and F. Ringer, "Soft drop groomed jet angularities at the LHC," *Phys. Lett. B*, vol. 793, pp. 41–47, 2019. DOI: `10.1016/j.physletb.2019.04.018`. arXiv: `1811.06983 [hep-ph]`.

[50] J. M. Campbell and E. Glover, "Double unresolved approximations to multiparton scattering amplitudes," *Nucl. Phys. B*, vol. 527, pp. 264–288, 1998. DOI: `10.1016/S0550-3213(98)00295-8`. arXiv: `hep-ph/9710255`.

[51] S. Catani and M. Grazzini, "Collinear factorization and splitting functions for next-to-next-to-leading order QCD calculations," *Phys. Lett. B*, vol. 446, pp. 143–152, 1999. DOI: `10.1016/S0370-2693(98)01513-5`. arXiv: `hep-ph/9810389`.

[52] S. Catani and M. Grazzini, "Infrared factorization of tree level QCD amplitudes at the next-to-next-to-leading order and beyond," *Nucl. Phys. B*, vol. 570, pp. 287–325, 2000. DOI: `10.1016/S0550-3213(99)00778-6`. arXiv: `hep-ph/9908523`.

[53] C. Bierlich *et al.*, "A comprehensive guide to the physics and usage of PYTHIA 8.3," Mar. 2022. arXiv: `2203.11601 [hep-ph]`.

[54] R. K. Ellis, W. J. Stirling, and B. R. Webber, *QCD and collider physics*. Cambridge University Press, Feb. 2011, vol. 8, ISBN: 978-0-511-82328-2, 978-0-521-54589-1. DOI: `10.1017/CBO9780511628788`.

[55] M. E. Peskin and D. V. Schroeder, *An Introduction to quantum field theory.* Reading, USA: Addison-Wesley, 1995, ISBN: 978-0-201-50397-5.

[56] M. D. Schwartz, *Quantum Field Theory and the Standard Model.* Cambridge University Press, Mar. 2014, ISBN: 978-1-107-03473-0, 978-1-107-03473-0.

[57] L. Faddeev and V. Popov, "Feynman diagrams for the yang-mills field," *Physics Letters B*, vol. 25, no. 1, pp. 29–30, 1967, ISSN: 0370-2693. DOI: `https://doi.org/10.1016/0370-2693(67)90067-6`. [Online]. Available: `https://www.sciencedirect.com/science/article/pii/0370269367900676`.

[58] K. G. Wilson and J. Kogut, "The renormalization group and the expansion," *Physics Reports*, vol. 12, no. 2, pp. 75–199, 1974, ISSN: 0370-1573. DOI: `https://doi.org/10.1016/0370-1573(74)90023-4`. [Online]. Available: `https://www.sciencedirect.com/science/article/pii/0370157374900234`.

[59] J. Collins, *Foundations of perturbative QCD.* Cambridge University Press, Nov. 2013, vol. 32, ISBN: 978-1-107-64525-7, 978-1-107-64525-7, 978-0-521-85533-4, 978-1-139-09782-6.

[60] S. Coleman and D. J. Gross, "Price of asymptotic freedom," *Phys. Rev. Lett.*, vol. 31, pp. 851–854, 13 Sep. 1973. DOI: `10.1103/PhysRevLett.31.851`. [Online]. Available: `https://link.aps.org/doi/10.1103/PhysRevLett.31.851`.

[61] A. Deur, S. J. Brodsky, and G. F. de Teramond, "The QCD Running Coupling," *Nucl. Phys.*, vol. 90, p. 1, 2016. DOI: `10.1016/j.ppnp.2016.04.003`. arXiv: `1604.08082 [hep-ph]`.

[62] R. D. Field, *Applications of Perturbative QCD.* 1989, vol. 77.

[63] G. Luisoni and S. Marzani, "QCD resummation for hadronic final states," *J. Phys. G*, vol. 42, no. 10, p. 103 101, 2015. DOI: `10.1088/0954-3899/42/10/103101`. arXiv: `1505.04084 [hep-ph]`.

[64] T. Kinoshita, "Mass singularities of Feynman amplitudes," *J. Math. Phys.*, vol. 3, pp. 650–677, 1962. DOI: `10.1063/1.1724268`.

[65] T. D. Lee and M. Nauenberg, "Degenerate Systems and Mass Singularities," *Phys. Rev.*, vol. 133, G. Feinberg, Ed., B1549–B1562, 1964. DOI: `10.1103/PhysRev.133.B1549`.

[66] G. F. Sterman and S. Weinberg, "Jets from Quantum Chromodynamics," *Phys. Rev. Lett.*, vol. 39, p. 1436, 1977. DOI: `10.1103/PhysRevLett.39.1436`.

[67] G. Altarelli and G. Parisi, “Asymptotic Freedom in Parton Language,” *Nucl. Phys. B*, vol. 126, pp. 298–318, 1977. DOI: `10.1016/0550-3213(77)90384-4`.

[68] S. Brandt, C. Peyrou, R. Sosnowski, and A. Wroblewski, “The Principal axis of jets. An Attempt to analyze high-energy collisions as two-body processes,” *Phys. Lett.*, vol. 12, pp. 57–61, 1964. DOI: `10.1016/0031-9163(64)91176-X`.

[69] A. Banfi, G. P. Salam, and G. Zanderighi, “Principles of general final-state resummation and automated implementation,” *JHEP*, vol. 03, p. 073, 2005. DOI: `10.1088/1126-6708/2005/03/073`. arXiv: `hep-ph/0407286`.

[70] M. Dasgupta and G. Salam, “Resummation of nonglobal QCD observables,” *Phys. Lett. B*, vol. 512, pp. 323–330, 2001. DOI: `10.1016/S0370-2693(01)00725-0`. arXiv: `hep-ph/0104277`.

[71] M. Dasgupta and G. P. Salam, “Accounting for coherence in interjet E(t) flow: A Case study,” *JHEP*, vol. 03, p. 017, 2002. DOI: `10.1088/1126-6708/2002/03/017`. arXiv: `hep-ph/0203009`.

[72] A. Banfi, F. A. Dreyer, and P. F. Monni, “Next-to-leading non-global logarithms in QCD,” *JHEP*, vol. 10, p. 006, 2021. DOI: `10.1007/JHEP10(2021)006`. arXiv: `2104.06416 [hep-ph]`.

[73] S. Catani, B. R. Webber, and G. Marchesini, “QCD coherent branching and semiinclusive processes at large x,” *Nucl. Phys. B*, vol. 349, pp. 635–654, 1991. DOI: `10.1016/0550-3213(91)90390-J`.

[74] Y. L. Dokshitzer, A. Lucenti, G. Marchesini, and G. P. Salam, “Universality of 1/Q corrections to jet-shape observables rescued,” *Nucl. Phys. B*, vol. 511, pp. 396–418, 1998, [Erratum: Nucl.Phys.B 593, 729–730 (2001)]. DOI: `10.1016/S0550-3213(97)00650-0`. arXiv: `hep-ph/9707532`.

[75] Y. L. Dokshitzer, G. Marchesini, and B. R. Webber, “Dispersive approach to power behaved contributions in QCD hard processes,” *Nucl. Phys. B*, vol. 469, pp. 93–142, 1996. DOI: `10.1016/0550-3213(96)00155-1`. arXiv: `hep-ph/9512336`.

[76] S. Catani, E. D’Emilio, and L. Trentadue, “The Gluon Form-factor to Higher Orders: Gluon Gluon Annihilation at Small Q^{-}transverse,” *Phys. Lett. B*, vol. 211, pp. 335–342, 1988. DOI: `10.1016/0370-2693(88)90912-4`.

[77] S. Catani and L. Trentadue, “Resummation of the QCD Perturbative Series for Hard Processes,” *Nucl. Phys. B*, vol. 327, pp. 323–352, 1989. DOI: `10.1016/0550-3213(89)90273-3`.

[78] E. G. Floratos, C. Kounnas, and R. Lacaze, “Higher Order QCD Effects in Inclusive Annihilation and Deep Inelastic Scattering,” *Nucl. Phys. B*, vol. 192, pp. 417–462, 1981. DOI: `10.1016/0550-3213(81)90434-X`.

[79] J. C. Collins and D. E. Soper, “The Theorems of Perturbative QCD,” *Ann. Rev. Nucl. Part. Sci.*, vol. 37, pp. 383–409, 1987. DOI: `10.1146/annurev.ns.37.120187.002123`.

[80] J. Owens and W.-K. Tung, “Parton distribution functions of hadrons,” *Annual Review of Nuclear and Particle Science*, vol. 42, pp. 291–332, Nov. 2003. DOI: `10.1146/annurev.ns.42.120192.001451`.

[81] V. N. Gribov and L. N. Lipatov, “Deep inelastic e p scattering in perturbation theory,” *Sov. J. Nucl. Phys.*, vol. 15, pp. 438–450, 1972.

[82] L. N. Lipatov, “The parton model and perturbation theory,” *Yad. Fiz.*, vol. 20, pp. 181–198, 1974.

[83] Y. L. Dokshitzer, “Calculation of the Structure Functions for Deep Inelastic Scattering and e+ e- Annihilation by Perturbation Theory in Quantum Chromodynamics.,” *Sov. Phys. JETP*, vol. 46, pp. 641–653, 1977.

[84] B. R. Webber, “Hadronization,” in *Summer School on Hadronic Aspects of Collider Physics*, Nov. 1994, pp. 49–77. arXiv: `hep-ph/9411384`.

[85] G. P. Korchemsky and G. F. Sterman, “Nonperturbative corrections in resummed cross-sections,” *Nucl. Phys. B*, vol. 437, pp. 415–432, 1995. DOI: `10.1016/0550-3213(94)00006-Z`. arXiv: `hep-ph/9411211`.

[86] M. Bahr *et al.*, “Herwig++ Physics and Manual,” *Eur. Phys. J. C*, vol. 58, pp. 639–707, 2008. DOI: `10.1140/epjc/s10052-008-0798-9`. arXiv: `0803.0883 [hep-ph]`.

[87] T. Sjostrand, S. Mrenna, and P. Z. Skands, “PYTHIA 6.4 Physics and Manual,” *JHEP*, vol. 05, p. 026, 2006. DOI: `10.1088/1126-6708/2006/05/026`. arXiv: `hep-ph/0603175`.

[88] A. Buckley, H. Hoeth, H. Lacker, H. Schulz, and J. E. von Seggern, “Systematic event generator tuning for the LHC,” *Eur. Phys. J. C*, vol. 65, pp. 331–357, 2010. DOI: `10.1140/epjc/s10052-009-1196-7`. arXiv: `0907.2973 [hep-ph]`.

[89] B. Andersson, *The Lund model.* Cambridge University Press, Jul. 2005, vol. 7, ISBN: 978-0-521-01734-3, 978-0-521-42094-5, 978-0-511-88149-7. DOI: `10.1017/CBO9780511524363`.

[90] J.-C. Winter, F. Krauss, and G. Soff, "A Modified cluster hadronization model," *Eur. Phys. J. C*, vol. 36, pp. 381–395, 2004. DOI: `10.1140/epjc/s2004-01960-8`. arXiv: `hep-ph/0311085`.

[91] T. Gleisberg, S. Hoeche, F. Krauss, M. Schonherr, S. Schumann, F. Siegert, and J. Winter, "Event generation with SHERPA 1.1," *JHEP*, vol. 02, p. 007, 2009. DOI: `10.1088/1126-6708/2009/02/007`. arXiv: `0811.4622 [hep-ph]`.

[92] S. Frixione, P. Nason, and C. Oleari, "Matching NLO QCD computations with Parton Shower simulations: the POWHEG method," *JHEP*, vol. 11, p. 070, 2007. DOI: `10.1088/1126-6708/2007/11/070`. arXiv: `0709.2092 [hep-ph]`.

[93] S. Alioli, A. Broggio, A. Gavardi, S. Kallweit, M. A. Lim, R. Nagar, D. Napoletano, C. W. Bauer, and L. Rottoli, "Matching nnlo predictions to parton showers using n3ll color-singlet transverse momentum resummation in geneva," *Phys. Rev. D*, vol. 104, p. 094 020, 9 Nov. 2021. DOI: `10.1103/PhysRevD.104.094020`. [Online]. Available: `https://link.aps.org/doi/10.1103/PhysRevD.104.094020`.

[94] S. Höche, "Introduction to parton-shower event generators," in *Theoretical Advanced Study Institute in Elementary Particle Physics: Journeys Through the Precision Frontier: Amplitudes for Colliders*, 2015, pp. 235–295. DOI: `10.1142/9789814678766_0005`. arXiv: `1411.4085 [hep-ph]`.

[95] M. Dasgupta, F. A. Dreyer, K. Hamilton, P. F. Monni, G. P. Salam, and G. Soyez, "Parton showers beyond leading logarithmic accuracy," *Phys. Rev. Lett.*, vol. 125, no. 5, p. 052 002, 2020. DOI: `10.1103/PhysRevLett.125.052002`. arXiv: `2002.11114 [hep-ph]`.

[96] M. Dasgupta, F. A. Dreyer, K. Hamilton, P. F. Monni, and G. P. Salam, "Logarithmic accuracy of parton showers: a fixed-order study," *JHEP*, vol. 09, p. 033, 2018, [Erratum: JHEP 03, 083 (2020)]. DOI: `10.1007/JHEP09(2018)033`. arXiv: `1805.09327 [hep-ph]`.

[97] A. Banfi, G. Corcella, and M. Dasgupta, "Angular ordering and parton showers for non-global QCD observables," *JHEP*, vol. 03, p. 050, 2007. DOI: `10.1088/1126-6708/2007/03/050`. arXiv: `hep-ph/0612282`.

[98] G. Marchesini and B. Webber, "Simulation of qcd jets including soft gluon interference," *Nuclear Physics B*, vol. 238, no. 1, pp. 1–29, 1984, ISSN: 0550-3213. DOI: `https://doi.org/10.1016/0550-3213(84)90463-2`. [Online]. Available: `https://www.sciencedirect.com/science/article/pii/0550321384904632`.

[99] A. J. Larkoski, I. Moult, and B. Nachman, “Jet Substructure at the Large Hadron Collider: A Review of Recent Advances in Theory and Machine Learning,” *Phys. Rept.*, vol. 841, pp. 1–63, 2020. DOI: `10.1016/j.physrep.2019.11.001`. arXiv: `1709.04464 [hep-ph]`.

[100] G. Bewick, S. Ferrario Ravasio, P. Richardson, and M. H. Seymour, “Logarithmic accuracy of angular-ordered parton showers,” *JHEP*, vol. 04, p. 019, 2020. DOI: `10.1007/JHEP04(2020)019`. arXiv: `1904.11866 [hep-ph]`.

[101] J. R. Forshaw, J. Holguin, and S. Plätzer, “Building a consistent parton shower,” *JHEP*, vol. 09, p. 014, 2020. DOI: `10.1007/JHEP09(2020)014`. arXiv: `2003.06400 [hep-ph]`.

[102] K. Hamilton, R. Medves, G. P. Salam, L. Scyboz, and G. Soyez, “Colour and logarithmic accuracy in final-state parton showers,” Nov. 2020. DOI: `10.1007/JHEP03(2021)041`. arXiv: `2011.10054 [hep-ph]`.

[103] K. Hamilton, A. Karlberg, G. P. Salam, L. Scyboz, and R. Verheyen, “Soft spin correlations in final-state parton showers,” Nov. 2021. arXiv: `2111.01161 [hep-ph]`.

[104] Z. Nagy and D. E. Soper, “Parton showers with more exact color evolution,” *Phys. Rev. D*, vol. 99, no. 5, p. 054 009, 2019. DOI: `10.1103/PhysRevD.99.054009`. arXiv: `1902.02105 [hep-ph]`.

[105] J. R. Forshaw, J. Holguin, and S. Plätzer, “Parton branching at amplitude level,” *JHEP*, vol. 08, p. 145, 2019. DOI: `10.1007/JHEP08(2019)145`. arXiv: `1905.08686 [hep-ph]`.

[106] M. De Angelis, J. R. Forshaw, and S. Plätzer, “Resummation and Simulation of Soft Gluon Effects beyond Leading Color,” *Phys. Rev. Lett.*, vol. 126, no. 11, p. 112 001, 2021. DOI: `10.1103/PhysRevLett.126.112001`. arXiv: `2007.09648 [hep-ph]`.

[107] G. P. Salam, “Towards Jetography,” *Eur. Phys. J. C*, vol. 67, pp. 637–686, 2010. DOI: `10.1140/epjc/s10052-010-1314-6`. arXiv: `0906.1833 [hep-ph]`.

[108] G. P. Salam and G. Soyez, “A Practical Seedless Infrared-Safe Cone jet algorithm,” *JHEP*, vol. 05, p. 086, 2007. DOI: `10.1088/1126-6708/2007/05/086`. arXiv: `0704.0292 [hep-ph]`.

[109] M. Cacciari, G. P. Salam, and G. Soyez, “FastJet User Manual,” *Eur. Phys. J. C*, vol. 72, p. 1896, 2012. DOI: `10.1140/epjc/s10052-012-1896-2`. arXiv: `1111.6097 [hep-ph]`.

[110] M. Cacciari, G. P. Salam, and G. Soyez, “The anti-k_t jet clustering algorithm,” *JHEP*, vol. 04, p. 063, 2008. DOI: `10.1088/1126-6708/2008/04/063`. arXiv: `0802.1189 [hep-ph]`.

[111] Y. L. Dokshitzer, G. D. Leder, S. Moretti, and B. R. Webber, “Better jet clustering algorithms,” *JHEP*, vol. 08, p. 001, 1997. DOI: `10.1088/1126-6708/1997/08/001`. arXiv: `hep-ph/9707323`.

[112] M. Wobisch and T. Wengler, “Hadronization corrections to jet cross-sections in deep inelastic scattering,” in *Workshop on Monte Carlo Generators for HERA Physics (Plenary Starting Meeting)*, Apr. 1998, pp. 270–279. arXiv: `hep-ph/9907280`.

[113] S. D. Ellis and D. E. Soper, “Successive combination jet algorithm for hadron collisions,” *Phys. Rev. D*, vol. 48, pp. 3160–3166, 1993. DOI: `10.1103/PhysRevD.48.3160`. arXiv: `hep-ph/9305266`.

[114] S. Catani, Y. L. Dokshitzer, M. H. Seymour, and B. R. Webber, “Longitudinally invariant K_t clustering algorithms for hadron hadron collisions,” *Nucl. Phys. B*, vol. 406, pp. 187–224, 1993. DOI: `10.1016/0550-3213(93)90166-M`.

[115] G. Dissertori and M. Schmelling, “An improved theoretical prediction for the 2-jet rate in e+e- annihilation,” *Phys. Lett. B*, vol. 361, 167–178. 13 p, Jul. 1995. DOI: `10.1016/0370-2693(95)01174-O`. [Online]. Available: `https://cds.cern.ch/record/287515`.

[116] R. Kogler *et al.*, “Jet Substructure at the Large Hadron Collider: Experimental Review,” *Rev. Mod. Phys.*, vol. 91, no. 4, p. 045 003, 2019. DOI: `10.1103/RevModPhys.91.045003`. arXiv: `1803.06991 [hep-ex]`.

[117] M. Cacciari and G. P. Salam, “Pileup subtraction using jet areas,” *Physics Letters B*, vol. 659, no. 1, pp. 119–126, 2008, ISSN: 0370-2693. DOI: `https://doi.org/10.1016/j.physletb.2007.09.077`. [Online]. Available: `https://www.sciencedirect.com/science/article/pii/S0370269307011094`.

[118] R. Field, “Min-Bias and the Underlying Event at the LHC,” *Acta Phys. Polon. B*, vol. 42, M. Praszalowicz, Ed., pp. 2631–2656, 2011. DOI: `10.5506/APhysPolB.42.2631`. arXiv: `1110.5530 [hep-ph]`.

[119] S. Chatrchyan *et al.*, “Measurement of the Underlying Event Activity at the LHC with $\sqrt{s} = 7$ TeV and Comparison with $\sqrt{s} = 0.9$ TeV,” *JHEP*, vol. 09, p. 109, 2011. DOI: `10.1007/JHEP09(2011)109`. arXiv: `1107.0330 [hep-ex]`.

[120] D. Milstead, “Measurements of the underlying-event properties with the ATLAS detector,” *PoS*, vol. DIS2016, p. 078, 2016. DOI: `10.22323/1.265.0078`.

[121] S. Chatrchyan *et al.*, “Studies of Jet Mass in Dijet and W/Z + Jet Events,” *JHEP*, vol. 05, p. 090, 2013. DOI: `10.1007/JHEP05(2013)090`. arXiv: `1303.4811 [hep-ex]`.

[122] G. Aad *et al.*, “Jet mass and substructure of inclusive jets in $\sqrt{s} = 7$ TeV pp collisions with the ATLAS experiment,” *JHEP*, vol. 05, p. 128, 2012. DOI: `10.1007/JHEP05(2012)128`. arXiv: `1203.4606 [hep-ex]`.

[123] A. M. Sirunyan *et al.*, “Measurements of the differential jet cross section as a function of the jet mass in dijet events from proton-proton collisions at $\sqrt{s} = 13$ TeV,” *JHEP*, vol. 11, p. 113, 2018. DOI: `10.1007/JHEP11(2018)113`. arXiv: `1807.05974 [hep-ex]`.

[124] D. E. Soper and M. Spannowsky, “Finding top quarks with shower deconstruction,” *Phys. Rev. D*, vol. 87, p. 054 012, 2013. DOI: `10.1103/PhysRevD.87.054012`. arXiv: `1211.3140 [hep-ph]`.

[125] F. A. Dreyer, G. P. Salam, and G. Soyez, “The Lund Jet Plane,” *JHEP*, vol. 12, p. 064, 2018. DOI: `10.1007/JHEP12(2018)064`. arXiv: `1807.04758 [hep-ph]`.

[126] A. J. Larkoski and J. Thaler, “Unsafe but Calculable: Ratios of Angularities in Perturbative QCD,” *JHEP*, vol. 09, p. 137, 2013. DOI: `10.1007/JHEP09(2013)137`. arXiv: `1307.1699 [hep-ph]`.

[127] A. J. Larkoski, G. P. Salam, and J. Thaler, “Energy Correlation Functions for Jet Substructure,” *JHEP*, vol. 06, p. 108, 2013. DOI: `10.1007/JHEP06(2013)108`. arXiv: `1305.0007 [hep-ph]`.

[128] G. Kasieczka, S. Marzani, G. Soyez, and G. Stagnitto, “Towards Machine Learning Analytics for Jet Substructure,” *JHEP*, vol. 09, p. 195, 2020. DOI: `10.1007/JHEP09(2020)195`. arXiv: `2007.04319 [hep-ph]`.

[129] P. Gras, S. Höche, D. Kar, A. Larkoski, L. Lönnblad, S. Plätzer, A. Siódmok, P. Skands, G. Soyez, and J. Thaler, “Systematics of quark/gluon tagging,” *JHEP*, vol. 07, p. 091, 2017. DOI: `10.1007/JHEP07(2017)091`. arXiv: `1704.03878 [hep-ph]`.

[130] A. J. Larkoski, J. Thaler, and W. J. Waalewijn, “Gaining (Mutual) Information about Quark/Gluon Discrimination,” *JHEP*, vol. 11, p. 129, 2014. DOI: `10.1007/JHEP11(2014)129`. arXiv: `1408.3122 [hep-ph]`.

[131] C. Frye, A. J. Larkoski, J. Thaler, and K. Zhou, “Casimir Meets Poisson: Improved Quark/Gluon Discrimination with Counting Observables,” *JHEP*, vol. 09, p. 083, 2017. DOI: `10.1007/JHEP09(2017)083`. arXiv: `1704.06266 [hep-ph]`.

[132] G. Brooijmans, “High pT Hadronic Top Quark Identification,” CERN, Geneva, Tech. Rep., Jan. 2008. [Online]. Available: `http://cds.cern.ch/record/1077731`.

[133] “A Cambridge-Aachen (C-A) based Jet Algorithm for boosted top-jet tagging,” Jul. 2009.

[134] G. Aad *et al.*, “Identification of boosted, hadronically decaying W bosons and comparisons with ATLAS data taken at $\sqrt{s} = 8$ TeV,” *Eur. Phys. J. C*, vol. 76, no. 3, p. 154, 2016. DOI: `10.1140/epjc/s10052-016-3978-z`. arXiv: `1510.05821 [hep-ex]`.

[135] A. J. Larkoski, S. Marzani, and J. Thaler, “Sudakov Safety in Perturbative QCD,” *Phys. Rev. D*, vol. 91, no. 11, p. 111 501, 2015. DOI: `10.1103/PhysRevD.91.111501`. arXiv: `1502.01719 [hep-ph]`.

[136] M. Beneke, “Renormalons,” *Phys. Rept.*, vol. 317, pp. 1–142, 1999. DOI: `10.1016/S0370-1573(98)00130-6`. arXiv: `hep-ph/9807443`.

[137] J. Thaler and K. Van Tilburg, “Maximizing Boosted Top Identification by Minimizing N-subjettiness,” *JHEP*, vol. 02, p. 093, 2012. DOI: `10.1007/JHEP02(2012)093`. arXiv: `1108.2701 [hep-ph]`.

[138] G. Aad *et al.*, “Search for $W' \to tb \to qqbb$ decays in pp collisions at $\sqrt{s} = 8$ TeV with the ATLAS detector,” *Eur. Phys. J. C*, vol. 75, no. 4, p. 165, 2015. DOI: `10.1140/epjc/s10052-015-3372-2`. arXiv: `1408.0886 [hep-ex]`.

[139] J. Cogan, M. Kagan, E. Strauss, and A. Schwarztman, “Jet-Images: Computer Vision Inspired Techniques for Jet Tagging,” *JHEP*, vol. 02, p. 118, 2015. DOI: `10.1007/JHEP02(2015)118`. arXiv: `1407.5675 [hep-ph]`.

[140] L. G. Almeida, M. Backović, M. Cliche, S. J. Lee, and M. Perelstein, “Playing Tag with ANN: Boosted Top Identification with Pattern Recognition,” *JHEP*, vol. 07, p. 086, 2015. DOI: `10.1007/JHEP07(2015)086`. arXiv: `1501.05968 [hep-ph]`.

[141] P. Baldi, K. Bauer, C. Eng, P. Sadowski, and D. Whiteson, “Jet Substructure Classification in High-Energy Physics with Deep Neural Networks,” *Phys. Rev. D*, vol. 93, no. 9, p. 094 034, 2016. DOI: `10.1103/PhysRevD.93.094034`. arXiv: `1603.09349 [hep-ex]`.

[142] A. M. Sirunyan *et al.*, “Identification of heavy, energetic, hadronically decaying particles using machine-learning techniques,” *JINST*, vol. 15, no. 06, P06005, 2020. DOI: `10.1088/1748-0221/15/06/P06005`. arXiv: `2004.08262 [hep-ex]`.

[143] J. Barnard, E. N. Dawe, M. J. Dolan, and N. Rajcic, "Parton Shower Uncertainties in Jet Substructure Analyses with Deep Neural Networks," *Phys. Rev. D*, vol. 95, no. 1, p. 014 018, 2017. DOI: `10.1103/PhysRevD.95.014018`. arXiv: `1609.00607 [hep-ph]`.

[144] F. Dulat, S. Hoeche, and S. Prestel, "Leading-Color Fully Differential Two-Loop Soft Corrections to QCD Dipole Showers," *Phys. Rev. D*, vol. 98, no. 7, p. 074 013, 2018. DOI: `10.1103/PhysRevD.98.074013`. arXiv: `1805.03757 [hep-ph]`.

[145] S. Plätzer, M. Sjodahl, and J. Thorén, "Color matrix element corrections for parton showers," *JHEP*, vol. 11, p. 009, 2018. DOI: `10.1007/JHEP11(2018)009`. arXiv: `1808.00332 [hep-ph]`.

[146] R. Ángeles Martínez, M. De Angelis, J. R. Forshaw, S. Plätzer, and M. H. Seymour, "Soft gluon evolution and non-global logarithms," *JHEP*, vol. 05, p. 044, 2018. DOI: `10.1007/JHEP05(2018)044`. arXiv: `1802.08531 [hep-ph]`.

[147] Z. Nagy and D. E. Soper, "What is a parton shower?" *Phys. Rev. D*, vol. 98, no. 1, p. 014 034, 2018. DOI: `10.1103/PhysRevD.98.014034`. arXiv: `1705.08093 [hep-ph]`.

[148] N. Fischer, S. Prestel, M. Ritzmann, and P. Skands, "Vincia for Hadron Colliders," *Eur. Phys. J. C*, vol. 76, no. 11, p. 589, 2016. DOI: `10.1140/epjc/s10052-016-4429-6`. arXiv: `1605.06142 [hep-ph]`.

[149] G. Agarwal, L. Hay, I. Iashvili, B. Mannix, C. McLean, M. Morris, S. Rappoccio, and U. Schubert, "Explainable AI for ML jet taggers using expert variables and layerwise relevance propagation," *JHEP*, vol. 05, p. 208, 2021. DOI: `10.1007/JHEP05(2021)208`. arXiv: `2011.13466 [physics.data-an]`.

[150] K. Datta and A. Larkoski, "How Much Information is in a Jet?" *JHEP*, vol. 06, p. 073, 2017. DOI: `10.1007/JHEP06(2017)073`. arXiv: `1704.08249 [hep-ph]`.

[151] B. Nachman and C. Shimmin, "AI Safety for High Energy Physics," Oct. 2019. arXiv: `1910.08606 [hep-ph]`.

[152] S. Choi, S. J. Lee, and M. Perelstein, "Infrared Safety of a Neural-Net Top Tagging Algorithm," *JHEP*, vol. 02, p. 132, 2019. DOI: `10.1007/JHEP02(2019)132`. arXiv: `1806.01263 [hep-ph]`.

[153] G. Louppe, K. Cho, C. Becot, and K. Cranmer, "QCD-Aware Recursive Neural Networks for Jet Physics," *JHEP*, vol. 01, p. 057, 2019. DOI: `10.1007/JHEP01(2019)057`. arXiv: `1702.00748 [hep-ph]`.

[154] G. Aad *et al.*, “Measurement of soft-drop jet observables in *pp* collisions with the ATLAS detector at $\sqrt{s}$ =13 TeV,” *Phys. Rev. D*, vol. 101, no. 5, p. 052 007, 2020. DOI: `10.1103/PhysRevD.101.052007`. arXiv: `1912.09837 [hep-ex]`.

[155] A. Lifson, G. P. Salam, and G. Soyez, “Calculating the primary Lund Jet Plane density,” *JHEP*, vol. 10, p. 170, 2020. DOI: `10.1007/JHEP10(2020)170`. arXiv: `2007.06578 [hep-ph]`.

[156] Z.-B. Kang, K. Lee, X. Liu, and F. Ringer, “The groomed and ungroomed jet mass distribution for inclusive jet production at the LHC,” *JHEP*, vol. 10, p. 137, 2018. DOI: `10.1007/JHEP10(2018)137`. arXiv: `1803.03645 [hep-ph]`.

[157] C. Oleari, “The POWHEG-BOX,” *Nucl. Phys. B Proc. Suppl.*, vol. 205-206, J. Blümlein, S.-O. Moch, and T. Riemann, Eds., pp. 36–41, 2010. DOI: `10.1016/j.nuclphysbps.2010.08.016`. arXiv: `1007.3893 [hep-ph]`.

[158] E. Gerwick, S. Hoeche, S. Marzani, and S. Schumann, “Soft evolution of multi-jet final states,” *JHEP*, vol. 02, p. 106, 2015. DOI: `10.1007/JHEP02(2015)106`. arXiv: `1411.7325 [hep-ph]`.

[159] T. Becher and M. D. Schwartz, “A precise determination of α_s from LEP thrust data using effective field theory,” *JHEP*, vol. 07, p. 034, 2008. DOI: `10.1088/1126-6708/2008/07/034`. arXiv: `0803.0342 [hep-ph]`.

[160] R. Abbate, M. Fickinger, A. H. Hoang, V. Mateu, and I. W. Stewart, “Thrust at N^3LL with Power Corrections and a Precision Global Fit for $\alpha_s(mZ)$,” *Phys. Rev. D*, vol. 83, p. 074 021, 2011. DOI: `10.1103/PhysRevD.83.074021`. arXiv: `1006.3080 [hep-ph]`.

[161] G. Abbiendi *et al.*, “Measurement of event shape distributions and moments in e+ e- —> hadrons at 91-GeV - 209-GeV and a determination of alpha(s),” *Eur. Phys. J. C*, vol. 40, pp. 287–316, 2005. DOI: `10.1140/epjc/s2005-02120-6`. arXiv: `hep-ex/0503051`.

[162] K. Abe *et al.*, “Measurement of alpha-s (M(Z)**2) from hadronic event observables at the Z0 resonance,” *Phys. Rev. D*, vol. 51, pp. 962–984, 1995. DOI: `10.1103/PhysRevD.51.962`. arXiv: `hep-ex/9501003`.

[163] O. Biebel, P. A. Movilla Fernandez, and S. Bethke, “C parameter and jet broadening at PETRA energies,” *Phys. Lett. B*, vol. 459, pp. 326–334, 1999. DOI: `10.1016/S0370-2693(99)00733-9`. arXiv: `hep-ex/9903009`.

[164] D. colaboration, “Energy dependence of event shapes and of s at lep 2,” *Physics Letters B*, vol. 456, no. 2, pp. 322–340, 1999, ISSN: 0370-2693. DOI: https://doi.org/10.1016/S0370-2693(99)00472-4. [Online]. Available: https://www.sciencedirect.com/science/article/pii/S0370269399004724.

[165] Y. L. Dokshitzer and B. R. Webber, “Calculation of power corrections to hadronic event shapes,” *Phys. Lett. B*, vol. 352, pp. 451–455, 1995. DOI: 10.1016/0370-2693(95)00548-Y. arXiv: hep-ph/9504219.

[166] T. Gehrmann, G. Luisoni, and P. F. Monni, “Power corrections in the dispersive model for a determination of the strong coupling constant from the thrust distribution,” *Eur. Phys. J. C*, vol. 73, no. 1, p. 2265, 2013. DOI: 10.1140/epjc/s10052-012-2265-x. arXiv: 1210.6945 [hep-ph].

[167] G. P. Korchemsky and S. Tafat, “On power corrections to the event shape distributions in QCD,” *JHEP*, vol. 10, p. 010, 2000. DOI: 10.1088/1126-6708/2000/10/010. arXiv: hep-ph/0007005.

[168] G. P. Korchemsky and G. F. Sterman, “Power corrections to event shapes and factorization,” *Nucl. Phys. B*, vol. 555, pp. 335–351, 1999. DOI: 10.1016/S0550-3213(99)00308-9. arXiv: hep-ph/9902341.

[169] D. d’Enterria *et al.*, “The strong coupling constant: State of the art and the decade ahead,” Mar. 2022. arXiv: 2203.08271 [hep-ph].

[170] *Les Houches 2017: Physics at TeV Colliders Standard Model Working Group Report*, Mar. 2018. arXiv: 1803.07977 [hep-ph].

[171] A. M. Sirunyan *et al.*, “Measurement of jet substructure observables in $\mathrm{t}\bar{\mathrm{t}}$ events from proton-proton collisions at $\sqrt{s} = 13$TeV,” *Phys. Rev. D*, vol. 98, no. 9, p. 092 014, 2018. DOI: 10.1103/PhysRevD.98.092014. arXiv: 1808.07340 [hep-ex].

[172] M. Tanabashi *et al.*, “Review of Particle Physics,” *Phys. Rev. D*, vol. 98, no. 3, p. 030 001, 2018. DOI: 10.1103/PhysRevD.98.030001.

[173] A. H. Hoang, “What is the Top Quark Mass?” *Ann. Rev. Nucl. Part. Sci.*, vol. 70, pp. 225–255, 2020. DOI: 10.1146/annurev-nucl-101918-023530. arXiv: 2004.12915 [hep-ph].

[174] S. Alekhin, A. Djouadi, and S. Moch, “The top quark and Higgs boson masses and the stability of the electroweak vacuum,” *Phys. Lett. B*, vol. 716, pp. 214–219, 2012. DOI: 10.1016/j.physletb.2012.08.024. arXiv: 1207.0980 [hep-ph].

[175] A. H. Hoang and I. W. Stewart, "Top Mass Measurements from Jets and the Tevatron Top-Quark Mass," *Nucl. Phys. B Proc. Suppl.*, vol. 185, G. Bellettini, G. Chiarelli, and R. Tenchini, Eds., pp. 220–226, 2008. DOI: `10.1016/j.nuclphysbps.2008.10.028`. arXiv: `0808.0222 [hep-ph]`.

[176] S. Moch, U. Langenfeld, and P. Uwer, "The Top-Quark's Running Mass," *PoS*, vol. RADCOR2009, p. 030, 2010. DOI: `10.22323/1.092.0030`. arXiv: `1001.3987 [hep-ph]`.

[177] F. Deliot and D. A. Glenzinski, "Top Quark Physics at the Tevatron," *Rev. Mod. Phys.*, vol. 84, p. 211, 2012. DOI: `10.1103/RevModPhys.84.211`. arXiv: `1010.1202 [hep-ex]`.

[178] A. Juste, S. Mantry, A. Mitov, A. Penin, P. Skands, E. Varnes, M. Vos, and S. Wimpenny, "Determination of the top quark mass circa 2013: methods, subtleties, perspectives," *Eur. Phys. J. C*, vol. 74, p. 3119, 2014. DOI: `10.1140/epjc/s10052-014-3119-5`. arXiv: `1310.0799 [hep-ph]`.

[179] S. Moch *et al.*, "High precision fundamental constants at the TeV scale," May 2014. arXiv: `1405.4781 [hep-ph]`.

[180] A. H. Hoang, "The Top Mass: Interpretation and Theoretical Uncertainties," in *7th International Workshop on Top Quark Physics*, Dec. 2014. arXiv: `1412.3649 [hep-ph]`.

[181] S. Weinzierl, "Precision on the top mass," in *50th Rencontres de Moriond on EW Interactions and Unified Theories*, May 2015, pp. 133–140. arXiv: `1505.00630 [hep-ph]`.

[182] P. Azzurri *et al.*, "Physics Behind Precision," P. Azzi, F. Blekman, E. Locci, F. Piccinini, and R. Tenchini, Eds., Mar. 2017. arXiv: `1703.01626 [hep-ph]`.

[183] J. Holguin, I. Moult, A. Pathak, and M. Procura, "A New Paradigm for Precision Top Physics: Weighing the Top with Energy Correlators," Jan. 2022. arXiv: `2201.08393 [hep-ph]`.

[184] H. Chen, I. Moult, X. Zhang, and H. X. Zhu, "Rethinking jets with energy correlators: Tracks, resummation, and analytic continuation," *Phys. Rev. D*, vol. 102, no. 5, p. 054 012, 2020. DOI: `10.1103/PhysRevD.102.054012`. arXiv: `2004.11381 [hep-ph]`.

[185] J. Tena-Vidal *et al.*, "Hadronization model tuning in genie v3," *Phys. Rev. D*, vol. 105, no. 1, p. 012 009, 2022. DOI: `10.1103/PhysRevD.105.012009`. arXiv: `2106.05884 [hep-ph]`.

[186] J. Baron, S. Marzani, and V. Theeuwes, "Soft-Drop Thrust," *JHEP*, vol. 08, p. 105, 2018, [Erratum: JHEP 05, 056 (2019)]. DOI: `10.1007/JHEP08(2018)105`. arXiv: `1803.04719 [hep-ph]`.

[187] G. Bell, R. Rahn, and J. Talbert, "Two-loop anomalous dimensions of generic dijet soft functions," *Nucl. Phys. B*, vol. 936, pp. 520–541, 2018. DOI: `10.1016/j.nuclphysb.2018.09.026`. arXiv: `1805.12414 [hep-ph]`.

[188] A. Kardos, G. Somogyi, and Z. Trócsányi, "Soft-drop event shapes in electron–positron annihilation at next-to-next-to-leading order accuracy," *Phys. Lett. B*, vol. 786, pp. 313–318, 2018. DOI: `10.1016/j.physletb.2018.10.014`. arXiv: `1807.11472 [hep-ph]`.

[189] S. Marzani, D. Reichelt, S. Schumann, G. Soyez, and V. Theeuwes, "Fitting the Strong Coupling Constant with Soft-Drop Thrust," *JHEP*, vol. 11, p. 179, 2019. DOI: `10.1007/JHEP11(2019)179`. arXiv: `1906.10504 [hep-ph]`.

[190] A. Kardos, A. J. Larkoski, and Z. Trócsányi, "Two- and Three-Loop Data for Groomed Jet Mass," 2020. arXiv: `2002.05730 [hep-ph]`.

[191] A. H. Hoang, S. Mantry, A. Pathak, and I. W. Stewart, "Nonperturbative Corrections to Soft Drop Jet Mass," *JHEP*, vol. 12, p. 002, 2019. DOI: `10.1007/JHEP12(2019)002`. arXiv: `1906.11843 [hep-ph]`.

[192] J. C. Collins and D. E. Soper, "Back-To-Back Jets in QCD," *Nucl. Phys. B*, vol. 193, p. 381, 1981, [Erratum: Nucl.Phys.B 213, 545 (1983)]. DOI: `10.1016/0550-3213(81)90339-4`.

[193] J. C. Collins and D. E. Soper, "Back-To-Back Jets: Fourier Transform from B to K-Transverse," *Nucl. Phys. B*, vol. 197, pp. 446–476, 1982. DOI: `10.1016/0550-3213(82)90453-9`.

[194] J. Kodaira and L. Trentadue, "Summing Soft Emission in QCD," *Phys. Lett. B*, vol. 112, p. 66, 1982. DOI: `10.1016/0370-2693(82)90907-8`.

[195] J. Kodaira and L. Trentadue, "Single Logarithm Effects in electron-Positron Annihilation," *Phys. Lett. B*, vol. 123, pp. 335–338, 1983. DOI: `10.1016/0370-2693(83)91213-3`.

[196] A. Banfi, B. K. El-Menoufi, and P. F. Monni, "The Sudakov radiator for jet observables and the soft physical coupling," *JHEP*, vol. 01, p. 083, 2019. DOI: `10.1007/JHEP01(2019)083`. arXiv: `1807.11487 [hep-ph]`.

[197] S. Catani, D. De Florian, and M. Grazzini, "Soft-gluon effective coupling and cusp anomalous dimension," *Eur. Phys. J. C*, vol. 79, no. 8, p. 685, 2019. DOI: `10.1140/epjc/s10052-019-7174-9`. arXiv: `1904.10365 [hep-ph]`.

[198] W. Giele and E. Glover, "Higher order corrections to jet cross-sections in e+ e- annihilation," *Phys. Rev. D*, vol. 46, pp. 1980–2010, 1992. DOI: `10.1103/PhysRevD.46.1980`.

[199] A. Gehrmann-De Ridder and E. Glover, "A complete (s)calculation of the photon + 1 jet rate in e+ e— annihilation," *Nuclear Physics B*, vol. 517, no. 1-3, pp. 269–323, Apr. 1998, ISSN: 0550-3213. DOI: `10.1016/s0550-3213(97)00818-3`. [Online]. Available: `http://dx.doi.org/10.1016/S0550-3213(97)00818-3`.

[200] T. Hahn, "Cuba library for multidimensional numerical integration," *Computer Physics Communications*, vol. 168, no. 2, pp. 78–95, Jun. 2005, ISSN: 0010-4655. DOI: `10.1016/j.cpc.2005.01.010`. [Online]. Available: `http://dx.doi.org/10.1016/j.cpc.2005.01.010`.

[201] E. W. Weisstein, *Polygamma function. from mathworld–a wolfram web resource*, `https://mathworld.wolfram.com/PolygammaFunction.html`.

[202] D. de Florian and M. Grazzini, "The Structure of large logarithmic corrections at small transverse momentum in hadronic collisions," *Nucl. Phys. B*, vol. 616, pp. 247–285, 2001. DOI: `10.1016/S0550-3213(01)00460-6`. arXiv: `hep-ph/0108273`.

[203] I. Wolfram Research, *Mathematica, Version 12.1*, Champaign, IL, 2020. [Online]. Available: `https://www.wolfram.com/mathematica`.

[204] D. de Florian and M. Grazzini, "Next-to-next-to-leading logarithmic corrections at small transverse momentum in hadronic collisions," *Phys. Rev. Lett.*, vol. 85, pp. 4678–4681, 2000. DOI: `10.1103/PhysRevLett.85.4678`. arXiv: `hep-ph/0008152`.

[205] S. Catani, D. de Florian, and M. Grazzini, "Universality of nonleading logarithmic contributions in transverse momentum distributions," *Nucl. Phys. B*, vol. 596, pp. 299–312, 2001. DOI: `10.1016/S0550-3213(00)00617-9`. arXiv: `hep-ph/0008184`.

[206] D. de Florian and M. Grazzini, "The Back-to-back region in e+ e- energy-energy correlation," *Nucl. Phys. B*, vol. 704, pp. 387–403, 2005. DOI: `10.1016/j.nuclphysb.2004.10.051`. arXiv: `hep-ph/0407241`.

[207] W. Furmanski and R. Petronzio, "Singlet Parton Densities Beyond Leading Order," *Phys. Lett. B*, vol. 97, pp. 437–442, 1980. DOI: `10.1016/0370-2693(80)90636-X`.

[208] G. Curci, W. Furmanski, and R. Petronzio, "Evolution of Parton Densities Beyond Leading Order: The Nonsinglet Case," *Nucl. Phys. B*, vol. 175, pp. 27–92, 1980. DOI: `10.1016/0550-3213(80)90003-6`.

[209] Y.-T. Chien and M. D. Schwartz, "Resummation of heavy jet mass and comparison to LEP data," *JHEP*, vol. 08, p. 058, 2010. DOI: `10.1007/JHEP08(2010)058`. arXiv: `1005.1644 [hep-ph]`.

[210] A. Banfi, H. McAslan, P. F. Monni, and G. Zanderighi, "A general method for the resummation of event-shape distributions in e^+e^- annihilation," *JHEP*, vol. 05, p. 102, 2015. DOI: `10.1007/JHEP05(2015)102`. arXiv: `1412.2126 [hep-ph]`.

[211] M. Dasgupta and B. K. El-Menoufi, "Dissecting the collinear structure of quark splitting at NNLL," *JHEP*, vol. 12, p. 158, 2021. DOI: `10.1007/JHEP12(2021)158`. arXiv: `2109.07496 [hep-ph]`.

[212] M. Dasgupta, F. Dreyer, G. P. Salam, and G. Soyez, "Small-radius jets to all orders in QCD," *JHEP*, vol. 04, p. 039, 2015. DOI: `10.1007/JHEP04(2015)039`. arXiv: `1411.5182 [hep-ph]`.

[213] D. Reichelt, S. Caletti, O. Fedkevych, S. Marzani, S. Schumann, and G. Soyez, "Phenomenology of jet angularities at the LHC," Dec. 2021. arXiv: `2112.09545 [hep-ph]`.

[214] "Study of quark and gluon jet substructure in dijet and Z+jet events from pp collisions," 2021.

[215] J. R. Andersen *et al.*, "Les Houches 2015: Physics at TeV Colliders Standard Model Working Group Report," in *9th Les Houches Workshop on Physics at TeV Colliders*, May 2016. arXiv: `1605.04692 [hep-ph]`.

[216] J. C. Collins and D. E. Soper, "Back-to-back jets in qcd," *Nuclear Physics B*, vol. 193, no. 2, pp. 381–443, 1981, ISSN: 0550-3213. DOI: `https://doi.org/10.1016/0550-3213(81)90339-4`. [Online]. Available: `https://www.sciencedirect.com/science/article/pii/0550321381903394`.

[217] J. C. Collins and D. E. Soper, "Back-to-back jets: Fourier transform from b to kt," *Nuclear Physics B*, vol. 197, no. 3, pp. 446–476, 1982, ISSN: 0550-3213. DOI: `https://doi.org/10.1016/0550-3213(82)90453-9`. [Online]. Available: `https://www.sciencedirect.com/science/article/pii/0550321382904539`.

[218] J. Kodaira and L. Trentadue, “Summing soft emission in qcd,” *Physics Letters B*, vol. 112, no. 1, pp. 66–70, 1982, ISSN: 0370-2693. DOI: `https://doi.org/10.1016/0370-2693(82)90907-8`. [Online]. Available: `https://www.sciencedirect.com/science/article/pii/0370269382909078`.

[219] J. Kodaira and L. Trentadue, “Single logarithm effects in electron-positron annihilation,” *Physics Letters B*, vol. 123, no. 5, pp. 335–338, 1983, ISSN: 0370-2693. DOI: `https://doi.org/10.1016/0370-2693(83)91213-3`. [Online]. Available: `https://www.sciencedirect.com/science/article/pii/0370269383912133`.

[220] W. Furmanski and R. Petronzio, “Singlet parton densities beyond leading order,” *Physics Letters B*, vol. 97, no. 3, pp. 437–442, 1980, ISSN: 0370-2693. DOI: `https://doi.org/10.1016/0370-2693(80)90636-X`. [Online]. Available: `https://www.sciencedirect.com/science/article/pii/037026938090636X`.

[221] G. Curci, W. Furmanski, and R. Petronzio, “Evolution of parton densities beyond leading order: The non-singlet case,” *Nuclear Physics B*, vol. 175, no. 1, pp. 27–92, 1980, ISSN: 0550-3213. DOI: `https://doi.org/10.1016/0550-3213(80)90003-6`. [Online]. Available: `https://www.sciencedirect.com/science/article/pii/0550321380900036`.

[222] S. Catani, G. Turnock, and B. Webber, “Heavy jet mass distribution in e+e- annihilation,” *Physics Letters B*, vol. 272, no. 3, pp. 368–372, 1991, ISSN: 0370-2693. DOI: `https://doi.org/10.1016/0370-2693(91)91845-M`. [Online]. Available: `https://www.sciencedirect.com/science/article/pii/037026939191845M`.

[223] P. Rakow and B. Webber, “Transverse momentum moments of hadron distributions in qcd jets,” *Nuclear Physics B*, vol. 191, no. 1, pp. 63–74, 1981, ISSN: 0550-3213. DOI: `https://doi.org/10.1016/0550-3213(81)90286-8`. [Online]. Available: `https://www.sciencedirect.com/science/article/pii/0550321381902868`.

[224] C. F. Berger, T. Kucs, and G. F. Sterman, “Event shape / energy flow correlations,” *Phys. Rev. D*, vol. 68, p. 014 012, 2003. DOI: `10.1103/PhysRevD.68.014012`. arXiv: `hep-ph/0303051`.

[225] D. Bertolini, J. Thaler, and J. R. Walsh, “The First Calculation of Fractional Jets,” *JHEP*, vol. 05, p. 008, 2015. DOI: `10.1007/JHEP05(2015)008`. arXiv: `1501.01965 [hep-ph]`.

[226] A. Gehrmann-De Ridder and E. W. N. Glover, “A Complete O (alpha alpha-s) calculation of the photon + 1 jet rate in e+ e- annihilation,” *Nucl. Phys. B*, vol. 517, pp. 269–323, 1998. DOI: `10.1016/S0550-3213(97)00818-3`. arXiv: `hep-ph/9707224`.

[227] S. Catani and M. H. Seymour, “The Dipole formalism for the calculation of QCD jet cross-sections at next-to-leading order,” *Phys. Lett. B*, vol. 378, pp. 287–301, 1996. DOI: `10.1016/0370-2693(96)00425-X`. arXiv: `hep-ph/9602277`.

[228] S. Catani and M. H. Seymour, “A General algorithm for calculating jet cross-sections in NLO QCD,” *Nucl. Phys. B*, vol. 485, pp. 291–419, 1997, [Erratum: Nucl.Phys.B 510, 503–504 (1998)]. DOI: `10.1016/S0550-3213(96)00589-5`. arXiv: `hep-ph/9605323`.

[229] P. E. L. Rakow and B. R. Webber, “Transverse Momentum Moments of Hadron Distributions in QCD Jets,” *Nucl. Phys. B*, vol. 191, pp. 63–74, 1981. DOI: `10.1016/0550-3213(81)90286-8`.

[230] A. J. Larkoski, I. Moult, and D. Neill, “Analytic Boosted Boson Discrimination at the Large Hadron Collider,” Aug. 2017. arXiv: `1708.06760 [hep-ph]`.

[231] “A Cambridge-Aachen (C-A) based Jet Algorithm for boosted top-jet tagging,” CERN, Geneva, Tech. Rep. CMS-PAS-JME-09-001, Jul. 2009. [Online]. Available: `http://cds.cern.ch/record/1194489`.

[232] D. E. Kaplan, K. Rehermann, M. D. Schwartz, and B. Tweedie, “Top Tagging: A Method for Identifying Boosted Hadronically Decaying Top Quarks,” *Phys. Rev. Lett.*, vol. 101, p. 142 001, 2008. DOI: `10.1103/PhysRevLett.101.142001`. arXiv: `0806.0848 [hep-ph]`.

[233] T. Plehn, G. P. Salam, and M. Spannowsky, “Fat Jets for a Light Higgs,” *Phys. Rev. Lett.*, vol. 104, p. 111 801, 2010. DOI: `10.1103/PhysRevLett.104.111801`. arXiv: `0910.5472 [hep-ph]`.

[234] A. J. Larkoski, I. Moult, and D. Neill, “Building a Better Boosted Top Tagger,” *Phys. Rev. D*, vol. 91, no. 3, p. 034 035, 2015. DOI: `10.1103/PhysRevD.91.034035`. arXiv: `1411.0665 [hep-ph]`.

[235] L. G. Almeida, S. J. Lee, G. Perez, G. Sterman, and I. Sung, “Template Overlap Method for Massive Jets,” *Phys. Rev. D*, vol. 82, p. 054 034, 2010. DOI: `10.1103/PhysRevD.82.054034`. arXiv: `1006.2035 [hep-ph]`.

[236] S. Catani, L. Trentadue, G. Turnock, and B. Webber, “Resummation of large logarithms in e+e- event shape distributions,” *Nuclear Physics B*, vol. 407, no. 1, pp. 3–42, 1993, ISSN: 0550-3213. DOI: `https://doi.org/10.1016/0550-3213(93)90271-P`. [Online]. Available: `https://www.sciencedirect.com/science/article/pii/055032139390271P`.

[237] T. Hahn, “CUBA: A Library for multidimensional numerical integration,” *Comput. Phys. Commun.*, vol. 168, pp. 78–95, 2005. DOI: `10.1016/j.cpc.2005.01.010`. arXiv: `hep-ph/0404043`.

[238] Y. L. Dokshitzer, V. A. Khoze, and S. Troian, “On specific QCD properties of heavy quark fragmentation (’dead cone’),” *J. Phys. G*, vol. 17, pp. 1602–1604, 1991. DOI: `10.1088/0954-3899/17/10/023`.

[239] L. H. Orr, Y. L. Dokshitzer, V. A. Khoze, and W. Stirling, “Gluon radiation and top width effects,” in *2nd International Workshop on Physics and Experiments with Linear e+ e- Colliders*, Jul. 1993, pp. 0670–675. arXiv: `hep-ph/9307338`.

[240] A. Banfi, M. Dasgupta, K. Khelifa-Kerfa, and S. Marzani, “Non-global logarithms and jet algorithms in high-pT jet shapes,” *JHEP*, vol. 08, p. 064, 2010. DOI: `10.1007/JHEP08(2010)064`. arXiv: `1004.3483 [hep-ph]`.

[241] A. Verbytskyi, A. Banfi, A. Kardos, P. F. Monni, S. Kluth, G. Somogyi, Z. Szőr, Z. Trocsányi, Z. Tulipánt, and G. Zanderighi, “Precise determination of α_S (M_Z) from global fits of e^+e^- data to NNLO+NNLL predictions,” *Nucl. Part. Phys. Proc.*, vol. 300-302, S. Narison, Ed., pp. 87–92, 2018. DOI: `10.1016/j.nuclphysbps.2018.12.016`.

[242] G. F. Sborlini, D. de Florian, and G. Rodrigo, “Double collinear splitting amplitudes at next-to-leading order,” *JHEP*, vol. 01, p. 018, 2014. DOI: `10.1007/JHEP01(2014)018`. arXiv: `1310.6841 [hep-ph]`.

[243] S. Catani, D. de Florian, and G. Rodrigo, “Space-like (versus time-like) collinear limits in QCD: Is factorization violated?” *JHEP*, vol. 07, p. 026, 2012. DOI: `10.1007/JHEP07(2012)026`. arXiv: `1112.4405 [hep-ph]`.

Appendices

Appendix A

Appendices for Chapter 4

A.1 Triple-Collinear splitting functions

We use the results in the form listed in Refs. [51], [52]. Following the notation of those references we define $\mathcal{T}$ as the squared matrix element for $e^+e^- \to 4$ partons. In the limit where three of the final partons are collinear, it can be shown that $\mathcal{T}$ satisfies the following factorized form:

$$\begin{aligned} \mathcal{T}(e^+e^- \to 4 \text{ partons}) &\simeq \mathcal{T}(e^+e^- \to q\bar{q}) \cdot \sum_k \mathcal{T}_k^{\text{coll}}(1 \to 3) \\ &= \mathcal{T}(e^+e^- \to q\bar{q}) \cdot \frac{(8\pi\alpha_s\mu^{2\epsilon})^2}{s_{123}^2} \sum_k \left\langle \hat{P}^k_{1\to 3} \right\rangle . \end{aligned} \tag{A.1}$$

Here, the k runs over the possible quark initiated $1 \to 3$ parton channels $q \to g_1g_2q_3$ ($\bar{q} \to g_1g_2\bar{q}_3$), $q \to q'_1\bar{q}'_2q_3$ ($\bar{q} \to \bar{q}'_1q'_2\bar{q}_3$) or $q \to q_1\bar{q}_2q_3$ ($\bar{q} \to \bar{q}_1q_2\bar{q}_3$), s_{123} is the squared invariant mass of the three collinear parton system, and $\left\langle \hat{P}^k_{1\to 3} \right\rangle$ are the process independent spin averaged triple-collinear splitting functions.

Hereinafter, we report the relevant expressions for the triple-collinear splitting functions [51]. Note that due to charge conjugation invariance, the splitting functions for the anti-quark initiated channels can be obtained from the corresponding functions for the quark initiated ones,. i.e. $\hat{P}_{\bar{q}'_1q'_2\bar{q}_3} = \hat{P}_{\bar{q}'_1q'_2q_3}$ and $\hat{P}_{\bar{q}_1q_2\bar{q}_3} = \hat{P}_{\bar{q}_1q_2q_3}$.
The spin-averaged splitting function for the $q \to g_1g_2q_3$ process can be written in terms of the different colour factors:

$$\left\langle \hat{P}_{g_1g_2q_3} \right\rangle = C_F^2 \left\langle \hat{P}^{(\text{ab})}_{g_1g_2q_3} \right\rangle + C_FC_A \left\langle \hat{P}^{(\text{nab})}_{g_1g_2q_3} \right\rangle \quad , \tag{A.2}$$

where the abelian and non-abelian contributions are

$$\begin{aligned} &\left\langle \hat{P}^{(\text{ab})}_{g_1g_2q_3} \right\rangle = \\ &\left\{ \frac{s_{123}^2}{2s_{13}s_{23}} z_3 \left[\frac{1+z_3^2}{z_1z_2} - \epsilon\frac{z_1^2+z_2^2}{z_1z_2} - \epsilon(1+\epsilon) \right] + \frac{s_{123}}{s_{13}} \left[\frac{z_3(1-z_1)+(1-z_2)^3}{z_1z_2} + \epsilon^2(1+z_3) \right.\right. \\ &\qquad \left.\left. - \epsilon(z_1^2+z_1z_2+z_2^2)\frac{1-z_2}{z_1z_2} \right] + (1-\epsilon)\left[\epsilon - (1-\epsilon)\frac{s_{23}}{s_{13}} \right] \right\} + (1 \leftrightarrow 2) \quad , \end{aligned} \tag{A.3}$$

$$\begin{aligned}\left\langle \hat{P}^{(\text{nab})}_{g_1 g_2 q_3} \right\rangle = \Bigg\{ & (1-\epsilon)\left(\frac{t^2_{12,3}}{4s^2_{12}} + \frac{1}{4} - \frac{\epsilon}{2}\right) + \\ & \frac{s^2_{123}}{2s_{12}s_{13}}\left[\frac{(1-z_3)^2(1-\epsilon)+2z_3}{z_2} + \frac{z_2^2(1-\epsilon)+2(1-z_2)}{1-z_3}\right] \\ & - \frac{s^2_{123}}{4s_{13}s_{23}} z_3 \left[\frac{(1-z_3)^2(1-\epsilon)+2z_3}{z_1 z_2} + \epsilon(1-\epsilon)\right] \\ & + \frac{s_{123}}{2s_{12}}\left[(1-\epsilon)\frac{z_1(2-2z_1+z_1^2) - z_2(6-6z_2+z_2^2)}{z_2(1-z_3)} + 2\epsilon\frac{z_3(z_1-2z_2)-z_2}{z_2(1-z_3)}\right] \\ & + \frac{s_{123}}{2s_{13}}\left[(1-\epsilon)\frac{(1-z_2)^3+z_3^2-z_2}{z_2(1-z_3)} - \epsilon\left(\frac{2(1-z_2)(z_2-z_3)}{z_2(1-z_3)} - z_1 + z_2\right)\right. \\ & \left. - \frac{z_3(1-z_1)+(1-z_2)^3}{z_1 z_2} + \epsilon(1-z_2)\left(\frac{z_1^2+z_2^2}{z_1 z_2} - \epsilon\right)\right]\Bigg\} + (1 \leftrightarrow 2)\,. \qquad \text{(A.4)}\end{aligned}$$

The spin-averaged splitting functions for non-identical fermions in the final state read

$$\begin{aligned}\left\langle \hat{P}_{\bar{q}'_1 q'_2 q_3} \right\rangle = & \\ \frac{1}{2}\, C_F T_R\, \frac{s_{123}}{s_{12}} & \left[-\frac{t^2_{12,3}}{s_{12}s_{123}} + \frac{4z_3+(z_1-z_2)^2}{z_1+z_2} + (1-2\epsilon)\left(z_1+z_2-\frac{s_{12}}{s_{123}}\right)\right]\ , \qquad \text{(A.5)}\end{aligned}$$

where

$$t_{ij,k} \equiv 2\,\frac{z_i s_{jk} - z_j s_{ik}}{z_i + z_j} + \frac{z_i - z_j}{z_i + z_j}\, s_{ij} \ . \qquad \text{(A.6)}$$

In the case of final-state fermions with identical flavour, the splitting function can be written in terms of Eq. (A.5), as

$$\left\langle \hat{P}_{\bar{q}_1 q_2 q_3} \right\rangle = \left[\left\langle \hat{P}_{\bar{q}'_1 q'_2 q_3} \right\rangle + (2 \leftrightarrow 3)\right] + \left\langle \hat{P}^{(\text{id})}_{\bar{q}_1 q_2 q_3} \right\rangle \ , \qquad \text{(A.7)}$$

where

$$\begin{aligned}\left\langle \hat{P}^{(\text{id})}_{\bar{q}_1 q_2 q_3} \right\rangle = C_F\left(C_F - \frac{1}{2}C_A\right)\Bigg\{ & (1-\epsilon)\left(\frac{2s_{23}}{s_{12}} - \epsilon\right) \\ & + \frac{s_{123}}{s_{12}}\left[\frac{1+z_1^2}{1-z_2} - \frac{2z_2}{1-z_3} - \epsilon\left(\frac{(1-z_3)^2}{1-z_2} + 1 + z_1 - \frac{2z_2}{1-z_3}\right) - \epsilon^2(1-z_3)\right] \\ & - \frac{s^2_{123}}{s_{12}s_{13}}\frac{z_1}{2}\left[\frac{1+z_1^2}{(1-z_2)(1-z_3)} - \epsilon\left(1 + 2\frac{1-z_2}{1-z_3}\right) - \epsilon^2\right]\Bigg\} + (2 \leftrightarrow 3)\,. \qquad \text{(A.8)}\end{aligned}$$

A.2 Integrals and pole structure

We illustrate our approach by referring explicitly to the calculations for $\mathcal{F}^{\rm pass}(\rho, \epsilon)$, though similar considerations apply to all our calculations. When all three partons contribute to the jet mass i.e. we have the delta function condition $\delta_\rho(1,2,3)$, we can eliminate the integral over an angle, say θ_{12}, by using the delta function condition. In order to perform the remaining integrals over the triple-collinear phase space $\mathrm{d}\Phi_3$, (see Eq. (4.18)) it proves to be convenient to exploit the fact that all partons are collinear, with a collinearity essentially set by the jet mass or more accurately by the parameter $\frac{\rho}{z_{\rm cut}}$. One may extract the overall $1/\rho$ scaling of $\mathrm{d}\Sigma/\mathrm{d}\rho$ by working in terms of rescaled angular variables $y = \frac{\theta_{23}^2}{\theta_{13}^2}$ and $x = \frac{\theta_{13}^2}{\rho}$. The limits on the x integral follow from the positivity of the Gram Determinant $\Delta > 0$, corresponding to the conditions $(\theta_{13}+\theta_{23})^2 > \theta_{12}^2 > (\theta_{13}-\theta_{23})^2$, which can be expressed in terms of our chosen variables as a condition on x:

$$\frac{1}{z_1(1-z_1)+yz_2(1-z_2)+2\sqrt{y}z_1z_2} < x \ , \tag{A.9}$$

$$x < \frac{1}{z_1(1-z_1)+yz_2(1-z_2)-2\sqrt{y}z_1z_2} \, . \tag{A.10}$$

It proves to be convenient to map the integral over x to one with simple limits i.e. 0 and 1 by introducing the change of variables $x = u(r_2 - r_1) + r_1$, where r_1 and r_2 are the lower and upper limits on x respectively. Our integration variables are then u and y for the angular integration, both lying in a range 0 to 1, and the energy fractions z_1 and z_2 (recall that $z_3 = 1 - z_1 - z_2$) or equivalently z and z_p.

We then have to consider the extraction of ϵ poles, to separate the integral into divergent and finite terms. Our strategy is to isolate the divergences and exploit the simplification of the integrand in divergent regions, to obtain the divergence structure analytically. This also generates finite terms that do not vanish as $\epsilon \to 0$, which are obtained via an ϵ expansion of the factors multiplying the poles. Additionally we also obtain a finite integral leftover from the removal of singular terms, which on the other hand is not a compact expression. However, being finite, it can always be integrated numerically.

Since we study the differential distribution rather than its integral, we work at fixed jet-mass which regulates both soft and collinear divergences. In general that leaves us with at most a $1/\epsilon^2$ singularity from an emission that does not set the jet mass. For the calculation of $\mathcal{F}^{\rm pass}$ in particular, the larger-angle emission passes $z_{\rm cut}$ and cannot produce any divergence, while the smaller angle emission produces divergences from the soft $z_p \to 1$ and collinear $y \to 0$ limits. Setting $1 - z_p = v$ we encounter a general integral of the standard form

$$I(\epsilon) = \int_0^1 \mathrm{d}v \int_0^1 \mathrm{d}y \frac{G\,(v, y, \epsilon)}{v^{1+2\epsilon} y^{1+\epsilon}}, \tag{A.11}$$

where $G(v, y, \epsilon)$ is finite as $v \to 0$ as well as $y \to 0$ and integration over the other variables is left implicit so as to focus on the divergences. We can re-express this result in the following form

$$I(\epsilon) = \\ \int_0^1 \mathrm{d}v \int_0^1 \mathrm{d}y \left[\frac{G(v,y,\epsilon) - G(v,0,\epsilon)}{v^{1+2\epsilon}y^{1+\epsilon}} + \frac{G(v,0,\epsilon) - G(0,0,\epsilon)}{v^{1+2\epsilon}y^{1+\epsilon}} + \frac{G(0,0,\epsilon)}{v^{1+2\epsilon}y^{1+\epsilon}}\right], \quad \text{(A.12)}$$

where by construction the first term on the LHS of the above has only a soft pole i.e. as $v \to 0$, the second term has only a collinear pole from $y \to 0$, while the final term has a double pole arising from $v \to 0$ and $y \to 0$. We define for convenience $f(v, \epsilon) = (G(v, 0, \epsilon) - G(0, 0, \epsilon))/v^{1+2\epsilon}$ where $f(v, \epsilon)$ is finite as $v \to 0$ and also define

$$h(v, y, \epsilon) = (G(v, y, \epsilon) - G(v, 0, \epsilon))/y^{1+\epsilon},$$

which is finite as $y \to 0$. Then one obtains the form

$$I(\epsilon) = \frac{G(0,0,\epsilon)}{2\epsilon^2} \\ -\frac{1}{\epsilon}\int_0^1 f(v,\epsilon)\mathrm{d}v - \frac{1}{2\epsilon}\int_0^1 h(0,y,\epsilon)\mathrm{d}y + \int_0^1 \mathrm{d}v \int_0^1 \frac{h(v,y,\epsilon) - h(0,y,\epsilon)}{v^{1+2\epsilon}}\mathrm{d}y \ . \quad \text{(A.13)}$$

The final integral on the RHS above is purely finite by construction and can be evaluated in the limit $\epsilon \to 0$ i.e in 4 dimensions. The above result shows explicitly the pole structure that emerges from the integral $I(\epsilon)$. The integrals multiplying the $1/\epsilon$ poles need only to be evaluated up to order ϵ terms i.e. one can expand the integrand in ϵ and retain only terms up to order ϵ. This strategy gives us all divergent and finite contributions in the limit $\epsilon \to 0$.

A.3 One-loop corrections to $1 \to 2$ collinear splittings

In addition to the case of two real emissions, for the jet mass distribution at order α_s^2, we also have to consider a real emission that sets the mass, ρ, alongside a one-loop virtual correction which is divergent and where the divergences cancel against those in the double-real emission case, to leave behind finite terms. The relevant real-virtual contribution to $\rho \mathrm{d}\Sigma_2/\mathrm{d}\rho$, may be collectively written in the form

$$\mathcal{V}_{1,1}(\rho, z, \epsilon) = \mathcal{V}_{1,1}^{C_F^2}(\rho, z, \epsilon) + \mathcal{V}_{1,1}^{C_F C_A}(\rho, z, \epsilon) + \mathcal{V}_{1,1}^{C_F T_R n_f}(\rho, z, \epsilon), \quad \text{(A.14)}$$

where we have separated out the various contributions according to the colour factor i.e. C_F^2, $C_F C_A$ and $C_F T_R n_f$ terms and in our notation $\mathcal{V}_{1,1}$ is the one-real, one-virtual correction to $q\bar{q}$ production, in the approximation of a real emission, which is collinear to the q or $\bar{q}$, passes grooming and sets a (normalised) jet mass ρ.

For $\mathcal{V}_{1,1}^{C_F^2}(\rho, z, \epsilon)$ there are two distinct contributions : firstly the one-loop correction to the Born level $q\bar{q}$ production, $\mathcal{V}(\epsilon)$ (see Eq. (4.8)) multiplying the squared matrix-element for a real collinear emission, and secondly the one-loop correction to a $1 \to 2$ collinear splitting [242]. The latter contribution can be explicitly obtained using the expression for $P^{(1)}_{q\to qg}$ in Eq. (103) of ref. [242], in the CDR scheme with $\alpha = 1$ and $\delta = 1$, and setting $s_{12} = \frac{Q^2}{4}\rho$, $\mu^2 = Q^2/4$ and $z_1 = 1 - z$. The Hypergeometric function in Eq. (103) of ref. [242] may be expressed in terms of a function

$$f\left(\epsilon, 1/x\right) = \frac{1}{\epsilon}\left[{}_2F_1\left(1, -\epsilon, 1-\epsilon, 1-x\right) - 1\right],$$

with the ϵ expansion [243]

$$f(\epsilon, x) = \ln x - \epsilon\left[\mathrm{Li}_2(1-x) + \sum_{k=1}^{\infty} \epsilon^k\, \mathrm{Li}_{k+2}(1-x)\right]. \tag{A.15}$$

Writing our result in terms of the renormalised $\overline{\mathrm{MS}}$ coupling, accounting for both hemispheres with a factor of two, we have

$$\mathcal{V}_{1,1}^{C_F^2}(\rho, z, \epsilon) = \left(\frac{C_F\alpha_s}{2\pi}\right)^2 \Bigg[2\,p_{qq}(z;\epsilon)\rho^{-\epsilon}(4z(1-z))^{-\epsilon}\left(-\frac{2}{\epsilon^2} + \frac{4\pi^2}{3} - 8 - \frac{3}{\epsilon}\right) \\ + p_{qq}(z,\epsilon)\rho^{-2\epsilon}(z(1-z))^{-\epsilon}\left(\frac{4}{\epsilon}\ln z + 4\,\mathrm{Li}_2\left(\frac{z-1}{z}\right)\right) - 2\Bigg]. \tag{A.16}$$

The corresponding result for the $C_F T_R n_f$ piece, after removal of UV poles via renormalisation (see e.g. ref. [243] for a detailed discussion), can be expressed as

$$\mathcal{V}_{1,1}^{C_F T_R n_f}(\rho, z, \epsilon) = 2C_F T_R n_f \left(\frac{\alpha_s}{2\pi}\right)^2 \frac{2}{3} p_{qq}(z,\epsilon)\left(\frac{1}{\epsilon}\rho^{-2\epsilon}(z(1-z))^{-\epsilon} + \ln\rho\right). \tag{A.17}$$

The result for the $C_F C_A$ piece has two distinct components i.e. a component derived like the corresponding C_F^2 piece using Eq. (103) of ref. [242] which includes the double poles that will cancel those in the real emission result, and a component involving the β function coefficient b_0 which is simply related to Eq. (A.17) via the replacement $\frac{2}{3}T_R n_f \to -\frac{11}{6}C_A$. The combined result can be expressed in the form

$$\mathcal{V}_{1,1}^{C_F C_A}(\rho, z, \epsilon) = 2C_F C_A \left(\frac{\alpha_s}{2\pi}\right)^2 \Bigg\{p_{qq}(z,\epsilon)\rho^{-2\epsilon}(z(1-z))^{-\epsilon} \\ \times\left[\frac{-1}{\epsilon^2} + \frac{1}{\epsilon}\left(\ln\frac{1-z}{z} - \frac{11}{6}\right)\right] + p_{qq}(z)\left[\mathrm{Li}_2\left(\frac{z}{z-1}\right) - \\ \mathrm{Li}_2\left(\frac{z-1}{z}\right) + \frac{2\pi^2}{3} - \frac{11}{6}\ln\rho\right] + 1\Bigg\}. \tag{A.18}$$

Appendix B

Appendices for Chapter 5

B.1 Exponentiation of soft emissions

Here we provide an explicit demonstration that all emissions satisfying $z_i < z_{\mathrm{cut}}$ can be dropped from $V_{\mathrm{sc}}^{\mathrm{simp}}(\{\tilde{p}\}, k_1, ..., k_n)$ up to power corrections in v, regardless of whether or not they are groomed away and thus can be fully exponentiated.
We start by considering an ensemble of soft and collinear emissions which are ordered in angle with an emission, (s), singled out as the one which, in configurations where the groomer does not remove all emissions, stops the groomer:

$$\begin{aligned}\Sigma^{\mathrm{real}} = \sum_{p=0}^{\infty}\sum_{m=0}^{p}\Bigg\{\prod_{j=0}^{m}\bar{\alpha}\int_0^{z_{\mathrm{cut}}}\frac{\mathrm{d}z_j}{z_j}\int_{\theta_s^2}^{1}\frac{\mathrm{d}\theta_j^2}{\theta_j^2}\Theta(\theta_j-\theta_{j+1})\bigg(\bar{\alpha}\int_0^{z_{\mathrm{cut}}}\frac{\mathrm{d}z_s}{z_s}\int_0^1\frac{\mathrm{d}\theta_s^2}{\theta_s^2}\Theta(z_{\mathrm{cut}}-z_i)\\ +\bar{\alpha}\int_{z_{\mathrm{cut}}}^{1}\frac{\mathrm{d}z_s}{z_s}\int_0^1\frac{\mathrm{d}\theta_s^2}{\theta_s^2}\Theta(v-V(k_s)-V(\{k_i\}))\bigg)\times\\ \prod_{i=0}^{p-m}\bigg(\bar{\alpha}\int_0^{z_{\mathrm{cut}}}\frac{\mathrm{d}z_i}{z_i}\int_0^{\theta_s^2}\frac{\mathrm{d}\theta_i^2}{\theta_i^2}+\bar{\alpha}\int_{z_{\mathrm{cut}}}^{1}\frac{\mathrm{d}z_s}{z_s}\int_0^{\theta_s^2}\frac{\mathrm{d}\theta_i^2}{\theta_i^2}\bigg)\Theta(\theta_i-\theta_{i+1})\Bigg\}\ , \qquad \text{(B.1)}\end{aligned}$$

where $\bar{\alpha} = \frac{C_F \alpha_s}{\pi}$. The term on the second line has $z_s > z_{\mathrm{cut}}$ and represents all configurations where the groomer is stopped, resulting in a massive jet, and thus all emissions at smaller angles (those on the final line) are retained and contribute to the observable. This term can be re-written as

$$
\begin{aligned}
\Sigma^{\text{real}}_{\text{massive}} = \sum_{p=0}^{\infty}\sum_{m=0}^{p}\Bigg\{\prod_{j=0}^{m}\bar{\alpha}\int_0^{z_{\text{cut}}}\frac{\mathrm{d}z_j}{z_j}\int_{\theta_s^2}^{1}\frac{\mathrm{d}\theta_j^2}{\theta_j^2}\Theta(\theta_j-\theta_{j+1})& \\
\left(\bar{\alpha}\int_{z_{\text{cut}}}^{1}\frac{\mathrm{d}z_s}{z_s}\int_0^1\frac{\mathrm{d}\theta_s^2}{\theta_s^2}\Theta(v-V_{\text{sc}}(k_s)-V_{\text{sc}}(\{k_i\}))\right)& \\
\prod_{i=0}^{p-m}\left(\bar{\alpha}\int_0^{z_{\text{cut}}}\frac{\mathrm{d}z_i}{z_i}\int_0^{\theta_s^2}\frac{\mathrm{d}\theta_i^2}{\theta_i^2}+\bar{\alpha}\int_{z_{\text{cut}}}^{1}\frac{\mathrm{d}z_s}{z_s}\int_0^{\theta_s^2}\frac{\mathrm{d}\theta_i^2}{\theta_i^2}\right)\Theta(\theta_i-\theta_{i+1})\Bigg\} =& \\
\int\frac{\mathrm{d}\nu}{2\pi i\nu}e^{\nu}\sum_{p=0}^{\infty}\sum_{m=0}^{p}\Bigg\{\prod_{j=0}^{m}\left(\bar{\alpha}\int_0^{z_{\text{cut}}}\frac{\mathrm{d}z_j}{z_j}\int_{\theta_s^2}^{1}\frac{\mathrm{d}\theta_j^2}{\theta_j^2}\Theta(\theta_j-\theta_{j+1})\right)& \\
\bar{\alpha}\int_{z_{\text{cut}}}^{1}\frac{\mathrm{d}z_s}{z_s}\int_0^1\frac{\mathrm{d}\theta_s^2}{\theta_s^2}e^{-\nu\frac{V_{\text{sc}}(k_s)}{v}}\prod_{i=0}^{p-m}\Bigg(\bar{\alpha}\int_{z_{\text{cut}}}^{1}\frac{\mathrm{d}z_i}{z_i}\int_0^{\theta_s^2}\frac{\mathrm{d}\theta_i^2}{\theta_i^2}e^{-\nu\frac{V_{\text{sc}}(k_i)}{v}}& \\
+\bar{\alpha}\int_0^{z_{\text{cut}}}\frac{\mathrm{d}z_i}{z_i}\int_0^{\theta_s^2}\frac{\mathrm{d}\theta_i^2}{\theta_i^2}+\left[\bar{\alpha}\int_0^{z_{\text{cut}}}\frac{\mathrm{d}z_i}{z_i}\int_0^{\theta_s^2}\frac{\mathrm{d}\theta_i^2}{\theta_i^2}(e^{-\nu\frac{V_{\text{sc}}(k_i)}{v}}-1)\right]\Bigg)\Theta(\theta_i-\theta_{i+1})\Bigg\}.& \qquad \text{(B.2)}
\end{aligned}
$$

where the step functions involving the observable have been written in their Laplace representation. Emissions at smaller angles (labelled with i) are now represented by three terms, one for emissions with $z > z_{\text{cut}}$, which always contribute to the observable, another accounting for emissions with $z < z_{\text{cut}}$ as if they do not contribute to the observable, and a correction (shown in square brackets and highlighted in red) accounting for the fact that emissions with $z < z_{\text{cut}}$ do in fact contribute to the observable. Emissions at smaller angles than θ_s can be exponentiated and the correction evaluated:

$$
\begin{aligned}
&\Sigma^{\text{real}}_{\text{massive}} = \\
&\int\frac{\mathrm{d}\nu}{2\pi i\nu}e^{\nu}\sum_{q=0}^{\infty}\Bigg\{\prod_{j=0}^{q}\left(\bar{\alpha}\int_0^{z_{\text{cut}}}\frac{\mathrm{d}z_j}{z_j}\int_{\theta_s^2}^{1}\frac{\mathrm{d}\theta_j^2}{\theta_j^2}\Theta(\theta_j-\theta_{j+1})\right)\bar{\alpha}\int_{z_{\text{cut}}}^{1}\frac{\mathrm{d}z_s}{z_s}\int_0^1\frac{\mathrm{d}\theta_s^2}{\theta_s^2}e^{-\nu\frac{V_{\text{sc}}(k_s)}{v}} \\
&\quad\exp\left[\bar{\alpha}\int_{z_{\text{cut}}}^{1}\frac{\mathrm{d}z}{z}\int_0^{\theta_s^2}\frac{\mathrm{d}\theta^2}{\theta^2}e^{-\nu\frac{V_{\text{sc}}(k)}{v}}+\bar{\alpha}\int_0^{z_{\text{cut}}}\frac{\mathrm{d}z}{z}\int_0^{\theta_s^2}\frac{\mathrm{d}\theta^2}{\theta^2}+\mathcal{O}(\bar{\alpha}_s z_{\text{cut}}^{a}\theta_s^{a+b})\right]\Bigg\}. \qquad \text{(B.3)}
\end{aligned}
$$

One can consider expanding this exponential to any order and observe that the term in square brackets (highlighted in red) will at most generate NNLL terms suppressed by powers of both v and z_{cut} once the integral over θ_s is carried out, which is sufficient to show that this term can be dropped unless one wants to capture power corrections in v and z_{cut}, which we do not. Equivalently, any emission softer than z_{cut} can be dropped from $V_s(\{\tilde{p}\}, k_1, ..., k_n)$, as we have made use of in the main text.

Appendix C

Appendices for Chapter 6

C.1 Finite τ approximations at fixed order

Here we explain the impact of the different approximations on emissions ρ_a and ρ_b, which enter the pre-factor for the resummed expressions in the small τ limit and for finite τ. In order to illustrate this we examine the differential distribution in a fixed-coupling approximation and at order $\bar{\alpha}^3$, which is the first order at which τ_{32} is non-zero. The finite τ result truncated at order $\bar{\alpha}^3$ is (from Eq. (6.12)):

$$\frac{\rho\tau}{\sigma}\frac{\mathrm{d}^2\sigma}{\mathrm{d}\rho\mathrm{d}\tau} \overset{\tau<1/2}{=} \bar{\alpha}^2\frac{1}{1-\tau} \int_\zeta^1 \frac{\mathrm{d}z_a}{z_a}\int_\zeta^1 \frac{\mathrm{d}z_b}{z_b}\int_0^\rho \frac{\mathrm{d}\rho_a}{\rho_a}\frac{\rho}{\rho-\rho_a}\Theta\left(\rho_a > \frac{1-\tau}{2-\tau}\rho\right)\Theta_{\rho_{\min}} R'((\rho-\rho_a)\tau), \tag{C.1}$$

where in a fixed-coupling approximation, and to leading-logarithmic accuracy, we have,

$$R'((\rho-\rho_a)\tau) = \bar{\alpha}\left(\ln\frac{1}{\rho-\rho_a} + \ln\frac{1}{\tau}\right). \tag{C.2}$$

We remind the reader that

$$\Theta_{\rho_{\min}} = \Theta\left(\min\left((\rho-\rho_a)(1-\tau), z_a z_b \max\left(\frac{\rho_a}{z_a}, \frac{(\rho-\rho_a)(1-\tau)}{z_b}\right)\right) > \rho_{\min}\right), \tag{C.3}$$

where $\frac{\rho_a}{z_a} = \theta_a^2$ and $\frac{(\rho-\rho_a)(1-\tau)}{z_b} = \frac{\rho_b}{z_b} = \theta_b^2$. For our illustrative purposes, let us take a specific contribution to the pre-factor that arises from the region $\theta_a^2 \gg \theta_b^2$ and $\rho_b = (\rho-\rho_a)(1-\tau) < z_b\rho_a$. We also assume values of the parameters so that $\frac{\rho_{\min}}{\rho} > \zeta$, again purely as part of our illustrative example [1]. The conclusions we derive will apply to other regions of phase space and parameter ranges too. For the region of phase space

---

[1] Strictly speaking the condition is $\frac{\rho_{\min}}{\rho} > \frac{\zeta}{1+\zeta}$.

considered we obtain the contribution

$$\frac{\rho\tau}{\sigma}\frac{\mathrm{d}^2\sigma}{\mathrm{d}\rho\mathrm{d}\tau} \overset{\tau<1/2}{=} \bar{\alpha}^2\frac{1}{1-\tau}$$
$$\int_\zeta^1 \frac{\mathrm{d}z_a}{z_a}\int_\zeta^1 \frac{\mathrm{d}z_b}{z_b}\int_0^\rho \frac{\mathrm{d}\rho_a}{\rho_a}\frac{\rho}{\rho-\rho_a}\Theta\left(\rho_a > \frac{1-\tau}{2-\tau}\rho\right) R'((\rho-\rho_a)\tau)\Theta\left((\rho-\rho_a)(1-\tau) > \rho_{\min}\right)$$
$$\Theta\left(\frac{\rho_a}{z_a} > \frac{(\rho-\rho_a)(1-\tau)}{z_b}\right)\Theta\left((\rho-\rho_a)(1-\tau) < z_b\rho_a\right). \quad \text{(C.4)}$$

The directly computed small τ limit result, corresponding to the result in section 6.3.2, is

$$\frac{\rho\tau}{\sigma}\frac{\mathrm{d}^2\sigma}{\mathrm{d}\rho\mathrm{d}\tau} = \bar{\alpha}^2\int_\zeta^1 \frac{\mathrm{d}z_a}{z_a}\int_\zeta^1 \frac{\mathrm{d}z_b}{z_b}\int_0^\rho \frac{\mathrm{d}\rho_b}{\rho_b}\Theta\left(\rho_b > \rho_{\min}\right)\times$$
$$\Theta\left(\rho_b < z_b\rho\right)\Theta\left(\rho > \frac{z_a}{z_b}\rho_b\right)\bar{\alpha}\left(\ln\frac{1}{\tau}+\ln\frac{1}{\rho_b}\right) \quad \text{(C.5)}$$

which gives

$$\frac{\rho\tau}{\sigma}\frac{\mathrm{d}^2\sigma}{\mathrm{d}\rho\mathrm{d}\tau} = \frac{1}{2}\bar{\alpha}^2\ln\frac{1}{\zeta}\ln^2\frac{\rho}{\rho_{\min}}\times\bar{\alpha}\left(\ln\frac{1}{\rho_{\min}}+\ln\frac{1}{\tau}+\frac{1}{3}\ln\frac{\rho_{\min}}{\rho}\right). \quad \text{(C.6)}$$

Evaluating the small τ limit of the exact result in our chosen configuration i.e. Eq. (C.4), gives:

$$\frac{\rho\tau}{\sigma}\frac{\mathrm{d}^2\sigma}{\mathrm{d}\rho\mathrm{d}\tau} = \frac{1}{2}\bar{\alpha}^2\ln\frac{1}{\zeta}\ln^2\frac{\rho}{\rho_{\min}}\times\bar{\alpha}\left(\ln\frac{1}{\rho_{\min}}+\ln\frac{1}{\tau}+\frac{1}{3}\ln\frac{\rho_{\min}}{\rho}\right)+\frac{3}{4}\bar{\alpha}^3\zeta(3)\ln\frac{1}{\zeta}, \quad \text{(C.7)}$$

which differs from Eq. (C.6) by a highly subleading $\bar{\alpha}^3\zeta(3)\ln\frac{1}{\zeta}$ term. The full τ dependent result from Eq. (C.4) reads

$$\frac{\rho\tau}{\sigma}\frac{\mathrm{d}^2\sigma}{\mathrm{d}\rho\mathrm{d}\tau} =$$
$$\frac{\bar{\alpha}^3}{1-\tau}\Bigg[\frac{1}{2}\ln\frac{1}{\zeta}\ln^2\frac{\rho}{\rho_{\min}}\times\left(\ln\frac{1}{\rho_{\min}}+\ln\frac{1}{\tau}+\frac{1}{3}\ln\frac{\rho_{\min}}{\rho}+\ln\left(1-\tau\right)\right)-$$
$$\ln\frac{1}{\zeta}\,\mathrm{Li}_3\left(\frac{1}{\tau-1}\right)\Bigg]. \quad \text{(C.8)}$$

We note that retaining the finite τ effects results in the appearance of three features : Firstly there is the overall $1/(1-\tau)$ multiplicative term, which has a significant impact on the result beyond the small τ region and is important to retain. Secondly there is a $\ln(1-\tau)$ term in addition to the large logarithms we resum. Given that we do not resum logarithms of $1-\tau$, and indeed focus on the region $\tau \sim 0.2$, this constitutes a negligible contribution relative to the logarithms we resum, dominated by the $\ln\frac{1}{\rho_{\min}}$ term. Finally there is a highly subleading $\bar{\alpha}^3\ln\frac{1}{\zeta}$ term accompanied by a trilogarithm in $1-\tau$ which we can safely neglect. Hence ignoring the τ dependence in the pre-factor, other than the $1/(1-\tau)$ term, is a valid approximation for our work.

C.2 Direct calculation of the cumulative background distribution

Here we provide an alternate derivation of $\rho\frac{\mathrm{d}\Sigma(\tau)}{\mathrm{d}\rho}$ that directly derives this distribution as opposed to integrating the double differential. We can start from the standard factorised formula for any number of emissions, similar to Eq. (6.9) but instead of fixing τ_{32} we set an upper bound $\tau_{32} < \tau$:

$$\begin{aligned}
&\frac{\rho}{\sigma}\frac{\mathrm{d}\sigma}{\mathrm{d}\rho\mathrm{d}\tau} = \bar{\alpha}^2 \\
&\int_\zeta^1 \frac{\mathrm{d}z_a}{z_a}\int_0^1 \frac{\mathrm{d}\rho_a}{\rho_a}\int_\zeta^1 \frac{\mathrm{d}z_b}{z_b}\int_0^{\rho_a} \frac{\mathrm{d}\rho_b}{\rho_b}\Theta(\min(\rho_b, z_a z_b \max(\frac{\rho_a}{z_a},\frac{\rho_b}{z_b})) > \rho_{min}) \exp\left[-\int_0^1 R(\rho')\frac{\mathrm{d}\rho'}{\rho'}\right] \\
&\qquad \sum_{p=1}^{\infty}\frac{1}{p!}\prod_{i=1}^{p}\int_0^{\rho_b} R'(\rho_i)\frac{\mathrm{d}\rho_i}{\rho_i}\rho\delta(\rho-\rho_a-\rho_b-\sum_{i\neq a,b}\rho_i)\,\Theta((\rho-\rho_a)(1-\tau)<\rho_b). \qquad \text{(C.9)}
\end{aligned}$$

The delta function can now be used to do the sum over emissions labelled with i, where it is crucial to notice that for any i, $\rho_i < \rho-\rho_a-\rho_b$ as implied by the delta function, and that the upper limit on ρ_i of ρ_b is weaker than this for $\tau < \frac{1}{2}$. Using the standard jet mass result for the sum over emissions, as we did before, we arrive at

$$\begin{aligned}
&\frac{\rho}{\sigma}\frac{\mathrm{d}\sigma}{\mathrm{d}\rho} \overset{\tau<1/2}{=} \bar{\alpha}^2 \\
&\quad\int_\zeta^1 \frac{\mathrm{d}z_a}{z_a}\int_\zeta^1 \frac{\mathrm{d}z_b}{z_b}\int_{\frac{1-\tau}{2-\tau}\rho}^{\rho} \frac{\mathrm{d}\rho_a}{\rho_a}\int_{(1-\tau)(\rho-\rho_a)}^{\min(\rho-\rho_a,\rho_a)} \frac{\mathrm{d}\rho_b}{\rho_b}\frac{\rho}{\rho-\rho_a-\rho_b}\Theta_{\rho_{\min}}(\rho_a,\rho_b,\tau,\rho_{\min},z_a,z_b) \\
&\qquad\qquad R'(\rho-\rho_a-\rho_b)\frac{\exp[-R(\rho-\rho_a-\rho_b)-\gamma_E R'(\rho-\rho_a-\rho_b)]}{\Gamma[1+R'(\rho-\rho_a-\rho_b)]}. \qquad \text{(C.10)}
\end{aligned}$$

We now wish to integrate over ρ_b which we note contains two regions, $\rho_a < \rho-\rho_a$ and $\rho_a > \rho-\rho_a$, the former of which vanishes if we neglect the τ dependence of the ρ_a integral limits as in section 6.3.3 [2]. Enforcing the condition $\rho_b > \rho_{\min}$, which is embodied in $\Theta_{\rho_{\min}}$ gives an upper limit on ρ_a of $\rho - \frac{\rho_{\min}}{1-\tau}$, which, within our accuracy we can approximate as ρ. To carry out this integral within single logarithmic accuracy, we can expand the radiator about some fixed ρ_b which we take as $(\rho-\rho_a)(1-\tau_0)$so that:

$$R(\rho-\rho_a-\rho_b) \simeq R((\rho-\rho_a)\tau_0) - R'((\rho-\rho_a)\tau_0)\ln\left(\frac{\rho-\rho_a-\rho_b}{(\rho-\rho_a)\tau_0}\right) + \mathcal{O}(R''), \qquad \text{(C.11)}$$

---

[2] The neglected term is proportional to $\alpha^3 L^2 L_\rho$ where L_ρ is a log of ρ or $\rho_{\min}$ while L is a log of the ratio or ζ. This is clearly beyond our accuracy.

where τ_0 should be chosen close to τ as values of ρ_b close to $(\rho - \rho_a)(1-\tau)$ are expected to dominate the integral. The integral can then be carried out to give

$$\begin{aligned}\frac{\rho}{\sigma}\frac{\mathrm{d}\sigma}{\mathrm{d}\rho} \overset{\tau<1/2}{=} \bar{\alpha}^2 \int_\zeta^1 \frac{\mathrm{d}z_a}{z_a} \int_\zeta^1 \frac{\mathrm{d}z_b}{z_b} \int_{\frac{1}{2}\rho}^{\rho} \frac{\mathrm{d}\rho_a}{\rho_a} \frac{\rho}{\rho-\rho_a} \Theta_{\rho_{\min}}\left(\rho_a, \rho_{\min}, z_a, z_b\right) \\ \left(\frac{\tau}{\tau_0}\right)^{R'((\rho-\rho_a)\tau_0)} {}_2F_1(1, R'(\rho-\rho_a)\tau_0, 1+R'(\rho-\rho_a)\tau_0, \tau) \\ \frac{\exp[-R((\rho-\rho_a)\tau_0) - \gamma_E R'((\rho-\rho_a)\tau_0)]}{\Gamma[1+R'((\rho-\rho_a)\tau_0)]}, \qquad \text{(C.12)}\end{aligned}$$

in perfect agreement with Eq. (6.16).

Although less convenient for making contact with the result reported in Eq. (6.16), we could equally well have integrated over ρ_a, leaving the ρ_b integral to be done numerically, as we could have done in section 6.3.3. To do this one would expand $R(\rho - \rho_a - \rho_b)$ around $\rho_a = \rho - \frac{\rho_b}{1-\tau}$ which would lead to:

$$\begin{aligned}\frac{\rho}{\sigma}\frac{\mathrm{d}\sigma}{\mathrm{d}\rho} \overset{\tau<1/2}{=} \\ \bar{\alpha}^2 \int_\zeta^1 \frac{\mathrm{d}z_a}{z_a} \int_\zeta^1 \frac{\mathrm{d}z_b}{z_b} \int_{\rho_{min}}^{\frac{\rho}{2}} \frac{\mathrm{d}\rho_b}{\rho_b} \frac{\rho}{\rho-\rho_b} \left(\frac{\tau(1-\tau_0)}{(1-\tau)\tau_0}\right)^{R'(\rho_b\frac{\tau_0}{1-\tau_0})} \Theta_{\rho_{\min}}\left(\rho_b, \rho_{\min}, z_a, z_b\right) \\ {}_2F_1(1, R'(\rho_b\frac{\tau_0}{1-\tau_0}), 1+R'(\rho_b\frac{\tau_0}{1-\tau_0}), \frac{\rho_b\tau_0}{(1-\tau_0)(\rho-\rho_b)}) \\ \frac{\exp[-R(\rho_b\frac{\tau_0}{1-\tau_0}) - \gamma_E R'(\rho_b\frac{\tau_0}{1-\tau_0})]}{\Gamma[1+R'(\rho_b\frac{\tau_0}{1-\tau_0})]}, \qquad \text{(C.13)}\end{aligned}$$

where again, τ_0 should be taken close to τ, and any τ dependence in the leading order pre-factor has been neglected.